IOWA STATE UNIVERSITY
Digital Repository

Graduate Theses and Dissertations | Graduate College

2012

Structural and magnetic properties of transition metal substituted $BaFe_2As_2$ compounds studied by x-ray and neutron scattering

Min Gyu Kim
Iowa State University

Follow this and additional works at: http://lib.dr.iastate.edu/etd

 Part of the Condensed Matter Physics Commons

Recommended Citation
Kim, Min Gyu, "Structural and magnetic properties of transition metal substituted $BaFe_2As_2$ compounds studied by x-ray and neutron scattering" (2012). *Graduate Theses and Dissertations*. 12952.
http://lib.dr.iastate.edu/etd/12952

This Dissertation is brought to you for free and open access by the Graduate College at Iowa State University Digital Repository. It has been accepted for inclusion in Graduate Theses and Dissertations by an authorized administrator of Iowa State University Digital Repository. For more information, please contact digirep@iastate.edu.

Structural and magnetic properties of transition metal substituted $BaFe_2As_2$ compounds studied by x-ray and neutron scattering

by

Min Gyu Kim

A dissertation submitted to the graduate faculty

in partial fulfillment of the requirements for the degree of

DOCTOR OF PHILOSOPHY

Major: Condensed Matter Physics

Program of Study Committee:

Alan I. Goldman, Co-major Professor

Andreas Kreyssig, Co-major Professor

Robert J. McQueeney

Bruce N. Harmon

James Cochran

Ralph E. Napolitano

Iowa State University

Ames, Iowa

2012

Copyright © Min Gyu Kim, 2012. All rights reserved.

TABLE OF CONTENTS

LIST OF TABLES

LIST OF FIGURES

CHAPTER 1. Introduction

In 2008, Kamihara *et al.* [1] discovered superconductivity in LaFeAsO (1111) compounds and Rotter *et al.* [2] found superconductivity in the $BaFe_2As_2$ (122) compounds. They are often called the FeAs-based superconductors or the iron pnictide superconductors and also include the Li-Fe-As system and the Fe-Te system.[3, 4] Superconductivity in materials containing "Fe" has been known but "Fe" in such materials are non-magnetic.[4] The significance of the FeAs-based superconductors is that Fe carries a moment and, in general, the presence of magnetic moments is detrimental to superconductivity because of spin-flip scattering (further discussion in the following section). The superconducting transition temperatures (T_c) of the FeAs-based superconductors are somewhat lower (< 60 K) compared to the cuprate superconductors, and the critical field in these superconductors is high (on the order of 50 - 100 T).[3, 4] Except the ceramic compounds such as RFeAsO (R = rare earth) superconductors, the FeAs-based superconductors are mechanically metals and feature malleability, weldability, ductility and so on. However, further studies are needed to fully characterize the mechanical properties before these materials can be applied for practical uses.

One of the major scientific concerns is the superconducting transition temperature. Naively speaking, if a room temperature superconductor would be found, it would change every way of using electricity. The ultimate goal of world-wide investigations on various properties of superconductors is to understand how superconductivity occurs so that one will be able to design materials that will superconduct at the room temperature or temperatures near room temperature. Therefore, understanding various properties of superconductors is necessary.

1.1 "Conventional" and "Unconventional" superconductors

Superconducting materials may be cast in two categories: (1) materials such as the elements [5, 6], NbTi, and Nb_3Sn alloys [6–9], and (2) other systems including the cuprate superconductors [10–14], heavy fermion superconductors [15, 16], some organic compounds [17], and now the FeAs-based superconductors. The former group has come to be termed as "conventional" superconductors while the latter group is generally accepted to be "unconventional" superconductors. This categorization is based on our current understanding of how conventional superconductivity occurs - the "BCS" theory of superconductivity.

The BCS theory was proposed by J. Bardeen, L. N. Cooper, and J. R. Schrieffer (BCS) in 1957.[18, 19] According to BCS, electrons in superconductors condense into pairs, "Cooper pairs",[18–20] which are bosons, consisting of one spin-up electron and one spin-down electron, that can occupy the same ground state (see Bose-Einstein condensation [21, 22]). This condensation state is highly collective so an energy to break a single pair or multiple pairs can not break the superconducting state unless the energy is high enough to break all Cooper pairs.[18–20] Therefore, Cooper pairs do not experience any resistance provided by energies that may break few pairs but are not sufficiently large to break all the pairs - zero electric resistivity. Because the Cooper pair consists of one spin-up and one spin-down electrons, any internal field supplied by local moments or external field supplied by magnets is detrimental to superconductivity. Internal/external fields flip spins of electrons to be parallel to the field direction of moments or magnets, which break the Cooper pairs.

In BCS theory, electrons can pair when an attractive potential exists, independent of the kind and strength of the attractive potential.[18, 19] The attractive potential in the "conventional" superconductors is provided by lattice vibration (phonon). Electrons attract positively charged ions in the lattice, which causes a more positively charged area in the lattice which, in turn, attracts another electron. Two electrons are bound to each other and it is called the Cooper pair.[18–20] This process is schematically shown in Figure 1.1. The coupling between electrons and lattice vibration (phonon) is important for Cooper pairing in the "conventional" superconductors and the BCS theory can predict many properties of the "conventional" super-

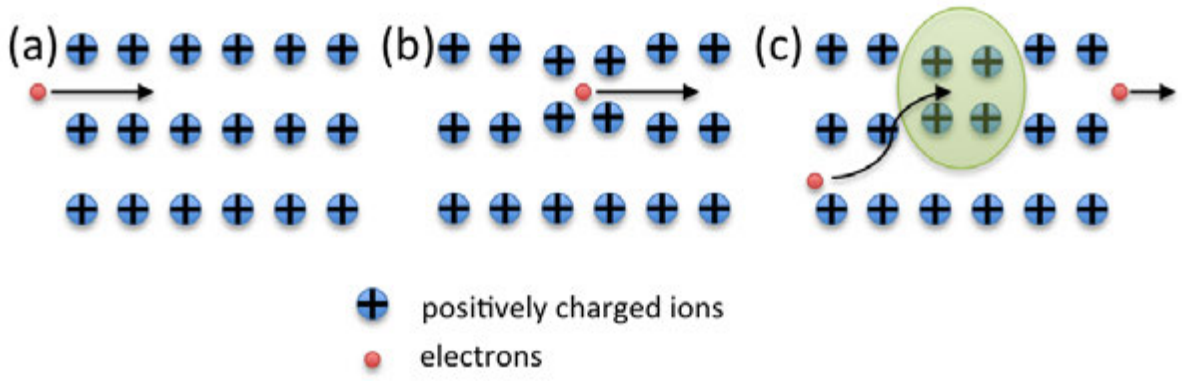

Figure 1.1 Electron-lattice interaction. (a) Electron entering in the lattice. The lattice is composed of positively charged ions. (b) Coulomb attraction brings electron and adjacent positive charges close together. (c) The attraction creates a more positively charged area (green circle) that attracts another electron. The two electrons are paired up as the Cooper pair. After Ref. [18, 19].

conductors including superconducting transition temperatures by knowing the electron-phonon coupling.[18, 19] The importance/effect of electron-phonon coupling has been confirmed by experiments, for example isotopic substitutions where a "heavier" isotope element, that is more difficult to be displaced in the lattice than the lighter one, results in weaker electron-phonon coupling and lower T_c.[23, 24]

"Unconventional" superconductivity can be understood on the basis of Cooper pairing. However, the origin of the potential may not be a lattice vibration (it can even be a repulsive potential). The BCS prediction of T_c based on the electron-phonon coupling fails in the "unconventional" superconductors, and the effect of isotope substitution is small or nonexistent.[3, 4, 25] The origin of the attractive potential is not completely known for the "unconventional" superconductivity, but it has been suggested that the spin fluctuations may play a key role in the FeAs-based superconductors.[26, 27] One of the simplest pairing process via spin fluctuations is illustrated in Fig. 1.2 for a localized antiferromagnetic system. Localized moments, m_1 and m_2 (blue arrows), are aligned anti-parallel (antiferromagnetically) through spin exchange coupling, I. Conduction electron, e_1, couples to a localized moment, m_1, through exchange coupling J and is polarized with spin-down in Fig. 1.2. Through spin exchange coupling, I, another conduction electron, e_2, is favorable to be polarized spin-up. In

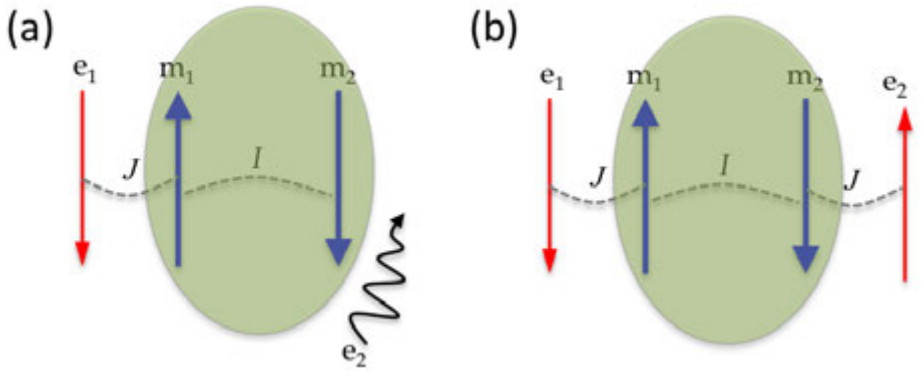

Figure 1.2 Illustration of one of the simplest mechanism of spin fluctuations mediated pairing. (a) Local moment, m_1 and m_2 (blue arrows), are aligned anti-parallel through spin fluctuations exchange coupling I. A conduction electron, e_1, is polarized as spin-down (red arrow). (b) When another electron, e_2, enters, spin fluctuations exchange coupling polarizes a local moment, m_2, which favors a spin-up polarization of an electron, e_2. Therefore, e_1 (spin-down) and e_2 (spin-up) can pair via spin fluctuations. After Ref. [28]

this way, the conduction electrons e_1 and e_2 can form a Cooper pair.[28]

1.2 Phase diagrams of "unconventional" superconductors

The best known "unconventional" superconductors to date are the heavy fermion superconductors (e.g. $CeCu_2Si_2$, $CeRhIn_5$, URu_2Si_2, etc.), [15, 16] the cuprate superconductors (e.g. $La_{2-x}Sr_xCuO_4$, $YBa_2Cu_3O_7$, etc) [11–14], and now, the newly discovered FeAs-based superconductors.[3, 4] The phase diagrams of the aforementioned "unconventional" superconductors display interesting similarities. Figure 1.3 shows the phase diagrams of (a) the heavy fermion superconductors, (b) the cuprate superconductors, and (c) the FeAs-based superconductors.[29] First, I note that superconductivity exists in a dome-like region over a finite range in pressure or doping. For the heavy fermion superconductors, superconductivity is induced most efficiently by applying external pressure if superconductivity is not present at ambient conditions. In the cuprate and the FeAs-based superconductors, electron or hole doping is frequently used to induce superconductivity. Typical superconducting transition temperatures are on the order of few degrees Kelvin in the heavy fermion superconductors, but on the order of > 100 K in the cuprate superconductors. The T_cs of the FeAs-based superconduc-

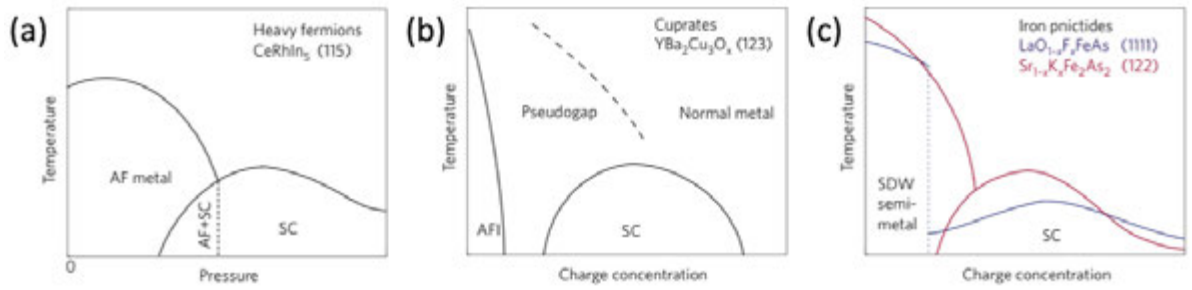

Figure 1.3 Representative schematic phase diagrams of (a) heavy fermion superconductors, (b) the cuprate superconductors, and (c) the FeAs-based (iron pnictide) superconductors. All phase diagrams show a close approximate occurrence of different ground states (e.g. antiferromagnetic ordering and superconductivity). After Ref. [29].

tors are approximately between 20 K and 60 K which locate the FeAs-based superconductors between the heavy fermion and the cuprate superconductors.[3, 4, 11–16, 30]

A second general characteristic of "unconventional" superconductors is the presence of an antiferromagnetic ground state in the "parent phase" materials. The "parent phase" materials are compounds without pressure or doping. For example, parent compounds in Figs. 1.3 (a) − (c) are $CeRhIn_5$ without pressure, $YBa_2Cu_3O_6$ without doping on the Y, Ba, Cu, or O sites, and LaFeAsO without doping on the La, Fe, As, or O sites, respectively. The antiferromagnetic ordering occurs as temperature is lowered in many of these materials as shown in Fig 1.3. In the heavy fermion superconductors [Fig 1.3 (a)], as the external pressure is increased, the antiferromagnetic ordering is suppressed continuously but extends into the superconducting dome (coexistence of antiferromagnetism and superconductivity), and the antiferromagnetism is identified with the rare-earth ions and is usually localized (one example of non-localized magnetism is Ce in which the magnetism is originated from quite extended and hybridized 4f band).[15, 16] In the cuprate superconductors where the undoped parent compounds are insulators[Fig 1.3 (b)], with doping, the antiferromagnetism is completely suppressed before superconductivity emerges (exclusion of antiferromagnetism and superconductivity) and the antiferromagnetic ordering is well understood in terms of the Heisenberg approximation so the cuprate superconductors are best characterized as localized moment systems.[11–14] Both

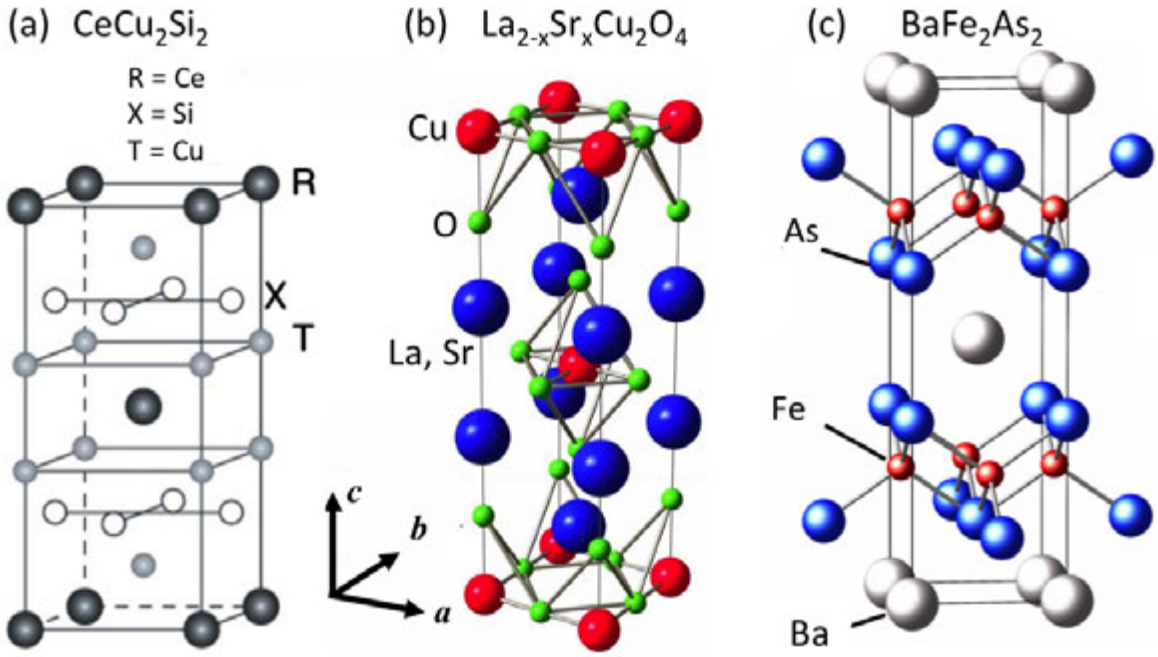

Figure 1.4 Representative crystal structure of (a) heavy fermion $CeCu_2Si_2$ superconductor, (b) the cuprate $La_{2-x}Sr_xCu_2O_4$ superconductors, and (c) the FeAs-based $BaFe_2As_2$ superconductors. See the text for details. After Ref. [14, 16].

the coexistence and exclusivity of antiferromagnetism and superconductivity are observed in the FeAs-based superconductors [Fig 1.3 (c)]. In some materials ($LaFeAsO_{1-x}F_x$ as shown in the figure), antiferromagnetism is completely suppressed before the superconductivity emerges whereas in other materials ($Sr_{1-x}K_xFe_2As_2$ as shown in the figure), the antiferromagnetism coexists with superconductivity over some finite range of doping.[30] The antiferromagnetism in the FeAs-based superconductors, which the undoped parent compounds are metallic, derives from the conduction electrons that are not localized.[3, 4, 30]

Finally, although it is not evident in the phase diagrams in Fig. 1.3, all systems are tetragonal or orthorhombic as shown in Fig. 1.4 and anisotropy in these unconventional superconductors seems important. Many measurements including resistivity, magnetization, and inelastic neutron scattering observed that these superconductors exhibit directionally different properties in the $\vec{a}\vec{b}$ plane and along the $\vec{c}$ axis. The anisotropy in the heavy fermion superconductors is small but they seem to exhibit higher T_c when the anisotropy is larger.[15, 16]

The cuprate superconductors are the well-known example of a two dimensional system and have large anisotropy,[11–14] and inelastic neutron scattering measurements have shown that the FeAs-based superconductors change their character from three dimensional to quasi-two dimensional as doping increases (moderate anisotropy compared to the heavy fermion and cuprate superconductors).[30] Figure 1.4 displays typical crystal structures of those systems: (a) the tetragonal $I4/mmm$ $ThCr_2Si_2$ type structure ($CeCu_2Si_2$) frequently found in heavy fermion superconductors[16], (b) the tetragonal $I4/mmm$ structure for $La_{2-x}Sr_xCuO_4$ compound which is a common structure among the cuprate superconductors[11–14] and, (c) the tetragonal $I4/mmm$ $ThCr_2Si_2$ type structure found in $BaFe_2As_2$ compound.[3, 4, 30] The cuprate and FeAs-based superconductors feature layered structures - CuO layers in the $\vec{a}\vec{b}$ plane stacked along the $\vec{c}$ axis and FeAs layers in the $\vec{a}\vec{b}$ plane stacked along the $\vec{c}$ axis, respectively. The heavy fermion superconductors were not viewed as a layered structure but some of them have the same $ThCr_2Si_2$ type structure as in the FeAs-based superconductors [Fig 1.4 (a) and (c)]. Hence the anisotropy found in the "unconventional" superconductors may be closely related to the layered structures.

Why are the FeAs-based superconductors interesting to study? As I discussed previously, these materials have very high critical fields and, unlike the cuprates, have mechanical properties that may be amenable to practical applications. The antiferromagnetism in the FeAs-based superconductors is derived from the conduction electrons that also participate in Cooper pairing below T_c so that the antiferromagnetism and superconductivity compete for the same electrons whereas, in the cuprate superconductors and some of the heavy fermion superconductors, localized electrons carrying moments seem to contribute to either Cooper pairing or antiferromagnetism. This difference, in other words itinerant system versus localized system, implies that the underlying physics may be different in those materials. Based upon the quasi-two dimensional character of the FeAs-based superconductors with relatively high T_c, the FeAs-based superconductors seem to locate between the heavy fermion superconductors (small anisotropy with low superconducting transition temperatures) and the cuprate superconductors (high anisotropy with high superconducting temperatures). Hence, studying AFM, SC, and interplay between AFM and SC as well as AFM, structure, and connection to dimensionality in

the FeAs-based superconductors are not only intriguing but also prerequisite for understanding the superconductivity in these materials. Ultimately, understanding the properties of the FeAs-based superconductors may lead to an understanding of various properties of "unconventional" superconductivity.

1.3 Purpose of dissertation

The purpose of my dissertation is to understand the structural and magnetic properties of the newly discovered FeAs-based superconductors and the interconnection between superconductivity, antiferromagnetism, and structure. X-ray and neutron scattering techniques are powerful tools to directly observe the structure and magnetism in this system. I used both x-ray and neutron scattering techniques on different transition substituted $BaFe_2As_2$ compounds in order to investigate the substitution dependence of structural and magnetic transitions and try to understand the connections between them. Experimental results presented in this dissertation were collected at several places: x-ray diffraction data at the Ames Laboratory, IA, x-ray resonant magnetic scattering data at the Argonne National Laboratory, IL, and neutron diffraction data at the Oak Ridge National Laboratory, TN and at the University of Missouri Research Reactor, MO.

The organization of my dissertation is as follows: In Chapter 2, I briefly summarize what has been reported about superconductivity, crystal structure, phase transitions, phase diagrams, and interplay between superconductivity, antiferromagnetism and structure of the FeAs-based superconductors in literature. Chapter 3 provides overviews of experimental techniques of x-ray and neutron scattering focusing on the practical aspect. Next, in Chapter 4, I will discuss my experimental results of structural and magnetic properties of transition metal (Co, Rh, Ru, and Mn) substituted $BaFe_2As_2$ compounds, and commensurate/incommensurate antiferromagnetic ordering in transition metal (Ni and Cu) substituted $BaFe_2As_2$ compounds in Chapter 5. Conclusions and outlook is given in Chapter 6.

CHAPTER 2. Introduction to the FeAs-based superconductors

In 2008, the FeAs-based superconductors (fluorine substituted $LaFeAsO_{1-x}F_x$ compounds, 1111 compounds) were discovered by Kamihara *et al.*[1] and invigorated the field of superconductivity once again. The substitution of 4% fluorine for the oxygen in $LaFeAsO_{1-x}F_x$ induced superconductivity at $T_c \sim 25$ K.[1] Superconductivity in this compound is not only realized by fluorine substitution on the oxygen site but also by oxygen deficiency or element substitutions on the La site, the Fe site, and/or the As site.[31–60] When other rare earth elements were used as a starting element instead of La, it was found that T_c rises rapidly and reached ~ 56 K in $Gd_{1-x}Th_xFeAsO$.[44]

Later that year, the $BaFe_2As_2$ compound (122 compound) was introduced as a possible candidate material for superconductivity, similar to RFeAsO compounds (R = rare earth elements).[2, 61] Indeed, K substitution on the Ba site of $BaFe_2As_2$ compounds showed $T_c = 38$ K for 40 % K substitution.[2] Substitutions on the AE site, the Fe site, and/or the As site of $AEFe_2As_2$ (AE = Ca, Sr, and Ba) also induces superconductivity, but the highest T_c in this family of compounds remains at 38 K.[62–105]

Much effort was put to search for other FeAs-based superconductors resulting in the discovery of the so-called 111 compounds and 11 compounds, LiFeAs and $FeSe_{1-x}Te_x$, respectively. Among the 111 compounds, the stoichiometric LiFeAs compounds show the highest $T_c \approx 20$ K.[106–117] The 11 compounds do not contain As but Te, Se, and/or S, and have a very similar crystallographic structure as other FeAs-based superconductors. The highest T_c was found in $FeSe_{1-x}Te_x$ ($x = 0.5$) and $FeSe_{1-x}S_x$ ($x = 0.2$) at ~ 15 K.[118–130]

An understanding of similarities and differences between each family of compounds is prerequisite to an understanding of the underlying physics of the FeAs-based superconductors. Therefore, in this chapter I provide a basic introduction to the essential features of these com-

pounds. This chapter is organized as follows. In Section 2.1, the superconductivity of each family compound will be summarized. Then, the commonalities of the crystallographic structures (Section 2.2), and the common structural and magnetic phase transitions (Section 2.3) will be introduced. Lastly, the interplay between superconductivity, magnetism, and structure together with origins of the antiferromagnetic ordering and structural transition will be discussed in Section 2.4.

2.1 Superconductivity

2.1.1 1111 family

The discovery of superconductivity in FeAs based superconductors originated from unceasing work in quaternary oxypnictides in Hosono's group. Hosono's group found superconductivity at $\sim$ 4 K and $\sim$ 3 K in LaFePO in 2006 and LaNiPO in 2007, respectively.[131, 132] The same group found superconductivity at $\sim$ 25 K in 4 % F substituted LaFeAsO in 2008,[1] opening a new chapter in the area of unconventional superconductivity that has dominated the literature on superconductivity for the past four years.

After the initial discovery of superconductivity in fluorine substituted samples, it was shown that superconductivity can also be induced in other RFeAsO compounds by fluorine substitution with R = La, Ce, Pr, Nd, Sm, and Gd.[1, 33–35, 37–39] The highest T_c in various 1111 compounds discussed in this section is summarized in Table 2.1. Secondly, not only fluorine substitution, but also a deficiency of oxygen can produce superconductivity in the 1111 family (RFeAsO$_{1-y}$).[40–42, 50] Third, it has also been reported that certain transition metal substitutions on the Fe site results in superconductivity. Transition metal elements, TM = Co, Ni, Rh, and Ir, in RFe$_{1-x}TM_x$AsO induce superconductivity [45–48, 52–55, 57–60] whereas TM = Mn, Cr, Zn, and Ru do not result in superconductivity.[52, 55, 133–135] Fourth, element substitutions on the R site or on the As site can also introduce superconductivity. It was first reported that Sr substitution on the La site in LaFeAsO compounds did not induce superconductivity by Kamihara *et al.*[1] However, other groups found superconductivity introduced by substitutions on the R site. Among all of the superconducting 1111 compounds and,

Table 2.1 The highest T_c in various 1111 compounds. x is substitution levels in given compounds.

Compound	x	T_c (K)	Reference	Note
$LaFeAsO_{1-x}F_x$	0.11	26	[1]	
$CeFeAsO_{1-x}F_x$	0.16	41	[38]	
$PrFeAsO_{1-x}F_x$	0.11	44	[34]	
$NdFeAsO_{1-x}F_x$	0.11	49	[35]	
$SmFeAsO_{1-x}F_x$	0.10	53	[37]	
$GdFeAsO_{1-x}F_x$	0.17	37	[39]	
$LaFeAsO_{1-x}$	0.15	31	[40]	
$CeFeAsO_{1-x}$	0.15	47	[40]	
$PrFeAsO_{1-x}$	0.15	51	[40]	
$NdFeAsO_{1-x}$	0.15, 0.50	54	[40, 42]	
$SmFeAsO_{1-x}$	0.15	55	[40]	
$GdFeAsO_{1-x}$	0.55	52	[41]	
$TbFeAsO_{1-x}$	0.30	53	[50]	under pressure, 5 GPa
$DyFeAsO_{1-x}$	0.30	52	[50]	under pressure, 5.5 GPa
$SmFe_{1-x}Co_xAsO$	0.10	15	[46]	
$SmFe_{1-x}Ni_xAsO$	0.06	11	[58]	
$NdFe_{1-x}Rh_xAsO$	0.10	15	[59]	
$GdFe_{1-x}Ir_xAsO$	0.20	19	[60]	
$La_{1-x}Sr_xFeAsO$	0.13	25	[32]	
$Pr_{1-x}Sr_xFeAsO$	0.20	16	[51]	
$Nd_{1-x}Sr_xFeAsO$	0.20	14	[49]	
$Gd_{1-x}Th_xFeAsO$	0.20	56	[44]	
$LaFeAs_{1-x}P_xO$	0.11	11	[56]	

perhaps, all FeAs-based superconductors, the highest superconducting transition temperature T_c is achieved by substitution on the R site at 56 K (R = Gd with 20% Th [44]). Finally, it was also found that P substitution on the As site brings superconductivity at 11 K in R = La with 11% P. Because the valence of P is the same as the valence of As (P^{3-} and As^{3-}), but the ionic radius of P (0.44 Å) is smaller than the ionic radius of As (0.58 Å)[136], P substitution on the As site in RFeAsO compounds has been considered as isoelectronic doping and introducing internal(chemical) pressure.[56] Superconductivity under external pressure is beyond the scope of my dissertation so that it will not be discussed.

Although the 1111 family has been widely studied, readers should be cautious about the compositions stated in the literature. For example, Köhler and Behr measured the compositions of their polycrystalline samples using the electron beam micro-probe analysis method, with both an energy dispersive x-ray detector and a wavelength dispersive x-ray detector, and found that the actual compositions in their $LaFeAsO_{1-x}F_x$ and $SmFeAsO_{1-x}F_x$ compounds were significantly different from the nominal compositions.[137] Since the most of the compositions in the literature were reported with nominal concentrations, one can not exclude that the real compositions may be very different from the reported values.

2.1.2 122 family

Since the 122 family compounds have the well-known $ThCr_2Si_2$ type structure (Section 2.2), the first member of this family, non-superconducting $BaFe_2As_2$ compound, was quickly discovered by Johrendt's group.[61] It was soon realized that this family forms large and homogeneous single crystals,[63, 66, 67, 69–71] and the availability of large single crystals has fostered many detailed studies of the 122 family.

Superconductivity in the 122 family was first observed for K substitution on the Ba site of $BaFe_2As_2$ compounds. Polycrystalline $Ba_{1-x}K_xFe_2As_2$ shows a superconducting transition temperature, T_c, at 38 K for $x = 0.4$.[2] $SrFe_2As_2$, $CsFe_2As_2$, KFe_2As_2, $EuFe_2As_2$ and $CaFe_2As_2$ compounds were studied, with T_c = 3.8 K in polycrystalline KFe_2As_2 compound and 2.6 K in polycrystalline $CsFe_2As_2$ compound[64], and these studies showed that $SrFe_2As_2$[62, 66, 68], $EuFe_2As_2$[68, 69], and $CaFe_2As_2$[70, 71] compounds are other parent compounds like $BaFe_2As_2$,

Table 2.2 The highest T_c in various 122 compounds. x is substitution levels in given compounds.

Compound	x	T_c (K)	Reference	Note
KFe_2As_2	-	3.8	[64]	polycrystalline
$CsFe_2As_2$	-	2.6	[64]	polycrystalline
$Ba_{1-x}K_xFe_2As_2$	0.40	38	[2]	polycrystalline
$Ca_{1-x}Na_xFe_2As_2$	0.40	26	[72]	polycrystalline
$Sr_{1-x}K_xFe_2As_2$	0.40	37	[64]	polycrystalline
$Sr_{1-x}Cs_xFe_2As_2$	0.40	37	[64]	polycrystalline
$Eu_{1-x}K_xFe_2As_2$	0.50	32	[78]	polycrystalline
$Ca(Fe_{1-x}Co_x)_2As_2$	0.03	17	[79]	single crystal
$Ca(Fe_{1-x}Ni_x)_2As_2$	0.03	15	[94]	single crystal
$Ca(Fe_{1-x}Rh_x)_2As_2$	0.075	19	[104]	polycrystalline
$Ca(Fe_{1-x}Ir_x)_2As_2$	0.065	22	[105]	single crystal
$Sr(Fe_{1-x}Co_x)_2As_2$	0.10	19	[73]	polycrystalline
$Sr(Fe_{1-x}Ni_x)_2As_2$	0.09	10	[90]	single crystal
$Sr(Fe_{1-x}Ru_x)_2As_2$	0.35	14	[87]	polycrystalline
$Sr(Fe_{1-x}Rh_x)_2As_2$	0.125	22	[85]	polycrystalline
$Sr(Fe_{1-x}Pd_x)_2As_2$	0.075	9	[85]	polycrystalline
$Sr(Fe_{1-x}Ir_x)_2As_2$	0.125	24	[85]	polycrystalline
$Sr(Fe_{1-x}Pt_x)_2As_2$	0.125	17	[101]	polycrystalline
$Ba(Fe_{1-x}Co_x)_2As_2$	0.08	22	[75]	single crystal
$Ba(Fe_{1-x}Ni_x)_2As_2$	0.05	21	[80]	single crystal
$Ba(Fe_{1-x}Ru_x)_2As_2$	0.375	22	[86]	polycrystalline
$Ba(Fe_{1-x}Rh_x)_2As_2$	0.057	24	[91]	single crystal
$Ba(Fe_{1-x}Pd_x)_2As_2$	0.043	19	[91]	single crystal
$Ba(Fe_{1-x}Ir_x)_2As_2$	0.10	28	[95]	polycrystalline
$Ba(Fe_{1-x}Pt_x)_2As_2$	0.05	24	[99]	single crystal
$BaFe_2(As_{1-x}P_x)_2$	0.32	30	[93]	polycrystalline
$EuFe_2(As_{1-x}P_x)_2$	0.30	26	[84]	polycrystalline

which have a possibility to induce superconductivity with substitutions. Indeed, it was found that substitutions on the AE site of AEFe$_2$As$_2$ (AE = Ca, Sr, Ba, and Eu) compounds introduce superconductivity [64, 64, 72, 78]). The highest T_c in various 122 compounds discussed in this section is summarized in Table 2.2.

Transition metal substitutions on the Fe site also induce superconductivity and are the main topic of my dissertation. $AE(Fe_{1-x}TM_x)_2As_2$ compounds exhibit superconductivity with AE = Ca, Sr, and Ba and TM = Co, Ni, Ru, Rh, Pd, Ir, and Pt.[73, 75, 79, 80, 85–87, 90, 91, 94, 95, 99, 101, 104, 105] TM = Cr [88], Mn [97], Cu [89, 92] and Mo [138] are also studied and do not show superconductivity.

P substitution on the As site is also found to induce superconductivity as in P substituted 1111 family compounds. The superconductivity occurs at $T_c \approx 26$ K (polycrystalline, AE = Eu, 30% P [84]) and 30 K (polycrystalline, AE = Ba, 32% P [93]).

I have loosely used the terms "polycrystalline" and "single crystal" since there are discrepancies in literature between T_c in compounds produced by different groups as well as between T_c in polycrystalline and single crystal samples. Unfortunately, the reason is not known.

2.1.3 111 family

LiFeAs and NaFeAs are two compounds in the 111 family. The most astonishing and important aspect of this family is that those compounds exhibit superconductivity without the introduction of substitutions. However, every reported compound shows excessive/deficient amounts of either Li/Na or Fe. Hence it has also been argued that these excessive/deficient concentrations act in a manner similar to doping.[106–109, 111] It was also found that superconductivity in this family is extremely sensitive to the amounts of excessive/deficient element, nearly stoichiometric compounds enhance superconductivity.[112] The highest superconducting transition temperatures are reported at 18 K in $LiFe_{1.03}As$ [113] and 12 K in $Na_{0.9}FeAs$ [113].

Transition metal substitution is also observed to enhance superconductivity. When Co and Ni are introduced in NaFeAs compound (T_c = 9 K), an increase of T_c was observed (T_c = 12 K with 1% Co).[114] However, Co and Ni substitutions in LiFeAs compounds do not enhance superconductivity but reduce T_c gradually.[116]

2.1.4 11 family

The 11 family does not contain FeAs layers but FeTe or FeSe layers. However, due to the similarities between the FeTe/Se and the FeAs layers (Section 2.2), it is considered as a member of FeAs-based superconductors. From its chemical formula (1:1) and crystallographic structure (Section 2.2), it is considered as the simplest FeAs-based superconductor. However, the subtleties of the physical properties, which are dependent on delicate changes in concentration, make this family more complex.

This complexity comes first from the existence of three different phases. FeSe can crystallize in: (a) a tetragonal α-PbO type structure (β phase which is widely called α phase in literature [123]); (b) various structures from hexagonal to monoclinic NiAs type structure (α phase), and; (c) a $FeSe_2$ phase.[118] Due to these three stable phases, secondary phases are almost always present in samples. The second complexity arises from the intercalation of excess Fe atom (Section 2.2). The intercalated Fe atom possesses a magnetic moment and the effect of the moment is not well understood. Nevertheless, the 11 family has attracted a great deal of attention due to a wide range of structural and magnetic properties which are resulted from the aforementioned complexity as well as the availability of large single crystals. I will keep the discussion of the 11 family as simple as possible throughout this chapter.

Stoichiometric FeSe and FeTe are non-superconducting. It was first observed that a deficiency of Se or excess of Fe induces superconductivity in FeSe compounds (not in FeTe compounds).[118, 120, 123, 125] Keeping in mind that the subtle difference in Se or Fe concentration changes the superconducting properties, $FeSe_{0.88}$ and $Fe_{1.01}Se$ shows $T_c = 8$ K [118] and 9 K [123], respectively. Superconductivity is also induced when Si, S, Se, Sb, or Te are introduced on the Se or Te site. The superconducting transition temperatures were reported at 10 K in $FeSe_{0.8}Si_{0.1}$ [130], 16 K in $FeSe_{0.8}S_{0.2}$ [122], 9 K in $Fe_{0.98}Te_{0.9}S_{0.15}$ [128], 11 K in $FeSe_{0.8}Sb_{0.1}$ [130], and 15 K in $FeSe_{0.5}Te_{0.5}$ [119]. Transition metal substitution on the Fe site was attempted with Co, Ni, and Cu and a continuous decrease of T_c [122, 126] was reported for all substitutions, and a solubility limit (30%) was reported for Cu [126].

2.2 Commonalities of the Crystallographic Structure

One of the interesting properties of FeAs-based superconductors is the similarity of the crystallographic structures of different families of compounds: they all contain FeAs or FeTe/Se layers (in tetrahedral coordination) and their high temperature structure is tetragonal.

The 1111 family compounds have a tetragonal $P4/nmm$, ZrCuSiAs type structure.[1] The representative crystal structure is shown in Figure 2.1 (a), and can be viewed as the alternating stacking of FeAs layers and R-O (R = rare earth) layers.

Similarly, for the 122 family compounds [shown in Figure 2.1 (b)], there are alternating FeAs layers and AE(= Ca, Sr, Ba) atoms (instead of R-O layers), and the high temperature crystal structure is the tetragonal $I4/mmm$, $ThCr_2Si_2$ type structure.[61]

The simpler 111 family compounds have a tetragonal $P4/nmm$, PbFCl type structure at high temperature [106–108] and feature Li or Na atoms between the FeAs layers as in Figure 2.1 (c). The simplest 11 family compounds form a high temperature tetragonal $P4/nmm$, α-PbO type structure with no additional layers nor atoms in between FeTe/Se layers [Fig. 2.1 (d)]. However, it was soon realized that growth of exact stoichiometric 11 compounds is extremely difficult and intercalation of Fe atoms [Fe(2) in Figure 2.1 (d)] in between FeTe/Se layers is unavoidable.[118–121, 123]

2.3 Phase Transitions : Structural and Magnetic Transitions

In addition to the superconducting phase transition, most FeAs-based superconductors undergo structural and/or magnetic phase transitions. As I showed in Figure 1.3, unconventional superconductors show different ground states (structural, magnetic, and superconducting) which are close to each other and sometimes compete to each other. Therefore, understanding the intriguing structural and/or magnetic phase transitions is important. I will first briefly introduce how we can detect the phase transitions using x-ray and neutron scattering techniques. Then I will discuss structural/magnetic properties, nature of phase transitions, and phase diagrams of each family studied by scattering techniques.

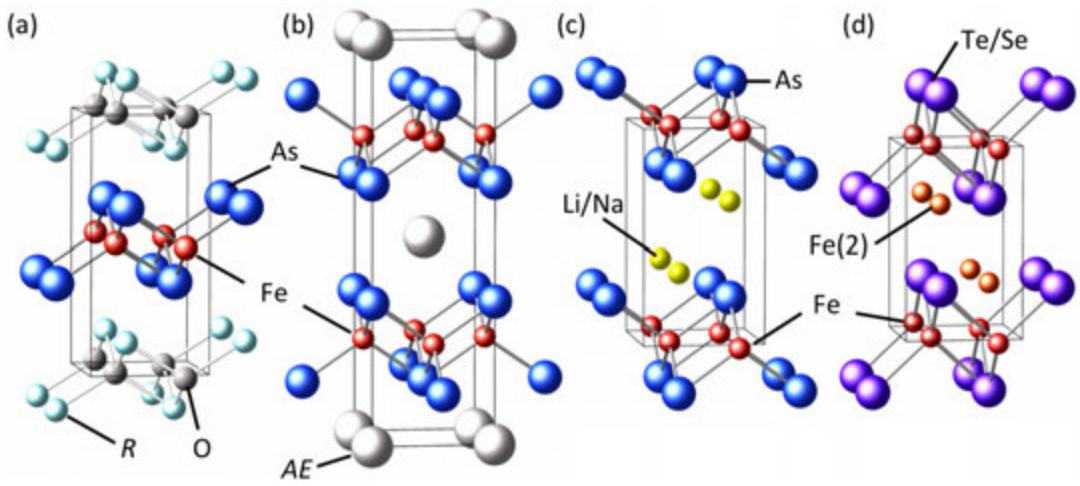

Figure 2.1 High temperature crystallographic structures: (a) the 1111 family compounds ($P4/nmm$),[147] (b) the 122 family compounds ($I4/mmm$),[167] (c) the 111 family compounds ($P4/nmm$),[106] and (d) the 11 family compounds ($P4/nmm$).[120] See the text for details.

Orthorhombic Distortion: structural phase transition

As will be discussed in the following subsections, many of the compounds of interest exhibit a tetragonal-to-orthorhombic structural phase transition. A tetragonal structure has the same length of the lattice parameters a and b ($= a$) whereas the lattice parameters a and b ($\neq a$) are different in an orthorhombic structure. For example, the (2, 0, 0) and (0, 2, 0) Bragg reflections from a tetragonal structure are indistinguishable in diffraction experiments, but they are distinguishable and appear at slightly different diffraction angles from an orthorhombic structure since $a \neq b$ (see Section 3.1.1). By measuring the difference in the peak positions, one can determine the respective lattice parameters and observe a tetragonal-to-orthorhombic structural phase transition. A typical measure of the tetragonal-to-orthorhombic phase transition is the distortion, δ, defined as $\delta = \frac{a-b}{a+b}$ and is generally termed the order parameter for the structural transition. Please refer to Sec. 4.1.2 for relations between a tetragonal and an orthorhombic structures.

Antiferromagnetic Order Parameter: magnetic phase transition

In diffraction experiments, Bragg peaks appear when the diffracted beam from parallel planes interfere constructively (see Section 3.1.1). The Bragg peaks depend on the periodicity

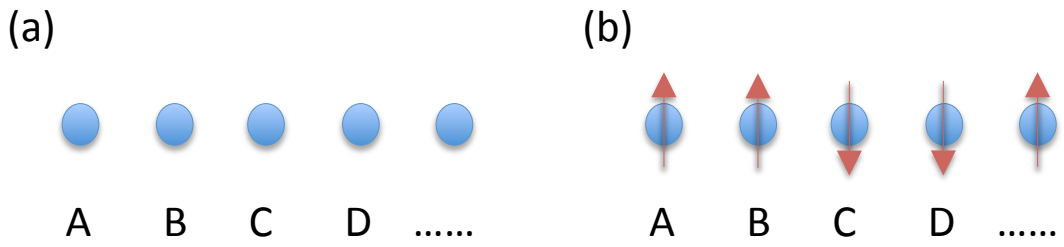

Figure 2.2 (a) Periodic 1-D mono-atomic arrangement. A, B, C, D ... are identical. (b) Introduction of an AFM ordering in the same 1-D arrangement. For instance, A and C became no longer identical due to different spin orientations noted with red arrows.

of the crystal structure.[139] In the vicinity of an antiferromagnetic (AFM) phase transition, the AFM ordering gives rise to a magnetic structure which has different symmetry elements (usually a subgroup of the crystallographic space group) from the crystal structure. For instance, in a 1-dimensional mono-atomic arrangement in Figure 2.2 (a), the A, B, C, and D sites are identical. When antiferromagnetic ordering is introduced as shown in Figure 2.2 (b), a new magnetic periodicity is introduced, introducing a new set of Bragg diffraction peaks associated with that periodicity. A measure of intensities of AFM Bragg peaks as a function of a control parameter, such as temperature, is termed the AFM order parameter.

A first-order phase transition is characterized by (1) a sudden change in the order parameter, (2) thermal hysteresis, and/or (3) coexistence between two different phases (e.g. a coexistence of tetragonal and orthorhombic structures). In contrast, a second-order phase transition is signaled by a continuous change in the order parameter and the absence of hysteresis and coexistence.

2.3.1 1111 family

Parent *R*FeAsO compounds

The 1111 family compounds undergo a structural phase transition from a high temperature tetragonal $P4/nmm$ to an orthorhombic $Cmma$ at low temperature. The structural transition was first noticed in macroscopic measurements. Kamihara *et. al.* found, in polycrystalline $LaFeAsO_{1-x}F_x$ compounds, that there were anomalies in the resistance and magnetization

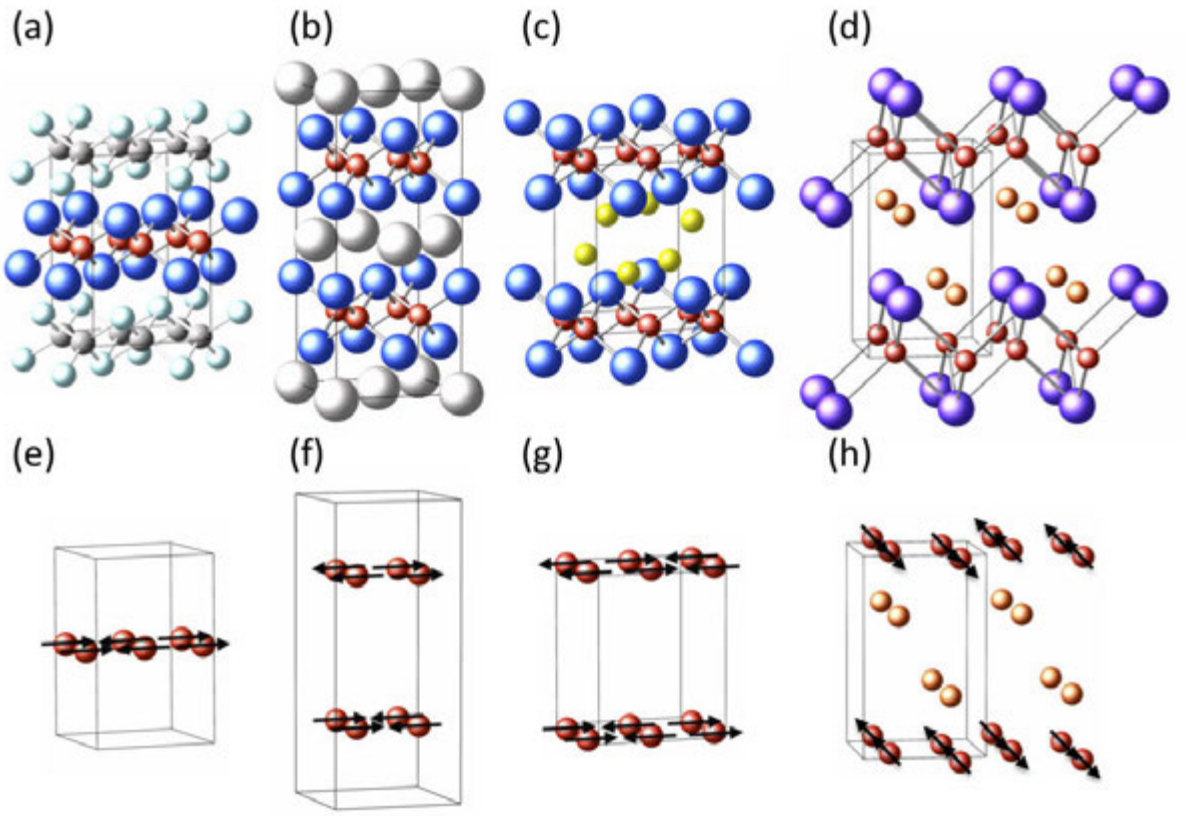

Figure 2.3 Low temperature crystallographic structures: (a) the 1111 family compounds ($Cmma$),[147] (b) the 122 family compounds ($Fmmm$),[167] (c) the 111 family compounds ($Cmma$),[109] and (d) the 11 family compounds ($Pnmm$).[120] The color scheme for different atoms is the same as in Figure 2.1. Only Fe atoms are shown with spin orientation with black arrows in (e) the 1111 family, (f) the 122 family, (g) 111 family, and (h) the 11 family compounds.[30] See the text for details.

data at around 150K,[1] which implied a possible onset of magnetic or structural phase transition. These anomalies disappear for samples with higher fluorine concentration. X-ray and neutron experiments quickly followed and showed that the anomalies in the bulk measurement correspond to a spin density wave antiferromagnetic transition in addition to a tetragonal-to-orthorhombic structural transition. The first diffraction measurements were done on polycrystalline $LaFeAsO_{1-x}F_x$ compounds and it was claimed that the parent LaFeAsO compound transforms from a tetragonal ($P4/nmm$) to a monoclinic ($P112/n$) phase at 155 K (= T_S, a structural transition temperature), closely followed by a spin density wave (SDW) or antifer-

romagnetic (AFM) transition at 137 K (= T_N).[140] They also proved that there is no longer either a structural or SDW (AFM) transitions in the $x = 0.8$ compound.[140] However, it was later realized that a more accurate description of the low temperature structure is orthorhombic $Cmma$[141] as shown in Figure 2.3 (a) [$P112/n$ is the primitive cell of an orthorhombic $Cmma$].[140] All undoped parent RFeAsO compounds undergo the similar structural and magnetic transitions.[140–159]

Several neutron diffraction measurements determined the magnetic structure for Fe ordering and found that the antiferromagnetism is commensurate.[140, 144, 145, 148, 149, 153, 156–158] As shown by arrows in Figure 2.3 (e), the Fe moments point along the orthorhombic $\vec{a}$ axis, and align antiferromagnetically along the orthorhombic $\vec{a}$ axis and ferromagnetically along the orthorhombic $\vec{b}$ axis ($a > b$).[140, 144, 145, 148, 149, 157, 159] Because stripes of parallel spins alternate antiferromagnetically along the orthorhombic $\vec{a}$ axis, this has become known as the "stripe" AFM structure. The correlation of Fe moments along the orthorhombic $\vec{c}$ axis differ in different RFeAsO compounds: antiferromagnetic alignment for R = La, Nd, and Sm[140, 144, 153, 159] and ferromagnetic alignment for R = Ce, Pr[145, 149]. Therefore, the antiferromagnetic $\vec{Q}$ vectors, sometimes called AFM propagation vectors, for Fe ordering are $\vec{Q}_{AFM}=(\frac{1}{2}, \frac{1}{2}, \frac{1}{2})_T$ in the tetragonal structure notation [$\equiv (1, 0, \frac{1}{2})_O$ in orthorhombic structure notation] for La, Nd, and Sm compounds [140, 144, 153, 159] and $\vec{Q}_{AFM}=(\frac{1}{2}, \frac{1}{2}, 0)_T \equiv (1, 0, 0)_O$ for Ce and Pr compounds.[145, 149]

Ordering of rare earth elements has also been observed. Some rare earth elements, such as Nd and Sm, display complex interplay with the Fe ordering: the effect of rare earth magnetism on the Fe moment direction and additional magnetic ordering temperatures.[157, 159] The structural transition temperatures (T_S), AFM (SDW) transition temperatures of Fe ($T_{N_{Fe}}$), magnetic transition temperatures of rare earth elements (T_{N_R}), and the ordered moment sizes, M, of Fe and rare earth elements in the parent 1111 compounds are listed in Table 2.3. In general, T_S and T_N are split ($T_S > T_N$) in the parent 1111 compounds and the small ordered magnetic moments measured ($< 1\mu_B$) for both the Fe and rare earth elements indicates that the system is itinerant.

Whether the phase transition is first-order or second-order is another point of interest in the

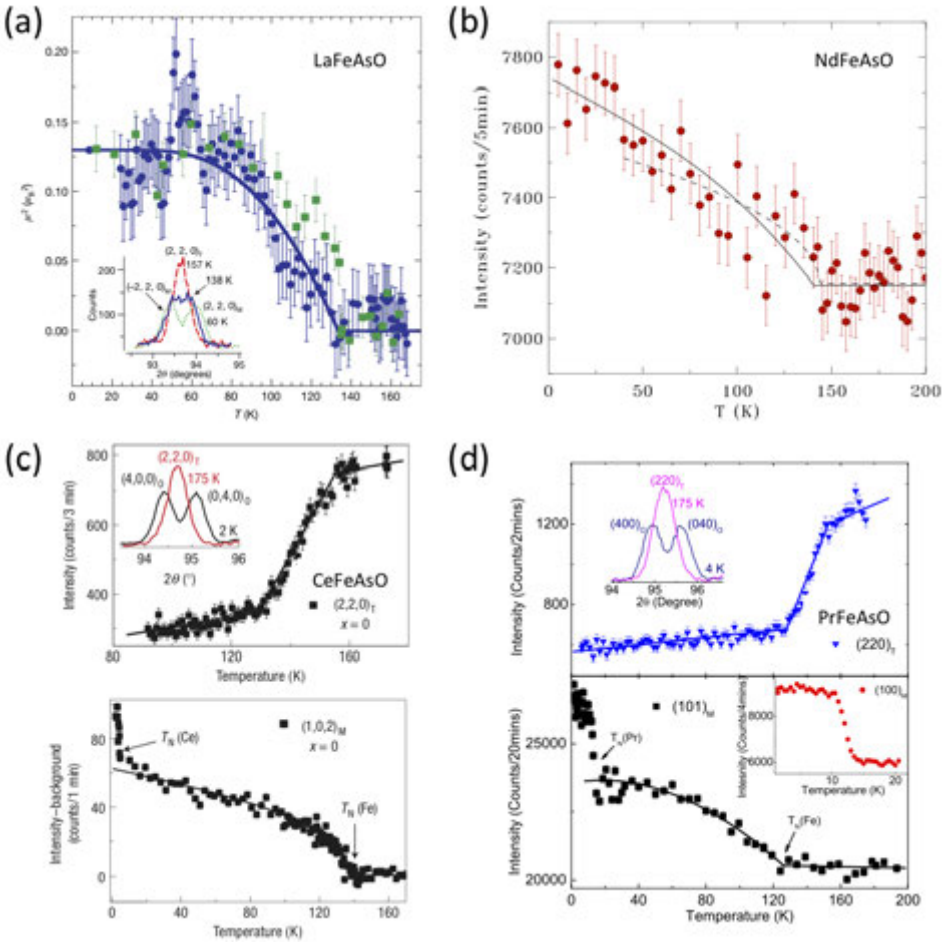

Figure 2.4 Antiferromagnetic order parameter of (a) LaFeAsO (nuclear peak splitting is shown in the inset),[140] (b) NdFeAsO,[144] (c) CeFeAsO [the bottom panel; temperature evolution of a nuclear peak intensity is shown on the top panel of (c)] [145] and (d) PrFeAsO [the bottom panel; temperature evolution of a nuclear peak intensity is shown in the top panel of (d)].[149]

FeAs-based superconductors. A second-order transition can be described by a critical exponent of the order parameter in a power law relation. The critical exponent of structural or magnetic order parameters are related to the critical exponents of thermodynamic order parameters, such as heat capacity. Second-order transitions can be categorized within a universality class which have the same value of critical exponent within a given model. For example, the critical exponents, β, of the magnetic order parameter are $\frac{1}{8}$ for Ising model with 1-dimensional (D) lattice and 1-D spin, 0.326 for Ising model with 1-D lattice and 3-D spin, 0.367 for Heisenberg model with 3-D lattice and 3-D spin, and $\frac{1}{2}$ for Mean-field with any dimensions of lattice and

Table 2.3 Structural transition temperature T_S and antiferromagnetic (spin density wave) transition temperature T_N in the parent RFeAsO compounds. In the superscript in the second, third, and fourth columns, "N" means that it was measured with neutrons and "X" means that x-ray measurements were used. "NO" = "no ordering" and "NR" = "not reported".

R	T_S (K)	$T_{N_{Fe}}$ (K)	T_{N_R} (K)	M_{Fe} (μ_B)	M_R (μ_B)	Reference
La	155^N	137^N	NO	0.36 @ 8 K	NO	[140]
	$\sim 160^X$	145^N	NO	NR	NO	[143]
Ce	$\sim 155^N$	$\sim 140^N$	NR	0.94(3) @ 1.7 K	0.83(2) @ 1.7 K	[145]
Pr	136^N	85^N	12^N	0.53(20) @ 1.4 K	0.83(9) @ 1.4 K	[148]
	153^N	127^N	14^N	0.48(9) @ 4 K	0.84(4) @ 4 K	[149]
	$154(2)^X$	NR	NR	NR	NR	[151]
Nd	$141(6)^N$	NR	NR	0.25(7) @ 30 K	NR	[144]
	$\sim 150^N$	NR	2^N	0.9(1) @ 0.3 K	1.55(4) @ 0.3 K	[146]
	$\sim 142^X$	$\sim 137^N$	15^N	0.54(3) @ 30 K	NR	[157]
Sm	130^X	NR	NR	NR	NR	[150]
	144^X	NR	NR	NR	NR	[152]
	NR	NR	NR	NR	$0.60(3)^N$ @ 1.6 K	[153]
	140^X	110^X	5^X, 110^X	NR	NR	[159]
Gd	135^X	NR	NR	NR	NR	[152]
Tb	126^X	NR	NR	NR	NR	[152]

spin.[160] Within a certain universality class, materials exhibit similar behavior at a transition. In contrast, a first-order transition does not have such a universality class and the properties differ by materials. Therefore, knowing the nature of transitions is interesting and important. As shown in Figure 2.4, the structural and antiferromagnetic transitions are continuous, second order in the 1111 family compounds.[140, 144, 145, 149, 150] Further careful studies on critical exponents of the order parameters in different materials are called for to decide which universality class the 1111 compounds would fit in.

Substitution effect on T_S, T_N, and Moment size - Phase Diagram

The general behavior of T_S, T_N, and ordered moment size M is that their values decrease as the amount of substitution increases and disappear when substitution is sufficient enough, as presented in the phase diagrams in Figure 2.5. For example, in the phase diagram of

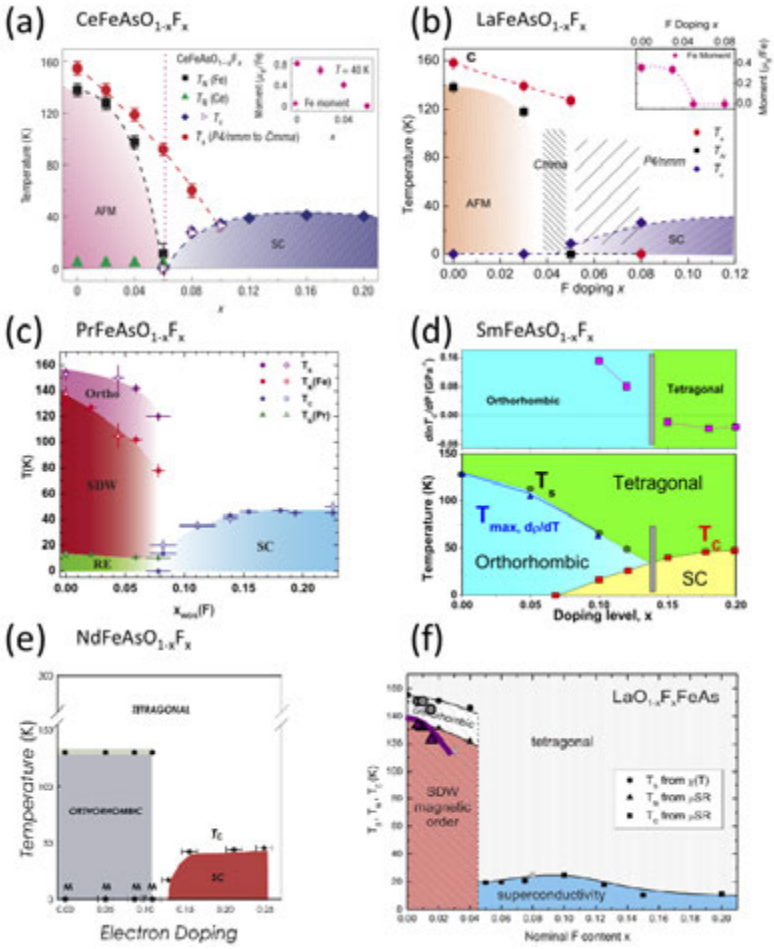

Figure 2.5 Phase diagrams of (a) $CeFeAsO_{1-x}F_x$,[145] (b) $LaFeAsO_{1-x}F_x$,[147] (c) $PrFeAsO_{1-x}F_x$,[151] (d) $SmFeAsO_{1-x}F_x$,[150] and (e) $NdFeAsO_{1-x}F_x$ [155] compounds. (f) Different phase lines of actual(gray and violet symbols) and nominal (black symbols) concentrations in $LaFeAsO_{1-x}F_x$ compounds.[137]

$CeFeAsO_{1-x}F_x$ shown in Figure 2.5 (a) [145], the structural transition temperature T_S, and the AFM transition temperature T_N, in the parent CeFeAsO compound are suppressed to lower temperatures and remain split when fluorine is introduced. However the suppression of T_S is slower than that of T_N so when the AFM transition is completely suppressed at $x \approx 0.06$, T_S has still a finite value. The moment sizes also decrease with increasing fluorine concentration as depicted in the inset of Figure 2.5 (a), and superconductivity emerges after a complete suppression of antiferromagnetic ordering. That is, superconductivity and magnetism appear to be mutually exclusive. It is also shown that superconductivity exists not only in the

orthorhombic structure, but also in the tetragonal structure.

However, it seems that the phase diagrams for the 1111 family differ somewhat in different compounds. For example, the phase diagram of the $LaFeAsO_{1-x}F_x$ compounds looks similar to that for $CeFeAsO_{1-x}F_x$ compounds although there is uncertainty of whether or not superconductivity emerges in the orthorhombic structure [Figure 2.5 (b)].[147] In case of $PrFeAsO_{1-x}F_x$ compounds in Figure 2.5 (c), superconductivity emerges only when the structural and AFM transitions are completely suppressed.[151] It should be noted that the disappearance of T_S and T_N are very abrupt in $PrFeAsO_{1-x}F_x$ compounds whereas it is more continuous in the $CeFeAsO_{1-x}F_x$ compounds.[151] It is difficult to tell in $LaFeAsO_{1-x}F_x$ compounds where the disappearance of T_S and T_N occur due to the paucity of data points.[147] For $SmFeAsO_{1-x}F_x$ compounds, even though the microscopic measurement of the AFM ordering has not been done for a wide range of compositions, x-ray measurements show that the orthorhombic structure persists in the superconducting compositions as shown in Figure 2.5 (d).[150, 154] A partial phase diagram (which means, no T_N was reported from a microscopic measurement) was also reported for $NdFeAsO_{1-x}F_x$. The authors determined the real compositions and found that $NdFeAsO_{1-x}F_x$ behaves rather different than any other compounds: the structural transition temperature is almost independent of changes in fluorine concentration and disappears suddenly as shown in Figure 2.5 (e).[155]

One must be careful in understanding the above-mentioned phase diagrams. As mentioned in Section 2.1.1, the actual compositions of studied materials can be very different from the reported nominal compositions. This is shown in Figure 2.5 (f). When the actual compositions are taken into account, the known slow suppression rates of T_S and T_N can become relatively fast suppression.[137] Nevertheless, it seems that the importance of real concentrations in the 1111 family compounds has been overlooked.

2.3.2 122 family

Parent $AE\mathbf{Fe_2As_2}$ compounds

The anomaly observed in macroscopic measurements on the parent $BaFe_2As_2$ compound appears at $\sim$ 140 K as temperature is lowered.[61] Powder x-ray diffraction measurements

were used to determine that a structural transition from a tetragonal $I4/mmm$ structure to an orthorhombic $Fmmm$ structure occurs at the same temperature where the anomaly appears.[2, 61] The low temperature orthorhombic structure is shown in Figure 2.3 (b). Single crystals of $SrFe_2As_2$, $CaFe_2As_2$, and $EuFe_2As_2$ compounds were also found to have the same tetragonal-to-orthorhombic structural transition at $\sim$ 200 K [62, 69, 161–166], $\sim$ 170 K [70, 167–171], and $\sim$ 190 K [69, 172, 173], respectively.

Several neutron diffraction measurements showed that the structural and AFM transitions are coincident in temperature, unlike the split transitions for the 1111 family compounds.[162–164, 167–169, 173–180] The magnetic structure of Fe was found to be commensurate as in the 1111 family compounds.[162, 163, 165, 167, 173, 174] Fe moments point along the orthorhombic $\vec{a}$ axis, and align antiferromagnetically along the orthorhombic $\vec{a}$ axis and along the orthorhombic $\vec{c}$ axis, and arrange ferromagnetically along the orthorhombic $\vec{b}$ ($< a$) axis (the "stripe" AFM structure). The AFM propagation vector $\vec{Q}_{AFM}$ is $\vec{Q}_{AFM}=(\frac{1}{2}, \frac{1}{2}, 1)_T$, in tetragonal notation, which is equivalent to $(1, 0, 1)_O$ in orthorhombic notation as displayed in Figure 2.3 (f).[162, 163, 167, 174] For $EuFe_2As_2$ compounds, the Eu ions also order antiferromagnetically at $\sim$ 19 K with a propagation vector $\vec{Q}_{AFM}(Eu) = (0, 0, 1)$.[173] No interplay between the Fe moments and the Eu moments has been reported.

I have summarized the structural transition temperatures (T_S), AFM (SDW) transition temperatures of Fe ($T_{N_{Fe}}$), AFM transition temperatures of Eu ($T_{N_{Eu}}$) for the $EuFe_2As_2$ compound, and the ordered moment sizes, M, of Fe (and M of Eu) in the parent 122 compounds in Table 2.4.

The structural and AFM transitions in the parent $AEFe_2As_2$ (AE = Ca, Sr, Ba, and Eu) compounds are concomitant in temperature.[162–164, 167–169, 173–180] However, the nature of the phase transitions varies in different compounds. For $CaFe_2As_2$ and $SrFe_2As_2$, the structural and AFM transitions are found to be first-order.[62, 70, 161–164, 166, 167] As seen in Figure 2.6 (a) and (b), these two compounds exhibit (1) discontinuous changes in the magnetic order parameters and the orthorhombic distortions, (2) hysteresis in temperature, and (3) the coexistence of two phases, which are all characteristics of a first-order phase transition. For $BaFe_2As_2$, it has been argued by some groups that the structural and AFM transitions

Table 2.4 Structural transition temperature T_S and antiferromagnetic (spin density wave) transition temperature T_N in the parent $AEFe_2As_2$ compounds. For $EuFe_2As_2$ compound, the values in the chevrons are the values for Eu atoms. In the superscription, "N" means that it measured in neutron measurements and "X" means that x-ray measurements were used. "NA" means "not available".

AE	T_S (K)	T_N (K)	M (μ_B)	Reference
Ca	$\sim 170^X$	NA	NA	[70]
	$\sim 173^N$	$\sim 173^N$	0.80(5) @ 10 K	[167]
Sr	$\sim 190^X$	NA	NA	[62]
	$203(1)^X$	NA	NA	[69]
	$\sim 210^X$	NA	NA	[161]
	$220(1)^N$	$220(1)^N$	0.94(4) @ 10 K	[162]
	NA	205^N	1.01(3) @ 1.5 K	[163]
	$201.50(25)^N$	$201.50(25)^N$	NA	[164]
	NA	NA	1.04(1) @ 10 K	[165]
Ba	$\sim 140^X$	NA	NA	[61]
	$\sim 85^X$	NA	NA	[63]*
	$\sim 142^N$	$143(4)^N$	0.87(3) @ 5 K	[174]
	$\sim 90^X$	$\sim 90^N$	NA	[175]*
	NA	136^N	NA	[178]
	NA	$\sim 136^N$	0.93(6) @ 3 K	[179]
Eu	$190(1)^X$	NA	NA <NA>	[69]
	NA	~ 190 <~ 19>^{N}	NA <NA>	[172]
	NA	~ 190 <~ 19>^{N}	0.98(8) <6.8(3)> @ 2.5 K	[173]

*: Sn incorporation on the Ba site during a single crystal growth using Sn flux has been reported.

are second-order by showing that the transition is continuous, [174, 179, 180] while first-order behavior such as a large hysteresis has been observed by other groups [177, 178] [Figure 2.6 (c)]. It is not yet clear whether the structural and AFM transitions in the parent $BaFe_2As_2$ compound are first-order or second-order and this is one of the issues addressed in this dissertation. The situation for the parent $EuFe_2As_2$ compound is similar to the parent $BaFe_2As_2$ compound: some neutron measurements observed a continuous transition[172, 173] while x-ray diffraction measurements display a (discontinuous) jump in the orthorhombic distortion with no hysteresis in the specific heat measurement.[69]

Therefore, studies of the nature of structural and antiferromagnetic transitions in the parent

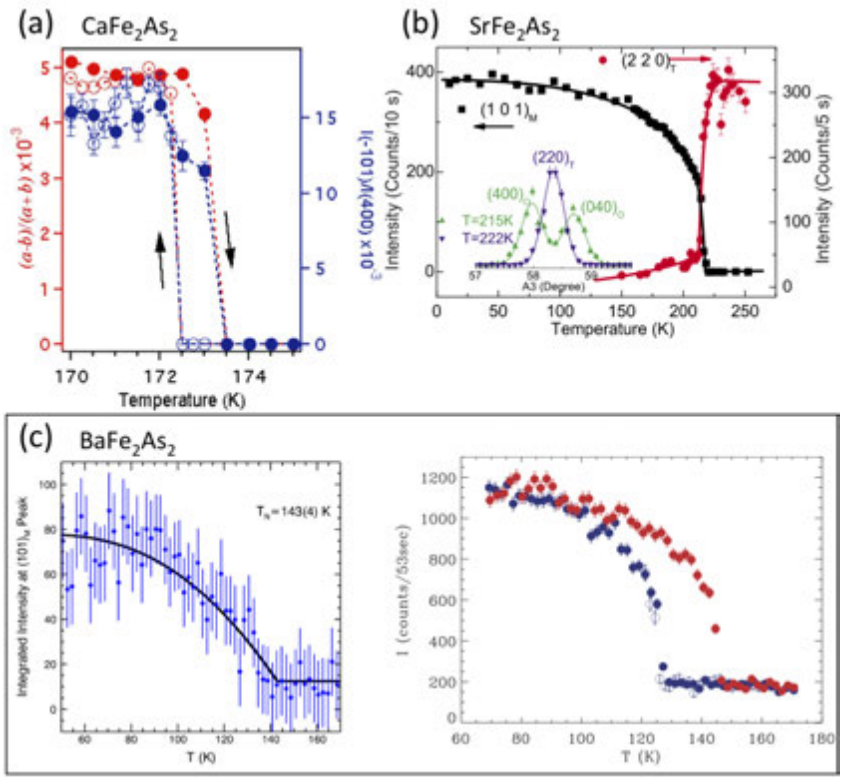

Figure 2.6 (a) Temperature dependent orthorhombic distortion and AFM order parameter of $CaFe_2As_2$ compound.[167] Open symbols are data measured during cooling and closed symbols are data measured during warming. (b) Temperature dependent AFM order parameter and evolution of a nuclear peak intensity of $SrFe_2As_2$ measured during cooling.[162] (c) AFM order parameter of $BaFe_2As_2$ compounds. In the right panel, red symbols are data measured during warming and blue symbols are measured during cooling.[177, 178]

$BaFe_2As_2$ and $EuFe_2As_2$ are important in order to understand the 122 family compounds as a whole.

Substitution effect on T_S, T_N, and Moment size - Phase Diagram

In a similar manner as the substitution effect in the 1111 family compounds, T_S, T_N, and ordered moment size, M, decrease as the level of substitution increases, and disappear with sufficient substitution. This is demonstrated in Figure 2.7 (a) for Co substituted $BaFe_2As_2$ compounds.[181–187] The structural and AFM transitions occur at the same temperature in the parent compound. When Co is introduced, T_S and T_N decrease and split ($T_S > T_N$). It should be noted that T_S and T_N track closely to each other. Then superconductivity emerges

at Co substitutions when T_S and T_N are sufficiently suppressed. The reduction of the moment size with increasing Co levels has been also observed. Unlike in the 1111 family compounds, however, superconductivity coexists with AFM. The same effects have also been observed in various transition metal Ni, Rh, and Ir substitutions in the $BaFe_2As_2$ compound.[188–191] It is widely believed that the transition metals on the right side of Fe in the periodic table introduce additional electrons and follow a simple band filling picture with e.g. +1 electron for Co and +2 electrons for Ni substitutions.[92, 192] Whether a simple band filling picture is valid for transition metal substitutions on the right side of Fe is another interesting issue to be discussed in this dissertation. For transition metal substituted $CaFe_2As_2$ compounds, the aforementioned behaviors are also present, but it has been shown in $Ca(Fe_{1-x}TM_x)_2As_2$ (TM = Co and Ni) compounds that the disappearance of T_S and T_N is abrupt [Figure 2.7 (b)].[94, 193] It seems that AFM and SC may coexist but the superconductivity appears in a very narrow concentration range.

To the left of Fe in the periodic table, Cr and Mn substitutions, which have been considered as hole doping, do not induce superconductivity at any substitution levels.[88, 194–197] Only few x-ray measurements had been done in Cr substituted $BaFe_2As_2$ compounds which generated contradictory results about the existence of a structural transition in the lightly doped compounds.[88, 194] Later, the same group performed systematic neutron[196] and x-ray [197] diffraction measurements and found that $Ba(Fe_{1-x}Cr_x)_2As_2$ compounds exhibit coupled structural/magnetic transitions and a monotonic suppression of T_S/T_N up to $x \approx 0.375$. They also found that above $x \geq 0.375$, a G-type antiferromagnetic ordering of Cr appears while the antiferromagnetic ordering of Fe is suppressed [Figure 2.7 (c)].[196] At the same time, $Ba(Fe_{1-x}Mn_x)_2As_2$ compounds were studied in our scattering group as one of my projects and will be discussed later.

Ru substitution on the Fe site, or P substitution on the As site, has also attracted attention since they are effectively isoelectronic substitutions. I utilized both x-ray and neutron diffraction measurements and studied the effects on the structural, magnetic, and superconducting properties by Ru substitution in $BaFe_2As_2$. What has been known for Ru substitution prior to my study and the result will be presented later in Sec. 4.3. However, the limitation of sam-

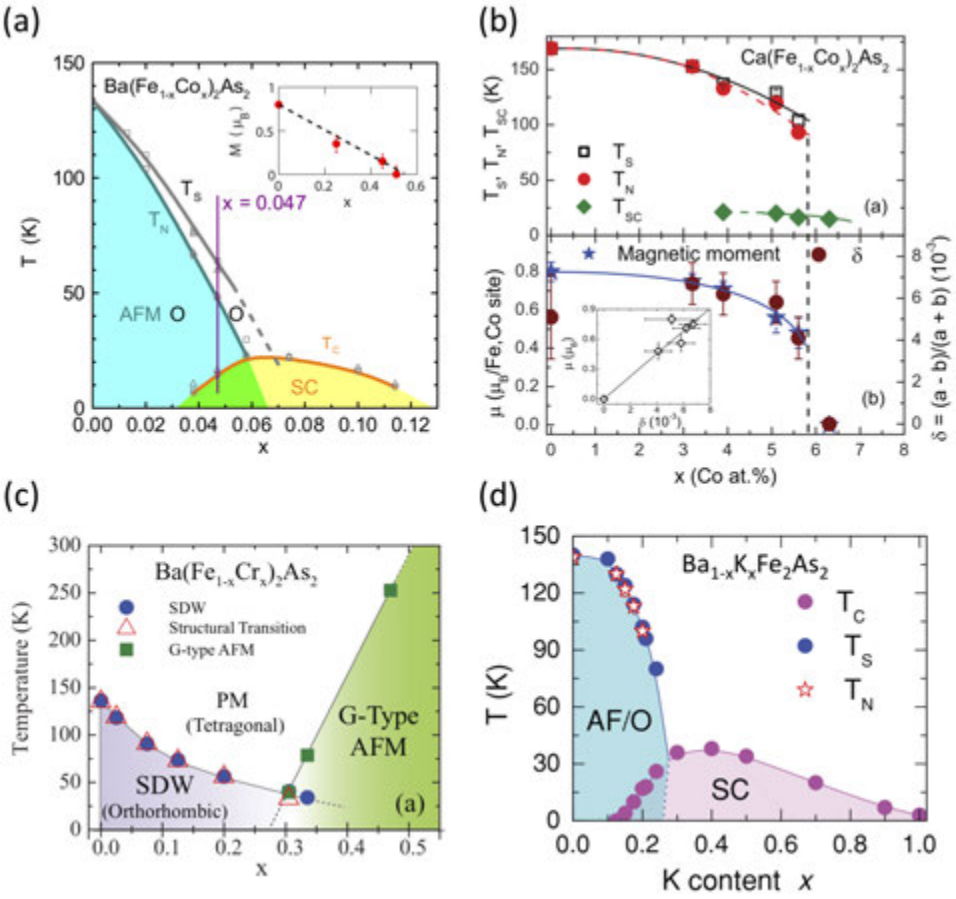

Figure 2.7 (a) The phase diagram of $Ba(Fe_{1-x}Co_x)_2As_2$ compounds. The inset is ordered moment sizes as a function of Co concentrations x.[182] (b) (Top) The phase diagram of $Ca(Fe_{1-x}Co_x)_2As_2$ compounds. (Bottom) Ordered moment sizes versus Co concentrations x (stars) and the orthorhombic distortion as a function of Co concentrations (circles).[193] (c) The phase diagram of $Ba(Fe_{1-x}Cr_x)_2As_2$ compounds.[196] (d) The phase diagram of $Ba_{1-x}K_xFe_2As_2$ compounds. See the text for details.[201]

ple sizes for P substituted compounds hinders microscopic studies of structural and magnetic transitions. Growing interest in the quantum criticality for P substitution [93, 198] calls for measurements of microscopic structural and magnetic properties.

As superconductivity is induced by substitution of AE site elements with, namely, K (Section 2.1), K substitution on the Ba site of $BaFe_2As_2$ compound also behaves as transition metal substituted compounds: suppression of T_S and T_N, reduced moment sizes, and induction of superconductivity with increasing level of K.[2, 63, 199–202] However, K substitution does not split the structural and AFM transitions ($T_S = T_N$ in all concentrations) as displayed in Figure 2.7 (d).[201, 202] There have been handful of discussions about whether the superconductivity and AFM coexist in $Ba_{1-x}K_xFe_2As_2$ compounds. It was initially believed that the superconductivity and AFM occur in different parts of the sample (phase separation),[199, 202, 203] but recently, it was argued that they are microscopically coexisting in superconducting samples.[204]

Rare earth substituted $CaFe_2As_2$ compounds have also been reported that they behave in a similar way to transition metal substituted $CaFe_2As_2$ compounds: abrupt disappearance of T_S and T_N.[205] It is also believed that the substitution on the AE site gives additional carriers.

Probably due to the wide belief that the structural and magnetic behaviors are similar with substitutions in all 122 family compounds, there have been less microscopic studies of substitution on the Fe site or the AE site in $SrFe_2As_2$ and $EuFe_2As_2$ compounds. Although there are phase diagrams formed by macroscopic measurements, it is important to study the microscopic properties and to determine the phase diagram.

2.3.3 111 family

Parent AFeAs compounds

As we saw in Section 2.1.3, there are only two kinds of compounds in this family: LiFeAs and NaFeAs. LiFeAs does not have structural and magnetic phase transitions [107] whereas the parent NaFeAs undergoes a tetragonal-to-orthorhombic transition from $P4/nmm$ [Figure 2.1 (c)] to $Cmma$ [Figure 2.3 (c)] at $T_S \approx 55$ K and AFM emerges at ~ 37 K.[206] The AFM structure in NaFeAs compound is found to be the same "stripe" structure [Figure 2.3 (g)] as in the 122 family compounds. The ordered moment in NaFeAs is 0.09(4) μ_B at $T = 5$ K, which is

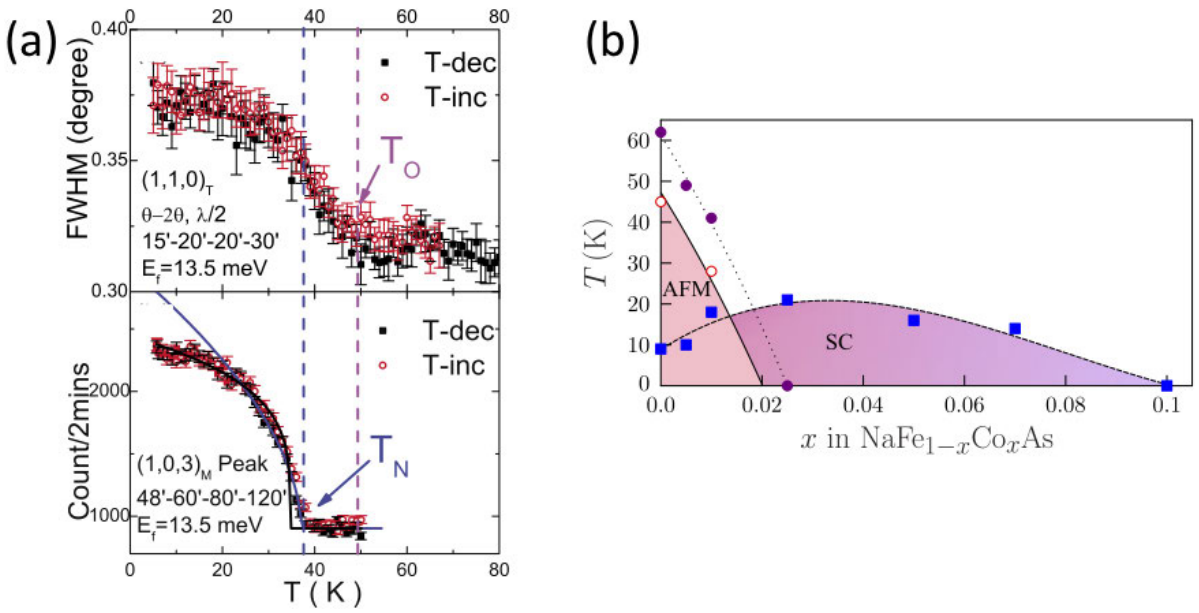

Figure 2.8 (a) Order parameters of structural (top panel) and AFM (bottom panel) phase transitions.[206] (b) The phase diagram of $NaFe_{1-x}Co_xAs$.[114] See the text for details.

the smallest among the FeAs-based superconductors.[206] Measurements of the ordered moment size was not possible from powder neutron diffraction measurements, but was achieved from single crystal neutron diffraction measurement.[206]

Powder neutron diffraction and powder x-ray diffraction measurements indicate that both antiferromagnetic and structural transitions are second order and split in temperature.[206] This is shown in Figure 2.8 (a). The top panel is the change of the Full Width at the Half Maximum (FWHM) of the $(1, 1, 0)_T$ Bragg peak as a structural order parameter. A measure of the change of FWHM is not a strong proof of the nature of the structural phase transition but it, at most, implies that the structural phase transition is likely smooth as in a second-order transition. The bottom panel is the AFM order parameter at the $(1, 0, 3)_M$ magnetic Bragg peak considering the magnetic structure and clearly shows a second-order transition.(See Ref. [206] for details)

Substitution effect on T_S, T_N, and Moment size - Phase Diagram

Systematic x-ray and neutron diffraction measurements on Co or Ni substituted NaFeAs

compounds have been performed. However, the small ordered moment in the parent compound restricts the range of systematic studies, focusing on the structural transitions.[114, 207] As Co or Ni is substituted in NaFeAs, the structural transition temperatures are suppressed very rapidly so that a little more than 2% of Co substitution suppresses the structural transition completely.[114, 207] Due to the lack of the microscopic data, it is difficult to say how T_{N} and the ordered moment size change with substitution. However, it appears that T_{N} and the ordered moment size likely decrease with increasing level of Co or Ni substitution based on local-probe measurements.[114] Neutron diffraction measurement on single crystals is required for definite answers. Figure 2.8 (b) is a phase diagram of $NaFe_{1-x}Co_xAs$, composed with data taken from neutron and μSR measurements:[114, 207] T_{S} and T_{N} are split in all concentration range; and SC and AFM coexist in a finite substitution range.

2.3.4 11 family

Parent FeTe or FeSe compounds

There are two ways to describe the stoichiometry of these compounds − Fe rich or Te/Se deficiency, for example, $Fe_{1.141}Te \equiv FeTe_{0.82}$,[120] and both ways have been confusingly used in literature, even in one report. The structural transitions are affected by subtle differences in the stoichiometry. A transition from a tetragonal $P4/nmm$ to a monoclinic $P2_1/m$ in $Fe_{1.125}Te$, $Fe_{1.068}Te$ and $FeTe_{0.9}$[120, 208], from a tetragonal $P4/nmm$ to an orthorhombic $Pmmn$ in $FeTe_{0.82}$[120], from a tetragonal $P4/nmm$ to a triclinic $P\bar{1}$ in $FeSe_{0.88}$[118], and from a tetragonal $P4/nmm$ to an orthorhombic $Cmma$ in $FeSe_{0.92}$[209, 210] all have been observed. The low temperature orthorhombic structure is shown in Figure. 2.3 (d). For monoclinic/triclinic structures, the crystal structure is almost identical to the orthorhombic structure shown in Figure. 2.3 (d) with the angle $\beta \approx 89.254°$[208] for the monoclinic structure, and $\gamma \approx 90.3°$[118] for the triclinic structure.

The parent 11 compounds also show an antiferromagnetic transition which is different, and complicated, for different compounds. Bao *et. al.* first found that slight changes in the stoichiometry alter the magnetic structure in the 11 family compounds.[120] They observed that $FeTe_{0.9}$ compounds exhibit a commensurate antiferromagnetic order with $\vec{Q}_{\mathrm{AFM}} = (\frac{1}{2}, 0, \frac{1}{2})_{\mathrm{T}}$

Table 2.5 Structural transition temperature T_S and antiferromagnetic (spin density wave) transition temperature T_N, and the ordered moment sizes M of Fe in the FeTe or FeSe layers in the parent FeTe or FeSe compounds. In the superscription, "N" means that it measured in neutron measurements and "X" means that x-ray measurements were used. "NA" means "not available".

	T_S (K)	T_N (K)	M (μ_B)	Reference
$Fe_{1.125}Te$	NA	NA	2.07(7) @ 4.2 K	[212]
$FeSe_{0.88}$	$\sim 105^X$	NA	NA	[118]
$FeSe_{0.92}$	$\sim 70^X$	NA	NA	[209]
$FeTe_{0.82}$	$\sim 63^N$	$\sim 63^N$	0.76(2) @ 8 K	[120]
$FeTe_{0.90}$	$\sim 75^N$	NA	NA	[120]
$Fe_{1.068}Te$	$\sim 67^N$	$\sim 67^N$	2.25(8) @ 5 K	[208]
$FeTe_{0.92}$	NA	NA	1.86(2) @ 10 K	[210]

in a tetragonal notation while $Fe_{1.141}Te$ compounds show incommensurate AFM order with $\vec{Q}_{AFM} = (0.38, 0, \frac{1}{2})_T$. Moreover, they also showed that the incommensurability ε in $\vec{Q}_{AFM} = (\varepsilon, 0, \frac{1}{2})_T$ can be tuned with changes of stoichiometry.[120] Details of the magnetic structure were also studied and are shown in Figure 2.3 (h). The important difference between the antiferromagnetic structure in the 11 family compounds, compared to 1111, 122, and 111 compounds, is that there are two rows of parallel Fe spins alternating antiferromagnetically to form the so called "double-stripe" AFM structure.[120, 208, 211]

As mentioned in Section 2.2, intercalation of Fe atoms brings another complication in that the intercalated Fe atoms may possess a considerable moment. Canted Fe moments in the FeTe or FeSe layers along the c axis have been observed and are thought to result from the intercalated Fe moment.[208] However, there exist other reports that did not find canting of Fe moments.[210]

The structural transition temperatures (T_S), AFM (SDW) transition temperatures of Fe (T_N), and the ordered moment sizes M of Fe in the FeTe or FeSe layers in the parent 11 compounds are summarized in Table 2.5.

The nature of structural and antiferromagnetic transitions in the 11 family compounds

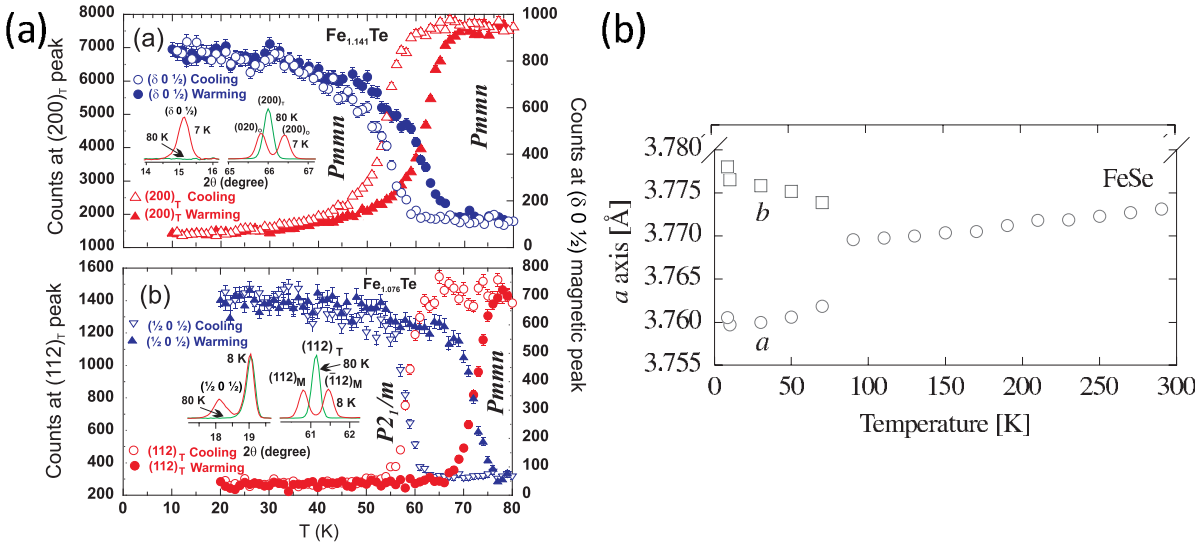

Figure 2.9 (a) Order parameters of structural and AFM phase transitions in $Fe_{1.141}Te$ (top panel) and $Fe_{1.076}Te$ (bottom panel).[120] (b) Change of a lattice parameter in FeSe compound. See the text for details.[214]

is not clear. In $FeTe_{0.82}$($\equiv Fe_{1.141}Te$) compounds, both the structural and antiferromagnetic transitions were observed at the same temperature and showed coexistence of the two phases and hysteresis in temperature [first-order. see Figure 2.9 (a)].[120] First-order phase transitions were also reported in $Fe_{1.068}Te$[208] and $Fe_{1.03}Te$ [213]. Although a change of the a lattice parameter as a function of temperature was also measured in FeSe by x-ray powder measurements, as shown in Figure 2.9 (b) [214], the temperature steps were too large to allow any conclusion about the nature of the structural phase transition. Within the reported information, it is likely that both the structural and antiferromagnetic phase transitions are first-order.

Substitution effect on T_S, T_N, and Moment size - Phase Diagram

In the 11 family compounds, it can be seen that the excessive Fe content or the deficient Te or Se content act as self-doping even in the parent compounds. For example, $T_S \approx T_N \approx$ 75 K in $FeTe_{0.90}$ and $T_S \approx T_N$ decrease to 63 K in $FeTe_{0.82}$.[120, 123]

As discussed in Section 2.1, substitution is usually achieved by Se for Te or Te for Se. As for other FeAs-based superconductors, the phase transition temperatures are suppressed as the level of substitution increases [120, 210, 211, 213–219], and a complete suppression of phase

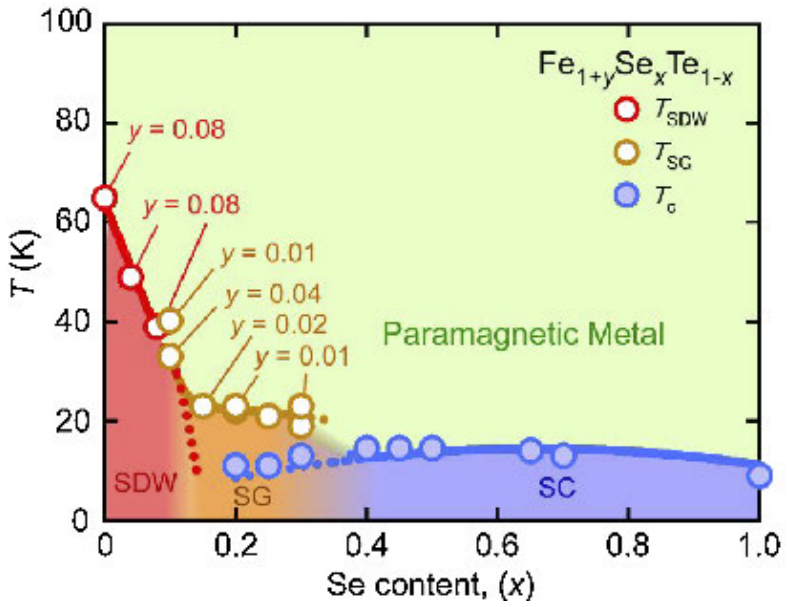

Figure 2.10 The phase diagram of $FeTe_{1-x}Se_x$.[216] See the text for details.

transitions enhances superconductivity(see Section 2.1.4).

For an easier description of substitution effects, I choose FeTe as the reference parent compound so that Se is a substitution element. The most interesting property of the 11 family compounds is that it exhibits a short-range incommensurate magnetic order which has not been observed in other FeAs-based superconductors. In $Fe_{1.08}Te_{0.67}Se_{0.33}$, $Fe_{1.07}Te_{0.75}Se_{0.25}$, $Fe_{1.03}Te_{0.75}Se_{0.25}$, $Fe_{1.02}Te_{0.85}Se_{0.15}$, $Fe_{1.04}Te_{0.90}Se_{0.10}$, and $Fe_{1.10}Te_{0.75}Se_{0.25}$, short-range antiferromagnetic order has been observed with correlation lengths ranging from 3.3 to 24 Å at $\vec{Q}_{AFM} = (\varepsilon, 0, \frac{1}{2})_T$ ($\varepsilon = 0.438 \sim 0.47$ reciprocal lattice units). These values are much smaller than the correlation lengths found for the commensurate AFM peak that is resolution limited, in all other compounds with Se concentration less than approximately 10%.[120, 213, 215, 216, 219] Katayama *et al.* [216] studied details of the short-range AFM ordering using both macroscopic and microscopic techniques, and argued that the short-range AFM transition is a spin-glass transition by observing apparent difference ($\approx$ 17 K) in the ordering temperature measured by neutron measurement (40 K) and magnetization measurement ($\approx$ 23 K), which is common in spin-freezing systems. Their phase diagram is the most complete and up-to-date (Figure 2.10) summarizes the effect of substitution in the 11 family compounds.[216]

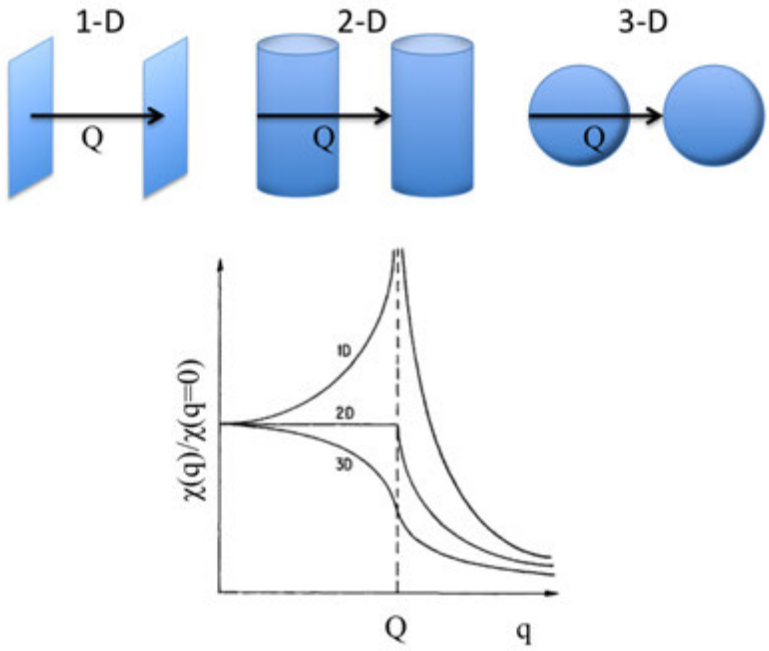

Figure 2.11 Fermi surface nesting in simple quasi 1-D (sheets), 2-D (cylinders), and 3-D (spheres) and the response function for each case. After Ref. [220, 221].

2.4 Interplay between Superconductivity, Antiferromagnetism, and Structure

Unprecedented interconnections between superconductivity and antiferromagnetism and between superconductivity and structure were found and have been widely-studied subjects in the FeAs-based superconductors. Since large and high-quality single crystals can be grown for $BaFe_2As_2$ compounds, most of work has been performed on various substitutions in $BaFe_2As_2$ compounds. In this section I will discuss the interplay between superconductivity, antiferromagnetism, and structure which has been found in various element substituted $BaFe_2As_2$ compounds.

2.4.1 Interplay between superconductivity and antiferromagnetism

Fermi surface nesting: the origin of AFM order

The antiferromagnetic ordering in the FeAs-based superconductors is believed to arise from the Fermi surface nesting driven spin-density-wave order (when parallel sheets of the Fermi

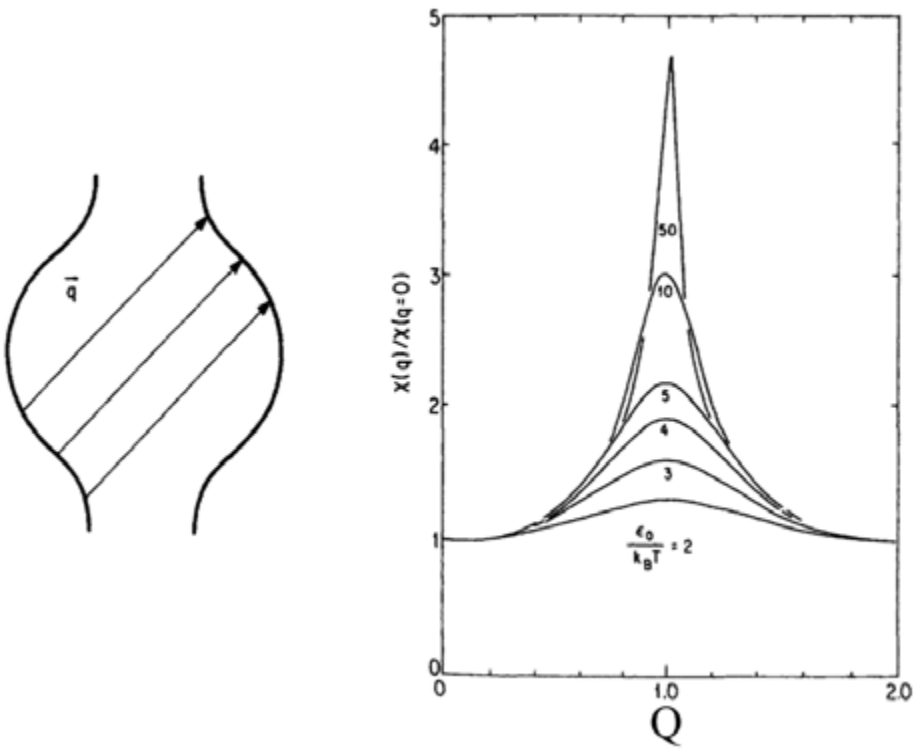

Figure 2.12 (Left) Sinusoidal quasi-one-dimensional Fermi surfaces. (Right) The response function of the Fermi surface on the left panel at various temperature. After Ref. [221].

surface can be translated by a nesting vector, $\vec{q}$, and superposed). A particular topology of Fermi surface results in a response to an external perturbation and the response of the charge or spin density can be written as [220]

$$\rho(\vec{q}) = \chi(\vec{q})\Phi(\vec{q}) \tag{2.1}$$

where $\Phi(\vec{q})$ is a time independent potential and $\chi(\vec{q})$ is the so-called Lindhard response function. The Lindhard response function is given in D dimensions by [220, 221]

$$\chi(\vec{q}) = \int \frac{d\vec{k}}{(2\pi)^D} \frac{f_k - f_{k+q}}{\epsilon_k - \epsilon_{k+q}} \tag{2.2}$$

where $f_k = f(\epsilon_k)$ is the Fermi function. The most important contribution to the integral of the response function comes from pairs of states which are separated by $\vec{q}$ at the same energy.[220] The response function is drawn in Fig. 2.11 for simple 1-D, 2-D, and 3-D Fermi surfaces. [220, 221] Another readily evaluative example is a sinusoidal quasi 1-D topology that

is considered at a finite temperature as shown in Fig. 2.12.[220] The Equation 2.2 can be evaluated and give

$$\chi(Q,T) = -e^2 n(\epsilon_{\mathrm{F}}) \ln \frac{1.14\epsilon_0}{k_{\mathrm{B}}T} \tag{2.3}$$

where ϵ_0 is an arbitrarily chosen cutoff energy (usually to be the Fermi energy ϵ_{F}).[220] For different $\frac{\epsilon_0}{k_{\mathrm{B}}T}$, the response function is shown in Fig. 2.12.[220]

If we consider a 2-D cylinder (Fig. 2.11) with a sinusoidal modulation (Fig. 2.12) of the cylinder wall, which looks similar to the Fermi surfaces of the FeAs-based superconductors in Fig. 5.1, the modulated cylinder-shaped Fermi surface can give rise to a peak in the response function whereas a cylinder-shaped Fermi surface (without modulation) does not result in a peak (Fig. 2.11).[221] In the FeAs based superconductors, it has been widely accepted that when the hole Fermi surface is translated by a nesting vector $\vec{q} = \vec{Q}_{\mathrm{AFM}}$, it leads to a peak in the response function and drives a spin density wave antiferromagnetic order.[222]

Coexistence of superconductivity and antiferromagnetism

In most of the FeAs-based superconductors (the 1111, 122, 111, and 11 families), superconductivity (SC) emerges when the structural and antiferromagnetic transitions are suppressed to low temperatures together with sufficiently smaller ordered moment sizes (M) as seen in Sections 2.1 and 2.3. Nevertheless, coexistence between superconductivity and magnetism as shown in the phase diagrams in Sections 2.3.1 - 2.3.4 has been observed in several different compounds.[223–228] Since antiferromagnetism in the FeAs-based superconductors originates from conduction electrons that also form the Cooper pairs below T_{c}, it is intriguing that superconductivity and antiferromagnetism compete for the same electrons which was not expected, especially when it is known that the magnetism is generally detrimental for superconductivity.

One might simply argue that superconductivity and antiferromagnetism occur in different volumes of a specimen. This was indeed thought to be the case in K doped $BaFe_2As_2$ as many reports claimed microscopic phase separation in K doped $BaFe_2As_2$ compounds,[199, 202, 203] which has been later argued that SC and AFM are microscopically coexisting in K substituted superconducting samples (Section 2.3.2).[204] In contrast, Co doped $BaFe_2As_2$ compounds were studied by local probe measurements (NMR, μSR, etc.) for possible phase separation and it was concluded that superconductivity and antiferromagnetism coexist microscopically in the

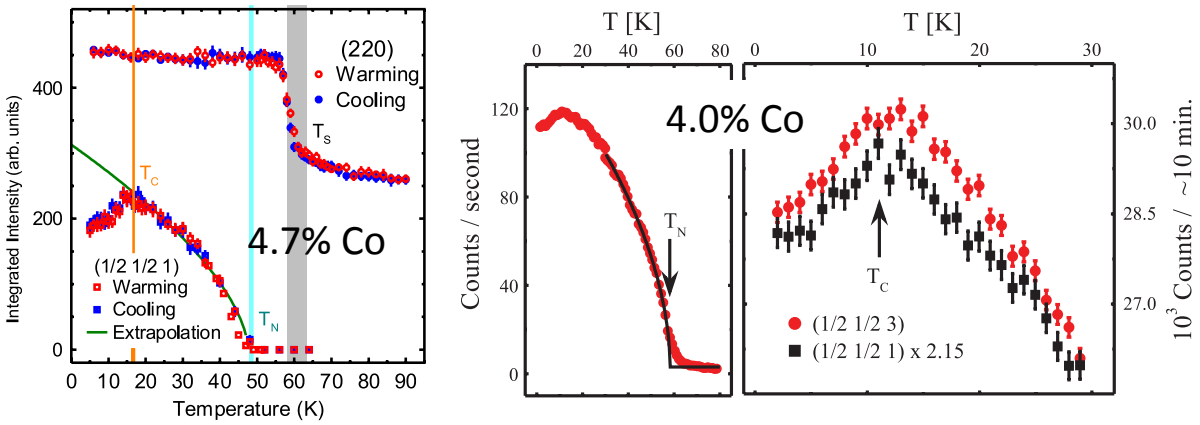

Figure 2.13 Suppression of AFM order parameter below the superconducting transition temperature T_c in 4.7% Co and 4.0% Co substituted $BaFe_2As_2$ compounds.[182, 183]

same volume of the compound.[182, 184, 203]

Competition between superconductivity and antiferromagnetism

Intriguing observations were reported by Pratt *et al.* [182] and Christianson *et al.* [183] They observed that the AFM ordering in approximately 4% Co substituted $BaFe_2As_2$ compounds is suppressed below the superconducting transition temperature T_c as shown in Figure 2.13. The authors noted "in $Ba(Fe_{0.953}Co_{0.047})_2As_2$, the observed reduction in the ordered moment below T_c is substantially larger than that observed for UPt_3 or UNi_2Al_3, demonstrating an unusually strong interaction between AFM and SC in the iron arsenides." [182] A systematic study of reduction of the AFM ordering below T_c with increasing Co substitution by the same group revealed that not only the unconventional pairing in the FeAs-based superconductors but also competition between AFM and SC for the same conduction electrons.[186] The suppression of the AFM order parameter below T_c shown in Fig. 2.13 can be modeled by the mean field theory considering $s^{\pm}$ pairing symmetry of Co substituted $BaFe_2As_2$ which explains the coexistence and competition between superconductivity and antiferromagnetism (see Pratt's Ph. D. dissertation [229] for theoretical consideration and further reading). The suppression of AFM order below T_c is also reported in Ni and Rh substituted $BaFe_2As_2$ compounds.[188–190] Recent neutron diffraction measurement on K substituted $BaFe_2As_2$ compounds [201] and μSR measurement on Co substituted NaFeAs compounds exhibit the reduction in the AFM order

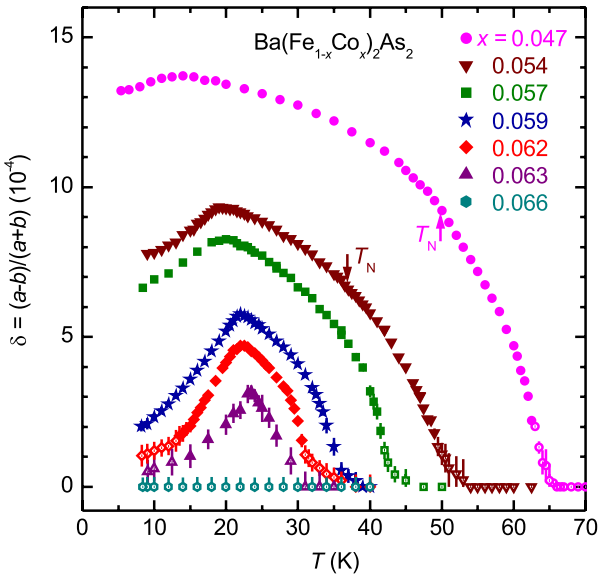

Figure 2.14 Suppression of orthorhombic distortion below the superconducting transition temperature T_c in $Ba(Fe_{1-x}Co_x)_2As_2$ compounds. After Ref. [185].

parameter below T_c.[207] It seems that the coexistence and competition between AFM and SC are universal in the FeAs-based superconductors.

2.4.2 Interplay between superconductivity and structure

Anomalous reduction in the orthorhombic distortion below T_c

Right after the observation of the suppression of AFM order in Co substituted $BaFe_2As_2$ compounds, a former graduate student Dr. Shibabrata Nandi and I measured orthorhombic distortions, δ ($= \frac{a-b}{a+b}$), in a series of Co substituted $BaFe_2As_2$ compounds using the high-resolution x-ray diffraction technique. We found an anomalous suppression of the orthorhombic distortion below superconducting transition temperatures as represented in Figure 2.14. Moreover, it turns out that the superconducting state stabilizes in a tetragonal structure at low temperature for a high Co concentration ($\sim 6\%$) as well as in an orthorhombic structure at low temperature for a lower Co concentrations ($\sim 5\%$). With the highest T_c occurring in a tetragonal structure ($> 6\%$ Co), superconductivity may favor a tetragonal structure.[185]

Nematic order: the origin of orthorhombic distortion

The suppression of the orthorhombic distortion, δ, can be understood as a direct intercon-

nection between superconductivity and the orthorhombic distortion. Similar to the free energy expansion described in Equation (4) in Ref. [186], the free energy can be written in terms of the superconducting order parameter Ψ and the distortion δ

$$F = \frac{a}{2}\left(|\Psi|^2 + \delta^2\right) + \frac{u}{2}\left(|\Psi|^2 + \delta^2\right)^2 + \frac{\gamma_\delta}{2}\delta^2|\Psi|^2 \tag{2.4}$$

here, γ_δ is a coupling constant. It can be rationalized as in Ref. [186] that the suppression of orthorhombic distortion below T_c arises from a strong competition between orthorhombic order and superconductivity since the temperature variation of the distortion δ is reminiscent of the behavior of the ordered magnetic moment as shown in Section 2.4.1. However, it requires a fine tuning of a coupling constant γ_δ, sufficiently large to suppress δ below T_c, but sufficiently small to avoid a first order transition between both states.[185]

For an alternative explanation of the observed behavior, nematic order φ has been introduced. The commensurate antiferromagnetic fluctuations, of the kind seen in the iron arsenides, have been shown to lead to an emergent, nematic order parameter $\varphi = \vec{m_1} \cdot \vec{m_2}$.[230] Here, $\vec{m_1}$ and $\vec{m_2}$ are sub-lattice magnetizations as shown in Figure 2.15 (a). The free energy expansion can be written as [231]

$$F = \frac{a}{2}\left(\varphi^2 + m^2\right) + \frac{u}{2}\left(\varphi^2 + m^2\right)^2 + \frac{C_s}{2}\delta^2 - g_0\varphi\left(\vec{m_1} \cdot \vec{m_2}\right) + \lambda\delta\varphi \tag{2.5}$$

where C_s is the bare shear modulus, λ is the magneto-elastic coupling, g_0 is the coupling between two sub-lattices, and the orthorhombic distortion is related to $\delta = -\frac{\lambda}{C_s}\varphi$.[185, 230] $\vec{m_1}$ and $\vec{m_2}$ are weakly coupled, and are fluctuating randomly above transition temperatures so that the time-averaged $\langle\vec{m_1} \cdot \vec{m_2}\rangle = 0$ and $\langle\vec{m_1}\rangle = \langle\vec{m_2}\rangle = 0$, which means no net magnetic moment [top of Figure 2.15 (b)]. When the nematic order sets in at T_S, their relative orientation is fixed so that while $\langle\vec{m_1}\rangle = \langle\vec{m_2}\rangle = 0$ (no net magnetic moment), the time-averaged $\langle\vec{m_1} \cdot \vec{m_2}\rangle \neq 0$. When $\langle\vec{m_1} \cdot \vec{m_2}\rangle = 1$, at a time-averaged instance, the two nearest-neighbor sub-lattice moments are fluctuating in a ferromagnetically correlated way. And antiferromagnetically correlated fluctuations of two nearest-neighbor moments occur when $\langle\vec{m_1} \cdot \vec{m_2}\rangle$ = -1 at a time-averaged instance. Therefore, when $\lambda\delta\langle\varphi\rangle > 0$, lattice contraction happens and $\lambda\delta\langle\varphi\rangle < 0$ causes lattice expansion as displayed in Figs. 2.15 (c) and (d).[230] An emergent nematic order at T_S leads to a

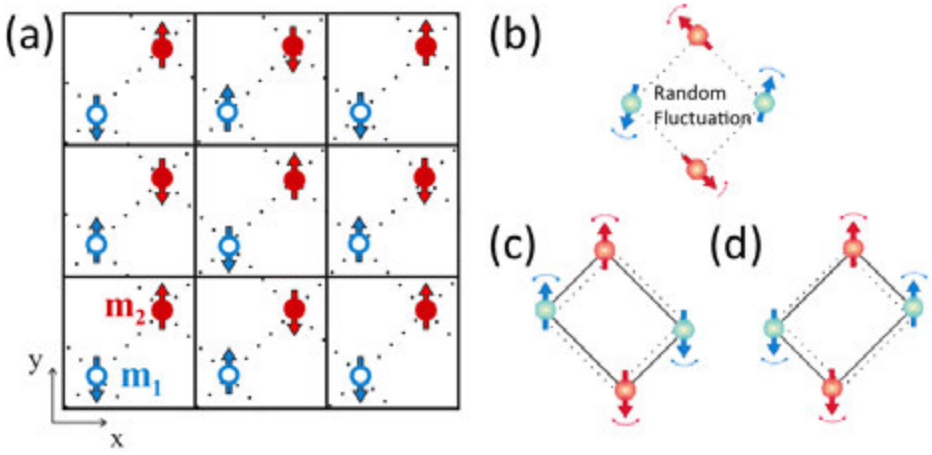

Figure 2.15 (a) Two magnetic sub-lattices. (b) Random fluctuation. (c, d) Degenerate nematic fluctuations. After Ref. [230].

broken Ising symmetry that chooses either (c) or (d) lattice configuration for the orthorhombic distortion. And when the magneto-elastic coupling, λ, is finite, the antiferromagnetic order occurs in the chosen orthorhombic lattice (refer to Sec. 4.1.4, 4.2.1, and 4.2.2 for locked or split structural and AFM transitions). Easily seen from the relation $\delta = -\frac{\lambda}{C_s}\varphi$, the nematic order and the orthorhombic distortion occur simultaneously at T_S.

CHAPTER 3. Overview of Experimental Techniques

X-ray and neutron scattering are the techniques used to identify the crystallographic and magnetic structures of materials. X-ray scattering has been used mostly for the determination of crystallographic structures, sometimes complemented by neutron scattering. Until the discovery of x-ray resonant magnetic scattering, neutron scattering has been used for identification of magnetic structures since the neutron has a moment which directly interacts with magnetic dipoles in the materials.

X-rays are electromagnetic waves with an energy range from 0.1 keV approximately to more than 100 keV. X-rays with energies up to $\sim$ 5 keV are termed "soft" and above $\sim$ 5 keV, "hard". The primary interaction between x-rays and electrons, known as Thomson scattering (scattering by charged particles), makes it possible to be used for determination of crystallographic structures. Due to the wave nature of x-ray and not having a magnetic moment, it had been long believed that the electromagnetic interaction between magnetism and x-rays is too weak to be detected, which had been true for conventional laboratory x-ray sources. With a technology breakthrough, synchrotron radiation provides about 8-17 orders of magnitude brighter x-ray than laboratory sources and enables the detection of the interaction between x-ray and magnetism.

Neutrons are spin $\frac{1}{2}$ particles with a mass of 1.675 x 10^{-27} kg, a magnetic dipole moment of -1.913 μ_N, and no charge. Useful energy for scattering ranges from 0.1 to 500 meV which is equivalent to wavelengths from 0.4 to 30 Å. Neutrons with energies less than 1 meV are called "cold" neutrons, between 1 meV and 0.025 eV are called "thermal" neutrons, between 0.025 eV and 10 keV are called "epithermal" neutrons, and above 10 keV are called "fast" neutrons. Because the neutron is not charged, it can overcome the Coulomb barrier of electrons and nuclei, and interact directly with the atomic nuclei (particle-particle interaction), and this makes

the neutron scattering one of the important techniques in crystallography. However, neutron scattering has not been used as much as x-ray for crystallographic structure determination since the probability of nuclear interaction is low, the brightness of neutrons from their source is about 2 orders of magnitude smaller than laboratory x-ray sources, and also neutron experiments involve large facilities (e.g. High Flux Isotope Reactor at Oak Ridge National Laboratory located at Oak Ridge, TN) that require advanced planning (i.e. those facilities are not readily usable). Since the neutron has a spin, it can directly interact with magnetic dipole moments of unpaired electrons in magnetic materials which can easily be detected. In addition, the energy scale of neutrons is in the order of energy of elemental excitations, such as phonon and spin excitations so inelastic neutron scattering techniques are often used to study excitations in materials. Neutron scattering is, therefore, a powerful technique to study magnetism in materials.

However, the neutron scattering experiments require a large mass (order of a gram), and neutron scattering is not an element specific technique. Also, it is difficult and sometimes impossible when the material contains neutron absorbing elements such as cadmium. On the other hand, x-ray resonant magnetic scattering is an element specific technique which employs the tuning of the incident energy of the x-ray to an absorption edge of an element. Therefore it permits multiple magnetic species to be studied. It also has a higher intrinsic resolution than the neutron scattering, and a small sample (order of several micron meters square of the surface area) can be studied.

3.1 X-ray Scattering Technique

3.1.1 High Resolution X-ray Diffraction

The x-ray charge scattering (the "charge scattering" is an intuitive term due to the interaction between charge density of electrons in materials and x-ray) has been the main workhorse in the crystallography since Bragg's law. Bragg's law is summarized in the relation $n\lambda = 2d\sin\theta$ where n is an integer, λ is the wavelength of x-ray, d is the interplanar distance, θ is the scattering angle. Bragg's law may also be described in terms of the Laue equations, $\Delta\vec{k} =$

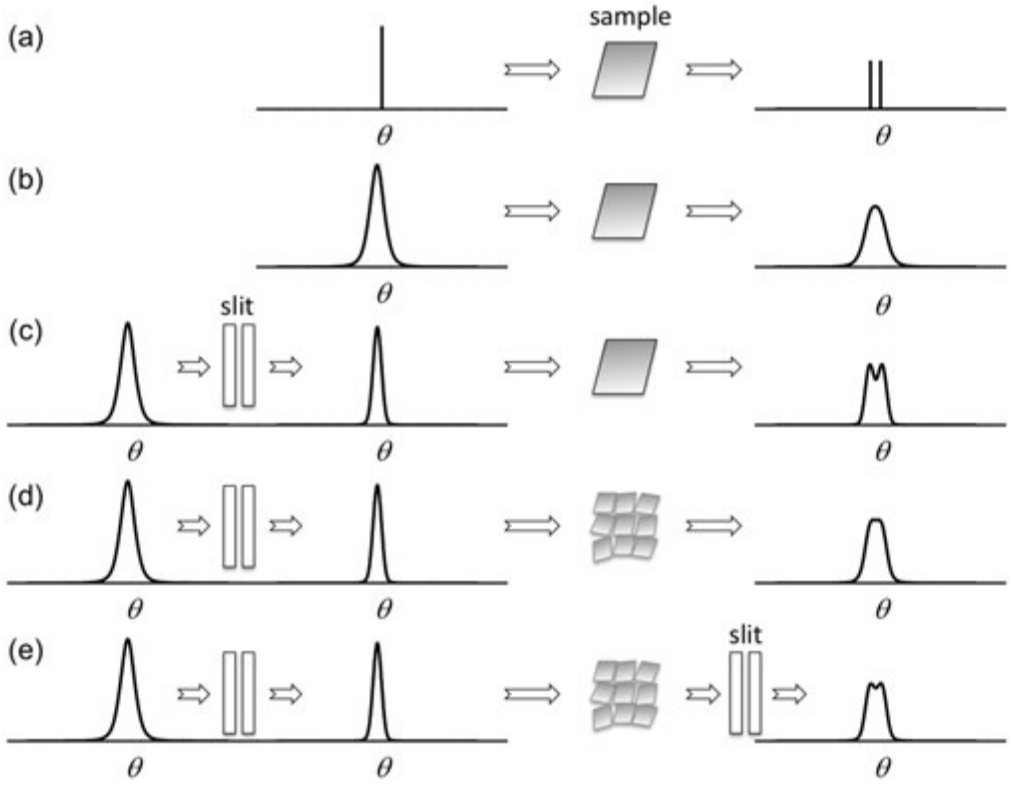

Figure 3.1 Illustration of resolution in x-ray diffraction experiments for two peaks located very closely. Diffraction on a perfect single crystal with (a) ideal incident x-ray as a delta function, (b) incident x-ray with a finite angular width, (c) higher incident x-ray resolution in angle after a slit. Diffraction on a mosaic crystal with (d) high incident x-ray resolution with slit and (e) higher diffracted x-ray resolution after a slit.

$\vec{G}$ where $\Delta\vec{k} = \vec{k}_i - \vec{k}_f$ is the scattering vector and $\vec{G} = h\vec{a}^* + k\vec{b}^* + l\vec{c}^*$ with reciprocal vectors $\vec{a}^*$, $\vec{b}^*$, and $\vec{c}^*$ and Miller indices h, k, and l.

When a material undergoes a structural change under a condition of temperature change, pressure change, etc. the structural symmetry of a material is lowered. As a result of lowering symmetry, the interplanar distances, d, change and result in changes in different or new peaks, or Bragg reflections. In this case, observing the appearance of additional peaks and/or shifts of peaks at/to new scattering angles, one realizes a structural change in a material.

Instrument Resolution - Incoming X-ray

The observation of a structural transition is sometimes difficult, for example, when the

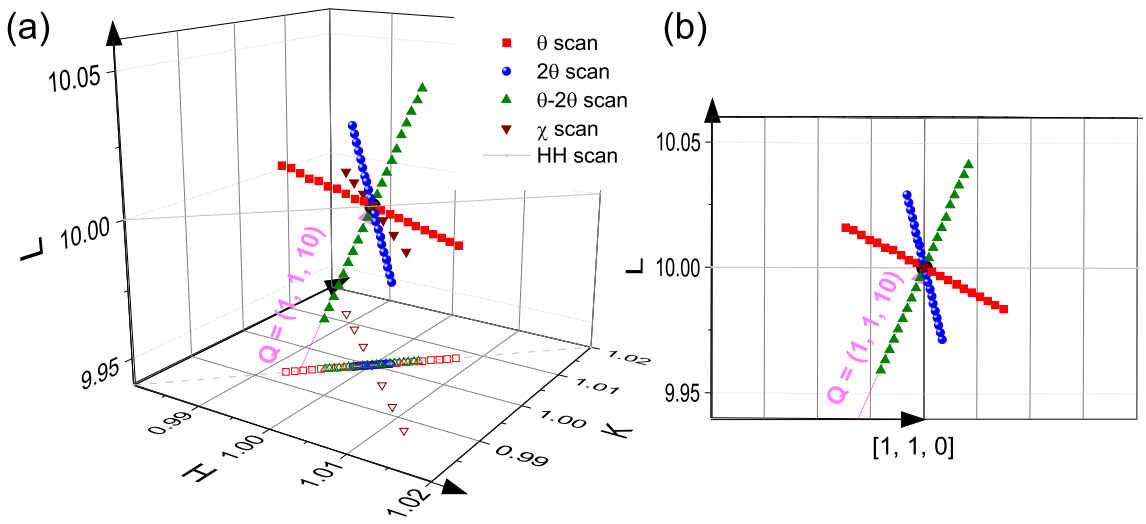

Figure 3.2 (a) Angular θ (red square), 2θ (blue circle), $\theta - 2\theta$ (green triangle), and χ (brown up-side-down triangle) and [H, H, 0] (gray line) scans around $\vec{Q}$ = (1, 1, 10) (pink arrow). Open symbols and dashed lines for each color are projections onto HK plane. (b) Seen from a side ([H, -H, 0] direction). The view is perpendicular to the scattering plane defined by [0, 0, L] and [H, H, 0]. Note that the figures are enlarged around (1, 1, 10) so the Q is not going through the origin of the plot.

changes of scattering angles are very small. Under ideal conditions, it should be possible to detect any changes of scattering angles as shown in Figure 3.1 (a). However, x-rays generated in the laboratory and synchrotron source have a finite divergence, which can make the observation difficult [Figure 3.1 (b)]. Moreover, the laboratory x-rays contain undesired components of the characteristic radiation. For example, the characteristic radiation from a Cu target has both K_α and K_β components. One must cut off the undesired radiation K_β by the means of filters (intensity reduction of K_β) or monochromators (angular discrimination of K_β). After getting rid of K_β, there remains K_{α_1}(desired) and K_{α_2}(undesired) radiations which are very closely located. Using both a monochromator and a slit, one can effectively cut away the K_{α_2} radiation by utilizing the fact that the scattering angle for K_{α_2} is slightly different from K_{α_1} (see Ref. [232] for details of the characteristics of laboratory x-ray radiation). Slits are also used for synchrotron x-ray radiation to define the divergence of the incoming beam. Figure 3.1 (c) illustrates how high resolution of the incoming x-ray achieved by slits enables observation of a structural transition.

Mosaicity of Sample

In addition to an instrument resolution, the mosaicity of a specimen is an another important factor. The illustration in Figure 3.1 (a)-(c) was made under the assumption of a perfect crystal. A mosaic crystal is composed of small single crystals with a typical size of $\sim$1000Å.[232] Those mosaic crystals are slightly misaligned to each other. If the distribution of misalignment is within ϵ degree, then the intensity of a charge peak at θ in a perfect crystal would be distributed between θ and $\theta + \epsilon$ in a mosaic crystal.[232] Therefore, the term *mosaicity* describes how close the crystal is to a perfect crystal and *mosaicity* is determined by an angular θ scan, a rocking scan.

The mosaicity of a specimen can be very important. To measure the tetragonal-to-orthorhombic structural distortion in the 122 system, two domains, one domain which is characterized by the longer orthorhombic $\vec{a}$ and another by the shorter orthorhombic $\vec{b}$, are probed in a [H, H, 0] scan using the four-circle diffractometer in our lab (see Fig. 3.3). A [H, H, 0] scan at $\vec{Q}$ = (1, 1, 10) is shown with a gray solid line in Fig. 3.2. A [H, H, 0] scan was chosen since it is close to the angular θ scan which has the best instrumental resolution in our setup of instrument. Because the [H, H, 0] scan is close to the θ scan, the measurement is sensitive to the mosaicity of a specimen. As shown in Figure 3.1 (d) with the same condition for the incoming x-ray as Figure 3.1 (c), a mosaic crystal broadens the width of the diffracted x-ray (mosaic spread) in θ and so does the [H, H, 0] scan, then it makes the observation of peak splitting difficult.

Instrument Resolution - Diffracted X-ray

Even for perfect, monochromatic radiation, since the incoming x-ray beam from both laboratory sources and synchrotrons is not perfectly parallel, the diffracted x-ray is also not parallel. The divergence of diffracted x-ray and can worsen the resolution. This can be improved by slits. One can select as much parallel x-rays by placing slits in front of the detector to improve the instrument resolution as illustrated in Figure 3.1 (e). However, care must be taken that the slits are not cutting too much signal by adjusting the size of slits in the diffracted x-ray.

Figure 3.3 displays the configuration for x-ray diffraction measurements at the Ames Laboratory. Each component discussed above is shown in the schematic diagram and photos that are connected with dashed lines.

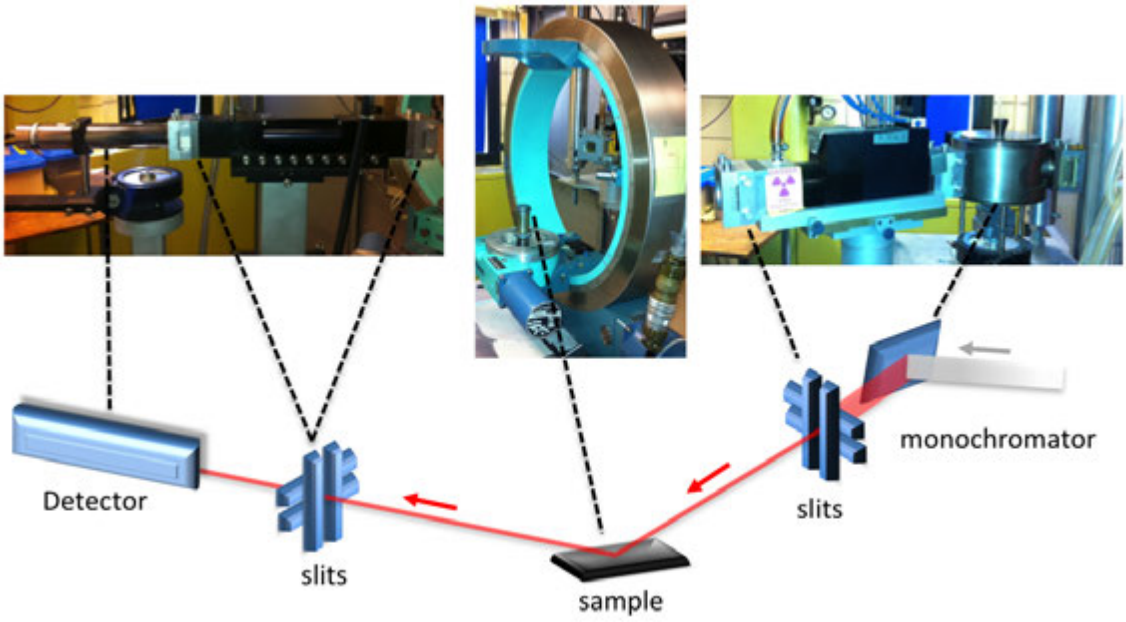

Figure 3.3 Schematic diagram showing configuration of instruments in the x-ray lab at Ames Laboratory and pictures of each part. The black dashed lines connect the equivalent parts in the diagram and the photos.

3.1.2 X-ray Resonant Magnetic Scattering (XRMS)

In addition to the x-ray charge scattering, x-ray as an electromagnetic wave also interacts with magnetism in materials. X-ray magnetic scattering was first reported by de Bergevin and Brunel with a laboratory x-ray source in 1972.[233] Because the interaction is so small, it had been practically impossible to employ the x-ray magnetic scattering until recently.

Synchrotron radiation was first recognized by R. V. Langmuir and co workers in 1947. Synchrotron radiation is photons emitted when charged particles accelerate. Until 1980s, synchrotron x-ray radiation was achieved as a parasitic operation mode from bending magnets of synchrotron operated for the experimental nuclear/high-energy physics which accelerates electrons and positrons. In 1980's, the first generation synchrotrons dedicated to producing x-rays were built world-wide from bending magnets. Then, an insertion device called a wiggler was developed. A wiggler is an array of oppositely polarized magnets. As electron passes through a wiggler, it experiences multiple accelerations due to a frequent change of magnetic fields and more radiation is emitted. So many of the first generation synchrotrons were evolved to the

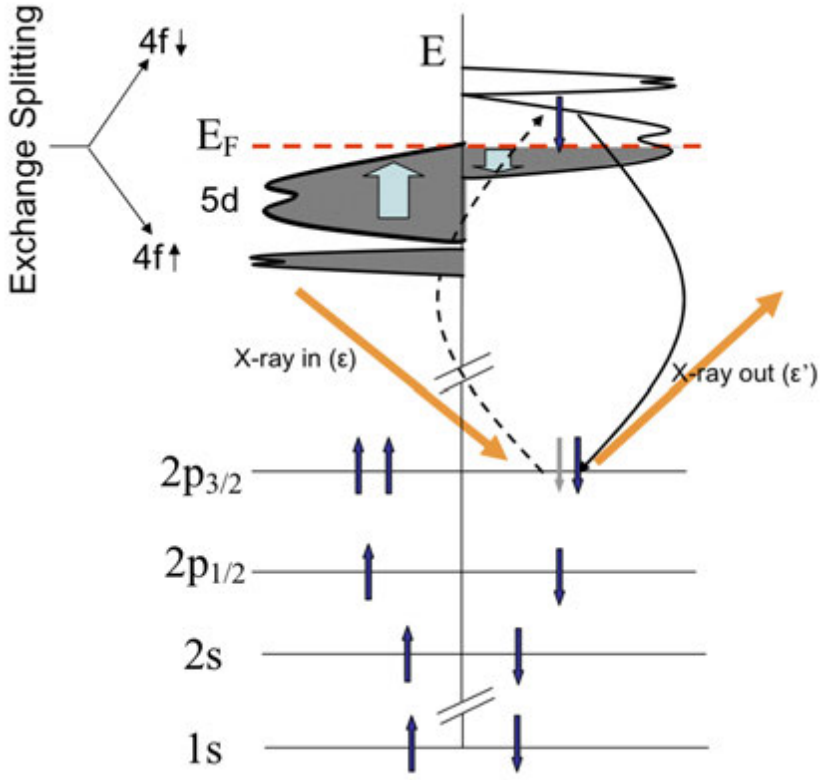

Figure 3.4 Illustration of resonant process in $4f$ elements. Incident x-ray with a suitable energy excites unpaired electrons in $2p_{3/2}$ level to an empty $4f$ level above the Fermi level. Spin polarized excited electrons are de-excited to its initial state and emit x-ray. After Ref. [245].

second generation synchrotron (e.g. National Synchrotron Light Source, NY). In 1990's, an undulator as an insertion device was developed (an undulator is similar to a wiggler in its form but with more number of magnets closely located and with, generally, slightly smaller magnetic field than wiggler. Sine the number of magnets, magnetic field strength, and distance between magnets are finely tuned in undulator, electrons oscillate with smaller amplitude and the emitted radiation interferes strongly which results in an intense beam with a narrow energy bandwidth) and lead to the third generation synchrotron (e.g. Advanced Photon Source, IL). X-ray magnetic scattering has since flourished with the development of synchrotron technology. The interesting history of synchrotron and the properties of synchrotron x-ray radiation are discussed in many books including Refs. [234, 235].

In 1990's, Gibbs *et al*. observed an enhancement of the diffracted signal in an antiferro-

magnetic Ho sample when the x-ray energy was tuned to an absorption edge of Ho [236]. The enhancement occurs because there is an emittance of elastically scattered photons when the electrons are de-excited to the core level after an appropriate energy of x-ray excites electrons from the core levels to the unoccupied states above the Fermi level. This is called a resonant process and illustrated in Figure 3.4 for $4f$ rare-earth elements. The theories of resonant/non-resonant magnetic scatterings (XRMS/XNRMS) are well developed and described in many textbooks including Ref. [237]. The essence of the non-resonant x-ray magnetic scattering is that the scattering amplitude depends on the Fourier transform of orbital and spin angular momentum densities [237]. For the x-ray resonant magnetic scattering, Hannon *et al*. explains that the resonance enhancement is determined by (1) the matrix elements for the transition, (2) the virtual core hole lifetime, and (3) the spin polarization of states [238], and they predicted much larger enhancements at M_4 and M_5 edges of actinides and it was soon confirmed experimentally.[239] It is noteworthy that the absolute relation between a resonance enhancement and the magnetic moment size of a material is not known which makes the XRMS unable to determine an absolute moment size of a material. Here, keeping the resonance process in mind, I will focus on the polarization analysis, an important tool in the XRMS measurement. Then I will review the XRMS measurements on $3d/4d/5d$ transition metals and their resonance enhancements.

3.1.2.1 Polarization Analysis

Synchrotron x-ray radiation is almost completely linearly polarized in the plane of the storage ring. The polarization of synchrotron x-ray is described by P_L:

$$P_L = \frac{A^2 - B^2}{A^2 + B^2}$$

where

$$A = \left(\frac{1}{\gamma^2} + \Psi^2\right) K_{2/3}(\xi)$$

$$B = \left(\frac{1}{\gamma^2} + \Psi^2\right)^{\frac{1}{2}} \Psi K_{1/3}(\xi)$$

$$\gamma = \frac{E}{m_0 c^2}$$

and Ψ is the angle (in radian) between the tangential direction of electrons' velocity and the direction of radiation, and $K_{1/3}$ and $K_{2/3}$ are the second-rank Bessel functions [234, 235, 240]. When $\Psi \approx 0$, $A \approx$ finite and $B \approx 0$, so $P_L \approx 1$. For example, $P_L = 0.999$ at Advanced Photon Source in Argonne National Laboratory (one of the third generation synchrotron) which operates at 7 GeV ($\gamma = 1.4 \times 10^{-4}$).

The polarization property of synchrotron x-rays is of great benefit for the XRMS since the polarization of the scattered x-ray can be modified by the *magnetic* scattering process. The polarization of the x-ray is not changed during *charge* scattering process. Therefore it is possible to discriminate magnetic scattering from charge scattering by analyzing the polarization of the scattered x-ray with respect to the polarization of the incoming x-ray. This also can be used to provide information concerning the magnetic moment direction in materials. Analyzing the polarization of scattered x-ray is similar to what we observe in reflected sunlight by the rear window of a car. On a sunny day, if the sun shines right above a car and one looks at the rear window of the car with polarized sunglasses, one can see dark patterns because reflected sunlight is linearly polarized parallel to the surface of the rear window (perpendicular to the scattering plane. See the definition of scattering plane in the next page). The polarization component in the scattering plane is completely suppressed when $\frac{\tan(\theta_i-\theta_s)}{\tan(\theta_i+\theta_s)}$=0 where θ_i and θ_s are incident and scattered angles, respectively. The equation is satisfied when $\theta_i + \theta_s$=90°. Therefore, in a specular reflection condition, when the scattering angle, 2θ becomes 90°, one can select/analyze polarization of the scattered x-ray. In the following, I will discuss how the polarization of the x-ray can be changed in the electric dipole transition and how it determines the components of magnetic moments.

Electric Dipole Transition ($E1$)

The resonant dipole scattering amplitude can be written in matrix form:

$$f_{E1}^{XRES} = F^{(0)} \begin{pmatrix} 1 & 0 \\ 0 & \cos 2\theta \end{pmatrix} \tag{3.1a}$$

$$- iF^{(1)} \begin{pmatrix} 0 & z_1 \cos\theta + z_3 \sin\theta \\ z_3 \sin\theta - z_1 \cos\theta & -z_2 \sin 2\theta \end{pmatrix} \tag{3.1b}$$

$$+ F^{(2)} \begin{pmatrix} z_2^2 & -z_2 \left(z_1 \sin\theta - z_3 \cos\theta\right) \\ z_2 \left(z_1 \sin\theta + z_3 \cos\theta\right) & -\cos^2\theta \left(z_1^2 \tan^2\theta + z_3^2\right) \end{pmatrix} \tag{3.1c}$$

where $F^{(i)}$s are the strength of resonance [241]. The first term (Eqn. 3.1a) contributes to the charge scattering. The second term (Eqn. 3.1b) contributes to the first-harmonic satellite peaks and the third term (Eqn. 3.1c) contributes to the second-harmonic satellite peaks in incommensurate antiferromagnets (in commensurate antiferromagnets, this term contributes magnetic intensity at the charge scattering peak position). In commensurate antiferromagnets, the second term (Eqn. 3.1b) describes the polarization dependence of the resonant scattering amplitude with respect to the magnetic moment directions in the scattering geometry shown in Figure 3.5 (a) [241]. Here, the scattering plane is defined by the incoming and outgoing (scattered) x-ray, the σ polarization is a linear polarization perpendicular to the scattering plane, and the π polarization is a linear polarization parallel to the scattering plane.

The matrix element in Equation 3.1b is

$$\begin{pmatrix} M_{\sigma\to\sigma} & M_{\pi\to\sigma} \\ M_{\sigma\to\pi} & M_{\pi\to\pi} \end{pmatrix} = \begin{pmatrix} 0 & z_1 \cos\theta + z_3 \sin\theta \\ z_3 \sin\theta - z_1 \cos\theta & -z_2 \sin 2\theta \end{pmatrix}. \tag{3.2}$$

Therefore, utilizing a polarization analyzer which selects a desired polarization from the scattered x-ray [Figure 3.5 (b) and (c)], one can determine the scattering amplitudes. $M_{\sigma\to\sigma} = 0$ means that the magnetic scattering amplitude is zero in the $\sigma - \sigma$ channel. The magnetic scattering amplitude can be detected in $\sigma - \pi$, $\pi - \sigma$, and/or $\pi - \pi$ channels due to non-zero matrix elements. Each non-zero matrix element is uniquely related to the directions of magnetic moment: $M_{\sigma\to\pi}$ and $M_{\pi\to\sigma}$ are sensitive to moment directions in the scattering plane (components along the z_1 and z_3 axes), and $M_{\pi\to\pi}$ is sensitive to the moment direction perpendicular to the scattering plane (a component along the z_2 axis).

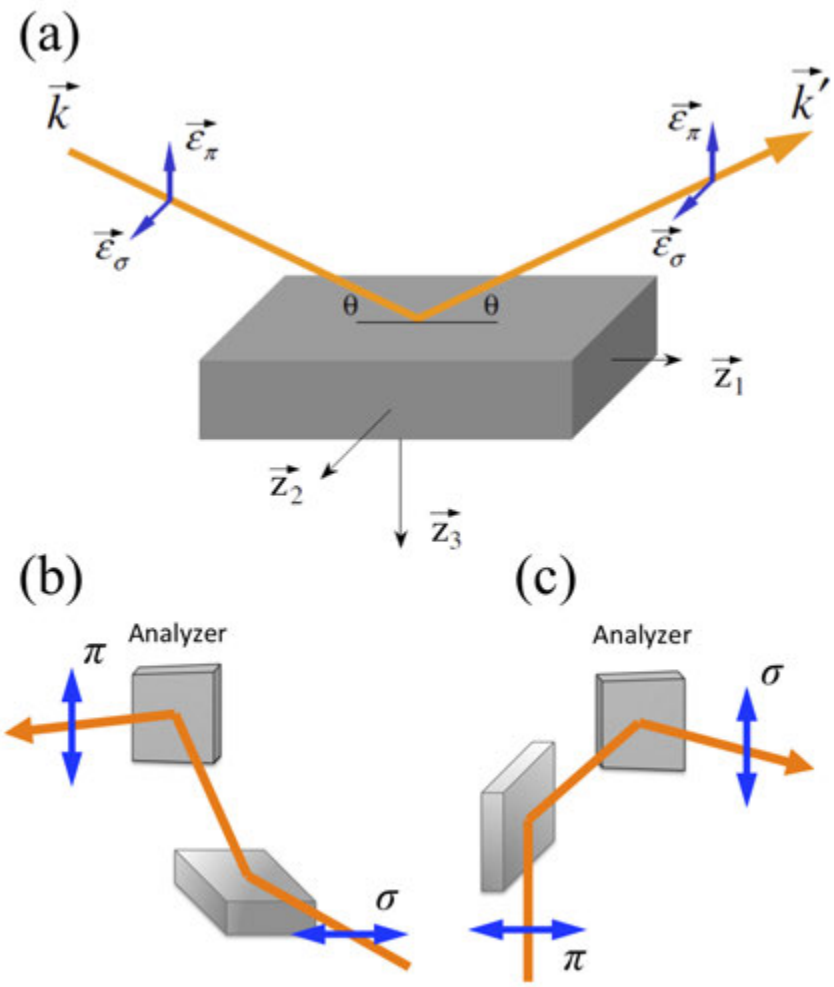

Figure 3.5 (a) Scattering geometry and definition of axes, $\vec{z}_i$. Orange arrows are the incoming and outgoing x-ray. Blue arrows are the directions of polarization. (b) $\sigma - \pi$ channel. (c) $\pi - \sigma$ channel. After Ref. [245].

Azimuth Dependence

The polarization properties of magnetic scattering amplitudes provide a possibility of an explicit determination of a magnetic moment direction in a matter. For the simplest example, imagine an antiferromagnet with a magnetic moment direction parallel to the sample surface as shown in Figure 3.6 (a). When the moment lies in the scattering plane as in Figure 3.6 (a), the magnetic scattering amplitude in the $\sigma - \pi$ or $\pi - \sigma$ channels are minimum or maximum, respectively. When the antiferromagnet is put by 90 degrees as in Figure 3.6 (b), the moment lies perpendicular to the scattering plane then the scattering amplitude becomes zero in the

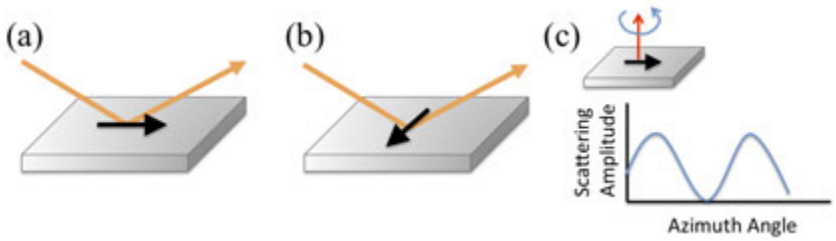

Figure 3.6 Illustration of an azimuth scan. (a) Magnetic moments (black arrow) are parallel to the surface and in the scattering plane. (b) Magnetic moments are parallel to the surface and perpendicular to the scattering plane. (c) Rotating the moment around the red arrow (azimuth angle) gives the sinusoidal change of scattering amplitude.

$\sigma - \pi$ ($\pi - \sigma$) channel. If one rotates the antiferromagnet with respect to an axis perpendicular to its surface, one will effectively rotate the moment direction and will observe a sinusoidal modulation of the magnetic scattering amplitude as shown in Figure 3.6 (c). This method is called azimuthal scans and are often written in matrix form:

$$\begin{pmatrix} 0 & z_1' \cos\theta + z_3' \sin\theta \\ z_3' \sin\theta - z_1' \cos\theta & -z_2' \sin 2\theta \end{pmatrix} \tag{3.3}$$

where $z_1' = z_1 \sin\alpha \cos\psi$, $z_2' = z_2 \sin\alpha \sin\psi$, and z_3' = -$z_3 \cos\alpha$ with an angle α between the magnetic moment and the scattering vector and the azimuthal angle ψ [242].

3.1.2.2 XRMS on 3d/4d/5d Transition Metal Elements

Despite the fact that the XRMS has been employed widely for investigations of the magnetism of 4f and 5f elements (lanthanides and actinides, respectively), there are only small number of reports of the XRMS on 3d, 4d, and 5d transition metal elements. This is largely due to a weak non-resonant scattering amplitude and a small resonant enhancement at the K edge of transition metal elements: electric dipole transitions ($E1$) at the K edge are from 1s to 4p and there is a small spin-orbit coupling in the p states leading to a weak spin polarization (the resonant enhancement depends on the spin polarization of the states [238]). It is also expected that the resonant enhancement will be large at $L_{2,3}$ edges of transition metal elements since the transitions are from p states to d states, where d states are highly polarized. However, $L_{2,3}$

edges of most transition metal elements lie in the"soft" x-ray regime. The soft x-ray is usually bad for diffraction experiments because (1) the soft x-ray is highly absorbed by air so that all the instruments should be placed in vacuum, (2) absorption by the sample is problematic, and (3) the wavelength of the soft x-ray is inevitably long so that there is a limited access to the reciprocal lattice. In this section, I will briefly review the XRMS on $3d$, $4d$, and $5d$ transition metal elements and their resonant enhancement (see references [243–245] for details about XRMS on $4f$ and $5f$ elements).

$3d$ and $4d$ Transition Metal Elements

Although many of the studies of resonant enhancements in the x-ray resonant magnetic scattering have been done on $4f$ and $5f$ elements, interestingly, the first x-ray magnetic scattering was performed on a $3d$ element, Ni in NiO, by F. De Bergevin and M. Brunel [233]. Since then, the x-ray magnetic scatterings on $3d$ transition metal elements, Cr, Mn, and Fe, were mainly exercised with the non-resonant scattering technique [246–248]. Even though there are different types of resonant experiments such as resonant charge scattering, I will mainly focus on the x-ray resonant magnetic scattering on antiferromagnetic materials. In 1985, Namikawa *et al*. first observed a small resonant enhancement at the Ni K edge in a ferromagnetic Ni single crystal [249]. Kao *et al*. studied a ferromagnetic Fe film at the Fe L_2 and L_3 edges and observed a large enhancement. Their experiment was not a diffraction experiment but a measurement of a reflectivity utilizing the resonance due to the limitation related to a small Ewald sphere in the soft x-ray regime [250]. Soon, much attention was paid to find the resonant enhancements at K and $L_{2,3}$ edges of $3d$ elements. It resulted in observations of the resonant enhancements at the Ni L_3 edge in antiferromagnetic Ag-Ni multilayers [251], the Ni K edge in antiferromagnet NiO [252], the Co K edge in antiferromagnet CoO [253], the Mn K edge in antiferromagnetic $RbMnF_3$ [254], the Cu K edge in antiferromagnetic cuprate $PrBa_2Cu_3O_{6.92}$ [255] and the antiferromagnetic Mott-Hubbard insulator $KCuF_3$ [256], and the Mn $L_{2,3}$ edges in the antiferromagnetic bilayer manganite $La_{2-2x}Sr_{1+2x}Mn_2O_7$ [257, 258]. As shown in Figure 3.7, the resonant enhancement at K edges of $3d$ transition metal elements is sometimes absent or small (factor of 2∼3) while the enhancement at $L_{2,3}$ is considerably larger (up to 3 orders of magnitude). [259]

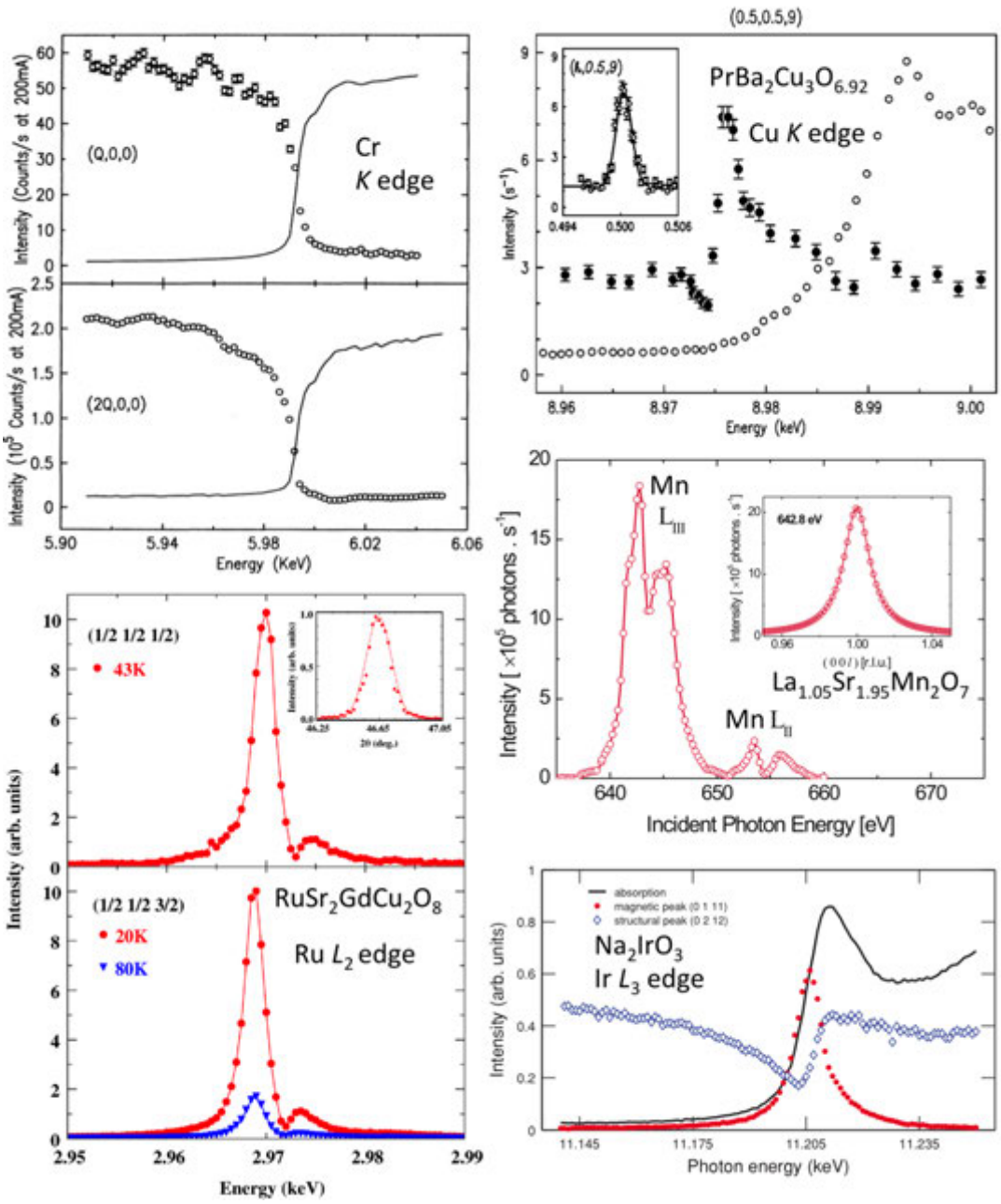

Figure 3.7 Examples of the resonant enhancement at K or L edges of $3d$, $4d$, and $5d$ elements. (Top Left) No resonant enhancement at the Cr K edge.[246] (Bottom Left) Strong enhancement at the Ru L_2 edge.[261] (Top Right) Small enhancement at the Cu K edge.[255] (Middle Right) Strong enhancement at the Mn $L_{2,3}$ edges.[258] (Bottom Right) Strong enhancement at the Ir L_2 edge.[266]

Table 3.1 Magnitude of the resonance enhancement for XRMS on d and f elements. "weak" corresponds to a factor of about "10^0", "medium" to about "10^2" and "strong" to "$\geq 10^3$".

Elements	Edge	Transition	Energy Range (keV)	Resonance Strength	Reference
$3d$	K	$1s \rightarrow 4p$	5-9	Weak	[259]
$3d$	L_1	$2s \rightarrow 3d$	0.5-1.2	Weak	[259]
$3d$	L_2, L_3	$2p \rightarrow 3d$	0.4-1.0	Strong	[259]
$4d$	L_2, L_3	$2p \rightarrow 4d$	2.5-3.5	Strong	[242, 260, 261]
$5d$	L_2, L_3	$2p \rightarrow 5d$	10-13	Strong	[262–267]
$4f$	K	$1s \rightarrow 4p$	40-63	Weak	[259]
$4f$	L_1	$2s \rightarrow 5d$	6.5-11.0	Weak	[259]
$4f$	L_2, L_3	$2p \rightarrow 5d$, $2p \rightarrow 4f$	6.0-10.0	Medium	[259]
$4f$	M_1	$3s \rightarrow 5p$	1.4-2.5	Weak	[259]
$4f$	M_2, M_3	$3p \rightarrow 5d$, $3p \rightarrow 4f$	1.3-2.2	Medium to strong	[259]
$4f$	M_4, M_5	$3d \rightarrow 4f$	0.9-1.6	Strong	[259]
$5f$	M_4, M_2	$3d \rightarrow 5f$	3.3-3.9	Strong	[259]

XRMS on $4d$ elements in antiferromagnetic materials has been found only in Ruthenium compounds. The large resonant enhancement was found at the Ru $L_{2,3}$ edges of antiferromagnetic Ca_2RuO_4, $Ca_3Ru_2O_7$, and $RuSr_2GdCu_2O_8$ [242, 260, 261].

5d Transition Metal Elements

Unlike $3d$ and $4d$ transition metal elements, the $L_{2,3}$ edges of $5d$ elements lie in the hard x-ray regime. This is a huge advantage to study $5d$ elements with XRMS since the resonant enhancement at $L_{2,3}$ edges is expected to be large and a large volume of reciprocal lattice is measurable. The resonant enhancement was observed at the Pt L_3 edge of the ferromagnet CoPt [262] and of UPtGe as induced moments [263], the Re L_3 edge of an antiferromagnet K_2ReCl_6 [264], and the Ir $L_{2,3}$ edges of Iridates such as Sr_2IrO_4, Na_2IrO_3, and $CaIrO_3$ [265–267]. The resonant enhancement is very large as shown in Figure 3.7.

For completeness, I present Table 3.1 summarizing resonance strength of d and f elements.

One should note that the resonant enhancement (the resonance strength) is a relative term between the resonant amplitude and the non-resonant amplitude so that a large resonant enhancement does not guarantee a large absolute resonance amplitude. For example, if the non-resonant amplitude was $\sim 10^{-3}$ counts per second and the resonant enhancement was 10^3, the observable resonant amplitude would be ~ 1 counts per second.

3.2 Neutron Scattering Techniques

As mentioned at the beginning of this chapter, the neutron is not charged so it scatters with the atomic nuclei. For this reason, the Bragg peaks are called nuclear peaks in neutron scattering. Due to the wave-particle duality, neutrons scatter as a wave satisfying the Bragg's law with neutrons' wavelength $\lambda = \frac{h}{\sqrt{2mE}}$ and $E \sim k_B T$ where k_B is the Boltzmann's constant and T is the temperature of a material that moderates the neutrons. This makes the neutron scattering a powerful technique to study crystallographic structures. What also makes the neutron scattering a preeminent technique is that neutron possesses a spin, which provides an ability to interact with dipole moments of unpaired electrons in a matter. The amplitude of the neutron magnetic scattering is comparable to the amplitude of nuclear scattering, and the scattering rate is efficient enough to provide measurable scattering by the magnetic structures [268–271].

Neutrons used in scattering experiments are generated mainly in two ways: nuclear fission and spallation. While the basic idea of the production of neutrons is to boil off neutrons from nuclei, the mechanisms are clearly different as their names indicate. Nuclear reactors provide a continuous flux of cold, thermal, and ephithermal neutrons with a brightness of $\sim 10^{15}$ $\mathrm{s^{-1}m^{-2}ster^{-1}}$ for thermal neutrons whereas spallation sources produce pulsed neutrons of a wide range of energies up to on the order of GeV with $\sim 10^{17}$ $\mathrm{s^{-1}m^{-2}ster^{-1}}$ in the pulse for thermal neutrons. It is difficult to say which neutron sources are better for various scattering experiments because different types of instrumentation with a given neutron source can provide different capabilities. For example, the time structure in the neutron pulse provided by spallation neutron sources is sometimes beneficial to diffraction experiments, i.e. different energies of neutrons in the pulse, together with a large area detector provide other types of experiments such as a one-shot experiment (all wavelengths can be used simultaneously). In

contrast, although monochromatic continuous neutrons from nuclear reactors will take longer time to gather the similar data to the data from a one-shot measurement, it provides better detailed information at a particular Q position. There are excellent books on neutron sources, scattering techniques, and principles of neutron scattering [268–273] so further readings should refer to those books. Here, I will focus on neutron diffraction (elastic scattering).

3.2.1 Aspects of Neutron Diffraction Experiment

Typical neutron diffraction instruments at nuclear reactors are shown in Figure 3.8: (a) is the double-axis diffractometer and (b) is the triple-axis spectrometer. Neutron diffraction experiments use the double-axis diffractometer but a triple-axis spectrometer can also be used. Neutrons from nuclear reactors come into a monochromator through a collimator with a width of α_0. The monochromator uses Bragg's law and selects an energy (wavelength) of interest then neutrons go through a collimator with a divergence angle of α_1 to the sample.

Double-axis Diffractometer

When the incident flux of neutrons coming to the monochromator is Φ_{I}, the width α_0 of the collimator before the monochromator, α_1 of the collimator after the monochromator before the sample, and the mosaicity of the monochromator η_{M} play important roles in the determination of the flux, the instrumental energy resolution, and the instrumental spatial Q resolution of the neutron beam going to a sample.

The flux of the neutron beam to the sample, Φ_{S}, is [269]

$$\Phi_{\mathrm{S}} = \frac{\Phi_{\mathrm{I}}}{4\pi} \cot\theta_{\mathrm{M}} \frac{\alpha_0 \alpha_1 \eta_{\mathrm{M}}}{\left(\alpha_0^2 + \alpha_1^2 + 4\eta_{\mathrm{M}}^2\right)^{\frac{1}{2}}} P_{\mathrm{M}} \tag{3.4}$$

where θ_{M} is a scattering angle of the monochromator and P_{M} is a reflectivity of the monochromator. The energy resolution, δE, is [269]

$$\frac{\delta E}{E} = 2\cot\theta_{\mathrm{M}} \left(\frac{\alpha_0^2\eta_{\mathrm{M}}^2 + \alpha_1^2\eta_{\mathrm{M}}^2 + \alpha_0^2\alpha_1^2}{\alpha_0^2 + \alpha_1^2 + 4\eta_{\mathrm{M}}^2} \right)^{\frac{1}{2}}. \tag{3.5}$$

The Q resolution, δQ, is [273]

$$\frac{\delta Q}{Q} = \sqrt{\frac{a_{22} - 2a_{12}\cot\theta_{\mathrm{S}} + a_{11}\cot^2\theta_{\mathrm{S}}}{2(a_{11}a_{22} - a_{12}^2)}} \tag{3.6}$$

where

$$a_{11} = \tan^2\theta_{\rm M}\left(\frac{4}{\alpha_0^2}+\frac{1}{\eta_{\rm M}^2}\right)$$
$$a_{12} = |\tan\theta_{\rm M}|\left(\frac{2}{\alpha_0^2}+\frac{1}{\eta_{\rm M}^2}\right)$$
$$a_{22} = \frac{1}{\alpha_0^2}+\frac{1}{\alpha_1^2}+\frac{1}{\eta_{\rm M}^2}.$$

For example, with $\alpha_0 = \alpha_1 = 40' \approx 0.0116$ radians, $\theta_{\rm M} = 45^\circ = 0.785$ radians, and $\eta_{\rm M} \approx 68' \approx 0.0198$ radians, $\delta E = 0.644$ meV for $E = 14.7$ meV from Equation 3.5. When the collimators are changed to the half of the previous ones $\alpha_0 = \alpha_1 = 20' \approx 0.00582$ radians, the change of flux at the sample, $\frac{\Phi_{\rm S}^{\alpha_0=\alpha_1=20'}}{\Phi_{\rm S}^{\alpha_0=\alpha_1=40'}} \approx 0.265$ using Equation 3.4 whereas the change of the spatial resolution $\frac{\delta Q^{\alpha_0=\alpha_1=20'}}{\delta Q^{\alpha_0=\alpha_1=40'}} \approx 0.507$ by Equation 3.6. An improvement of the Q resolution by a factor of two with tightening collimators by half results in a reduction of the neutron flux by a factor of 4.

Then, neutrons with $\Phi_{\rm S}$ are diffracted by a sample (S) with $\theta_{\rm S}$, going through a collimator α_2, and are counted in a detector (DET). The flux, energy resolution and spatial resolution of neutrons reaching to a detector are also influenced by collimators α_1 and α_2, the sample scattering angle $\theta_{\rm S}$ and the mosaicity of the sample $\eta_{\rm S}$. This can be easily realized from Equations 3.4 - 3.6 by substituting corresponding parameters.

Triple-axis Spectrometer

In the triple-axis spectrometer, the diffracted neutrons from the sample go through one more component, an analyzer which selects an energy (wavelength) of the scattered neutron. The ability in a triple-axis spectrometer to analyze an energy of the scattered neutron is used for inelastic neutron scattering experiments. Nevertheless, it complicates the determination of the flux, energy resolution, and spatial resolution. For instance, the energy resolution (Eqn. 3.5) for the triple-axis spectrometer becomes

$$\delta E = \sqrt{E_i^2\left(\frac{\delta E_i}{E_i}\right)^2 + E_f^2\left(\frac{\delta E_f}{E_f}\right)^2} \tag{3.7}$$

where

$$\frac{\delta E_f}{E_f} = 2\cot\theta_{\rm A}\left(\frac{\alpha_2^2\eta_{\rm A}^2+\alpha_3^2\eta_{\rm A}^2+\alpha_2^2\alpha_3^2}{\alpha_2^2+\alpha_3^2+4\eta_{\rm A}^2}\right)^{\frac{1}{2}}. \tag{3.8}$$

and $\frac{\delta E_i}{E_i}$ is Equation 3.5 [273]. Therefore, when $\alpha_0 = \alpha_1 = \alpha_2 = \alpha_3 = 0.01164$ radians, $\eta_{\mathrm{M}} = \eta_{\mathrm{A}}$ = 0.01978 radians, and $\theta_{\mathrm{M}} = \theta_{\mathrm{A}} = 0.7854$ radians, then $\delta E \approx 0.9113$ meV for $E_i = E_f =$ 14.7 meV.

For diffraction experiments both double-axis diffractometers and triple-axis spectrometers can be used. Whereas double-axis diffractometers can provide accurate integrated intensities in both rocking (θ) and $\theta - 2\theta$ scans, integrated intensities measured by the triple-axis spectrometers were found to be accurate only in $\theta - 2\theta$ measurements since the energy resolution of diffracted neutrons is limited which often causes underestimation of intensities of Bragg peaks in triple-axis spectrometer measurements.[273] On the other hand, the limited (selected E_i and E_f) energy resolution provided by triple-axis spectrometers results in a better signal-to-noise ratio which is usually smaller in double-axis diffractometer measurements.[273] However, care must be taken in using triple-axis spectrometers for diffraction experiments since (1) when the sample size or beam size is comparable to or smaller than the size of collimators, collimator blades can screen some of neutrons, cause distorted neutron intensity distribution, and result in non-uniform, non-Gaussian peak shapes, (2) when the sample mosaic is roughly larger than 60', the Lorentz factor, $\frac{1}{\sin 2\theta_{\mathrm{S}}}$, can become no longer valid, and (3) when two collimators were mistakenly placed in a row (for example, two parallel collimators α_2 and α_3 without an analyzer), slight misalignment between those collimators can cause larger uncertainty in measured intensity.[273]

3.2.1.1 Neutron Magnetic Diffraction

In contrast to XRMS, neutron diffraction is able to measure a magnetic moment size of a material when the integrated intensity is measured accurately. The intensity in neutron diffraction experiments is measured by the differential cross section

$$\frac{d\sigma}{d\Omega} = \frac{C}{\Phi d\Omega}$$

where C is the neutron count rate, Φ is the incident neutron flux, and $d\Omega$ is a small solid angle.

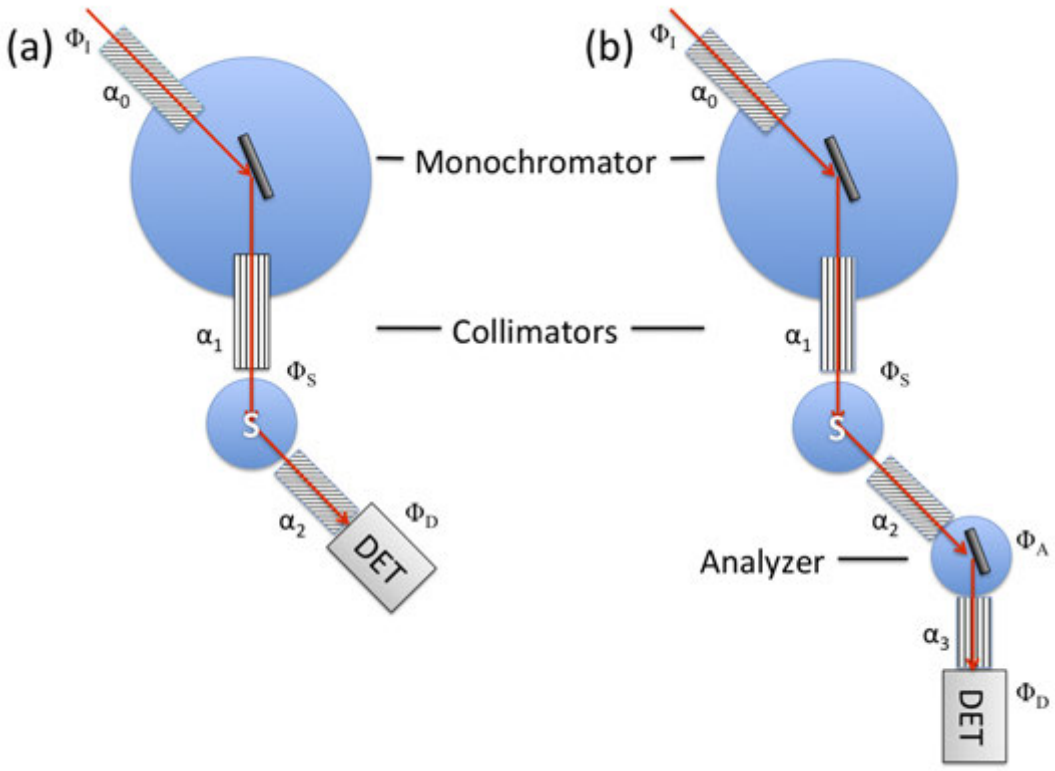

Figure 3.8 (a) Schematic diagram of the double-axis diffractometer and (b) of the triple-axis spectrometer. Red arrow indicates the neutron path. "S" notes the sample position. α_i denote collimation widths. Φ shows the flux at noted positions. Black bars are a monochromator or an analyzer. After Ref. [273].

The differential cross section from a magnetically ordered material is

$$\frac{d\sigma}{d\Omega} = \frac{1}{N_M}\frac{(2\pi)^3}{v_0}\sum_{\vec{\tau}_{\vec{M}}}\delta(\vec{Q}-\vec{\tau}_{\vec{M}})\left|\vec{F}_{\vec{M}_\perp}(\vec{\tau}_{\vec{M}})\right|^2 \tag{3.9a}$$

$$\vec{F}_{\vec{M}_\perp} = \widehat{Q}\times\vec{F}_{\vec{M}}\times\widehat{Q} \tag{3.9b}$$

$$\vec{F}_{\vec{M}}(\vec{Q}) = \gamma r_0\sum_{\vec{d}} f_d(\vec{Q})\left\langle\vec{\mu}_{\vec{d}}\right\rangle e^{i\vec{Q}\cdot\vec{d}}e^{-W(\vec{Q})} \tag{3.9c}$$

where $\vec{F}_{\vec{M}_\perp}$ is the magnetic structure factor, $\vec{F}_{\vec{M}}(\vec{Q})$ is often called the magnetic unit-cell structure factor, $\vec{\tau}_{\vec{M}}$ is the reciprocal lattice vector of the magnetic structure, γ is the gyromagnetic constant, r_0 is the electron radius ($0.28179\times10^{-12}\ cm$), $f(\vec{Q})$ is the magnetic form factor, $\vec{\mu}$ is the magnetic moment, $\vec{d}$ is the atomic position, and $e^{-W(\vec{Q})}$ is the Debye-Waller factor [269, 271, 273]. "$\langle\ \rangle$" means averaging over domains.

The Equations (3.9b) and (3.9c) show that the component of the magnetic moment which is perpendicular to the scattering vector $\vec{\mathrm{Q}}$ contributes to the diffracted neutron intensity. The Equations (3.9a) and (3.9c) indicate that $\frac{d\sigma}{d\Omega} \propto \left|\vec{\mathrm{F}}_{\vec{\mathrm{M}}_\perp}(\vec{\tau}_{\vec{\mathrm{M}}})\right|^2 \propto \left\langle|\vec{\mu}|^2\right\rangle$, in words, the intensity is proportional to the square of the magnetic moment size. Therefore, the differential cross section, $\frac{d\sigma}{d\Omega}$, contains information of both magnetic moment direction and the size of the moment in a magnetically ordered material: $\left\langle|\vec{\mu}|^2\right\rangle = \mu^2\left(1 - \left\langle\cos^2\eta\right\rangle\right)$ where η is the angle between $\vec{\mu}$ and $\vec{\mathrm{Q}}$. The expression $\left\langle\cos^2\eta\right\rangle$ are known for different kind of unitcells in the literature [273]. For instance, in an orthorhombic magnetic unitcell, $\left\langle\cos^2\eta\right\rangle = \left(h^2a^{*2}\cos^2\phi_a + k^2b^{*2}\cos^2\phi_b + l^2c^{*2}\cos^2\phi_c\right)\frac{d^2}{4\pi^2}$ where $\vec{\mathrm{Q}} = h\vec{a^*} + k\vec{b^*} + l\vec{c^*}$ and $\phi_{a,b,c}$ are angles between $\vec{\mu}$ and each crystallographic axis. For the stripe antiferromagnetic structure found for the FeAs-based superconductors with $\vec{\mathrm{Q}}$ = (1, 0, 1) and the moment direction along (1, 0, 0) in the orthorhombic magnetic unit cell (a = 5.564 Å, b = 5.542 Å, and c = 12.96 Å), $\left\langle\cos^2\eta\right\rangle = 0.8444$ and $\left\langle|\vec{\mu}|^2\right\rangle = 0.1556\mu^2$. Therefore, measuring the integrated intensity of magnetic Bragg peaks provides information of the magnetic structure and the moment size. Another example of using the relation $\frac{d\sigma}{d\Omega} \propto \left\langle|\vec{\mu}|^2\right\rangle = \mu^2\left(1 - \left\langle\cos^2\eta\right\rangle\right)$ is that when one knows the magnetic moment size in a particular material (say, the parent compound), one can estimate the moment size of the daughter compound which a magnetic element of the material is substituted with another nonmagnetic element. A comparison of integrated intensities of the same magnetic Bragg peaks of both compounds is essentially the same as a comparison of the magnetic moments square: $\frac{\mathrm{I}_{parent}}{\mathrm{I}_{daughter}} \approx \frac{\mu^2_{parent}}{\mu^2_{daughter}}$.

CHAPTER 4. Structural and Magnetic properties of Transition metal (TM = Co, Rh, Ru, and Mn) substituted $BaFe_2As_2$ compounds

In the previous chapters, 2 and 3, I described the progress in the study of the structural and magnetic properties of the FeAs-based superconductors and the experimental considerations for x-ray and neutron scattering measurements. Particularly, in chapter 2, I described: (1) the ambiguity in the nature of phase transitions in the parent $BaFe_2As_2$ compound, (2) the substitution effects on T_S, T_N, and ordered moment size M in Ru substituted $BaFe_2As_2$ compounds, and (3) the substitution effects on T_S, T_N, and ordered moment size M in Mn substituted $BaFe_2As_2$ compounds.

In this chapter, I will first discuss measurements of the various phase transitions in the parent $BaFe_2As_2$ compounds (Section 4.1) and how the nature of phase transitions changes with transition metal substitution. I will discuss my findings on the change of the nature of phase transitions with a small amount of substitution (electron-doping) in Section 4.2. Then, in Section 4.3, my observation of the effect of Ru substitution (isoelectronic-doping) in $BaFe_2As_2$ will be presented in comparison to the materials discussed in Section 4.2. Lastly, I will present the results of my study on Mn substituted (hole-doped) $BaFe_2As_2$ in Section 4.4, and the discussion and summary follow in Section 4.5.

4.1 Nature of Phase Transitions in the parent $BaFe_2As_2$ compound

4.1.1 Experimental Details

Temperature-dependent, high-resolution, single-crystal x-ray diffraction measurements were performed on a four-circle diffractometer using Cu K_{α_1} radiation from a rotating anode x-ray source, selected by a germanium (1, 1, 1) monochromator. For these measurements, the plate-

like single crystals (see Refs. [274] for growth and characterization) with typical dimensions of $3 \times 3 \times 0.5\,\mathrm{mm}^3$ were attached to a flat copper sample holder on the cold finger of a closed-cycle displex refrigerator with the tetragonal (H, H, L) plane coincident with the horizontal scattering plane [(0, 0, 1) - (1, 1, 0) scattering geometry]. The mosaicity of the $BaFe_2As_2$ single crystals was less than 0.02° full-width-at-half-maximum (FWHM) as measured by the rocking curves of the $(1, 1, 10)_T$ reflection at room temperature. The diffraction data were obtained as a function of temperature between room temperature and 8 K, the base temperature of the refrigerator.

The x-ray resonant magnetic scattering measurements were performed on the 6ID-B undulator beamline with top-up operation mode at the Advanced Photon Source (APS), Argonne. The 6ID-B beamline uses a double-crystal Si (1, 1, 1) monochromator and the incident beam was 99.9% linearly polarized parallel to the storage ring plane with the resolution $(\Delta E/E) \sim 1 \times 10^{-4}$ (approximately 0.8 eV energy resolution at the Fe K-absorption edge). The spatial cross section of the incident beam was 1.0 mm (horizontal) × 0.2 mm (vertical). Temperature-dependent single-crystal x-ray diffraction measurements were performed using the same experimental configuration. Three beryllium domes were used to ensure a well-defined temperature of the sample down to 4 K, the base temperature of the refrigerator. The inner Be dome is to maintain the sample temperature using an exchange gas (He). The middle Be dome serves as a radiation heat shield and the outer Be dome maintains vacuum inside of the displex unit. The temperature was measured at a sensor mounted to the copper block holding the sample, and was stable within ± 0.002 K. Care was taken to minimize heating effects associated with the incident x-ray beam by measuring charge and magnetic reflections in close proximity and using the appropriate incident beam attenuation. The attenuations were 10 or less (approximately 0.31 % or higher percentage of the synchrotron x-ray transmits to the sample) for the x-ray resonant magnetic scattering measurement at the Fe K-edge and 10 or more (approximately 0.31 % or lower percentage transmission) for the measurement of the structural transition. The difference in the attenuation for XRMS and charge peak scattering is necessary since the charge scattering is much stronger than XRMS and over-exposure of the detector occurs when the attenuation for XRMS was used for the charge scattering. However, using different attenuations

can cause a change in the measured sample temperature due to the additional heating by the x-rays. Therefore, for simultaneous measurements of XRMS and charge scattering, I used the same attenuation between 0 (full transmission) and 4 (9.6 % transmission) for both measurements but rotated the detector by some angle (2∼10°) when I measured the charge peak. In this way, particles consisting the air scatter intense diffracted x-ray so that the intensity of the scattered beam from the sample decreases. Using the air-scattering over-illumination of the detector was prevented.

For XRMS, we used the $\sigma - \pi$ polarization analysis. In the $\sigma - \pi$ channel, the incoming beam is linearly polarized perpendicular to the scattering plane and the component of the outgoing beam with a polarization parallel to the scattering plane is measured. Polarization analysis in the $\sigma - \pi$ channel was performed using a Cu crystal. The (2, 2, 0) reflection of the Cu analyzer crystal ($2d = 2.553$ $\AA$) yields a diffraction angle of $2\theta = 86.1°$ at the Fe K-edge. A suppression of the charge and fluorescence background by a factor of 200 was achieved relative to the magnetic scattering signal due to the analyzer crystal.

4.1.2 Orthorhombic twin domains and the AFM Bragg peak

The $BaFe_2As_2$ compounds undergo a high-temperature tetragonal to a low-temperature orthorhombic structural transition. The orthorhombic structure is related to the tetragonal structure in the following way. The basal $\vec{a}$ - $\vec{b}$ plane of the orthorhombic structure is rotated by 45° with respect to the $\vec{a}$ - $\vec{b}$ plane of the tetragonal structure so the lattice parameter a_O ($a_O > b_O$) of the orthorhombic structure is approximately $\sqrt{2}\times a_T$ ($a_T = b_T$) of the tetragonal structure. The Miller indices (H, K, L)$_O$ in orthorhombic notation are given by (h + k, h - k, l)$_O$ with (h, k, l)$_T$ in tetragonal notation [e.g. (2, 0, 8)$_O$ = (1, 1, 8)$_T$]. I will use both notations here since, in some cases, one notation is more straight-forward than another. For example, the orthorhombic notation is more straight forward when the AFM order is discussed because the AFM order occurs in the orthorhombic structure. In the orthorhombic phase, twin domains are formed due to the orientation degeneracy of the orthorhombic distortion (see Fig. 2 in Ref. [275]). For some peaks, this yields four Bragg peaks in close proximity as illustrated in Fig. 4.1 (a) where the two left peaks with $H \sim 2.00$ are related to (2, 0, 8)$_O$ reflections

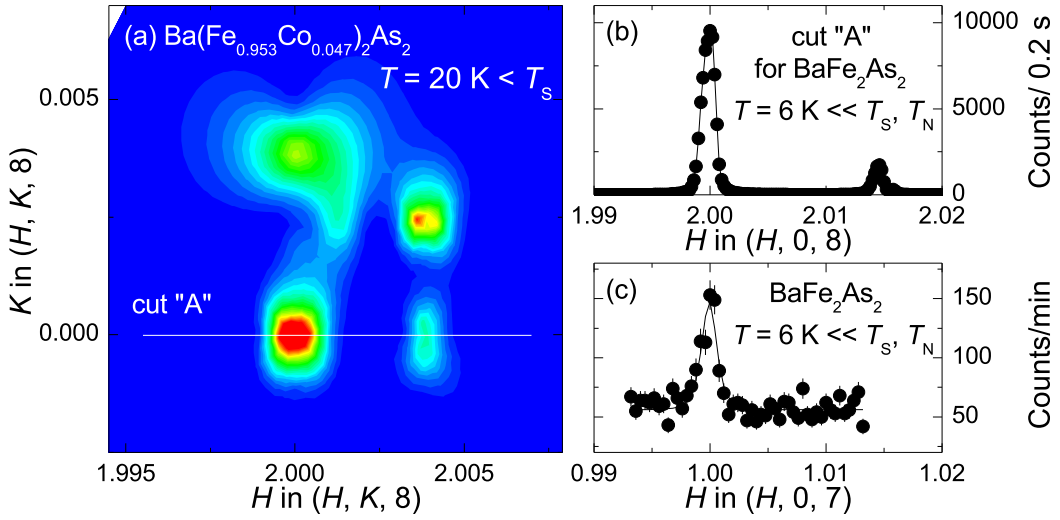

Figure 4.1 (a) Representative map of charge Bragg peaks related to four orthorhombic twin domains in $Ba(Fe_{1-x}Co_x)_2As_2$ with $x = 0.047$ below T_S. (b) $\vec{Q}$ scan through cut "A" marked in (a) for the undoped $BaFe_2As_2$ at $T = 6$ K. (c) Scattering measured in the σ- π channel at the magnetic Bragg position. Note that the figures are presented in the orthorhombic notation.

and the larger lattice parameter a_O, whereas the two right peaks are related to $(0, 2, 8)'_O$ reflections which arise from other domains and are related to the smaller lattice parameter ($b_O < a_O$).[174, 177, 179] In cuts through the charge peak positions both types of Bragg peaks occur as shown in Fig. 4.1 (b). However, in the corresponding cuts through magnetic peak positions only peaks on the left side related to the enlarged lattice parameter a_O are seen as demonstrated by the $(1, 0, 7)_O$ Bragg peak in Figs. 4.1 (c). This is consistent with previous neutron measurements of the magnetic propagation vector $\vec{Q}_{AFM} = (1, 0, 1)_O$ in $BaFe_2As_2$.[167] The moment direction along the $\vec{a}_O$ direction is supported by the observation of large dipole resonant magnetic scattering for the $(1, 0, 7)_O$ Bragg peak in the $\sigma - \pi$ XRMS channel.[238] Therefore, the observation of scattering at $(1, 0, 7)_O$ and the absence of scattering at $(0, 1, 7)_O$ is consistent not only with the propagation vector but also with the moment direction along $\vec{a}_O$ in the magnetic structure of $BaFe_2As_2$.

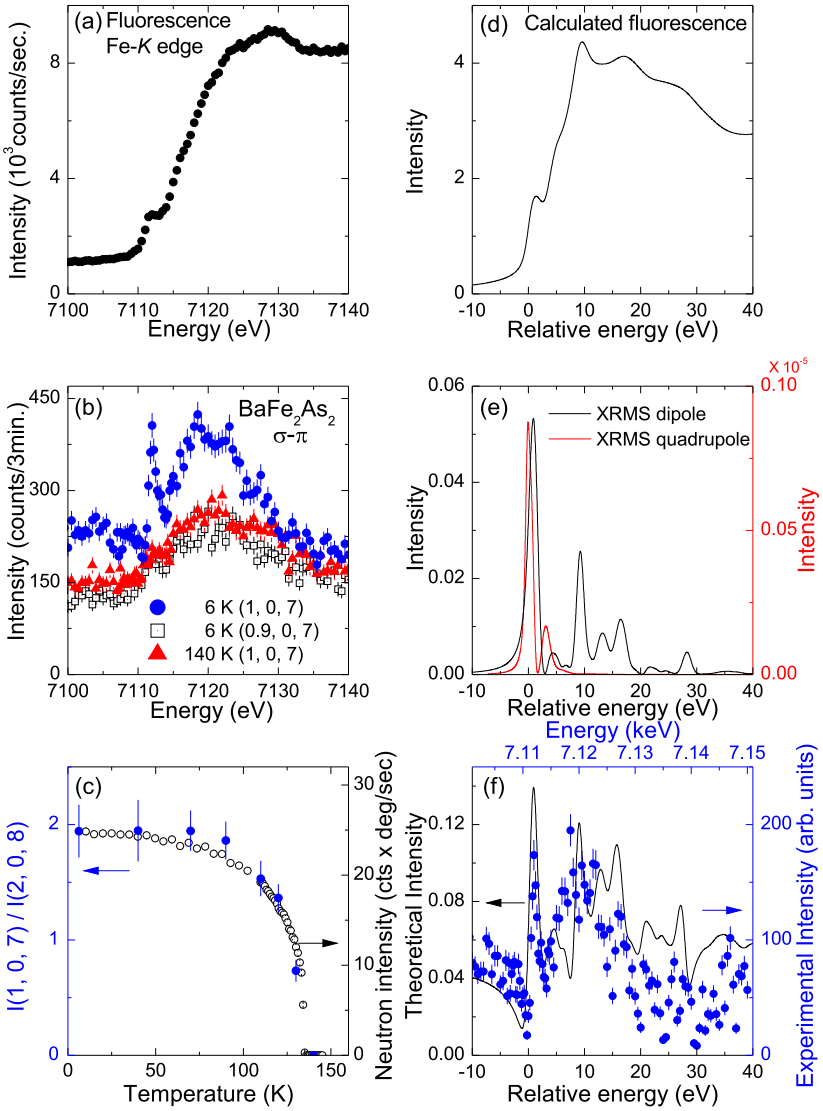

Figure 4.2 (a) Measured fluorescence spectrum. (b) Energy scan through the $(1, 0, 7)_O$ magnetic peak above (filled triangles) and below (filled circles) T_N, and at low temperature away from $(1, 0, 7)_O$ (open squares). (c) Antiferromagnetic order parameter as a function of temperature measured by XRMS at the Bragg position $(1, 0, 7)_O$ (filled circles) and measured with neutrons at the Bragg position $(1, 0, 3)_O$ (open circles). (d) Calculated fluorescence spectrum. (e) Calculated XRMS due to the dipole (black line) and the quadrupole (red line) transitions. Note that the intensity from quadrupole transition is about 5 orders of magnitude smaller than dipole transition. (f) Theoretical XRMS spectrum (line) which is a sum of spectra from dipole and quadrupole transitions and corrected for interference. The experimental XRMS spectrum is corrected for absorption and the background is subtracted (close circles).

4.1.3 XRMS spectra

To ensure that the observed Bragg peak at the $\vec{Q}_{\rm AFM} = (1, 0, 7)_{\rm O}$ is magnetic in nature, we measured the energy spectrum associated with the resonant scattering from $BaFe_2As_2$ and the intensity at this $\vec{Q}$ position as a function of temperature. In Fig. 4.2 (b) we show the raw data from energy scans at constant $\vec{Q}_{\rm AFM} = (1, 0, 7)_{\rm O}$ at $T = 6$ K, well below $T_{\rm N}$. To determine the background at this scattering vector, energy scans were also performed at $(1, 0, 7)_{\rm O}$ for $T = 140$ K, just above $T_{\rm N}$, and at $\vec{Q} = (0.9, 0, 7)_{\rm O}$, away from the magnetic peak, at $T = 6$ K. The shape of the background in the vicinity of the Fe K-edge is consistent with an increase in the fluorescence from the sample [Fig. 4.2 (a)]. We subtracted the background from the energy scan measured at $T = 6$ K, corrected the energy scan for the absorption, and display it with closed circles in Fig. 4.2 (f). There are three distinctive features in the energy spectrum. First, an energy-independent contribution is most clearly visible below the absorption edge which arises from nonresonant magnetic scattering. Second, there is a noticeable dip in the scattering intensity just below the absorption edge, due to interference between the nonresonant and resonant magnetic scattering as the phase of the resonant scattering changes across the absorption edge. Third, we observed a sharp feature close to the absorption threshold and broad scattering that extends to energies more than 20 eV above the absorption edge. This broad energy spectrum is similar to what was observed in previous XRMS measurements in the σ - π scattering channel at the Ni K-edge for NiO[252, 276] and can be attributed to the dipole channel from the $1s$ initial state to the unoccupied $4p$ states that are weakly polarized through hybridization with $3d$ states near the Fermi energy. The sharp feature close to the absorption threshold may also contain a contribution from quadrupole allowed channel from the $1s$ to $3d$ states, and our calculations suggest that the dipole contribution is the dominant one. However, an unambiguous separation of the dipole and quadrupole contributions will require further measurements of the angular dependence of the scattering as well as the σ - σ scattering channel.

Figure 4.2 (c) shows the magnetic order parameter as a function of temperature, measured at $(1, 0, 7)_{\rm O}$. It shows that as the sample temperature increases, the intensity of the magnetic peak

decreases until it can no longer be observed above background at $T_N \approx 140$ K, in agreement with previous neutron-scattering measurements[174] and our neutron measurement [Fig. 4.2 (c)]. Together with the energy spectrum through the Fe K-absorption edge and the temperature dependent AFM order parameter, we conclude that the Bragg peak at $(1, 0, 7)_O$ is magnetic in nature.

To model the resonant scattering spectra, Lee and Harmon used a full-potential linear-augmented plane-wave (FLAPW) method [277] with a local density functional.[278] To obtain a self-consistent charge and potential, they chose 810 $\vec{k}$ points in the irreducible Brillouin zone (IBZ), and set $R_{MT} \times k_{max} = 8.0$, where R_{MT} is the smallest muffin-tin radius and k_{max} is the basis set cutoff (the maximum value of $|\vec{k} + \vec{K}_i|$ included in the basis). The muffin-tin radii are 2.4 a.u., 2.2 a.u., and 2.2 a.u. for Ba, Fe, and As, respectively. The self-consistent calculation was iterated until the total energy convergence reached 0.01 mRy/cell. For the x-ray absorption spectra [Fig. 4.2 (d)] and XRMS [Figs. 4.2 (e) and (f)] they calculated empty states up to 40 eV above the Fermi energy with 1320 $\vec{k}$ points in the IBZ and with the calculated self-consistent potential. To model the interference between the resonant and nonresonant scattering close to the absorption edge, an energy-independent scattering amplitude, which is equal to the resonant scattering contribution, was added to the real part of the resonant scattering, based upon previous XRMS K-edge measurements which note a resonant enhancement of the magnetic scattering equal to the nonresonant magnetic scattering.[252, 276] The calculated energy spectrum was broadened with a 1.25 eV Lorentzian[279] to account for the core-hole lifetime, and a 1 eV Gaussian for the instrumental resolution. The calculated absorption and resonant scattering spectra are displayed in Figs. 4.2 (d) - (f). Seen in Fig. 4.2 (e), the quadrupole contribution to the sharp feature close to the absorption threshold is much smaller than the dipole contribution. The total XRMS in Fig. 4.2 (f) captures the essential features of the measurements including the three features discussed above.

4.1.4 Nature of Phase transitions

In Fig. 4.3(a), I display $[\xi, \xi, 0]_T$ scans through the $(1, 1, 10)_T$ charge peak, obtained using the laboratory source, for the parent $BaFe_2As_2$ compound measured with temperature steps

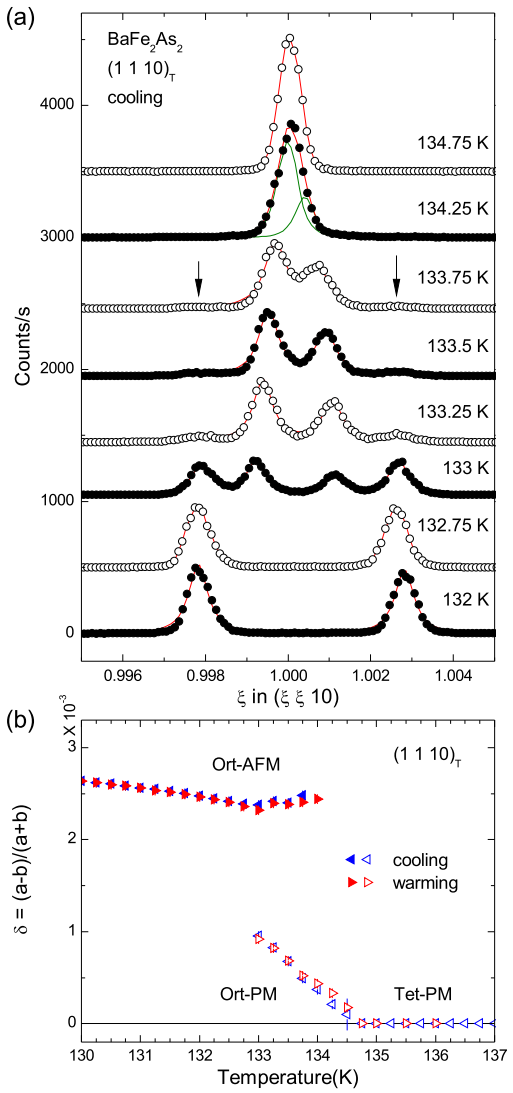

Figure 4.3 (a) X-ray diffraction scans, measured using the laboratory source, along the [ξ, ξ, 0] direction through the position of the tetragonal (1, 1, 10)$_{\mathrm{T}}$ reflection for selected temperatures in the parent $BaFe_2As_2$ upon cooling. The lines present the fitted curves using a Lorentzian-squared line shape. The two-component fit to broadened peaks is illustrated for T = 134.25 K. The arrows denote the positions of peaks associated with Ort-AFM as discussed in the text. At this temperature, the integrated intensity of the Ort-AFM peaks are approximately 5% of the Ort-PM diffraction peaks. (b) The orthorhombic distortion as a function of temperature upon cooling and warming determined from fits to the (1, 1, 10)$_{\mathrm{T}}$ Bragg diffraction peak.

of 0.25 K. Above the structural transition temperature, T_S = 134.5 K, a single sharp peak is observed, consistent with the tetragonal structure. Upon cooling below T_S, the $(1, 1, 10)_T$ charge peak continuously broadens and, then, clearly splits at T = 133.75 K, concomitant with the abrupt appearance of two additional peaks at this temperature [vertical arrows in Fig. 4.3(a)] bracketing the two inner peaks. Upon further cooling, the splitting of the two inner peaks evolves continuously as their intensities decrease, whereas the positions of the outer peaks change only slowly as their intensities increase. Below T = 133.0 K, the two inner peaks disappeared leaving only the outer peaks in evidence. Please note that these observations are qualitatively consistent with similar diffraction measurements on an annealed sample of $BaFe_2As_2$ recently reported by Rotundu *et al.*[280] although the transition temperatures for their annealed sample were approximately 5 K higher.

Having described the temperature evolution of the diffraction peaks qualitatively, it is useful to introduce some labeling of the corresponding phases. The tetragonal paramagnetic phase is denoted as Tet-PM. Anticipating the results of our XRMS study, I label the orthorhombic phase that evolves continuously over a very narrow temperature range below T_S [corresponding to the inner pair of peaks in Fig. 4.3(a)] as Ort-PM. I further label the orthorhombic phase that abruptly appears at T = 133.75 K [corresponding to the two outer bracketing peaks in Fig. 4.3(a)] as Ort-AFM. Structurally, I assume that Ort-PM and Ort-AFM differ only with respect to the values of their lattice constants and orthorhombic distortion at a given temperature.

Figure 4.3(b) describes the temperature evolution of these phases. Upon cooling, a second-order transition from Tet-PM to Ort-PM occurs at T_S = 134.5 K followed by a first-order transition to Ort-AFM at T_N = 133.75 K. There is a region of coexistence between Ort-AFM and Ort-PM from 133.75 K to 133.0 K, and only the Ort-AFM phase is observed below this temperature. Upon warming, Ort-PM appears at 133.0 K and coexists with Ort-AFM up to T'_N = 134.0 K, where Ort-AFM disappears. The orthorhombic distortion associated with Ort-PM decreases continuously up to T_S = 134.5 K, where Tet-PM is recovered. I find no hysteresis in the transformations from Tet-PM to Ort-PM and $\leq$ 0.25 K hysteresis associated with the appearance/disappearance of Ort-AFM.

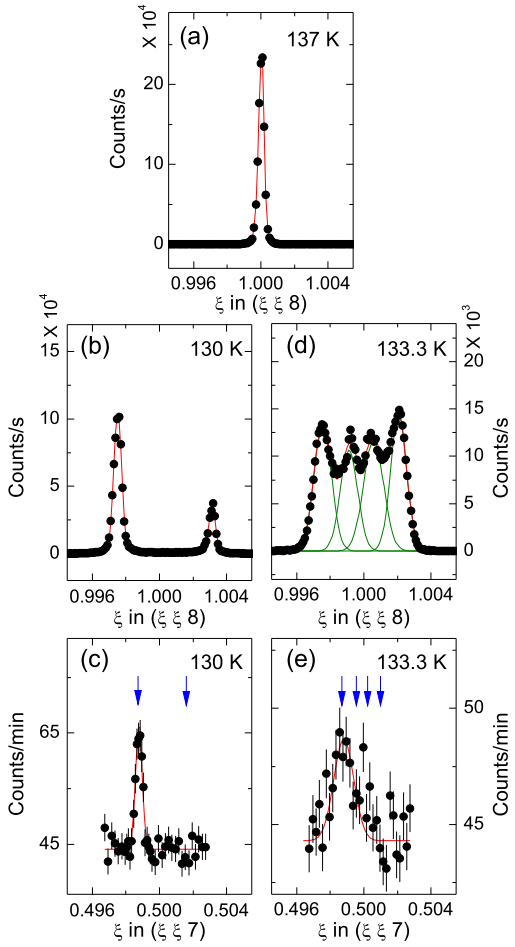

Figure 4.4 (a) The measured $(1, 1, 8)_{\mathrm{T}}$ charge diffraction peak above the structural/magnetic transitions. Panels (b) and (c) show the $(1, 1, 8)_{\mathrm{T}}$ charge peak and $(\frac{1}{2}, \frac{1}{2}, 7)_{\mathrm{T}}$ magnetic peak at $T = 130$ K, well below the transition region. Panels (d) and (e) show the measured intensities at the $(1, 1, 8)_{\mathrm{T}}$ charge peak and $(\frac{1}{2}, \frac{1}{2}, 7)_{\mathrm{T}}$ magnetic positions at $T = 133.3$ K. The arrows in (c) and (e) indicate the calculated magnetic peak positions corresponding to each of the charge peaks in (b) and (d), respectively. The fitted value for the width of the charge and magnetic peaks are the same.

In order to investigate the relationship between the structural transition and AFM ordering in this system I have performed a combined study using high-resolution x-ray diffraction and XRMS measurements. These simultaneous measurements eliminate concerns regarding disparities in the temperature calibration of sensors for different experiments. Using the configuration at the APS described in Section 4.1.1, I measured the scattering at both the charge and magnetic Bragg peak positions for several temperatures close to the structural transition. In Fig. 4.4(a) I show a $[\xi,\ \xi,\ 0]_{\mathrm{T}}$ scan through the $(1,\ 1,\ 8)_{\mathrm{T}}$ charge Bragg peak at $T = 137$ K, well above the structural transition temperature. At $T = 130$ K, below T_{N} and T_{S}, two well-separated peaks were observed [Fig. 4.4(b)]. These are the $(2,\ 0,\ 8)_{\mathrm{O}}$ and $(0,\ 2,\ 8)_{\mathrm{O}}$ charge Bragg peaks of the orthorhombic phase. The difference in intensity arises from different populations of the domains within the illuminated volume of the sample. At this same temperature, a single peak is found at the $(\frac{1}{2}, \frac{1}{2}, 7)_{\mathrm{T}}[\equiv (1,\ 0,\ 7)_{\mathrm{O}}]$, magnetic peak position for the orthorhombic phase, [Fig. 4.4(c)] in agreement with previous measurements of a magnetic propagations vector given by $\vec{Q}_{\mathrm{AFM}} = (\frac{1}{2},\ \frac{1}{2},\ 1)_{\mathrm{T}}$ $[(1,\ 0,\ 1)_{\mathrm{O}}]$ with lattice constants $a_{\mathrm{O}} > b_{\mathrm{O}}$, keeping in mind that the magnetic peaks are displaced from $\xi = \frac{1}{2}$ because of the orthorhombic distortion. [174, 177–179]

The principal result conveyed in Figs. 4.4(b) and (c) is that the expected AFM order exists in the Ort-AFM phase. The question, however, is whether this AFM order is also associated with the Ort-PM intermediate phase. Figures 4.4(d) and (e) show $[\xi,\ \xi,\ 0]_{\mathrm{T}}$ scans through the $(1,\ 1,\ 8)_{\mathrm{T}}$ charge and $(\frac{1}{2},\ \frac{1}{2},\ 7)_{\mathrm{T}}$ magnetic peak positions at $T = 133.3$ K. Similar to what was found in our laboratory-based measurement [Fig. 4.3(a)] we observed four charge peaks [two outer peaks from Ort-AFM and two inner peaks from Ort-PM]. However, Fig. 4.4(e) shows only a single magnetic peak. The arrows in this panel denote the expected positions for magnetic peaks associated with each of the charge peaks in Fig. 4.4(d) and we see that the magnetic peak is found at a position that corresponds to one of the two outer peaks associated with the Ort-AFM phase. This allows us to conclude that the magnetic order is associated only with the Ort-AFM phase. Taken together, the x-ray diffraction and XRMS measurements suggest that: (1) The orthorhombic distortion at T_{S} is best described as a second-order transition; (2) the structural and AFM transitions in the as-grown $BaFe_2As_2$ compound are separated

in temperature by approximately 0.75 K and; and (3) a first-order magnetic transition at T_N drives the discontinuity in the structural order parameter at 133.75 K.

4.2 Evolution of the Nature of Phase transition in Co and Rh substituted $BaFe_2As_2$ compounds

4.2.1 High-resolution x-ray diffraction and resistance measurements of $Ba(Fe_{1-x}Co_x)_2As_2$ and $Ba(Fe_{1-x}Rh_x)_2As_2$

To further substantiate the conclusions from Section 4.1.4, I now turn to a study of the evolution of the structural transition in lightly Co or Rh substituted (electron-doped) $BaFe_2As_2$ compounds.

I have performed high-resolution x-ray diffraction measurements on four different levels of substitutions in $BaFe_2As_2$ samples: $Ba(Fe_{1-x}Co_x)_2As_2$ for $x = 0.018$ and 0.047, and $Ba(Fe_{1-x}Rh_x)_2As_2$ for $x = 0.012$ and 0.040. Figures 4.5 and 4.6 display the raw diffraction data, the orthorhombic distortion (δ) and diffraction peak widths derived from fits to the data, and the electrical resistance measured as a function of temperature. Temperature-dependent ac electrical resistance data ($f = 16$ Hz, $I = 3$ mA) were collected by A. Thaler using a Quantum Design Magnetic Properties Measurement System (MPMS) with a Linear Research LR700 resistance bridge. Electrical contact was made to the sample using Epotek H20E silver epoxy to attach Pt wires in a four-probe configuration.

Turning first to the compounds at lower substitution concentrations, $Ba(Fe_{0.982}Co_{0.018})_2As_2$ and $Ba(Fe_{0.988}Rh_{0.012})_2As_2$ (Fig. 4.5), below T_S both samples manifest a lattice distortion that evolves continuously as temperature is lowered, until the onset of magnetic ordering where a step-like feature in the structural order parameter (δ) is observed. At T_N a distinct broadening of the split orthorhombic diffraction peaks is evident over a narrow range in temperature. In contrast, the temperature dependence of the order parameter and peak widths for the higher substitution concentrations, $Ba(Fe_{0.953}Co_{0.047})_2As_2$ and $Ba(Fe_{0.960}Rh_{0.040})_2As_2$ (Fig. 4.6), is decidedly different near T_N. For these samples, the structural distortion evolves continuously, with only a mild kink in evidence at T_N and without the attendant peak broadening at T_N.

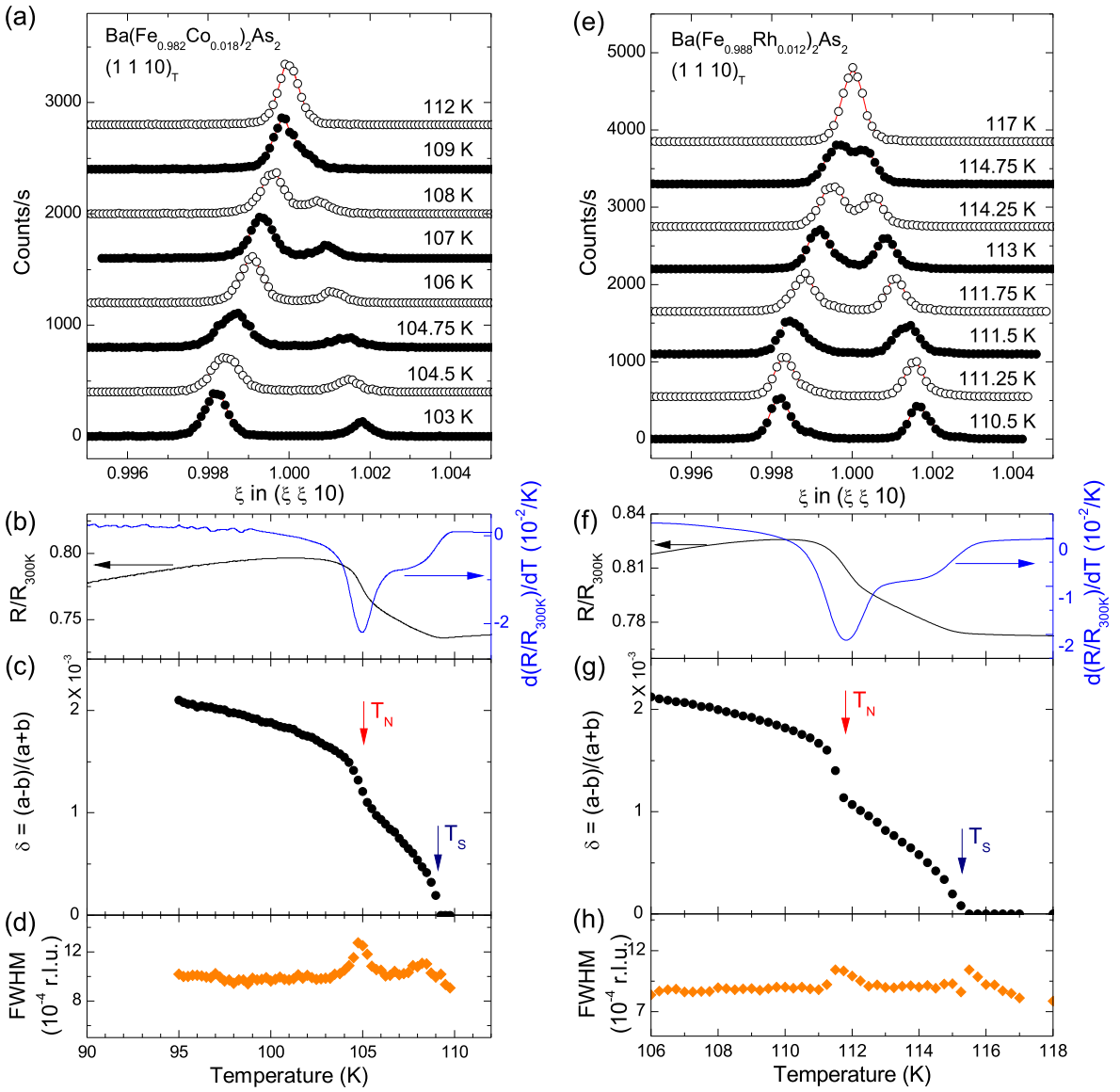

Figure 4.5 (a) X-ray data, (b) resistance (black line) and its temperature derivative (blue line), (c) orthorhombic distortion and (d) FWHM of the split $(1, 1, 10)_{\mathrm{T}}$ Bragg peaks measured for $Ba(Fe_{1-x}Co_x)_2As_2$ with $x = 0.018$. For $Ba(Fe_{1-x}Rh_x)_2As_2$ with $x = 0.012$, (e) x-ray data, (f) resistance (black line) and its temperature derivative (blue line), (g) orthorhombic distortion and (h) FWHM of the split $(1, 1, 10)_{\mathrm{T}}$ Bragg peaks measured. In panel (c) and (g) the structural and magnetic transition temperatures are marked.

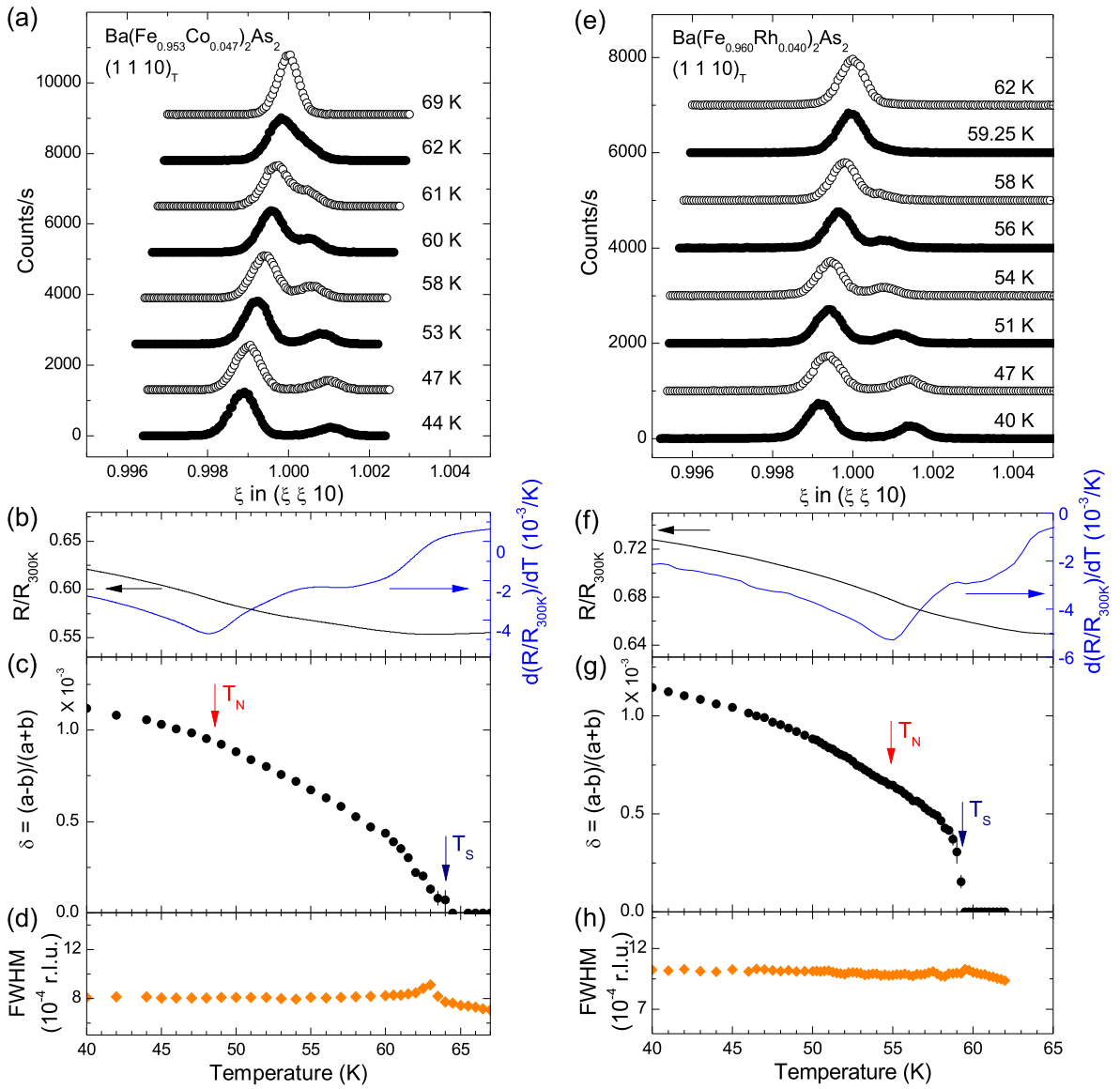

Figure 4.6 (a) X-ray data, (b) resistance (black line) and its temperature derivative (blue line), (c) orthorhombic distortion and (d) FWHM of the split $(1, 1, 10)_{\mathrm{T}}$ Bragg peaks measured for $Ba(Fe_{1-x}Co_x)_2As_2$ with $x = 0.047$. For $Ba(Fe_{1-x}Rh_x)_2As_2$ with $x = 0.040$, (e) x-ray data, (f) resistance (black line) and its temperature derivative (blue line), (g) orthorhombic distortion and (h) FWHM of the split $(1, 1, 10)_{\mathrm{T}}$ Bragg peaks measured. In panel (c) and (g) the structural and magnetic transition temperatures are marked.

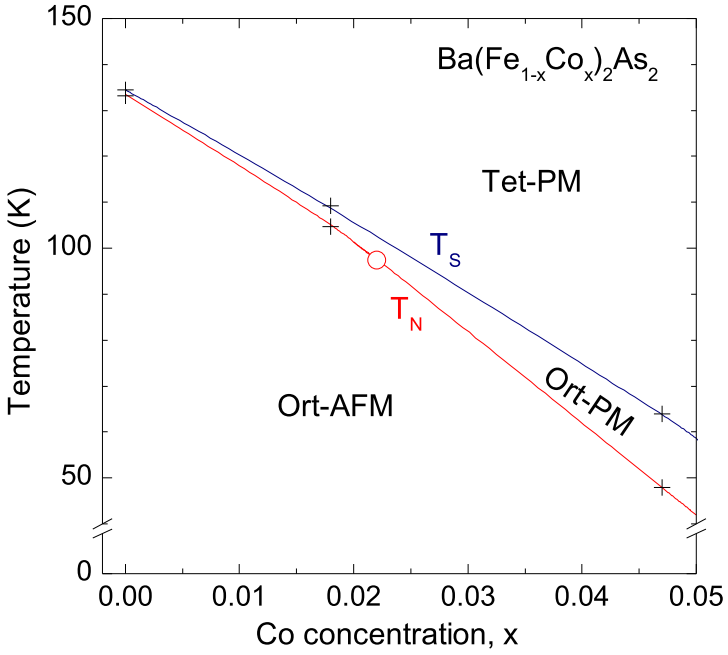

Figure 4.7 Diagram showing the nature of the structural and magnetic phase transitions for $Ba(Fe_{1-x}Co_x)_2As_2$ at T_S and T_N, respectively. The thick line denotes a first-order transition whereas the thinner lines represent second-order transitions. The crosses denote values for T_S and T_N determined from our measurements. The open circle denotes the approximate position of a tricritical point as described in the text.

The differences between the lower and higher substitution concentrations are consistent with a change in the nature of the magnetic transition from first-order for low substitution, to second-order for higher substitution levels. At low-substitution, as for the parent $BaFe_2As_2$ compound, there is a second-order transition from the Tet-PM to the Ort-PM structure as temperature is decreased below T_S. The step in the orthorhombic distortion (δ) at T_N is a consequence of the abrupt appearance of Ort-AFM coincident with a first-order AFM transition. I note that throughout this temperature range only two broadened peaks are observed in contrast to what was shown above for the parent compound. This is expected, however, since the larger separation of T_S and T_N allows δ to evolve to a value for the Ort-PM phase that is close to its magnitude for the Ort-AFM phase. The anomalous increase in the widths of the x-ray diffraction peaks at T_N arises from the coexistence and near coincidence in position of the Ort-AFM and Ort-PM diffraction peaks over a narrow temperature range. For the higher

substitution levels, within our experimental resolution, the absence of a distinct step in δ or peak broadening at $T_{\rm N}$ is consistent with second-order AFM and structural transitions as found previously.[185, 186]

The results are summarized in Fig. 4.7 which displays a phase diagram for $Ba(Fe_{1-x}Co_x)_2As_2$ focusing on the concentration range of the present study. The structural transition, over the entire range is second-order, whereas the magnetic transition changes from first-order to second-order at a tricritical point as discussed below. By definition, a tricritical point is the point where a second-order phase line meets with a first-order phase line (in addition, when two second-phase lines cross, the crossing point is a tetra-critical point and when two second-order phase lines meet with a first-order phase line at a point, it is a bi-critical point).[281]

4.2.2 Discussion

To understand the existence, and estimate the location of a magnetic tricritical point in the phase diagram of $Ba(Fe_{1-x}Co_x)_2As_2$ one can, at first, rationalize the interplay between the magnetic and elastic degrees of freedom in terms of a simple Ginzburg-Landau model as shown in Section 2.4.2. R. Fernandes and J. Schmalian re-wrote the effective free energy in Eq. (2.5) as:

$$F_{\rm eff} = \left(\frac{a_\delta}{2}\delta^2 + \frac{u_\delta}{4}\delta^4\right) + \left(\frac{a_m}{2}m^2 + \frac{u_m}{4}m^4\right) - \lambda\delta\, m^2 \tag{4.1}$$

with $a_\delta = a_{\delta,0}\,(T - T_{\rm S,0})$, $a_m = a_{m,0}\,(T - T_{\rm N,0})$, and positive constants u_δ, u_m, λ. Here, m is the antiferromagnetic order parameter and $T_{\rm S,0}$, $T_{\rm N,0}$ denote the bare structural and magnetic transition temperatures respectively. For $T_{\rm S,0} < T_{\rm N,0}$, this model describes a simultaneous magnetic/structural first-order transition. However, for $T_{\rm S,0} > T_{\rm N,0}$, this model describes a second-order structural transition at $T_{\rm S} = T_{\rm S,0}$, followed by a magnetic transition at $T_{\rm N}$ ($T_{\rm N,0} < T_{\rm N} < T_{\rm S}$), which can be either first-order or second-order. Considering that $T_{\rm N}$ and $T_{\rm S}$ change with substitution (doping), the magnetic tricritical point takes place at the concentration $x_{\rm tri}$ where $u_m a_{\delta,0}\,(T_{\rm S} - T_{\rm N}) = \lambda^2$. Experimentally, we know that $(T_{\rm S} - T_{\rm N})$ increases with substitution, x. Therefore, it is straightforward to conclude from the mean-field solution of Eq. (4.1) that, close to the magnetic tricritical point, the jump in the orthorhombic order parameter across the first-order magnetic transition changes with substitution as $\Delta\delta \equiv$

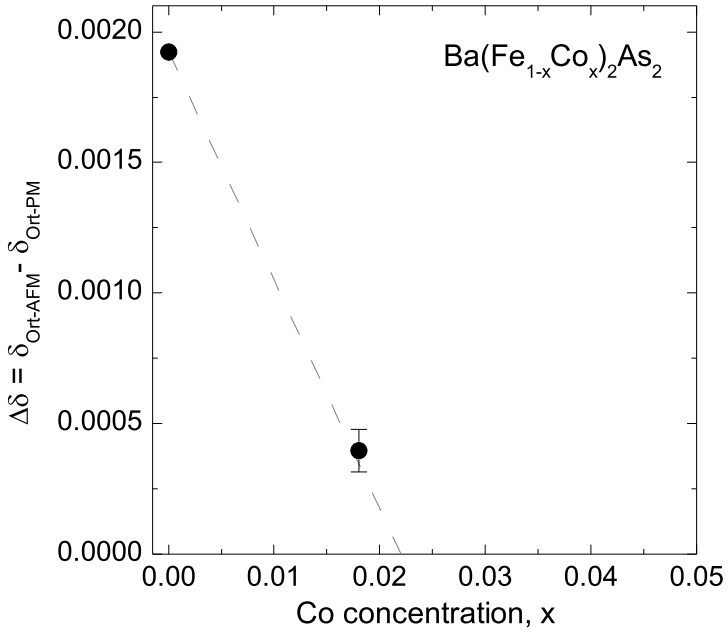

Figure 4.8 Jump of the orthorhombic order parameter $\Delta\delta \equiv \delta_{\mathrm{Ort-AFM}} - \delta_{\mathrm{Ort-PM}}$ across the first-order magnetic transition, as function of x. The linear relationship $\Delta\delta \propto (x - x_{\mathrm{tri}})$ (dashed line) follows from the mean-field solution of Eq. (4.1).

$\delta_{\mathrm{Ort-AFM}} - \delta_{\mathrm{Ort-PM}} \propto (x - x_{\mathrm{tri}})$. Extrapolating this linear relation and using the values of $\Delta\delta$ from Figs. 4.3 and 4.5, we estimate that the magnetic tricritical point is located at $x_{\mathrm{tri}} \approx 0.022$, as shown in Fig. 4.8.

The main issue with the model in Eq. (4.1) is that it requires a fine tuning of the independent structural and magnetic transition temperatures $T_{\mathrm{S},0}$ and $T_{\mathrm{N},0}$ across the phase diagram. In all of the phase diagrams of the FeAs-based compounds, it is observed that the two transition lines track each other very closely, even within the superconducting dome (see phase diagrams in Section 2). This suggests that these two states are strongly coupled, rather than independent, as assumed by the previous model. To address this issue, it has been proposed that the particular magnetic structure of the FeAs-based superconductors gives rise to emergent Ising-nematic degrees of freedom that couples to the lattice, inducing the tetragonal-to-orthorhombic phase transition [230, 282, 283]. In the magnetically ordered phase, there are two degenerate ground states characterized by in-plane spin stripes along each of the two orthogonal Fe-Fe bond directions. These ground states can be described in terms of two interpenetrating AFM sublattices

with staggered magnetization $\vec{m}_1$ and $\vec{m}_2$, such that $\vec{m}_1$ is either parallel or antiparallel to $\vec{m}_2$ (Section 2.4.2 and see Fig. 2.15).

Within this description, the magnetic free energy of the system F_{mag} has contributions from each sublattice F_i and from the coupling between them, F_{12}. The former is given by:

$$F_i = \frac{1}{2}\int \frac{d^3q}{(2\pi)^3}\,\chi_i^{-1}\left(\vec{q}\right)\vec{m}_i\left(\vec{q}\right)\cdot\vec{m}_i\left(-\vec{q}\right) + \frac{u}{4}\int \frac{d^3x}{v}\,\vec{m}_i^{\,4} \tag{4.2}$$

where $\chi_i\left(\vec{q}\right) = \chi_0\left(r_0 + q_{\parallel}^2 a^2 - 2\eta_z\cos q_{\perp}c\right)^{-1}$ is the static susceptibility of each sublattice,[230] u is a positive coupling constant, and the momentum $\vec{q}$ is measured relative to the magnetic ordering vector. Here, χ_0^{-1} is a magnetic energy scale, r_0 measures the distance to the magnetic tricritical point, a and c are the lattice parameters of the unit cell of volume v containing two Fe atoms, and η_z is the inter-plane AFM coupling. The coupling between the two sublattices is given by:

$$F_{12} = -\frac{g}{2}\int \frac{d^3x}{v}\left(\vec{m}_1\cdot\vec{m}_2\right)^2 \tag{4.3}$$

with $g > 0$, favoring configurations where $\vec{m}_1$ and $\vec{m}_2$ are either parallel or antiparallel. In a description of the magnetically ordered phase in terms of localized moments, this term originates from quantum and thermal spin fluctuations [284]. On the other hand, within an itinerant approach, where the magnetic moments arise from the conduction electrons, the same term appears as a consequence of the ellipticity of the electron pockets [285].

As shown in the discussion of interplay between superconductivity and structure in Section 2.4.2, the coupling in Eq. (4.3) between the sublattices gives rise to an emergent Ising-nematic degree of freedom $\varphi = \vec{m}_1\cdot\vec{m}_2$ [284], which may be finite even in the absence of magnetic order (i.e. $\langle\varphi\rangle \neq 0$, but $\langle\vec{m}_i\rangle = 0$) as long as the magnetic fluctuations are strong enough [230]. A finite value, $\langle\vec{m}_1\cdot\vec{m}_2\rangle \neq 0$, breaks the Ising symmetry embedded in Eq. (4.3) and, consequently, the tetragonal symmetry. This can be seen explicitly through the magneto-elastic term:

$$F_{\text{mag-el}} = \lambda\int \frac{d^3x}{v}\,\delta\left(\vec{m}_1\cdot\vec{m}_2\right) \tag{4.4}$$

where $\lambda > 0$ is the magneto-elastic coupling and δ is the orthorhombic distortion. From the bilinear coupling of δ and φ in Eq. (4.4), both the nematic and structural transitions are simultaneous. This mechanism for the tetragonal-to-orthorhombic transition explains why the

magnetic and structural transitions track each other closely in all the phase diagrams of the FeAs-based superconductors. Furthermore, it also explains several experimental observations, such as the softening of the lattice in the tetragonal phase and its hardening in the superconducting state,[230] as well as the suppression of the orthorhombic distortion below the superconducting transition temperature.[185]

In the case where the elastic free energy is harmonic, $F_{el} = C_s\delta^2/2$ (where C_s is the shear modulus) the only effect of the elastic degree of freedom is to renormalize the sublattice coupling constant g in Eq. (4.3), yielding $g \to g + \lambda^2/C_s$ [230]. In a mean-field approach, this implies that the two transitions remain split and second order. Although fluctuations could induce a simultaneous first-order transition [286, 287], it is unclear whether they could explain a second-order structural transition split from a first-order magnetic transition, as our data for low substitution levels in $BaFe_2As_2$ suggests.

To account for my observations, R. Fernandes and J. Schmalian moved beyond the harmonic lattice approximation to consider the effects of anharmonic elastic terms (for more details on the formalism, see Ref. [288]). In the tetragonal phase, the most general form of the free energy can be written as $F_{\rm el} = \frac{1}{2}\bar{C}_{ij}\epsilon_i\epsilon_j + \frac{1}{6}\bar{C}_{ijk}\epsilon_i\epsilon_j\epsilon_k$, where $\bar{C}_{ij}$ are given in terms of the six independent elastic constants and the strain components ϵ_i are:

$$\begin{aligned}
\epsilon_1 = &\quad u_{xx} + u_{yy} + u_{zz} &;&\quad \epsilon_4 = 2u_{yz} \\
\epsilon_2 = &\quad (u_{xx} + u_{yy} - 2u_{zz})/6 &;&\quad \epsilon_5 = 2u_{xz} \\
\epsilon_3 = &\quad (u_{xx} - u_{yy})/\sqrt{2} &;&\quad \epsilon_6 = 2u_{xy}
\end{aligned} \tag{4.5}$$

with $u_{ij} = (\partial_i u_j + \partial_j u_i)/2$ and $\vec{u} = (u_x, u_y, u_z)$ denoting the displacement vector. In this notation, the orthorhombic distortion $\delta = \epsilon_6/2$ and the shear modulus $C_s \equiv 4\bar{C}_{66}$. To describe the transition from the tetragonal to the orthorhombic phase, they retain only the essential anharmonic terms that contain ϵ_6 because ϵ_6 is the elastic stiffness in $[1, 0, 0]_{\rm T}$ and $[0, 1, 0]_{\rm T}$ directions [289]:

$$\begin{aligned}
F_{\rm el} \;=\; & \frac{1}{2}\bar{C}_{11}\epsilon_1^2 + \frac{1}{2}\bar{C}_{22}\epsilon_2^2 + \bar{C}_{12}\epsilon_1\epsilon_2 + \frac{1}{2}\bar{C}_{44}\left(\epsilon_4^2 + \epsilon_5^2\right) + \\
& \frac{1}{2}\bar{C}_{66}\epsilon_6^2 + \frac{1}{2}\left[\bar{C}_{166}\epsilon_1 + \bar{C}_{266}\epsilon_2\right]\epsilon_6^2 + \bar{C}_{456}\epsilon_4\epsilon_5\epsilon_6
\end{aligned} \tag{4.6}$$

Minimization with respect to the other strain components yields an effective elastic free energy in terms only of $\epsilon_6 = 2\delta$:

$$F_{\rm el}\left[\delta\right] = \frac{1}{2}C_s\delta^2 + \frac{1}{4}U\delta^4 + \frac{1}{6}W\delta^6 \tag{4.7}$$

where the sixth-order term $W > 0$ is included to ensure stability of the functional. Note that since:[288]

$$\frac{U}{16} = U_0 - \frac{\left(\bar{C}_{22}\bar{C}_{166}^2 - 2\bar{C}_{12}\bar{C}_{166}\bar{C}_{266} + \bar{C}_{11}\bar{C}_{266}^2\right)}{2\left(\bar{C}_{11}\bar{C}_{22} - \bar{C}_{12}^2\right)} \tag{4.8}$$

the fourth-order coefficient can be negative, depending on the magnitudes of the anharmonic terms $\bar{C}_{ijk}$. Here, U_0 is the bare coefficient coming from higher-order quartic anharmonic terms.

In what follows, they consider all elastic coefficients to be temperature independent, and that the only minimum of Eq. (4.7) is at $\delta = 0$. Thus, different from the model in Eq. (4.1), the system has no intrinsic structural instability, and the elastic phase transition results solely from the magneto-elastic coupling in Eq. (4.4). In the case of a harmonic lattice, it was shown that nematic fluctuations renormalize the shear modulus in the tetragonal phase, making it vanish when the magnetic correlation length achieves a threshold value[230]. Here, not only C_s will be renormalized by nematic fluctuations, but also the anharmonic term U in Eq. (4.7), which gives rise to a much richer phase diagram.

To calculate the total free energy of the system, the 'mean-field $1/N$ approach' is used [230, 282]. Basically, it assumes that the magnetic order parameter $\vec{m}_i$ has N components and expand to leading order for large N. Then self-consistent equations involving the magnetic correlation length ξ, the nematic order parameter φ, the magnetic order parameter $m = |\langle\vec{m}_1\rangle| = |\langle\vec{m}_2\rangle|$, and the orthorhombic distortion δ are obtained. The latter is obtained by minimizing the effective elastic free energy $F_{\rm eff} = F_{\rm el} + \tilde{F}$, where $\tilde{F}$ is an implicit function of δ, arising from the $1/N$ solution of the magnetic problem with free energy $F_{\rm mag} + F_{\rm mag-el}$. Thus, $\tilde{F}$ describes how magnetism changes the elastic free energy.

Parameters were chosen to yield relative temperatures and jumps comparable to those observed experimentally (see Section 4.1.4). They are $\eta_z = 2{\times}10^{-3}$, $\lambda = 0.3\chi_0^{-1}$, $U \approx -2{\times}10^7\chi_0^{-1}$, and $W \approx 2\times10^{12}\chi_0^{-1}$. The relative orders of magnitude between $C_s \sim 10^2\chi_0^{-1}$, U, and W are associated with the equilibrium value of the orthorhombic distortion, $\delta \sim 10^{-3}$. To illustrate

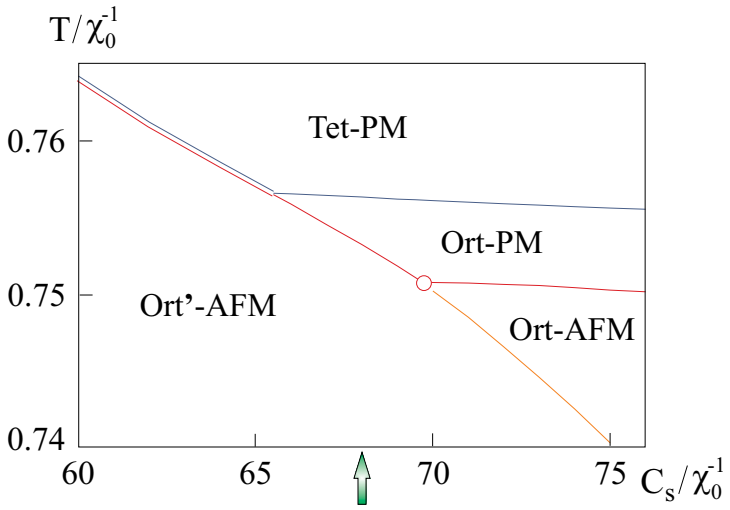

Figure 4.9 Phase diagram of the system with anharmonic elastic terms. T denotes temperature, C_s is the bare shear modulus, and χ_0^{-1} is a magnetic energy scale. Thin (thick) lines refer to second-order (first-order) phase transitions, with the red (blue) lines denoting magnetic (structural) transitions; the simultaneous first-order transition line is denoted by the double line. We use the notation Ort' to emphasize that the orthorhombic distortion jumps across the first-order magnetic transition. The orange dotted line signals the occurrence of a jump in both the magnetic and orthorhombic order parameters, without symmetry breaking. The open circle refers to the magnetic tricritical point, while the arrow indicates the value of C_s for which we calculate the temperature dependence of both the magnetic and orthorhombic order parameter (see Fig. 4.10).

the richness of the resulting phase diagram, in Fig. 4.9 I show the results obtained after fixing all parameters but the bare shear modulus C_s. For smaller values of C_s, the system undergoes a simultaneous first-order structural/magnetic transition from the tetragonal/paramagnetic phase to the orthorhombic/antiferromagnetic phase. This corresponds to a direct first-order transition from the Tet-PM phase to the Ort-AFM phase, which has not been observed in the experiments in Section 4.1.4, however, has been observed e.g. in $CaFe_2As_2$.[167]

As the bare shear modulus increases, the two transitions split: at higher temperatures, the system undergoes a *second-order* structural transition and then a *first-order* magnetic transition at lower temperature. The latter is accompanied by a discontinuity in the orthorhombic order parameter δ due to the magneto-elastic coupling. This is precisely the sequence observed in my experiments described in Section 4.1.4 for the parent $BaFe_2As_2$ and substituted compounds for

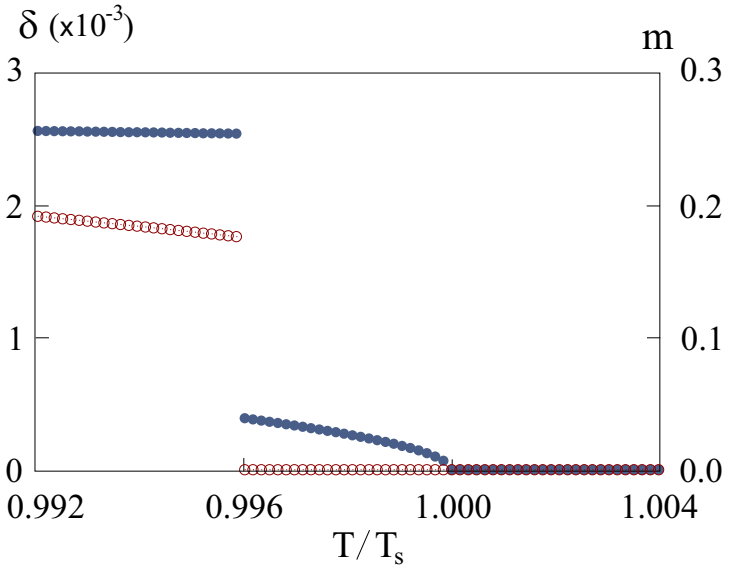

Figure 4.10 Magnetic (m, open symbols) and orthorhombic (δ, filled symbols) order parameters as function of temperature T (in units of the structural transition temperature T_S) for the system indicated by the green arrow in the phase diagram of Fig. 4.9.

low concentrations (Tet-PM $\rightarrow$ Ort-PM $\rightarrow$ Ort-AFM). Note that this is not another structural phase transition, but a consequence of the first-order character of the magnetic transition. To show this explicitly, in Fig. 4.10, both δ and m are plotted as function of temperature for the value of C_s indicated by the arrow in Fig. 4.9. Not only is the relative size of the step comparable to that measured experimentally for $BaFe_2As_2$, but also the relative temperature at which the step occurs (see Fig. 4.3(b), where $T_S \approx 134.6$ K and $T_N \approx 134$ K). The discontinuity in the orthorhombic distortion accompanying the first-order magnetic transition is a very general feature that holds regardless of the specific values of the parameters. Thus, it supports the interpretation that the experimental data in Fig. 4.3 on the parent compound, $BaFe_2As_2$, describe a second-order structural transition followed by a first-order magnetic transition.

Returning to the phase diagram of Fig. 4.9, as the shear modulus is increased even further, the transitions remain split but the magnetic transition becomes second-order, as it is observed for higher doping concentrations in $Ba(Fe_{1-x}Co_x)_2As_2$ and $Ba(Fe_{1-x}Rh_x)_2As_2$. At low temperatures, there is another line that marks a simultaneous jump in both the magnetic and the orthorhombic order parameter, without any symmetry breaking, and a magnetic tri-

critical point. However, it should be pointed out that in the $1/N$ approach, a key feature of the magnetically ordered state, i.e. the reconstruction of the Fermi surface, has not been taken into account. For instance, $x_{\rm tri} \approx 0.02$ is close to the composition where evidence for a Lifshitz transition, below $T_{\rm N}$, in $Ba(Fe_{1-x}Co_x)_2As_2$ has been reported by thermoelectric power, Hall coefficient measurements and angle-resolved photoemission.[92, 290] Therefore, features in the model deep in the magnetically ordered phase, such as this extended line, are likely to change once the reconstruction of the Fermi surface is considered. For instance, one possibility is that this extended line terminates at a finite temperature and leaves a magnetic tricritical point.

Furthermore, although in the phase diagram of Fig. 4.9 only the bare shear modulus was changed, it is unlikely that this is the only modified parameter as substitution (doping) is introduced in the parent compound. In particular, the increase in the splitting between the transitions is much more modest in Fig. 4.9 than found experimentally (Fig. 4.7). It is possible, then, that other parameters controlling the splitting are also changed, such as the magneto-elastic coupling, λ, and the inter-plane magnetic coupling, η_z. The main objective of the phase diagram presented here is to illustrate the various possible phase transitions once anharmonic elastic terms are taken into account. It is interesting to note that, in the simple phase diagram in Fig. 4.9, systems with softer lattices are more likely to display simultaneous first-order transitions. Indeed, $CaFe_2As_2$, which is significantly softer than $BaFe_2As_2$, presents relatively strong simultaneous first-order transitions.[167]

4.3 The Effect of Ru substitution on the parent $BaFe_2As_2$ compounds

I have so far presented the nature of the phase transitions in the parent $BaFe_2As_2$ compounds and its evolution with electron doping by Co or Rh substitution. I have also shown in Section 2.3.2 that the substitution of Co, Ni, or Rh for Fe in the parent $BaFe_2As_2$ compound results in new and interesting behavior.[181–183, 185, 186, 188–190, 274, 291] As doping is increased, both the structural and magnetic transitions are suppressed and split, with the structural transition occurring at higher temperature. In $Ba(Fe_{1-x}Co_x)_2As_2$, for Co concentrations $0.03 \leq x \leq 0.06$, we enter a region of the phase diagram where magnetism and superconductivity coexist and compete.[186, 274] Within this region, the magnetic and struc-

tural transitions are well-separated in temperature, and continuous in nature (see for example, Figs. 2.13 and 2.14).

Whereas all of the studies above describe measurements performed on electron-doped materials, it is also important to consider the response of these systems to isoelectronic doping. For example, superconductivity is observed with a maximum $T_c \sim 30$ K by the isoelectronic doping of P at the As site in $BaFe_2As_2$.[93] Furthermore, Klintberg *et al.*[292] have discussed the equivalence of chemical and physical pressure in $BaFe_2(As_{1-x}P_x)_2$ by showing that the temperature-pressure phase diagrams are similar, but shifted for different x. Nevertheless, the maximum superconducting transition temperatures are identical. It is believed that superconductivity in this compound originates from steric effects arising from the smaller ionic radius of P. Only small modifications of the Fermi surface were observed.[293] Superconductivity has also been reported in $Sr(Fe_{1-x}Ru_x)_2As_2$ compounds with T_c up to 20 K, but at much higher doping levels than required for the electron-doped series (e.g. Co, Ni, Rh).[87] Ru substitution on the Fe site in $Ba(Fe_{1-x}Ru_x)_2As_2$ was recently reported to exhibit properties similar to the electron-doped $BaFe_2As_2$ series but, again, at higher doping compositions.[86, 102, 294] The structural and AFM transition temperatures are suppressed with increasing x and superconductivity occurs at $x \approx 0.16$.

Thaler *et al.* [102] have made an interesting comparison between the phase diagrams of Ru-doped $BaFe_2As_2$ and the parent $BaFe_2As_2$ compound under pressure. Although the unit cell volume increases with Ru doping, they found a striking similarity between the phase diagrams for Ru doping and physical pressure when scaled by the lattice parameter c/a ratio. Only a single feature corresponding to a magnetic, structural, or joint magnetic/structural transition has been observed in resistance and magnetization data for $Ba(Fe_{1-x}Ru_x)_2As_2$ ($x \leq 0.37$), quite different from the behavior of electron doped $BaFe_2As_2$. Interestingly, I note that in the case of P doping on the As site, a splitting between the structural and magnetic transitions, that increases with P concentration, was noted in resistance measurements.[96] It is, therefore, particularly important to clarify the microscopic nature of the magnetic and/or structural transitions for the case of isoelectronic doping on the Fe site in $Ba(Fe_{1-x}Ru_x)_2As_2$, as well as the interaction between magnetism, structure and superconductivity in this series.

4.3.1 Experimental Details

Temperature-dependent, high-resolution, single-crystal x-ray diffraction measurements were performed on a four-circle diffractometer as described in Section 4.1.1. Temperature-dependent ac electrical resistance data were collected using a Quantum Design Magnetic Properties Measurement System (MPMS) as in Section 4.2.1. Magnetization data were also measured using a MPMS. The measurements using MPMS were done by Thaler.

Neutron diffraction measurements were performed on the HB1A spectrometer at the High Flux Isotope Reactor at Oak Ridge National Laboratory using samples with a typical mass of approximately 25 mg. The beam collimators before the monochromator-between the monochromator and sample-between the sample and analyzer-between the analyzer and detector were 48'-40'-40'-136'. HB1A operates at a fixed incident neutron energy of 14.7 meV, and two pyrolytic graphite filters were employed to effectively eliminate higher harmonics in the incident beam. The samples were aligned such that the $(H, H, L)_{\rm T}$ reciprocal lattice plane was coincident with the scattering plane of the spectrometer, and were mounted in a closed-cycle refrigerator. The temperature dependence of the scattering was studied at several nuclear Bragg peak positions and at $\vec{Q}_{\rm AFM} = (\frac{1}{2}, \frac{1}{2}, L{=}{\rm odd})_{\rm T}$ positions corresponding to the AFM order in the parent and electron-doped $BaFe_2As_2$ compounds.

4.3.2 Effects on $T_{\rm S}$, $T_{\rm N}$, and ordered moment

Figures 4.11 (a) and (b) show neutron and x-ray data for $Ba(Fe_{1-x}Ru_x)_2As_2$ with $x = 0.073$ at selected temperatures. Above $T_{\rm S} = T_{\rm N} = 109{\pm}1$ K, no scattering is observed at $\vec{Q}_{\rm AFM} = (\frac{1}{2}, \frac{1}{2}, 3)_{\rm T}$, but as the temperature is lowered below $T_{\rm N}$, the scattering increases smoothly. The magnetic wave vector is identical to that for $BaFe_2As_2$ compounds indicating that the magnetic structure is the same "stripe" AFM structure observed for all AFM ordered $AEFe_2As_2$ compounds (AE = Ca, Sr, and Ba), with AFM alignment of the moments along the orthorhombic $\vec{a}$ and $\vec{c}$ axes and FM alignment along the $\vec{b}$ axis. Analysis of the intensity ratios of different AFM reflections at selected temperatures confirmed that the moment direction is along the elongated orthorhombic $\vec{a}$ direction. From the high-resolution x-ray measurements,

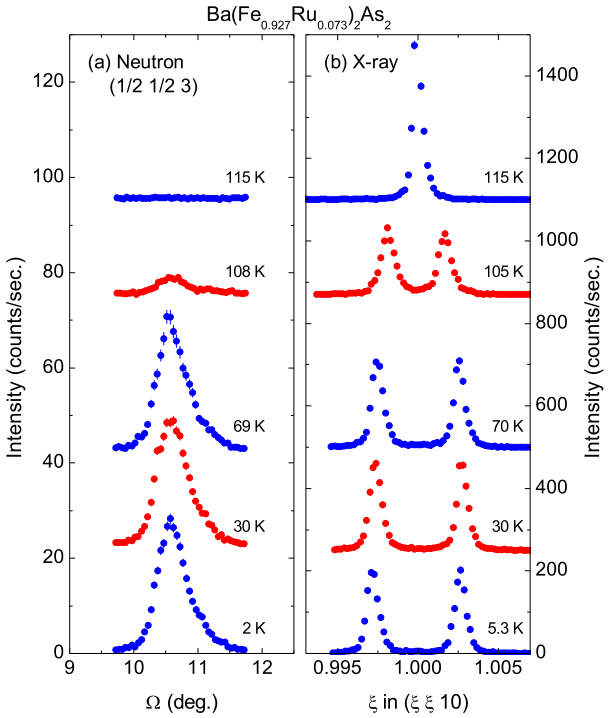

Figure 4.11 Temperature evolution of (a) the neutron diffraction rocking scans through the $(\frac{1}{2}, \frac{1}{2}, 3)_{\mathrm{T}}$ magnetic peak and (b) high-resolution x-ray diffraction $[\xi, \xi, 0]_{\mathrm{T}}-$scans through the $(1, 1, 10)_{\mathrm{T}}$ peak in $Ba(Fe_{0.927}Ru_{0.073})_2As_2$. For this sample $T_{\mathrm{S}} = T_{\mathrm{N}} = 109\pm1$ K. The data are shown with arbitrary offsets.

it is shown [Fig. 4.11 (b)] that the $(1, 1, 10)_{\mathrm{T}}$ Bragg peak exhibits a sharp single peak above $T_{\mathrm{S}} = T_{\mathrm{N}} = 109\pm1$ K consistent with a tetragonal structure and splits into two peaks below T_{S}, characteristic of the tetragonal-to-orthorhombic transition.

Figures 4.12 (a) and (b) summarize the magnetization and resistance measurements on $Ba(Fe_{1-x}Ru_x)_2As_2$ with $x = 0.073$. A sharp feature attributed to $T_{\mathrm{S}}/T_{\mathrm{N}}$ is observed at 107 K in the derivatives of magnetization and resistance. In Fig. 4.12 (c) and (d), the orthorhombic distortion, $\delta = \frac{a-b}{a+b}$, and the integrated magnetic scattering intensity, measured from rocking scans through $\vec{Q}_{\mathrm{AFM}} = (\frac{1}{2}, \frac{1}{2}, 3)_{\mathrm{T}}$, are plotted as a function of temperature for $x = 0.073$. These measurements show that $T_{\mathrm{S}} = T_{\mathrm{N}} = 109\pm1$ K, in reasonable agreement with the thermodynamic and transport measurements given the inherent uncertainty in assigning transition temperatures to features in the magnetization and resistance. Figures 4.12 (e) and (f) sum-

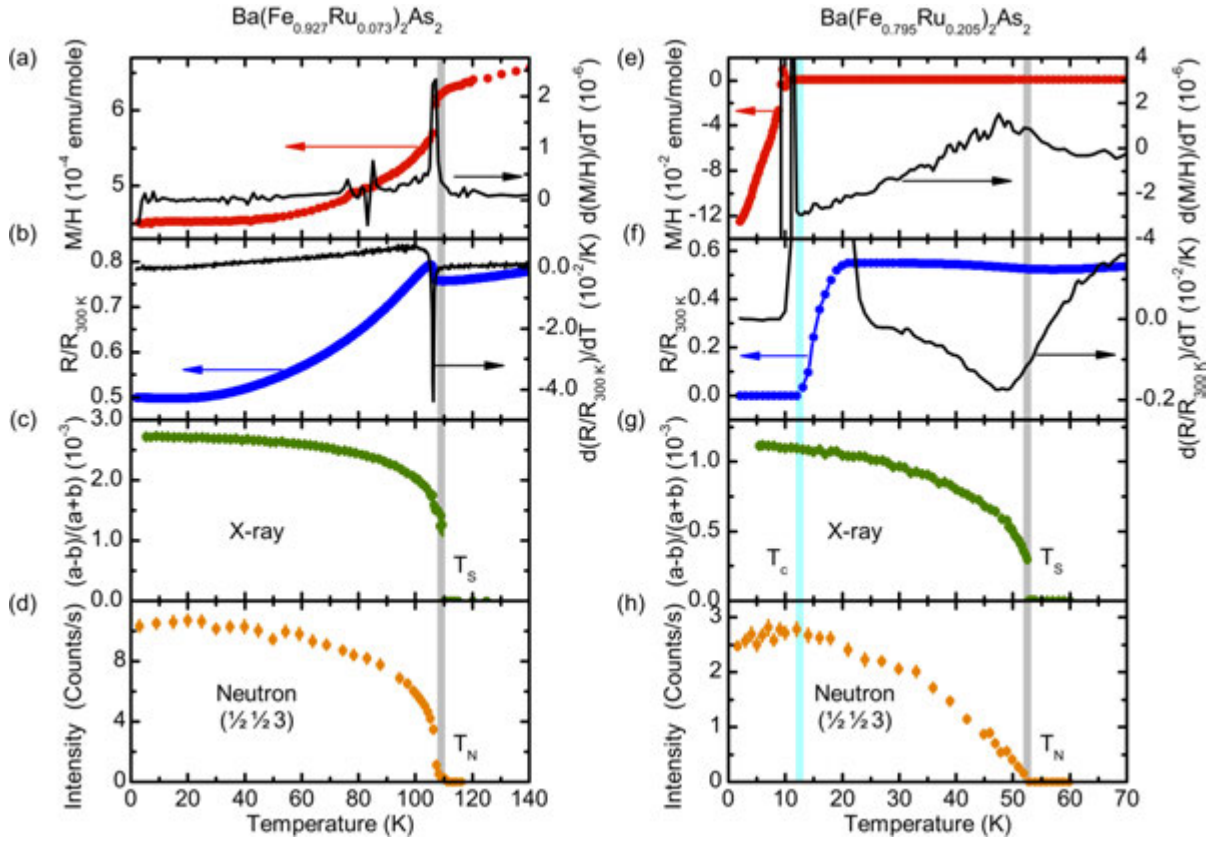

Figure 4.12 Plots of magnetization ($\frac{M}{H}$) and its temperature derivative, $\frac{d(\frac{M}{H})}{dT}$, the resistance ratio ($\frac{R}{R_{300\ \mathrm{K}}}$) and its temperature derivative, the measured orthorhombic distortion ($\delta = \frac{a-b}{a+b}$), and the integrated magnetic intensity at $(\frac{1}{2}, \frac{1}{2}, 3)_{\mathrm{T}}$ for $Ba(Fe_{0.927}Ru_{0.073})_2As_2$ in panels (a)-(d) and $Ba(Fe_{0.795}Ru_{0.205})_2As_2$ in panels (e)-(h). For $x = 0.073$ the measured magnetization, resistance and their derivatives show sharp signatures at $T_{\mathrm{S}} = T_{\mathrm{N}} = 107$ K, close to the value (109±1 K) measured by the x-ray and neutron scattering measurements. For $x = 0.205$, the signatures at $T_{\mathrm{S}} = T_{\mathrm{N}}$ are significantly broader. The maxima of the derivatives of the magnetization and resistance are found at 49 K whereas the x-ray and neutron scattering value is 52±1 K.

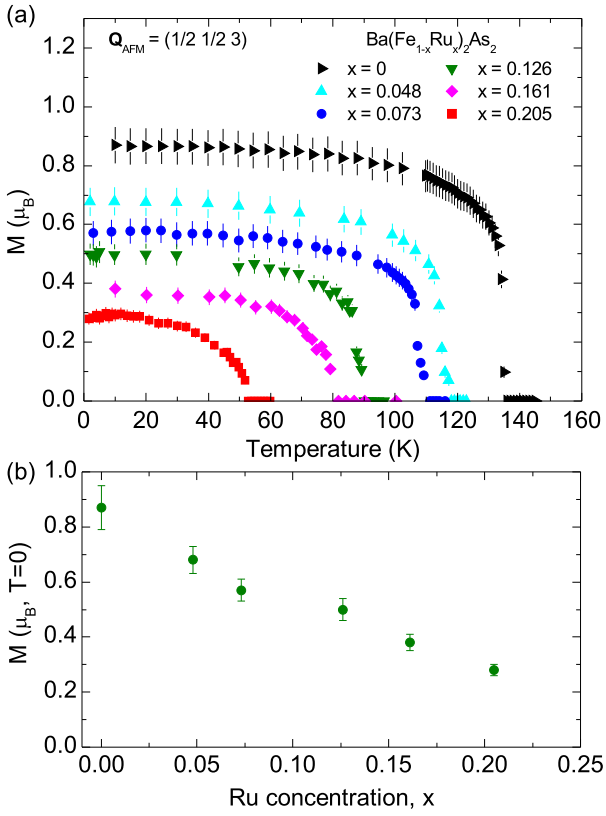

Figure 4.13 (a) Temperature dependence of the ordered magnetic moment calculated from the integrated intensity of the $(\frac{1}{2}, \frac{1}{2}, 3)_{\mathrm{T}}$ magnetic Bragg peak from $Ba(Fe_{1-x}Ru_x)_2As_2$. (b) The extrapolated ordered moment at zero temperature as a function of Ru concentration, x.

marize the magnetization and resistance measurements on $Ba(Fe_{1-x}Ru_x)_2As_2$ with $x = 0.205$. The reason why $x = 0.205$ was chosen is because it is the highest concentration studied, that shows structural and magnetic transitions as well as superconducting transition. Here, the characteristic features are much broader. According to the criteria of Ref. [102], T_S/T_N is assigned to the maxima of the derivatives of magnetization and resistance, which is 49 K. The x-ray and neutron data of Figs. 4.12 (g) and (h) display the orthorhombic distortion δ and the magnetic integrated intensity at $\vec{Q}_{\mathrm{AFM}} = (\frac{1}{2}, \frac{1}{2}, 3)_{\mathrm{T}}$ for $x = 0.205$ and yield $T_S = T_N = 52 \pm 1$ K. The transition temperatures derived from the criteria of Ref. [102] are up to 3 K lower than the observed transition temperatures derived from the x-ray and neutron diffraction measurements. Most importantly, however, I find that, within experimental error, the structural and magnetic

transitions remain locked together with increasing Ru doping and this behavior clearly differs from that found for the electron-doped compounds.

$Ba(Fe_{1-x}Ru_x)_2As_2$ crystals with $x = 0$, 0.048, 0.126, and 0.161 were also examined by neutron diffraction and the results for the entire series are summarized in Fig. 4.13. The magnetic integrated intensities were, again, determined from rocking scans through the magnetic peak at $(\frac{1}{2}, \frac{1}{2}, 3)_T$ as a function of temperature and put on an absolute basis using the known mass of the samples and the magnetic diffraction from the parent compound, $BaFe_2As_2$, measured under identical conditions.[186] The ordered moment as a function of temperature for each sample is presented in Fig. 4.13(a), and the ordered moments extrapolated to $T = 0$ are shown in Fig. 4.13(b). As the Ru concentration increases, the ordered moment decreases monotonically.

4.3.3 Effect of Superconductivity on AFM ordering and Structural distortion

Turning now to the effects of superconductivity on the AFM ordering and structural distortion, we first note that for the $x = 0.205$ sample, the resistance and magnetization data show the existence of superconductivity below $T_c \approx 13$ K in Figs. 4.12 (e) and (f). For this sample, in Fig. 4.12 (h), I observed a suppression of the AFM order below T_c similar to what was reported previously for Co, Ni, and Rh substituted $BaFe_2As_2$,[182, 188–190] where the presence of both AFM and superconductivity has been attributed to microscopically coexisting states that compete for the same itinerant electrons. It has also been established that the onset of superconductivity leads to a suppression of the orthorhombic distortion in the electron-doped compounds. Refs. [185] and [189], for example, described this effect below T_c for both Co and Rh substituted $BaFe_2As_2$, respectively. Because $\frac{T_c}{T_N}$ for $Ba(Fe_{0.795}Ru_{0.205})_2As_2$ is approximately half the value of $\frac{T_c}{T_N}$ for $Ba(Fe_{0.953}Co_{0.047})_2As_2$, the magnitude of suppression of AFM order at the base temperature of our measurement is correspondingly smaller [Fig. 4.14 (a)], and the reduction of the orthorhombic distortion is not clearly observed [Figs. 4.12 (g) and 4.14(b)]. Therefore, I have also studied an additional concentration, $x = 0.246 \pm 0.005$ ($T_c \approx$ 14 K), by high-resolution x-ray diffraction and, as shown in Fig. 4.14 (b), see the suppression of the orthorhombic distortion below T_c.

In contrast to electron doped $BaFe_2As_2$ in which the suppression of transition temperatures

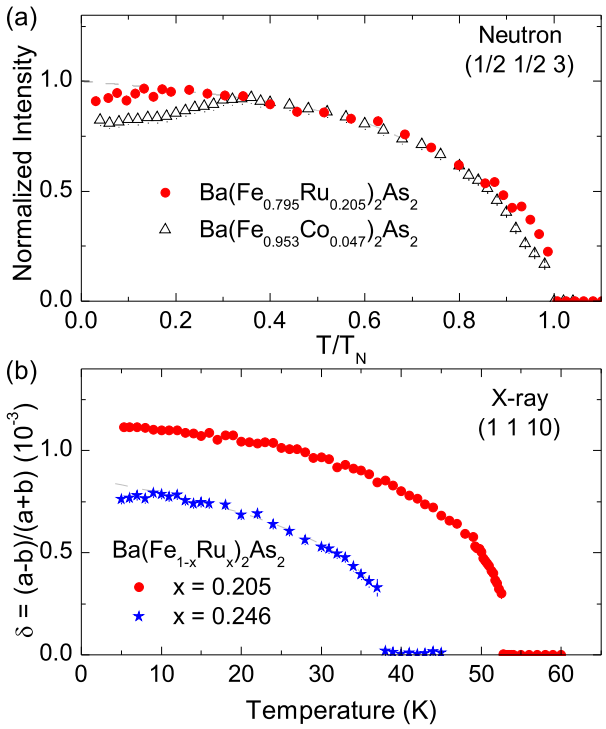

Figure 4.14 (a) Comparison of the suppression of AFM order below T_c between the 20.5% Ru (filled circles) and the 4.7% Co (open triangles) (from Ref. [186]) substituted $BaFe_2As_2$ samples. Intensities are normalized for comparison. (b) Orthorhombic distortion for $Ba(Fe_{1-x}Ru_x)_2As_2$ with $x = 0.205$ (circles) and 0.246 (stars). The reduction in the distortion below T_c is not clearly observable for $x = 0.205$ but it is evident for $x = 0.246$. The gray dashed lines are guides for eyes.

(T_S, T_N, and T_c) can be understood by carrier doping or shift of the chemical potential [186], Ru substitution is isoelectronic, which does not introduce extra carrier, but the reason why Ru substitution behaves similar to electron doping is arguable. Some groups argued that Ru substitution strongly modifies the electronic structure by increasing both the number of carriers and their mobility by reducing correlation effects based on their Hall effect and angle-resolved photoemission spectroscopy measurements.[294, 295] Other groups observed no change in neither chemical potential nor the shape of Fermi surface in their angle-resolved photoemission spectroscopy measurements [296] and argued that magnetic dilution by Ru substitution plays a crucial role in suppression of T_S and T_N.

4.4 The Effect of Mn substitution on the parent $BaFe_2As_2$ compounds

I have shown how similar/different the structural and magnetic properties are in electron-doped and isoelecton-doped $BaFe_2As_2$ by changing the substitution elements from Co, Ni, or Rh (on the right side of Fe in the periodic table) to Ru (in the same column as Fe) [see Sec 2.3.2].

In strong contrast to what is found for the electron-doped $AEFe_2As_2$ (AE = Ca, Sr, and Ba) compounds, hole doping on the Fe site through the introduction of Cr [88, 194] and Mn [97] has, so far, failed to produce superconducting samples for any doping level, although superconductivity is realized by hole doping through the substitution of K for the AE. [2, 63] This indicates that the number of additional electrons or holes is not the sole controlling factor for superconductivity. Furthermore, unlike the suppression and eventual elimination of magnetic ordering with increasing x found for electron-doped compounds, recent neutron studies of $Ba(Fe_{1-x}Cr_x)_2As_2$ indicate that, for $x \geq 0.30$, the "stripelike" AFM structure is replaced by the G-type "checkerboard-type" structure (collinear antiferromagnetic alignment between nearest neighbor spins in the $\vec{a}-\vec{b}$ plane and also antiferromagnetic alignment between the plane along the $\vec{c}$ axis) as found for $BaMn_2As_2$ [195] and proposed for $BaCr_2As_2$.[297] Given the strong coupling between structure, magnetism, and superconductivity already established for the FeAs-based superconductors, such differences in magnetic and structural behavior in hole-doped materials demand attention.

4.4.1 Effects on T_S, T_N, and ordered moment

Temperature-dependent ac electrical resistance data were collected using a Quantum Design Magnetic Properties Measurement System (MPMS) by A. Thaler as in Section 4.2.1. In Fig. 4.15 I show the resistance data (solid symbols) normalized to their room-temperature values, and their temperature derivatives (open symbols) for a representative subset of three compositions, x = 0.074, 0.102, and 0.118. A sharp anomaly, characteristic of all samples for $x \leq 0.074$ is found at approximately 80 K for x = 0.074, which broadens and shifts to lower temperature for x = 0.102 and then to higher temperature for x = 0.118. If I associate these features with magnetic and/or structural transitions,[182, 274, 291] the nonmonotonic behavior

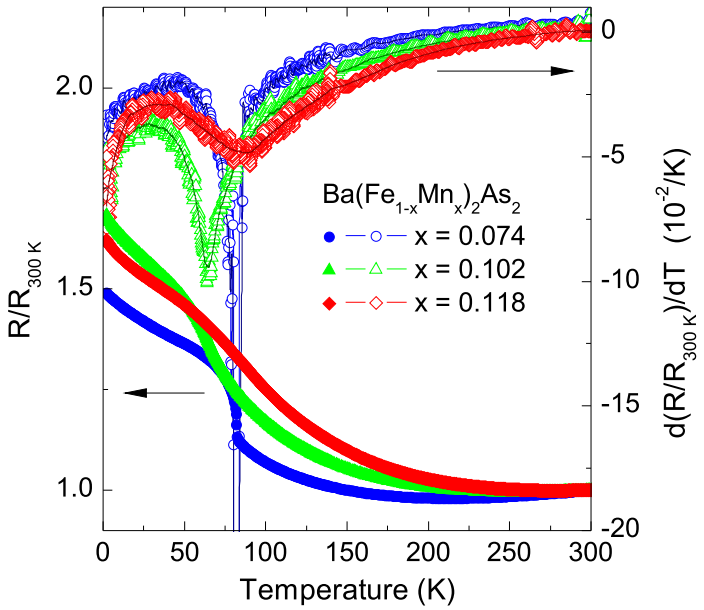

Figure 4.15 Resistance, normalized to the value at $T = 300$ K, and the temperature derivative of the resistance ratio for the $Ba(Fe_{1-x}Mn_x)_2As_2$ samples with $x = 0.074$, 0.102, and 0.118. Lines are guides to the eyes.

of the characteristic temperature is highly unusual for the iron arsenides. Only a single feature is observed in the derivative curve indicating that the magnetic and structural transitions are likely coincident in temperature, and superconductivity is absent in all samples for $T \geq 2$ K.

The principal results of my scattering studies are summarized in Figs. 4.16 and 4.17 for a representative subset of the compositions, $x = 0.074$, 0.102, and 0.118. The neutron diffraction data in Figs. 4.16 (a) and (b) show the magnetic Bragg peak at $(\frac{1}{2}, \frac{1}{2}, 3)_T$ for both $x = 0.102$ and x =0.118, consistent with the "stripelike" AFM order found for the FeAs-based compounds. However, the x-ray data in Figs. 4.16 (c) and (d) demonstrate that the orthorhombic distortion, evident from the splitting of the $(1, 1, 10)_T$ charge peak for the $x = 0.102$ composition, was not observed for $x = 0.118$. Figure 4.17 displays the temperature evolution of the magnetic order, measured by neutron diffraction, and the orthorhombic distortion, measured by x-ray diffraction, for these same compositions as described in Secs. 4.1.1 and 4.3.1. The integrated intensities of the magnetic scattering (filled circles) were measured at the $(\frac{1}{2}, \frac{1}{2}, 3)_T$ magnetic

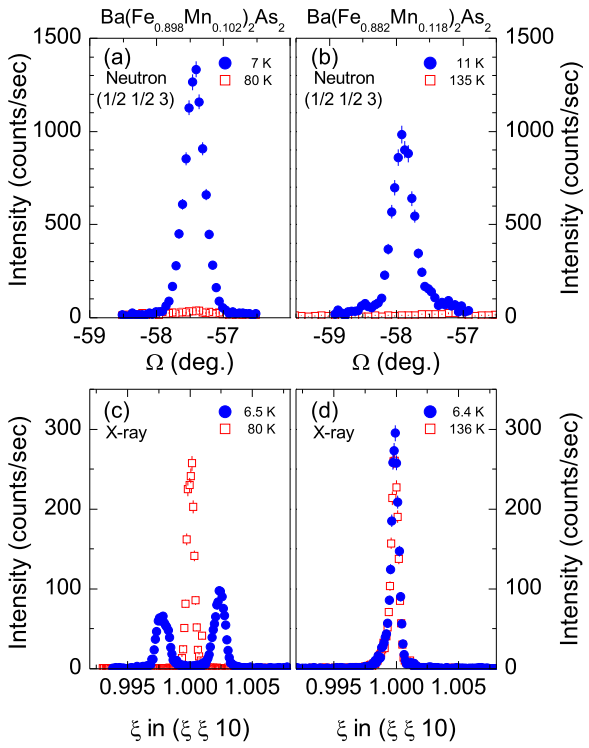

Figure 4.16 Neutron diffraction rocking scans through the $(\frac{1}{2}, \frac{1}{2}, 3)_T$ magnetic Bragg peak above (open squares) and below (filled circles) the AFM transition for (a) $Ba(Fe_{0.898}Mn_{0.102})_2As_2$ and (b) $Ba(Fe_{0.882}Mn_{0.118})_2As_2$. Panels (c) and (d) show x-ray diffraction scans along the $[\xi, \xi, 0]_T$ direction through the $(1, 1, 10)_T$ charge reflection above (open squares) and below (filled circles) the structural transition for these samples. Note the splitting for the $x = 0.102$ sample and its absence for $x = 0.118$.

Bragg position as the sample angle was scanned [see Figs. 4.16 (a) and (b)]. The orthorhombic distortion, δ, was calculated from the splitting of peaks observed in $(\xi, \xi, 0)_T$ scans through the $(1, 1, 10)_T$ Bragg peak [see Figs. 4.16 (c) and (d)]. For samples with $x \leq 0.074$ [Figs. 4.17 (a)], I observed a well-defined AFM and structural transitions that are, within our resolution, coincident in temperature. For $x = 0.102$ [Fig. 4.17 (b)], a weak "tail" of magnetic scattering extends to temperatures above the structural transition and, for $x \geq 0.118$, the structural transition is absent (the sample remains tetragonal down to at least $T = 6.4$ K within our resolution for δ of 1×10^{-4}) and the temperature evolution of the AFM order is quite different

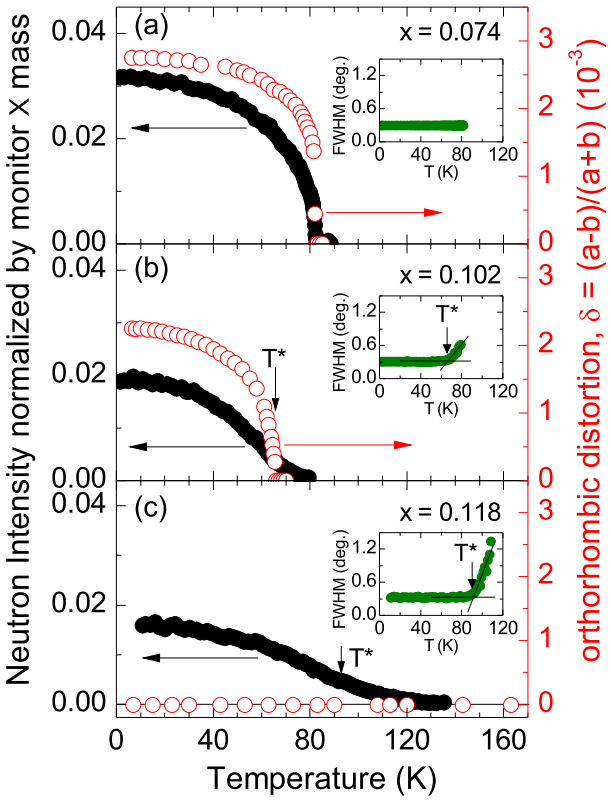

Figure 4.17 Temperature dependence of the integrated intensities of the $(\frac{1}{2}, \frac{1}{2}, 3)_{\mathrm{T}}$ magnetic Bragg peak (filled circles) and the orthorhombic distortion (open circles) measured at $(1, 1, 10)_{\mathrm{T}}$ charge peak positions for (a) $x = 0.074$, (b) $x = 0.102$, and (c) $x = 0.118$ of $Ba(Fe_{1-x}Mn_x)_2As_2$. The insets to each panel show the temperature dependence of the broadening of the $(\frac{1}{2}, \frac{1}{2}, 3)_{\mathrm{T}}$ magnetic peak and the definition of T^*.

from what is observed for $x = 0.074$. For $x \geq 0.118$, a distinct broadening of the magnetic peak beyond the resolution of the measurement is observed for temperatures above T^*, as defined below and in the insets of Figs. 4.17 (b) and (c).

In Fig. 4.18 (a) I have used the neutron, x-ray and resistance data to construct a phase diagram in the low Mn substitution regime for $Ba(Fe_{1-x}Mn_x)_2As_2$. The phase line between the paramagnetic/tetragonal and AFM/orthorhombic phase for $x \leq 0.074$ was easily determined from the well-defined onset of the distortion and the appearance of a resolution limited magnetic Bragg peak at $(\frac{1}{2}, \frac{1}{2}, 3)_{\mathrm{T}}$. For $x \geq 0.102$, however, the onset of long-range magnetic order is more

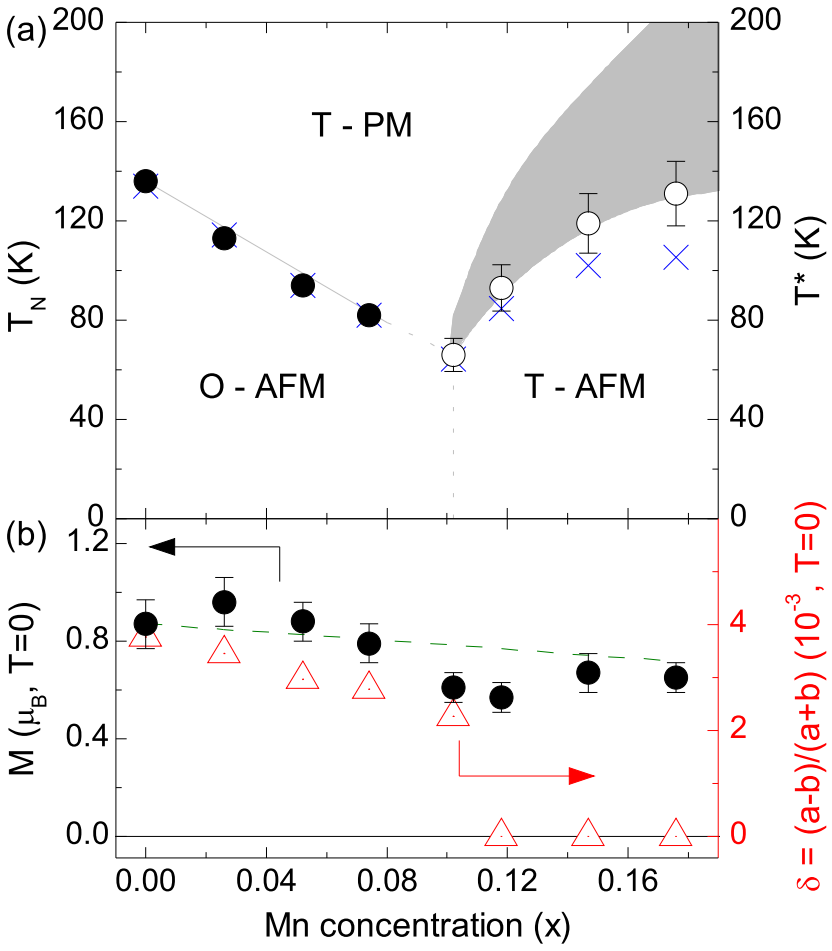

Figure 4.18 (a) The compositional phase diagram for $Ba(Fe_{1-x}Mn_x)_2As_2$ determined from neutron and x-ray diffraction measurements. Closed circles denote T_N and open circles represent T^* as described in the text. Crosses denote the temperature corresponding to minima of $\frac{dR}{dT}$ found in Fig. 4.15. The shaded region denotes the extent of the magnetic scattering above T^*. The vertical dashed line marks the approximate composition for the change from an orthorhombic to tetragonal structure. (b) The magnetic moment and structural distortion as a function of Mn-concentration. The dashed line represents the value of the magnetic moment per Fe atom rather than Fe/Mn site as a function of Mn substitution.

difficult to identify. Therefore, I have defined a characteristic temperature, T^*, which denotes the temperature below which the width of the magnetic peak is limited by the instrumental resolution (approximately 0.3° FWHM). The values of T^* follow the same trend seen for the maxima in $\frac{dR}{dT}$ in Fig. 4.15. The gray band in the phase diagram represents the temperature range, above T^*, where magnetic scattering at $(\frac{1}{2}, \frac{1}{2}, 3)_{\mathrm{T}}$ persists [see Figs. 4.17 (b) and (c)]. In Fig. 4.18 (b) I plot the measured structural distortion and the magnetic moment per Fe/Mn site, extrapolated to $T = 0$, as a function of substitution concentration.

From the aforementioned results, I first note that the data for $Ba(Fe_{1-x}Mn_x)_2As_2$ for $x \leq 0.074$ unambiguously show that the structural and magnetic transitions remain locked together, unlike the separation of the structural and AFM transitions found for Co, Ni, and Rh substitution (Section 2.3.2). Furthermore, at $x = 0.102$, I find a broadened magnetic peak at $(\frac{1}{2}, \frac{1}{2}, 3)_{\mathrm{T}}$ above the structural transition and, for $x \geq 0.118$, I observe the magnetic Bragg peak at $(\frac{1}{2}, \frac{1}{2}, 3)_{\mathrm{T}}$ in the absence of an orthorhombic distortion, a surprising observation that will be discussed below. Finally I note that the magnetic moment per Fe/Mn site as well as the magnitude of the structural distortion vary only weakly with composition for $x \leq 0.102$ whereas, for Co substitution, the suppression of the magnetic moment and structural distortion with doping is much more severe.

4.4.2 AFM order in $Ba(Fe_{1-x}Mn_x)_2As_2$ for $x \geq 0.118$

The observation of the AFM ordering at $(\frac{1}{2}, \frac{1}{2}, 3)_{\mathrm{T}}$ in the absence of an orthorhombic distortion is unprecedented in the FeAs-based compounds. To understand this, it is useful to compare these results to what has recently been found for an another hole-doped $Ba(Fe_{1-x}Cr_x)_2As_2$ compounds.[196, 197] At much higher Cr concentrations, $x \geq 0.30$, Ref. [196] reports that the "stripelike" magnetic structure is replaced by a G-type, checkerboard, magnetic order as shown by polarized and unpolarized neutron diffraction measurements of the integrated intensity of the $(1, 0, 1)_{\mathrm{T}}$ Bragg peak (Fig. 3 in Ref. [196]). G-type AFM order has been proposed for the parent $BaCr_2As_2$ compound,[297] and measured for $BaMn_2As_2$,[195] so it is not unreasonable to expect this change in magnetic structure at high enough Cr, or Mn, substitution. However, my unpolarized neutron diffraction measurements of the $(1, 0, 1)_{\mathrm{T}}$ peaks for the highest Mn

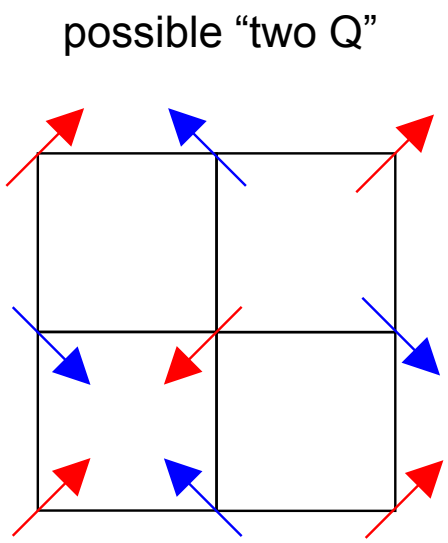

Figure 4.19 Two-Q structure for $\vec{\Delta}_1 \perp \vec{\Delta}_2$ and $\left|\vec{\Delta}_1\right| = \left|\vec{\Delta}_2\right|$. See the text for details.

concentrations, $x = 0.147$ and 0.176, find no evidence of G-type ordering below $T = 300$ K. More specifically, I find no significant change (less than 5 % change) in the $(1, 0, 1)_{\mathrm{T}}$ peak between 12 and 300 K. I cannot exclude G-type ordering that develops well above room temperature given the high ordering temperature of the parent compound [195] but view this as unlikely in light of the substantial dilution of Mn in the samples. For both Cr and Mn substitution, the moment per Fe-site remains constant (Cr) [196], or decreases only weakly (Mn) [Fig. 4.18 (b)] with increasing concentration up to $x = 0.20$. Indeed, as the dashed line in Fig. 4.18 (b) shows, the decrease in the measured moment is consistent with the decreasing Fe concentration implying that the Mn moment does not contribute to the magnetic AFM order characterized by the $(\frac{1}{2}, \frac{1}{2}, 1)_{\mathrm{T}}$ propagation vector. Furthermore, for Mn substitution I find an increase in the characteristic temperature (T^*) associated with magnetic ordering with this propagation vector for $x > 0.102$ whereas for Cr substitution, the ordering temperature for this propagation vector continues to decrease until the transition is completely suppressed at $x = 0.335$, where the G-type AFM structure is observed.[196] All of this points to interesting differences in the phase diagrams between $Ba(Fe_{1-x}Mn_x)_2As_2$ and $Ba(Fe_{1-x}Cr_x)_2As_2$.

Models for “stripelike” AFM order in the FeAs-based superconductors anticipate an atten-

dant orthorhombic distortion due to magneto-elastic effects.[185, 282, 283] Furthermore, this observation is difficult to reconcile with current theories that promote orbital ordering [298, 299] as the driving force for the "stripelike" magnetic phase and the orthorhombic distortion. A second key result of this study is the qualitative change in the temperature dependence of the magnetic ordering for compositions in excess of $x = 0.102$ and the distinct broadening of the magnetic peak for $T > T^*$. At this point it is not clear whether the scattering above T^* for $x > 0.102$ is purely elastic or has a quasi-elastic component within the finite energy window of our neutron measurements, a point that should be investigated further.

The change in the temperature dependence of the magnetic peak points to a strong perturbation of the magnetic ordering, perhaps through disorder effects associate with the introduction of the more localized Mn moments. Furthermore, the abruptness of this change with composition (over a narrow range of $\Delta x < 2\%$) offers the intriguing possibility that the magnetic structure of $Ba(Fe_{1-x}Mn_x)_2As_2$ is modified for $x > 0.102$. In recent theoretical work, Eremin and Chubukov [285] point out that a generic spin configuration for the magnetic iron layers has the form, $\vec{\Delta_1}e^{i\vec{Q_1}\cdot R} + \vec{\Delta_2}e^{i\vec{Q_2}\cdot R}$, where $\vec{\Delta_1}$ and $\vec{\Delta_2}$ correspond to two order parameters for ordering at wave vectors $\vec{Q}_1 = (0, \pi)$ and $\vec{Q}_2 = (\pi, 0)$, respectively, in the unfolded Brillouin zone. The observed "stripelike" magnetic structure occurs when $\vec{\Delta_1} = 0$ and $\vec{\Delta_2} \parallel \vec{Q}_2$. However, when they consider a coupling between the second hole pocket at the Γ point with the elliptical electron pocket at $(0, \pi)$, a two-$\vec{Q}$ structure with both $\vec{\Delta_1} \neq 0$ and $\vec{\Delta_2} \neq 0$ can emerge. For $\vec{\Delta_1} \perp \vec{\Delta_2}$ and $\left|\vec{\Delta_1}\right| = \left|\vec{\Delta_2}\right|$, this two-$\vec{Q}$ structure (Fig. 4.19) does not break the tetragonal symmetry and, therefore, does not yield an orthorhombic distortion of the lattice, consistent with our results.

4.5 Discussion and Summary

To compare the effect of Ru substitution (isoelectronic-doping) and Mn substitution (hole-doping) with the effect of Co, Ni, or Rh substitution (electron-doping), I present the phase diagrams of Co, Ru, and Mn substituted $BaFe_2As_2$ compounds in Fig. 4.20. Summarizing the trends illustrated in Fig. 4.20 (a), for the Co-substituted series at low substitution, the magnetic and structural transitions split with increasing Co concentration, superconductivity

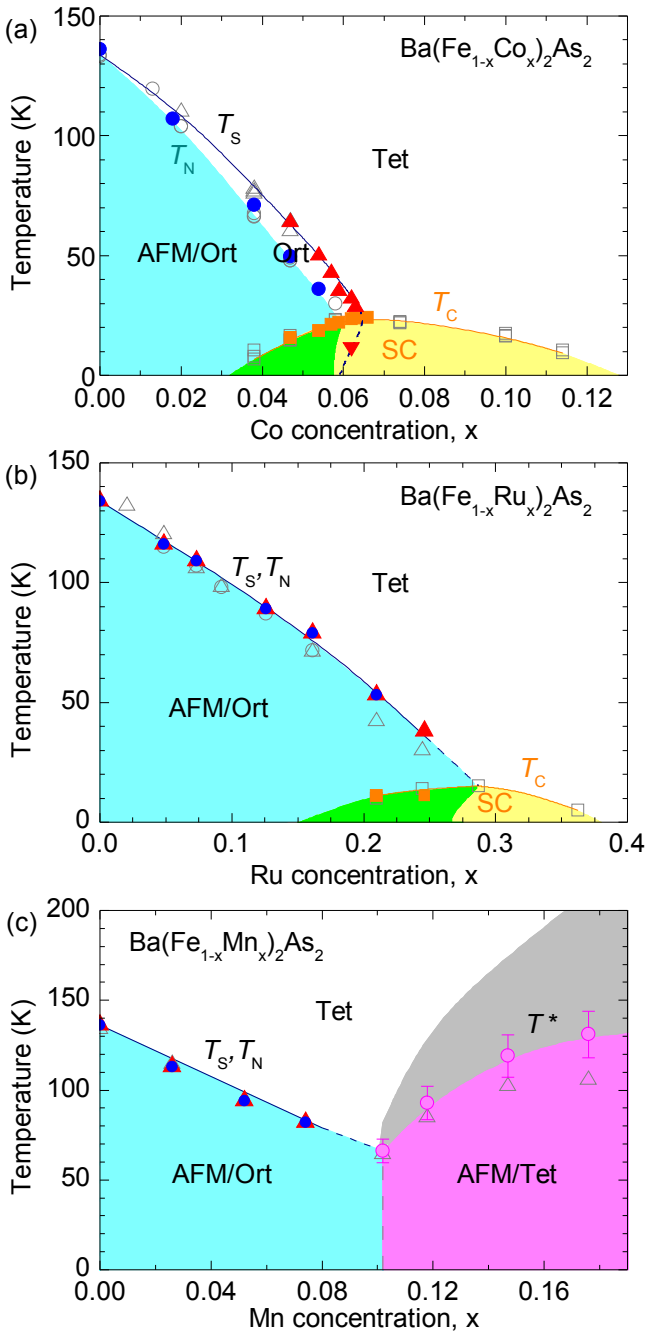

Figure 4.20 Compositional phase diagrams for (a) $Ba(Fe_{1-x}Co_x)_2As_2$ from Nandi *et al.* [185], (b) $Ba(Fe_{1-x}Ru_x)_2As_2$ from the present work and Thaler *et al.* [102], and (c) $Ba(Fe_{1-x}Mn_x)_2As_2$. The gray open triangles and open circles denote data taken from resistance and magnetization data respectively. The gray open squares denote bulk measurements of T_c. Filled red triangles denote T_S measured by x-ray diffraction, filled blue circles denote T_N measured by neutron diffraction, and the filled orange squares represent values for T_c from the x-ray and neutron data. Filled magenta circles denote T^* determined for the Mn doped sample by neutron measurements.

emerges over a finite compositional range and coexists with AFM order over an even more limited range of Co substitution. The back-bending of the AFM and structural distortion phase lines in the superconducting region identify the reentrance of the paramagnetic and tetragonal phases at low temperature. Figs. 4.20 (a) and (b) display both the similarities and differences between $Ba(Fe_{1-x}Co_x)_2As_2$ and $Ba(Fe_{1-x}Ru_x)_2As_2$. As found for Co substitution, Ru substitution results in the suppression of the AFM and structural transitions and superconductivity emerges over a finite range of Ru concentration. The suppression of both the AFM order and orthorhombic distortion in the superconducting region suggests that reentrance of the paramagnetic tetragonal phase may also be found at some Ru substitution concentration as well. However, for Ru substitution, the AFM and structural transitions remain locked together over an extended compositional range with respect to the phase diagram for Co substitution. In Fig. 4.20 (c), the compositional phase diagram for Mn substitution is re-drawn for a close comparison, which is quite different from what is found for either Co or Ru substitution on the Fe site. To recapitulate, superconductivity is not in evidence at any Mn concentration and, while the AFM and structural transitions remain locked together with increasing Mn concentration, as found for $Ba(Fe_{1-x}Ru_x)_2As_2$, the structural distortion abruptly disappears for Mn substitution in excess of $x > 0.102$ although the AFM Bragg peak characteristic of "stripelike" ordering persists. I have proposed that the scattering at $\vec{Q}_{\rm AFM} = (\frac{1}{2}, \frac{1}{2}, L{=}\text{odd})_{\rm T}$ positions may also be explained by the presence of a two-$\vec{Q}$ magnetic structure that is again consistent with tetragonal symmetry.

For electron doping on the Fe site, a rigid band picture appears to be applicable, at least to first order, in explaining the phenomenology of magnetism, structure and superconductivity (Section 2.3.2). Substitution with Mn, however, clearly introduces strong perturbations on both the electronic and chemical structure, likely as a consequence of the more localized nature of the Mn magnetic moment. Substitution with Ru provides a new interesting case study where, nominally, no electrons or holes are added to the system although the first band-structure calculations indicated that Ru substitution introduces additional electron carriers.[86] However, Hall effect and angle-resolved photoemission spectroscopy measurements[294, 295] have shown that the Ru substitution does not induce electron or hole doping, but does strongly modify the

electronic structure by increasing both the number of carriers and their mobility by reducing correlation effects. It is clear that the interactions associated with structural, magnetic and superconducting instabilities in the $AE\mathrm{Fe_2As_2}$ compounds are not simple but finely balanced and can be readily tuned through chemical substitution, evident in my experimental observations.

CHAPTER 5. Commensurate/Incommensurate antiferromagnetic order in transition metal substituted $BaFe_2As_2$ compounds

5.1 Introduction

The parent 122 compounds exhibit a commensurate antiferromagnetic order (see Section 2.3.2). The Fermi surface nesting between electron and hole pockets occurs at the antiferromagnetic propagation vector $\vec{Q}_{\rm AFM}$ and is shown by detailed band structure calculations [300, 301] and angle resolved photo-emission data [290, 302, 303]. The Fermi surface for the parent $BaFe_2As_2$ is shown in Fig. 5.1 [304]. Taking one electron and one hole pocket, I draw sets of schematics to elucidate the Fermi surface nesting assuming two dimensional Fermi surfaces (ignoring the $\vec{c}$ direction) for simplicity in Fig. 5.2 [222]. If the size of electron pocket (blue) and hole pocket (red) are the same, they nest perfectly as shown in Fig. 5.2 (a) and results in a commensurate AFM order with $\vec{Q}_{\rm AFM}$ [222]. When the shapes of electron and hole pockets are different but two pockets have the same size in one of the directions as in Fig. 5.2 (b), it still results in a commensurate AFM order.[222] However, when the sizes of electron and hole pockets are different as in Figs. 5.2 (c) and (d), the nesting becomes imperfect with a commensurate AFM vector $\vec{Q}_{\rm AFM}$ that causes a shift of the Fermi surface for more nesting and results in an incommensurate AFM order with $\vec{\tau} = \vec{Q}_{\rm AFM}+\vec{\varepsilon}$.[222]

In the scattering experiment, the difference between a commensurate antiferromagnetic (C-AFM) order and an incommensurate antiferromagnetic (IC-AFM) order is whether the periodicity in the magnetic structure coincides with the periodicity in the crystallographic structure. Examples of a commensurate AFM order are displayed in Fig. 2.2 (b) and Fig. 5.3 (a). The directions of spins alter on each site but the periodicity (black solid line) matches with the periodicity in the crystallographic structure (red dashed line). One example of an

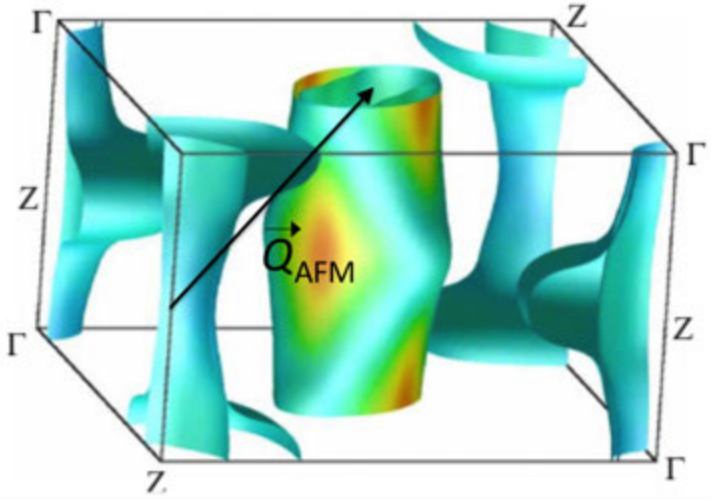

Figure 5.1 Fermi surface of $BaFe_2As_2$ for the LDA internal coordinates, shaded by band velocity. The nesting vector is the same as $\vec{Q}_{\mathrm{AFM}}$. After Ref. [304].

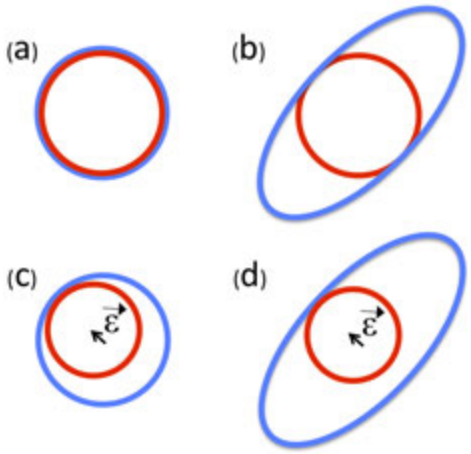

Figure 5.2 Schematic diagrams of Fermi surface nesting. Hole (red) pockets are shifted by $\vec{Q}_{\mathrm{AFM}}$. (a) Perfect nesting between electron (blue) and hole (red) pockets. (b) Imperfect nesting due to different shapes of electron and hole pockets. In one direction (from lower-right to upper-left), both sides of electron and hole pockets are partially nested. (c) Imperfect nesting due to different sizes of electron and hole pockets. The hole pocket is shifted with $\vec{\varepsilon}$ for more nesting. (d) Imperfect nesting due to different sizes and shapes of electron and hole pockets. The hole pocket is shifted with $\vec{\varepsilon}$ for more nesting. After Ref. [222].

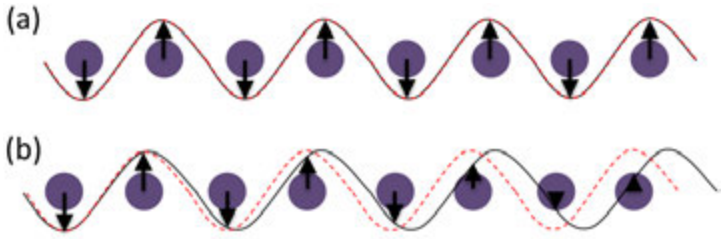

Figure 5.3 (a) Example of a commensurate AFM order. (b) Example of an incommensurate AFM order. The arrows indicate spin directions. The crystallographic (red dashed) and antiferromagnetic (balck solid) periodicities are displayed with sinusoidal lines. Two lines are overlaid in (a) but not in (b).

incommensurate AFM order is that the varying magnitude of the spins (the periodicity) does not match with the periodicity of the crystallographic structure as in Fig. 5.3 (b).

Either C-AFM order or IC-AFM order are predicted by detailed band structure calculations, [305, 306] and several local probe measurements such as ^{75}As nuclear spin resonance [184], ^{57}Fe Mössbauer [307, 308], and muon spin resonance measurements [309] showed that it is probable that it is indeed an IC-AFM structure in $Ba(Fe_{1-x}TM_x)_2$ (TM = Co and Ni) compounds. Therefore, it is interesting to investigate the details of AFM order, C-AFM or IC-AFM, in different transition metal substituted $BaFe_2As_2$ compounds.

This chapter is organized as follows. First I will explain another important experimental detail to investigate C/IC-AFM order in Section 5.2. Secondly, in Section 5.3.1, I will present my XRMS data on 4.7% Co substituted $BaFe_2As_2$ compounds and make clear that the AFM order is commensurate in this compound. Then I will show that IC-AFM occurs in higher Co substituted $BaFe_2As_2$ compounds in Section 5.3.2. Fourth, in Section 5.3.3, I will present the similarities and differences in Ni and Cu substituted $BaFe_2As_2$ compounds compared to Co substituted $BaFe_2As_2$ compounds. Lastly, I will summarize.

5.2 Experimental details

To investigate an incommesurability in transition metal substituted $BaFe_2As_2$ compounds, I utilized both XRMS and neutron diffraction measurements. As I discussed in Chapter 3, XRMS

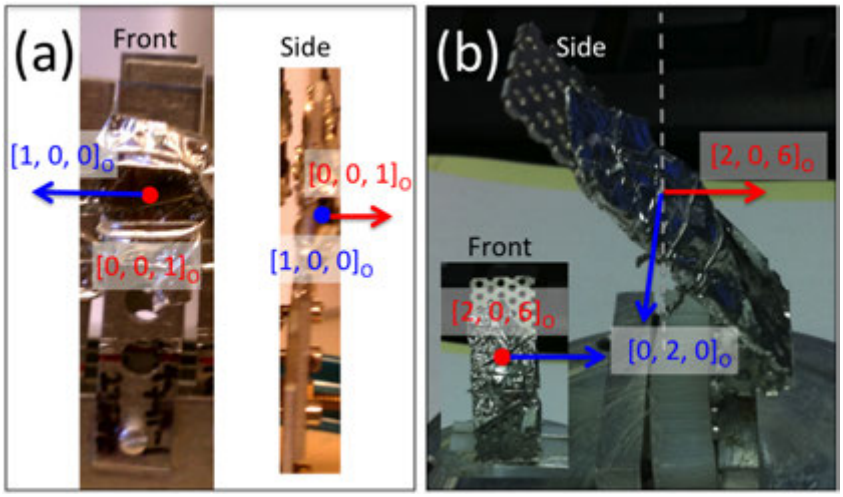

Figure 5.4 (a) Sample mounted in the $(H, 0, 0)_O$-$(0, 0, L)_O$ zone. Representative directions are color-coded. The $[1, 0, 0]_O$ direction (blue) is in the plane of the sample and the $[0, 0, 1]_O$ direction (red) is perpendicular to the surface of the sample. (b) Sample mounted in the $(0, K, 0)_O$-$(H, 0, nH)_O$ zone. Representative directions are color-coded. The gray dashed line indicates a line perpendicular to the ground. The $[0, 2, 0]_O$ direction (blue) is in the plane of the sample and the $[2, 0, 6]_O$ direction (red) is perpendicular to the gray dashed line.

measurements have an intrinsically better resolution than the resolution provided by neutron diffraction measurements. However, as shown in Sections 3.1.2 and 4.1.3, XRMS signal from the Fe K edge is weak. In consequence, only limited substitution levels that give practically measurable signals can be studied with the XRMS measurement. I chose 4.7% Co substituted $BaFe_2As_2$ compound since XRMS signals are anticipated to be measurable and local probe measurements claimed an IC-AFM structure in compounds close to 4.7% Co substitution. Technical details of the XRMS measurement are discussed in Sec. 4.1.1.

For neutron measurements, in addition to the experimental consideration discussed in Chapter 2, the geometry of the sample with respect to the scattering geometry is important in order to study the incommensurate AFM order. Previously, samples were mounted on a sample holder (Al plate) as shown in Fig. 5.4 (a) so that $[0, 0, L]_{T,O}$ directions are perpendicular to the sample surface (red arrow) and $[h, h, 0]_T = [H(=h+h), 0, 0]_O$ directions are in the scattering plane (in horizontal direction, blue arrow). In this sample geometry, the neutron scattering

plane is in the $(H, 0, 0)_O$-$(0, 0, L)_O$ zone [$\equiv (h, h, 0)_T$-$(0, 0, L)_T$ zone] and the measurements have, generally speaking, the best resolution in scans in the scattering plane (the worst resolution in scans out of the scattering plane). Therefore, in this sample geometry it is the best to investigate a potential incommensurability along the $[H, 0, 0]_O$ and $[0, 0, L]_O$ directions (in the scattering plane) but not along the $[0, K, 0]_O$ direction (out of the scattering plane). In order to have the best resolution in the $[0, K, 0]_O$ direction, it is necessary to bring the $[0, K, 0]_O$ direction in the scattering plane. Figure 5.4 (b) displays the sample geometry that brings the $[0, K, 0]_O$ direction in the scattering plane. With respect to the gray dashed line drawn perpendicular to the ground in the figure, the $[H, 0, nH]_O$ (n=odd integer) ($\equiv [h, h, nh]_T$ with n=2×{odd integer}) direction (red arrow) is perpendicular to the gray line and the $[0, K, 0]_O$ ($\equiv [h, -h, 0]_T$) direction in the scattering plane (blue arrow). In this sample geometry, the neutron scattering plane is in the $(0, K, 0)_O$-$(H, 0, nH)_O$ zone [$\equiv (h, -h, 0)_T$-$(h, h, nh)_T$ zone]. It gives the best resolution along the $[0, K, 0]_O$ and $[H, 0, nH]_O$ directions (in the scattering plane) which is suitable to investigate an IC-AFM along the $[0, K, 0]_O$ direction.

5.3 Commensurate to Incommensurate transition

5.3.1 Commensurate AFM order: XRMS on $Ba(Fe_{0.953}Co_{0.047})_2As_2$ compound

Local probe studies such as muon spin relaxation (μSR) and ^{75}As nuclear magnetic resonance (NMR) measurements have proposed that the magnetic order is, in fact, incommensurate. NMR measurements [184, 308, 310] by some groups on underdoped $Ba(Fe_{1-x}Co_x)_2As_2$ (x = 0.02, 0.04)[310] and (x = 0.06)[184] found a strong broadening of the ^{75}As lines attributable to the appearance of a distribution of internal fields at low temperatures in the magnetically ordered state. A strong anisotropy was also observed, with the broadening more pronounced for $\mathbf{H} \parallel \vec{c}$ than for $\mathbf{H} \parallel \vec{a}\vec{b}$.[184] A quantitative comparison of the line broadening for the two field directions led to the conclusion that there is a small incommensurability in the magnetic structure such that the commensurate wave vector $(\frac{1}{2}, \frac{1}{2}, l)_T$ (with l odd) in the undoped parent compound is given by $(\frac{1}{2} - \varepsilon, \frac{1}{2} - \varepsilon, l)_T$, with ε estimated to be approximately 0.04 reciprocal lattice units (rlu), in the lightly Co-doped compounds.[184]

In contrast to the observations of local probe measurements, neutron diffraction measurements display a sharp commensurate peak in 4.7% Co substituted $BaFe_2As_2$ compounds which FWHM was limited by the resolution given by the instrument.[182, 186] To resolve the discrepancy between local probe and neutron measurements, I performed high-resolution x-ray resonant magnetic scattering measurements at the Fe K edge for the 4.7% Co doped $Ba(Fe_{0.953}Co_{0.047})_2As_2$ compound. I find that the magnetic Bragg peaks are commensurate and scans along the [h, h, 0] and [h, -h, 0] directions allow me to place limits on the magnitude of a potential incommensurability that are much smaller than any value proposed previously.

Figure 5.5 shows scans along the $[h, h, 0]_T$ and transverse $[h, -h, 0]_T$ directions through the $(\frac{1}{2}, \frac{1}{2}, 7)_T$ magnetic Bragg peak position. For the $[h, h, 0]_T$ scan, the position of this peak is referenced to the $(1, 1, 8)_T$ charge peak and is displaced from $h=\frac{1}{2}$ because of the orthorhombic distortion. Along the $[h, h, 0]_T$ direction [Figs. 5.5 (a) and (c)] below T_N=47 K, I observe a single peak, whereas an incommensurability of magnitude ε would result in two peaks split by 2ε. The solid bar beneath the data in Figs. 5.5 (a) and (c) describes the measured FWHM of the $(1, 1, 8)_T$ charge peak and represents the experimental resolution along $[h, h, 0]_T$. Therefore, the FWHM of 0.0007(1) rlu for the $(\frac{1}{2}, \frac{1}{2}, 7)_T$ magnetic Bragg peak along this direction places an upper limit on the potential incommensurability ($\varepsilon \approx 3.5 \times 10^{-4}$) which is two orders of magnitude smaller than the value proposed in Ref. [184]. I have also checked along the transverse $[h, -h, 0]_T$ direction for any evidence of incommensurability as shown in Figs. 5.5 (b) and (d). However, for the present experimental configuration, the resolution along this direction is coarser [0.0067(15) rlu]. Nevertheless, these data still allow me to place an upper limit on the incommensurability ($\varepsilon \approx 3.3 \times 10^{-3}$) that is more than an order of magnitude smaller than that proposed.[184] Furthermore, a comparison of the scans at 20 and 4.5 K shows that there is no evidence of additional line broadening for this compound below the superconducting transition (T_c=17 K).

The dashed bars in Figs 5.5 (a) and (c) represent the experimental resolution for the previous neutron diffraction measurements by Pratt *et al.* [182] on the $Ba(Fe_{0.953}Co_{0.047})_2As_2$ compound along the $[h, h, 0]_T$ direction. Even with the poorer resolution of this measurement, an incommensurability of $\varepsilon \approx 0.04$ rlu would have been clearly observed in scans performed

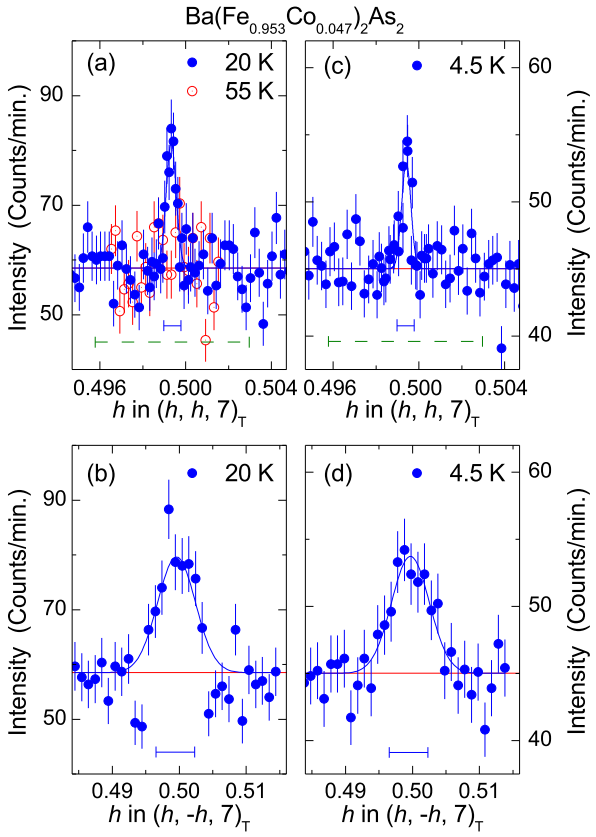

Figure 5.5 (a) $[h,\ h,\ 0]_{\mathrm{T}}$ scan through the magnetic Bragg peak position of the stripelike AFM phase at above (55 K) and below (20 K) T_{N} for the $Ba(Fe_{0.953}Co_{0.047})_2As_2$ compound. The solid bar represents the experimental resolution for the x-ray measurements along this direction while the dashed bar denotes the resolution of the previous neutron measurements along this direction.(Pratt et al.) (b) $[h,\ -h,\ 0]_{\mathrm{T}}$ scan through the magnetic Bragg peak position below T_{N}. The solid bar represents the experimental resolution along this direction of the x-ray measurement. The resolution width for neutron measurements along the $[h,\ -h,\ 0]_{\mathrm{T}}$ is a factor of ten larger. (c) and (d) correspond to (a) and (b), respectively, at the base temperature of 4.5 K. The difference in the vertical scale between panels (a), (b) and (c), (d) arises from small differences in the beam conditions for measurements performed several months apart.

along the $[h,\ h,\ 0]_{\mathrm{T}}$ direction. The XRMS measurements, however, now place a strong limit on the magnitude of any incommensurability for the $Ba(Fe_{0.953}Co_{0.047})_2As_2$ compound. In this light, the broadened line shapes observed in local measurements [184, 308, 310] must arise from other causes. Density-functional-theory (DFT) calculations by Kemper *et al.* [311] indicate that although the nonmagnetic scattering potential associated with Co doping in the FeAs planes is relatively well localized, the magnetic potential significantly perturbs the spin-density-wave state over much longer length scales. This, in turn, leads to a large distribution of hyperfine fields, as pointed out by Dioguardi *et al.* [312] who suggest that the origin of the broadening in their NMR studies of Co and Ni doped $BaFe_2As_2$ is consistent with doping induced disorder in the AFM state rather than incommensurate order.

5.3.2 Incommensurate AFM order in $Ba(Fe_{1-x}TM_x)_2As_2$ compounds (TM=Co)

Knowing that the AFM ordering in the $Ba(Fe_{0.953}Co_{0.047})_2As_2$ compound is commensurate, D. Pratt and I measured a series of $Ba(Fe_{1-x}Co_x)_2As_2$ compounds with $x \geq 0.054$ using neutron diffraction measurements in the sample geometry shown in Fig. 5.4 (b). (From now on, I exclusively use the orthorhombic notation and I drop the subscript "O" noting the orthorhombic notation.) We found that IC magnetic order does indeed develop near optimally doped compositions of $Ba(Fe_{1-x}Co_x)_2As_2$ with $x \geq 0.056$, just before long-range magnetic ordering is completely suppressed at $x \approx 0.06$. The IC propagation vector $\vec{\tau} = \vec{Q}_{\mathrm{AFM}}+(0,\ \varepsilon,\ 0)$ with $\vec{Q}_{\mathrm{AFM}} = (1, 0, 1)$ corresponds to a transverse splitting ($\varepsilon \approx 0.02 - 0.03$) whose value depends on composition.

Fig. 5.6 (b) shows a typical transverse $[0,\ K,\ 0]$ neutron diffraction scan for the $x = 0.059$ sample at $T \approx T_{\mathrm{c}} < T_{\mathrm{N}}$ where magnetic Bragg intensity is at maximum. We observed that a pair of Bragg peaks appear symmetrically at positions $(0,\ \pm\varepsilon,\ 0)$ around $\vec{Q}_{\mathrm{AFM}}$ in the transverse scan. Therefore, a clear IC magnetic order with propagation vector $\vec{\tau} = (1,\ \varepsilon,\ 1) = \vec{Q}_{\mathrm{AFM}}+(0,\ \varepsilon,\ 0)$, as illustrated in Fig. 5.6 (a), exists in this compound ($x = 0.059$). No splitting is observed in the longitudinal $[H,\ 0,\ 0]$ neutron diffraction scan as shown in Fig. 5.6 (c).

Turning to the compositional and temperature dependences of the incommensurability, Figure 5.7 shows the transverse $[0,\ K,\ 0]$ scans through $(1,\ 0,\ 3)$ for the $Ba(Fe_{1-x}Co_x)_2As_2$

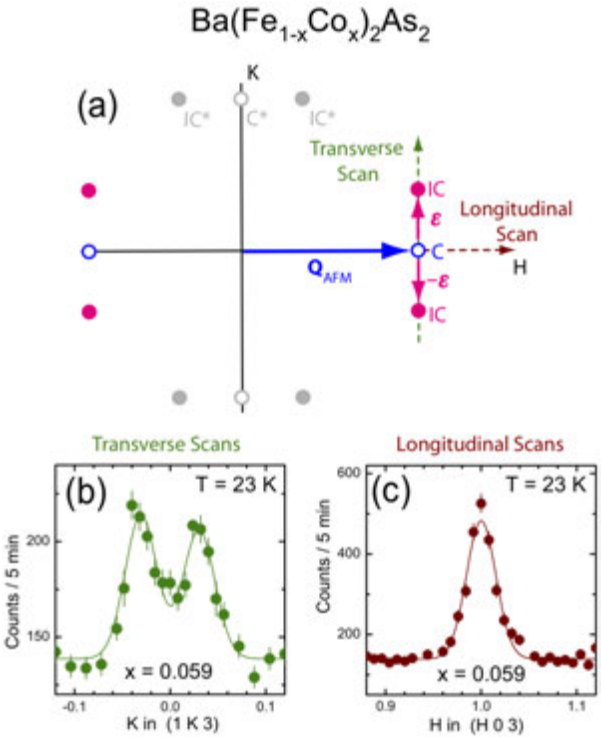

Figure 5.6 (a) Reciprocal space plane with L = *odd* indicating commensurate (C, empty circles) and incommensurate (IC, filled circles) magnetic Bragg peak positions at $\vec{Q}_{\mathrm{AFM}}$ = (1, 0, L = *odd*) and $\vec{\tau}$ = (1, ε, L = *odd*), respectively, in orthorhombic notation. The size of the incommensurability parameter is exaggerated for clarity. Shaded points labeled C* and IC* show the location of magnetic Bragg peaks that are present due to orthorhombic twinning. Dashed arrows illustrate the direction of longitudinal [H, 0, 0] and transverse [0, K, 0] neutron diffraction scans. Raw (b) transverse and (c) longitudinal scans for $Ba(Fe_{0.941}Co_{0.059})_2As_2$ at T = 23 K $\approx$ T_c. The lines are Gaussian fits to the data.

compounds. The background was estimated from scans performed at temperatures above T_S. We observed only a single resolution-limited peak for the $x = 0.054$ sample in the transverse [0, K, 0] scans and, combined with x-ray resonant magnetic diffraction results (see Sec. 5.3.1), establish "stripe" C-AFM order at $\vec{Q}_{\mathrm{AFM}}$ for all Co compositions below approximately 0.054. Broad peaks split in the transverse direction are observed in [0, K, 0] scans for $x = 0.056$, 0.057, and 0.059, clearly establishing the transition to an IC magnetic phase with propagation vector $\vec{\tau}$. For the $x = 0.056$ sample, both C and IC peaks are observed, suggesting that the transition is first-order in its dependence on Co concentration with the phase boundary

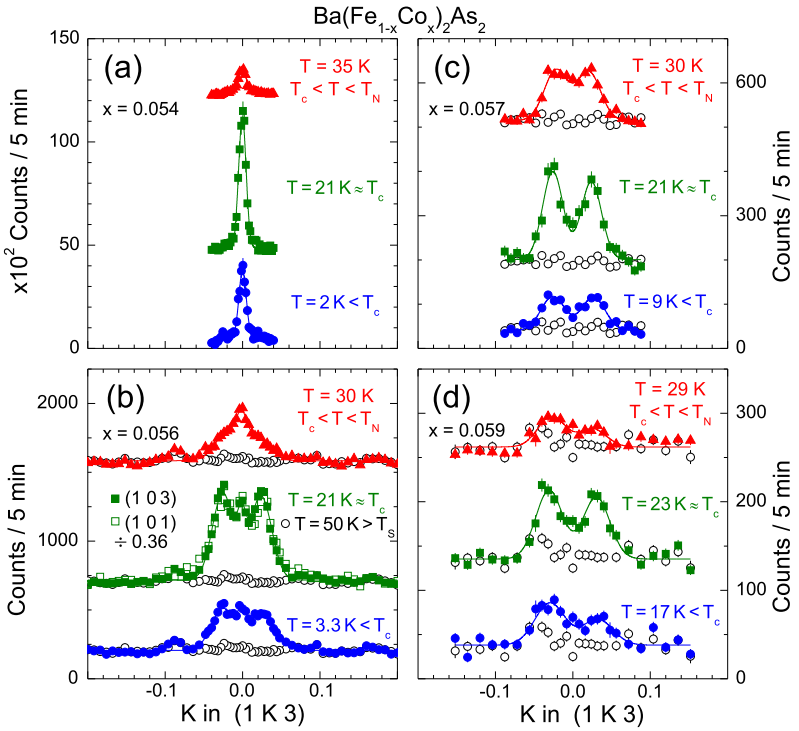

Figure 5.7 Transverse neutron diffraction scans at temperatures $T < T_c$ (blue circles), $T \approx T_c$ (green squares), $T_c < T < T_N$ (red triangles), and $T > T_S$ (empty circles) for $Ba(Fe_{1-x}Co_x)_2As_2$ with x = (a) 0.054, (b) 0.056, (c) 0.057, and (d) 0.059. Scans with $T > T_S$ are an estimate of the background. All scans are performed through the (1, 0, 3) position except the empty green squares in (b), which are measured through (1, 0, 1) and with the intensity divided by a factor of 0.36. The lines are Gaussian fits to the data.

close to $x = 0.056$. The coexistence of C and IC phases could arise from a small spread in the Co concentration across the sample. However, the sharpness of the superconducting transition, predictable evolution of T_S and T_N with relatively small changes in composition, and uniformity of the actual concentration at multiple locations on the crystals confirm good chemical homogeneity with compositional spread $\frac{\Delta x}{x} < 5\%$.[274] Figure 5.7 (b) shows that the lineshapes at (1, 0, 3) and (1, 0, 1) positions are equivalent with an integrated intensity ratio of 0.36(9), close to that expected for collinear C-AFM order with the magnetic moment pointing along the $\vec{a}$ axis. No signatures of higher harmonics have been observed, indicating a sinusoidal modulation of the moment size along the $\vec{b}$ direction. For $x = 0.054$ [Fig. 5.7 (a)],

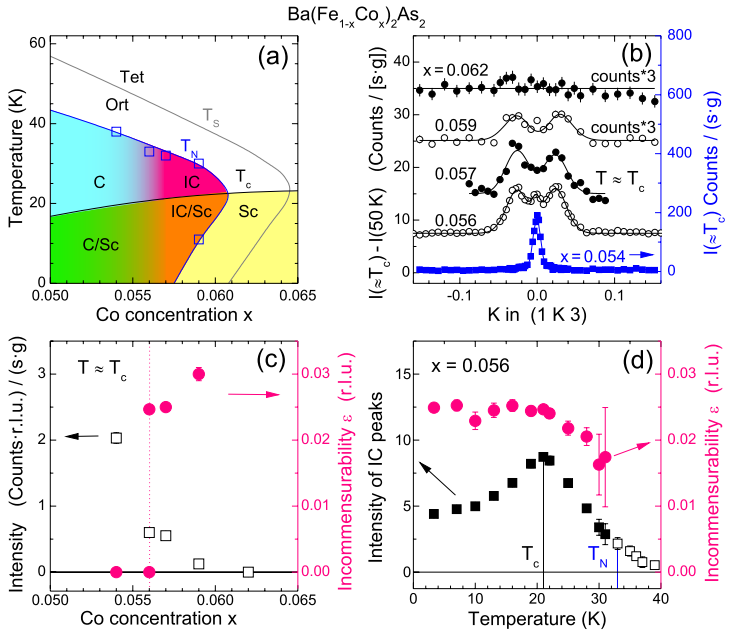

Figure 5.8 (a) Experimental phase diagram for $Ba(Fe_{1-x}Co_x)_2As_2$ showing commensurate (C) and incommensurate (IC) antiferromagnetic order below T_N. Tetragonal (Tet) and orthorhombic (Ort) phases are separated by the phase line at T_S. Superconductivity (SC) appears below T_c and can coexist with both commensurate (C/SC) and incommensurate (IC/SC) magnetic order. Open squares represent the magnetic phase transition temperatures determined in this study. (b) Background subtracted transverse neutron diffraction scans at $T \approx T_c$. Scans are offset vertically and scaled (where noted) for clarity. Integrated intensity (squares) and incommensurability parameter ε (circles) (c) as a function of Co concentration at $T \approx T_c$ and (d) as a function of temperature for $x = 0.056$. Open squares in (d) represent the total magnetic intensity where C and IC peaks cannot be separated.

the suppression of the integrated intensity (magnetic order parameter) below T_c was observed and indicates the competition of C-AFM with superconductivity, as reported previously.[182, 183, 186] The magnetic intensity in Figs. 5.7 (b) - (d) show a similar suppression below T_c implying that the IC-AFM state also competes with superconductivity.

Figure 5.8 (a) shows the experimental phase diagram of $Ba(Fe_{1-x}Co_x)_2As_2$ delineating regions of magnetic order, superconductivity, and structural phases as based on the phase diagram (Fig. 4.20) shown in Section 4.5. This work, summarized in Figs. 5.8 (a) - (d), has allowed us to outline regions of C and IC magnetic order in the phase diagram. Fig. 5.8 (b) shows the evolution from C (at $x = 0.054$) to IC-AFM order (from $x = 0.056 - 0.059$) in

transverse scans performed at $T \approx T_c$. The $x = 0.062$ sample has no detectable magnetic order. The composition dependence of both the integrated magnetic intensity and incommensurability is plotted in Fig. 5.8 (c) at $T \approx T_c$, again highlighting that the transition to IC magnetic order occurs at $x \approx 0.056$ in the limit where the magnetic intensity (moment size) is very small. The incommensurability grows slightly at higher compositions, reaching a value of 0.030(2) at $x = 0.059$. Figure 5.8 (d) displays the temperature dependence of the integrated intensity of IC-AFM Bragg peaks for the $x = 0.056$ sample, which has the characteristic suppression in the superconducting state, as alluded to above. Figure 5.8 (d) shows the incommensurability parameter, ε, of the $x = 0.056$ sample remains relatively constant below T_c.

The magnetic phase diagram shown in Fig. 5.8 (a) contains a first-order C-to-IC transition with electron doping in $Ba(Fe_{1-x}Co_x)_2As_2$ that bears a strong similarity to the alloys of the canonical spin-density-wave (SDW) system, Cr. Pure Cr orders into an IC-SDW state that is driven by nesting between electron and hole Fermi surfaces whose areas are slightly mismatched.[313] Electron doping of Cr (in this case by alloying with Mn [314] or Ru [315]) equalizes the Fermi surface areas and results in a first-order transition to C-SDW order. This simple picture considers only the Fermi surface topology and the free energy of competing C and IC-SDW states and has led to a detailed theoretical understanding of the magnetic phase diagram of Cr alloys.[316]

The development of C-SDW or IC-SDW order has also been studied in the iron arsenides using an effective two-dimensional, two-band Ginzburg-Landau approach.[222, 300] In a spirit similar to Cr, IC-SDW order is favored when nesting occurs between electron and hole pockets having circular cross-sections of unequal area at the Fermi level. The introduction of more realistic elliptical electron pockets favor C-SDW order as long as the electron and hole pocket areas are not too strongly mismatched, as is the case for the parent $BaFe_2As_2$ compounds. However, even with elliptical electron pockets, doping detunes the two pockets and eventually results in a mismatch that favors IC-SDW order. This analysis suggests that Fermi surface nesting is a crucial factor in stabilizing both C and IC phases in the magnetic phase diagram of the $BaFe_2As_2$ compounds.

Unlike Cr, the doped iron arsenides are superconductors, and both C and IC-SDW order

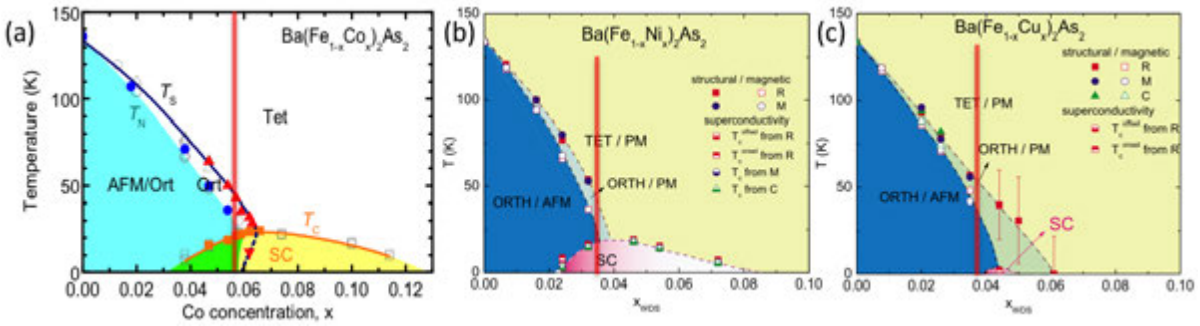

Figure 5.9 Phase diagrams of $Ba(Fe_{1-x}TM_x)_2As_2$ for (a) TM = Co,[63, 182, 185, 186] (b) Ni,[317] and (c) Cu.[317] For Co substitution, the phase diagram was completed with x-ray/neutron data together with bulk data. For Ni and Cu substitutions, bulk measurement data were used for the data points on the phase diagram. The red vertical lines indicate the substitution level that were compared in this dissertation.

are observed to coexist with superconductivity. Ginzburg-Landau models [222, 300] indicate that the competition and coexistence of superconductivity with either C or IC-SDW order is much more likely with an unconventional $s^{\pm}$ pairing symmetry. Thus, a simple two-band approach appears to capture many of the essential features of the phase diagram of the $BaFe_2As_2$ arsenides in terms of Fermi surface nesting, C and IC-SDW order, and unconventional $s^{\pm}$ superconductivity. The resulting theoretical phase diagram in Ref. [222] bears close resemblance to the experimental diagram in Fig. 5.8 (a).

5.3.3 Incommensurate AFM order in $Ba(Fe_{1-x}TM_x)_2As_2$ compounds (TM=Ni, Cu)

I now discuss the incommensurability for other transition metal substitutions, Ni and Cu. Motivated by similarities in the phase diagrams of Co substituted and Ni substituted $BaFe_2As_2$ compounds and differences in Co (Ni) substituted and Cu substituted compounds, it is interesting to investigate the incommensurability in $Ba(Fe_{1-x}Ni_x)_2As_2$ and $Ba(Fe_{1-x}Cu_x)_2As_2$ compounds. The phase diagrams of $Ba(Fe_{1-x}TM_x)_2As_2$ compounds are established by others and shown in Figure 5.9: (a) for TM = Co, (b) for Ni, and (c) for Cu.[63, 182, 185, 186, 317] The

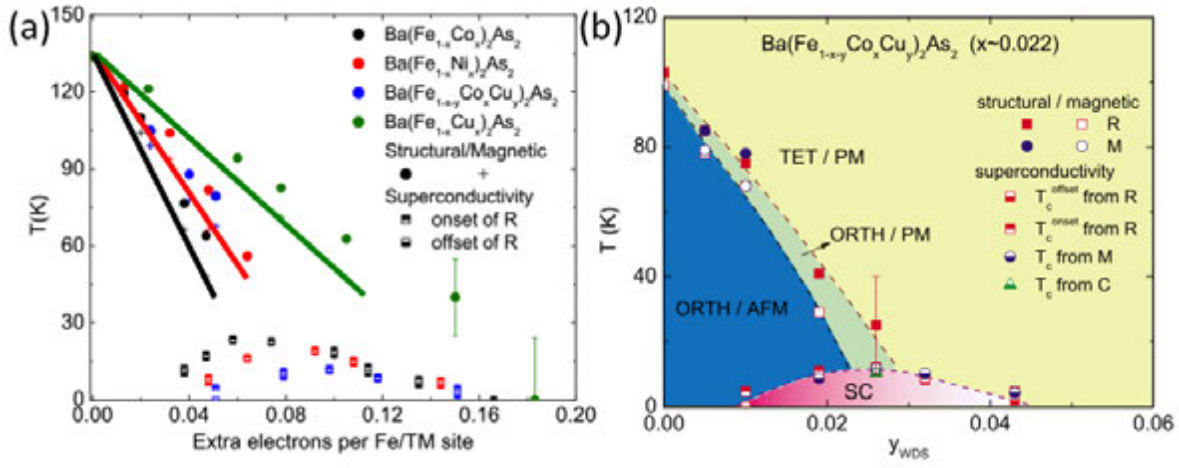

Figure 5.10 (a) Phase diagrams as a function of extra electrons per Fe/TM site. Black, red, and green lines indicate the antiferromagnetic transition temperature for Co, Ni, and Cu substitutions, respectively. Black, red, and green symbols are data points for Co, Ni, and Cu substitutions obtained from bulk measurement, respectively.[89] Note that the AFM transition temperatures and superconducting domes for Co and Ni substitution are nearly on top of each other whereas Cu substitution does not match with Co and Ni substitution. (b) Phase diagram of $Ba(Fe_{0.978-y}Co_{0.022}Cu_y)_2As_2$ compounds.[317] With y=0 in $Ba(Fe_{0.978}Co_{0.022})_2As_2$ compound is non-superconducting. As Cu concentration y increases, superconductivity is first promoted and then suppressed.

two phase transitions are suppressed and split as the substitution levels increase. Superconductivity emerges in a dome-like region for Co and Ni substitutions whereas Cu substitution does not support superconductivity[89, 291] except, perhaps, below 2 K over a very narrow range in composition.[317] However, for Co/Cu co-substitutions in $BaFe_2As_2$, Ni *et al.* reported that at a fixed non-superconducting Co concentration, the addition of Cu first *promotes* and then *suppresses* T_c as shown in Figure 5.10 (b).[317] Canfield *et al.* [89] and Fernandes *et al.* [318] have suggested that previously neglected impurity effects play an important role in this behavior. Canfield *et al.* [89] showed the phase diagrams of Co and Ni substitutions as a function of extra electrons per Fe/TM site [Fig. 5.10 (a)], the phase transition temperatures and superconducting dome of Co and Ni substitutions match quite well , but the Cu substitution does not. Therefore, a simple rigid-band picture for at least TM = Co and Ni substitutions

seems to adequately account for the evolution of phase transition and superconducting transition temperatures as well as angle-resolved photoemission spectroscopy (ARPES) (by Liu *et al.*[192]), Hall effect, and thermoelectric power measurements (by Mun *et al.*[92]) with concentration. The rigid-band model has also been used successfully to model the suppression of the AFM transition temperature and ordered moment in $Ba(Fe_{1-x}Co_x)_2As_2$ for "underdoped" samples, shown by Fernandes *et al.*[186] Nevertheless, this approach now faces strong challenges from recent theoretical and experimental studies (by Wadati *et al.*[319], Bittar *et al.*[320], and Levy *et al.*[321]). Further comparative studies of Co, Ni and Cu substitutions are needed and may provide clues regarding both the nature of unconventional superconductivity in the iron pnictides and clarify the effects of TM substitutions.

I performed single crystal neutron diffraction measurements of the magnetic ordering in $Ba(Fe_{1-x}TM_x)_2As_2$ with TM either Ni or Cu. Observations of incommensurate spin-density-wave order, in particular, are a very sensitive probe of the nature of Fermi-surface nesting in the iron pnictides and, therefore, may be used to study impurity effects as a function of the TM doping. I find that, like the Co-substituted compound in Sec 5.3.2, Ni substitution also manifests incommensurate (IC) AFM order over a narrow range of x. However, the AFM ordering for Cu substitution remains commensurate (C) up to $x \approx 0.044$, where AFM order is absent.

Neutron diffraction measurements were done on the TRIAX triple-axis spectrometer at the University of Missouri Research Reactor employing an incident neutron energy of 14.7 meV with 2 pyrolytic graphite filters and 60'-40'-40'-80' collimation. Samples were studied in the vicinity of $\vec{Q}_{\rm AFM} = (1, 0, 3)$ in the $(\zeta, K, 3\zeta)$ plane which is similar to what is shown in Fig. 5.4, allowing a search for incommensurability along the $\vec{b}$ axis (transverse $[0, K, 0]$ direction) as found for $Ba(Fe_{1-x}Co_x)_2As_2$.

Figures 5.11 (a) and (b) show the low-T scattering for transverse $[0, K, 0]$ scans through the (1, 0, 3) magnetic Bragg point for several Ni and Cu compositions. For $Ba(Fe_{1-x}Ni_x)_2As_2$, a transition from a C-AFM order for $x < 0.035$ (with resolution limited magnetic Bragg peaks) to an IC-AFM order for $x \geq 0.035$ is clearly demonstrated by the symmetric pair of peaks at $(1, \pm\varepsilon, 3)$. For $x > 0.037$, no long-range AFM order was observed. These data show that, as

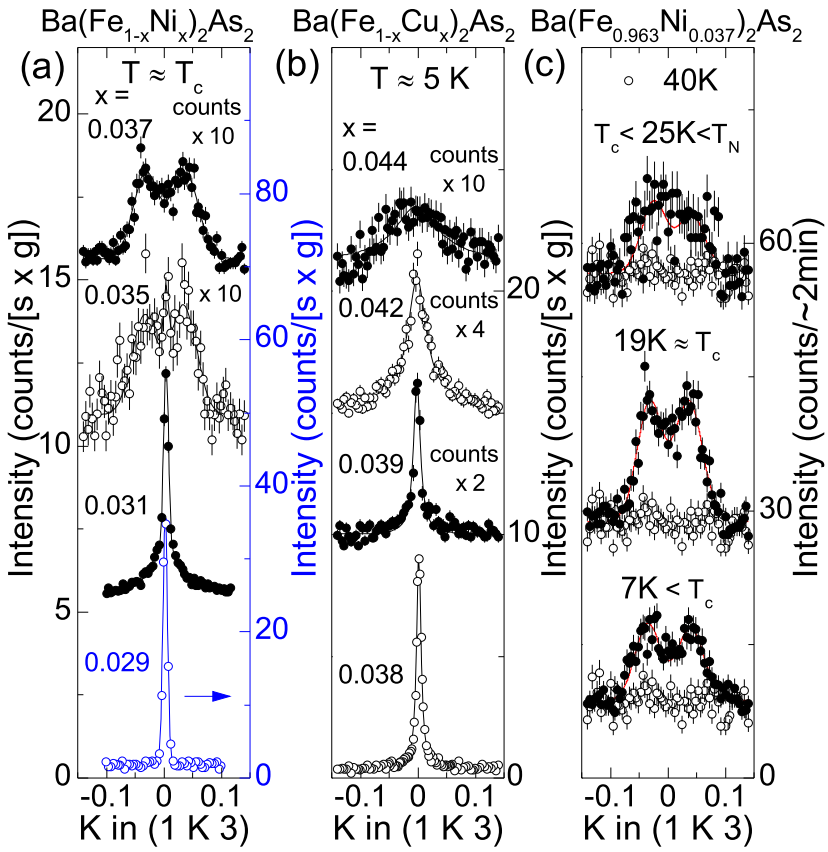

Figure 5.11 Scattering near the (1, 0, 3) magnetic Bragg point for $Ba(Fe_{1-x}M_x)_2As_2$ where M is (a) Ni and (b) Cu. (c) Temperature dependence of the scattering near the (1, 0, 3) magnetic Bragg point for $Ba(Fe_{0.963}Ni_{0.037})_2As_2$. Intensities are normalized by mass of the samples to facilitate comparisons. Lines are fits to the data, as described in the text.

previously observed for Co substitution, Ni substitution results in an abrupt change from C to IC-AFM order at $x_c = 0.035 \pm 0.002$. The ratio (≈ 0.6) of this critical concentration to $x_c = 0.056$ for Co in Sec. 5.3.2, seems consistent with a rigid-band filling where Ni "donates" roughly twice the number of electrons as Co. As discussed previously for Co substitutions (see Sec. 5.3.2), the abrupt transition between C and IC magnetic structures is similar to what has been observed for dilute substitutions of Mn or Ru in the canonical SDW system, Cr.[322] Detailed theoretical studies of the nesting and free energy of the competing C-SDW and IC-SDW states in $BaFe_2As_2$ may shed further light on this behavior.

The lines in Fig. 5.11 (a) are fits to the data using a single Gaussian for $x = 0.029$, a convoluted Gaussian + Lorentzian line shape for $x = 0.031$, three Gaussians for $x = 0.035$ (to

account for the presence of the dominant IC and residual C components), and two Gaussians for $x = 0.037$. The detailed description of the IC structure based on these fits is very similar for Co and Ni substitution. The incommensurability, ε, derived from fits to these data was 0.033 ± 0.003 reciprocal lattice units (r.l.u.), close to the value found of ε for Co samples. Also, there is a significant broadening of the IC magnetic diffraction peaks as compared to the C magnetic peaks indicating a much reduced magnetic correlation length ($\xi \sim 60$ Å), again consistent with the broadening found for the Co substituted samples (Sec. 5.3.2). The peak widths obtained from these fits are given in Fig. 5.12 (a) and show that the C component remains resolution limited, whereas the IC peaks are more than 5 times broader. Recent measurements on Ni substituted samples by Luo *et al.*[323] are consistent with my results. The temperature dependence of the transverse [0, K, 0] scans through the magnetic Bragg peaks for superconducting $Ba(Fe_{0.963}Ni_{0.037})_2As_2$ is illustrated in Fig. 5.11(c). The integrated intensity of the magnetic scattering increases below T_N, reaches a maximum at the superconducting transition temperature (T_c), and decreases monotonically below T_c as observed previously for Co substituted samples,[182, 183, 186] demonstrating, again, that magnetic order competes with superconductivity. The positions and widths of the IC magnetic peaks appear to be temperature independent within the resolution of our measurement.

In striking contrast to the data for Co substituted samples (Sec. 5.3.2) and here for Ni substituted, Figure 5.11 (b) shows no evidence of a C-to-IC transition versus x for $Ba(Fe_{1-x}Cu_x)_2As_2$. Instead, the C magnetic Bragg peak is well described by a single Lorentzian lineshape that broadens strongly for $x \geq 0.039$ [see Figs. 5.11(b) and 5.12(a)], and no AFM long-range order is found for $x \geq 0.044$. To further emphasize the differences between Co, Ni and Cu substitutions, Fig. 5.12(b) displays the maximum ordered magnetic moment (at T_c for Co and Ni substitution and at our base temperature, 5 K for Cu substitution) as a function of extra electron count under the often-used assumption that Co, Ni, and Cu donate 1, 2, and 3, respectively, to the d-bands. The maximum ordered moment was estimated from the integrated intensity of the magnetic Bragg peaks using the commensurate magnetic structure factor normalized by the mass of the samples, as described previously.[186] Under the stated assumption, Co and Ni act similarly to suppress the moment over a range of x that mimics a rigid-band

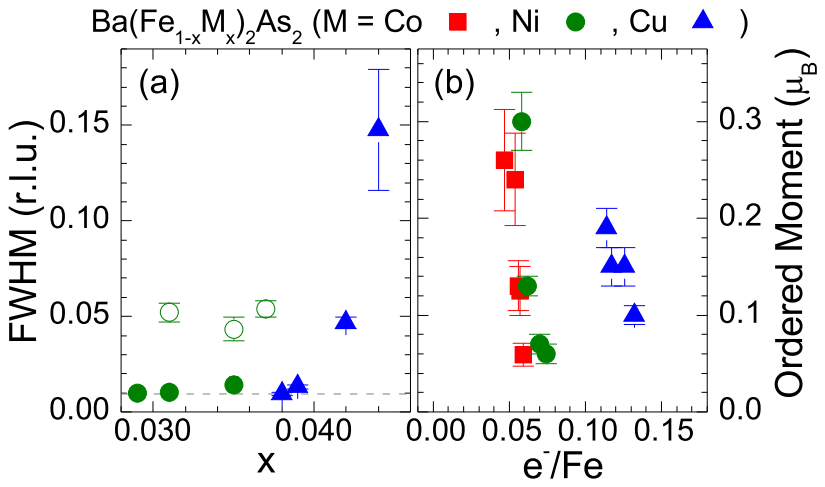

Figure 5.12 Trends in the FWHM and maximum ordered moment for M substitution. (a) Evolution of the FWHM of the magnetic peaks vs. concentration. The solid(open) circles represent the FWHM of the C-AFM(IC-AFM) peaks. (b) Measured ordered moment derived from the integrated intensity of the magnetic Bragg peaks as a function of the extra electron count, assuming that Co donates 1, Ni 2, and Cu 3, extra-electrons to the d-band. The data for $Ba(Fe_{1-x}Co_x)_2As_2$ are taken from Pratt *et al.*[182] and Fernandes *et al.*[186].

picture. This is clearly not the case for Cu substitution (although rescaling the electron count by 1.5 would move the results on top of Co and Ni). Nevertheless, the IC-AFM order found for Ni and Co substitutions in this regime is not found for Cu substitution.

5.4 Discussion and summary

First, in order to show that the observed IC-AFM order in Co and Ni substituted $BaFe_2As_2$ compounds can be understood as a spin density wave (SDW) driven Fermi surface nesting, Lee and Harmon performed *ab initio* density functional calculations of magnetic susceptibility.[322] Previous calculations show maxima in the generalized spin susceptibility away from a commensurate magnetic propagation vector $\vec{Q}_{\mathrm{AFM}}$ in doped $AEFe_2As_2$ compounds and therefore point to a tendency for IC-SDW order.[306, 324] To gain insight into potential incommensurability at doping levels where it was observed in Co substituted $BaFe_2As_2$,[187] Lee and Harmon performed calculations of the generalized bare susceptibility employing the full-potential linearized augmented plane wave (FPLAPW) method,[277] with a local density functional.[278]

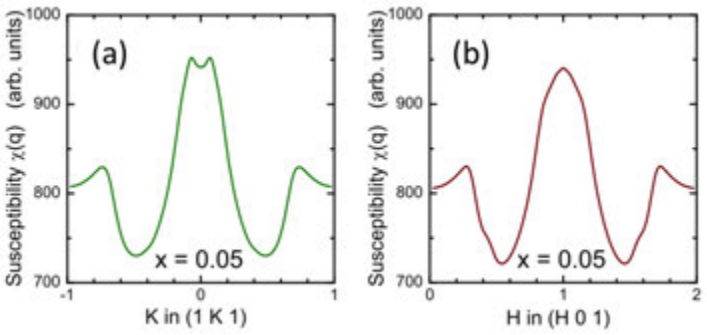

Figure 5.13 *Ab initio* calculations of the generalized susceptibility in the (a) transverse and (b) longitudinal directions through $\mathbf{Q}_{\mathrm{AFM}}$

They used $R_{\mathrm{MT}} \times K_{\mathrm{max}} = 8.0$ and $R_{\mathrm{MT}} = 2.4$, 2.2 and 2.2 for Ba, Fe and As, respectively. To obtain self-consistency we chose 550 $\vec{k}$-points in the irreducible Brillouin zone and used 0.01 mRy/cell as the total energy convergence criteria. The virtual crystal approximation was used to consider Co-doping effects and the whole reciprocal unit cell is divided into $80 \times 80 \times 80$ parallelepipeds, corresponding to 34061 irreducible $\vec{k}$-points. The calculations of the generalized susceptibility for electron doping with $x = 0.05$ show splitting in the transverse direction and a single peak in the longitudinal direction in Figs 5.13 (a) and (b), respectively, consistent with other doping dependent calculations.[306, 324] The *ab initio* calculations, therefore, show a tendency for IC-SDW order with propagation vector $\vec{\tau} \approx \vec{Q}_{\mathrm{AFM}} + (0, \varepsilon, 0)$ in agreement with experimental observations.

Next, in order to elucidate the differences between Co/Ni and Cu doping in $BaFe_2As_2$, Khan, Lee, Alam, Harmon, and Johnson employed two electronic-structure methods: full-potential linear augmented plane waves[277] with supercells and, in the parent compound unit cell, the Korringa-Kohn-Rostoker method using the Coherent-Potential Approximation (KKR-CPA) to address the effects of substitution on the density of states (DOS), and solute disorder (impurity) scattering on the Fermi surfaces (i.e., the Bloch spectral functions $A(\vec{k}; E_{\mathrm{F}})$ at the Fermi energy E_{F}).[325–327]

Figure 5.14 (a) shows that the KKR-CPA *d*-band partial DOS of Co and Ni are common-band-like (e.g. overlap with the Fe *d*-bands), whereas Cu exhibits split-band behavior with its *d*-states located ∼4 eV below E_{F}. Only *s*-*p* states participate at E_{F} and, therefore, Cu behaves

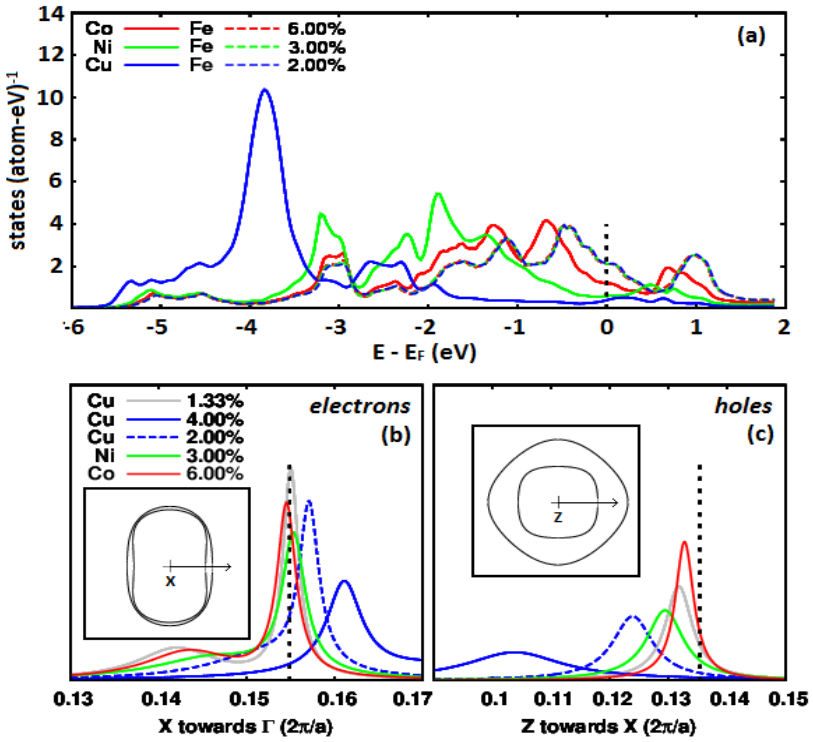

Figure 5.14 For $Ba(Fe_{1-x}TM_x)_2As_2$, the KKR-CPA (a) site-projected DOS versus $E - E_F$ at 6% Co, 3% Ni (fixed e^-/Fe), and 2% Cu (the Fe DOS changes negligibly with TM); and Bloch spectral functions, $A(\vec{k}; E_F)$, along specific $\vec{k}$-directions versus at. % TM for (b) electrons, and (c) holes. Insets: $\vec{k}$-direction of the cut across *electron* (centered at X) and *hole* (centered at Z) states. Peak locations of electron/hole states are compared to the "rigid-band" expectations (vertical dashed lines) from parent compound at fixed e^-/Fe and three at. % Cu values.

almost as a +1 *s-p* valence with very different scattering behavior from Co and Ni. I note that these results are consistent with ordered DFT calculations at large x.[319] Figures 5.14 (b) and (c) illustrate the behavior of the Fermi-surfaces for "*electrons*" and "*holes*" at a fixed solute concentrations for Co (6%) and Ni (3%) [red and green lines] compared to the "rigid-band" expectation [vertical dashed lines] from the parent compound at a fixed e^-/Fe (0.06). These solute concentrations are close to the respective x_c for the observed C to IC magnetic ordering. As the solute concentration increases, the electron(hole) surfaces expand(contract) and the spectral broadening due to chemical disorder scattering is evident. Due to common *d*-band behavior for Co and Ni, spectral peaks for the electrons clearly mimic rigid-band behavior at fixed e^-/Fe, but the holes less so. However, with the split *d*-band behavior for Cu, rigid-band

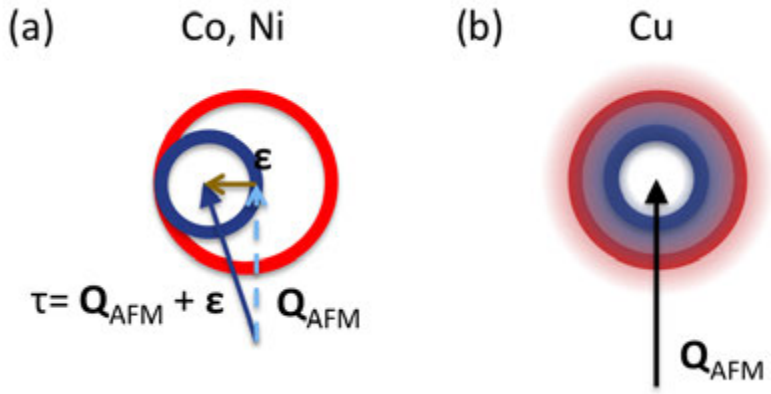

Figure 5.15 (a) Sharply defined Fermi surface topology for electron pocket (blue) and hole pocket (red) with a circular topology. (b) Broadened Fermi surface due to the impurity scattering. Blurring of each pocket indicates broadening. As electrons are introduced, the sizes of hole and electron pockets changes, and mismatching of Fermi surfaces leads IC AFM ordering with $\vec{\tau} = \vec{Q}_{\rm AFM} + \vec{\varepsilon}$ in Co and Ni substitution. With Cu substitution, strong impurity scattering broadens the Fermi surface and leads a sufficient overlapping between electron and hole pockets as in (b).

concepts are invalid. To emphasize this we show results for Cu doping up to the 4% substitution measured in our experiments. As a stronger scatterer than Fe, Co, or Ni, 1.33% Cu (rather than 2% Cu assuming a +3 valence) acts like 6% Co or 3% Ni [see also Fig. 5.12 (b)]. Most importantly, the Cu hole states are especially sensitive to doping, with a rapid loss of intensity and increased disorder broadening evident. This dramatically diminishes the contributions of Fermi-surface nesting (between the electron- and hole-like Fermi surfaces) to the magnetic susceptibility measured at ∼4% Cu substitution.

We propose that the absence of IC AFM order in $Ba(Fe_{1-x}Cu_x)_2As_2$ arises from enhanced impurity scattering effects associated with the stronger potential for Cu. The small incommensurability measured for Co and Ni substituted $BaFe_2As_2$ requires relatively well-defined features in the Fermi surface topology. Figure 5.15 displays a schematic diagram showing how impurity scattering would affect the Fermi-surface nesting [Fig. 5.15 (b)]. Disorder due to impurity scattering introduces spectral broadening in both energy and momentum to the extent that the magnetic structure remains C rather than IC. This is in substantial agreement with recent work by Berlijn *et al.*,[328] who point out that TM substitution in the iron pnictides

leads to the loss of coherence and a smearing of the Fermi surface that is relatively weak for Co substitution, but much stronger for Zn.

Finally, I note that such impurity effects are expected to impact superconductivity in the iron pnictides as well. Essential elements of the under-doped regions of the phase diagram for electron-doped $BaFe_2As_2$ are captured by considering both inter- and intra-band impurity scattering.[318, 329] Although impurity scattering introduced by TM substitution causes pair breaking and suppresses T_c, it can be even more damaging for spin-density-wave ordering so that T_N is suppressed more rapidly, allowing superconductivity to emerge at finite substitution levels. Interestingly, the phenomenological model by Fernandes *et al.*[318] indicates that the behavior of T_c for $s^{\pm}$ pairing is a non-monotonic function of impurity concentration, depending on the strength of the impurity potential and the ratio of the intra-band (Γ_0) to inter-band (Γ_π) impurity scattering, which may vary strongly between Co and Cu. Indeed, they find a range in $\frac{\Gamma_0}{\Gamma_\pi}$ where T_c first increases and then decreases with impurity concentration, very similar to that observed for Co/Cu co-substitutions in $BaFe_2As_2$. It should also be noted that Zn substitution in the 1111 compounds does not induce superconductivity. However, similar to Co/Cr co-substitution, Zn first enhances superconductivity slightly when it was introduced into a superconducting fluorine doped R = La compound then suppresses T_c.[55]

CHAPTER 6. Conclusions and Outlook

6.1 Conclusions

High-resolution x-ray diffraction, x-ray resonant magnetic scattering, and neutron diffraction measurements have been used to study structure, magnetism, and the interplay between them in transition metal (TM) substituted $BaFe_2As_2$ compounds. High-resolution x-ray diffraction measurements are sufficient to observe the small orthorhombic distortion that is generally difficult to be seen in neutron diffraction measurements because of its poorer resolution. X-ray resonant magnetic scattering measurements at the Fe K edge add another example of resonance enhancement at the K edge of $3d$ element (in this case Fe) and definitely show that no incommensurate (IC) magnetic ordering exists in $< 5.4\%$ Co substituted $BaFe_2As_2$ compounds. Neutron diffraction measurements were employed to study the antiferromagnetic order parameter, the commensurate(C)-to-incommensurate(IC) transition seen in $> 5.4\%$ Co substitution, the origin of incommensurability, and its relation to the impurity scattering effect in different transition metal substituted $BaFe_2As_2$ compounds.

The structural and antiferromagnetic transitions are split in the parent $BaFe_2As_2$ compound with structural transition temperature (T_S) higher than the AFM transition temperature (T_N) in contrast to the coupled transitions in the parent $AEFe_2As_2$ (AE = Ca and Sr). I also showed that the structural transition is second-order ($T_S = 134.5$ K) but the AFM transition is first-order with a small but finite temperature hysteresis (~ 0.25 K), which drives a jump in the orthorhombic distortion. Upon substitutions by Co and Rh, which are considered as electron doping, the structural and AFM transition temperatures are suppressed to lower temperature and split further. The AFM transition changes its nature from first-order to second-order with substitutions and the magnetic critical point in Co substituted compounds was found

around 2.2% Co concentration whereas the structural transition is second-order in the whole composition range. This observation is consistent with the view of nematic order: the structural transition is derived by the "stripe" antiferromagnetic ordering and fluctuations. Together with the earlier observation by Nandi *et al*. [185] of superconductivity existing in both orthorhombic and tetragonal structures, the structural transition may purely be a side effect of the "stripe" AFM ordering and fluctuations, and not be prerequisite for superconductivity in the FeAs-based superconductors. In addition, the structural anisotropy (orthorhombicity) seems not important but the underlying anisotropy due to the "stripe" AFM ordering might have a close relation to other anisotropic physical properties, such as anisotropic resistivity, observed in the FeAs-based superconductors.

In contrast to the electron doping, in isoelectronic Ru substituted $BaFe_2As_2$ compounds, the structural and AFM transitions are locked at the same temperature, and superconductivity emerges with higher doping concentrations than Co doping. I showed that Ru substitution also exhibits the coexistence and competition between AFM and superconductivity (SC) based on the observation of suppression of orthorhombic distortion and AFM ordering below the superconducting transition temperature (T_c). On the other hand, similar to electron doping, suppression of the "stripe" AFM ordering induces superconductivity. Together with the already established observations, which show that the suppression of the "stripe" AFM ordering by means of electron doping (Co and Rh) enhances AFM fluctuations in the FeAs-based superconductors, [30] suppression of the "stripe" AFM ordering by means of internal pressure or magnetic dilution in Ru doping also induces superconductivity. This implies that if one can enhance the "stripe" AFM fluctuations or eliminate AFM order by any means, superconductivity can emerge in the FeAs-based superconductors.

In the hole doping case, the Mn substituted $Ba(Fe_{1-x}Mn_x)_2As_2$ compound, which do not show superconductivity at all substitution levels, the T_S and T_N occur at the same temperature up to approximately $x = 0.102$. Above $x \approx 0.11$, the orthorhombic distortion is not observed while the AFM signal from the antiferromagnetic propagation vector $\vec{Q}_{AFM}$ of the "stripe" AFM structure remains. I also showed that the AFM signal persists even at higher temperatures than T_N of $x \leq 0.102$. This observation is surprising because models for "stripelike" AFM order in the

FeAs-based superconductors anticipate the orthorhombic distortion. Therefore, my observation offers a possibly different magnetic structure in $Ba(Fe_{1-x}Mn_x)_2As_2$ compounds for $x \geq 0.11$. I proposed that my observation can be understood in terms of a two-$\vec{Q}$ structure discussed by Eremin and Chubukov.[285] This observation supports the nematic order for the structural transition and provides an additional evidence that the "stripe" AFM ordering or fluctuations are crucial for superconductivity but other magnetic ordering (possible two-$\vec{Q}$ or the G-type structure) or fluctuations (recent observation of spin fluctuations at the G-type AFM gamma point in the presence of "stripe" AFM ordering and fluctuations by Tucker *et al.* [330]) are detrimental to superconductivity.

One of the longstanding issues in the FeAs-based superconductors is the possible occurrence of incommensurate AFM ordering. I showed that the AFM ordering is commensurate for $x = 0.047$ in $Ba(Fe_{1-x}Co_x)_2As_2$ compound, and Pratt *et al.* [187] found that the AFM ordering changes abruptly (first-order) to incommensurate for $x \geq 0.056$. In addition, I observed that Ni substituted $Ba(Fe_{1-x}Ni_x)_2As_2$ compounds also develop first-order C-to-IC transition at a composition $x = 0.035$. The *ab initio* calculation done for Co doped $BaFe_2As_2$ by Lee and Harmon showed that the observed IC-AFM order can be understood as a spin density wave (SDW) driven Fermi surface nesting. Moreover, in terms of extra electrons per Fe/TM site provided by Co and Ni, the critical concentrations for C-to-IC transitions for Co and Ni introduce approximately same amount of extra electrons, which fit within the rigid-band picture. However, Cu substitutions do not develop incommensurate AFM ordering at all concentrations and the ordered moment size, when scaled with extra electrons per Fe/TM site, do not match with Co and Ni. The rigid-band picture fails to explain the difference in Cu substitution. The difference between Co, Ni and Cu can be understood with (1) different character of bands and (2) enhanced impurity scattering. First, due to common d-band behavior for Co and Ni, the band structure calculations by Khan *et al.* show that spectral peaks for the electrons clearly mimic rigid-band behavior at fixed e^-/Fe, but the holes less so. However, with the split d-band behavior for Cu, rigid-band concepts are invalid. Next, disorder due to impurity scattering introduces spectral broadening in both energy and momentum to the extent that the magnetic structure remains C rather than IC. Therefore, enhanced impurity scattering in Cu substitution

than Co and Ni substitutions broadens the Fermi surface topology and leads to C-AFM order because the small incommensurability observed in Co and Ni substitutions requires a relatively well-defined Fermi surface topology. This new experimental observations reveal the crucial role of impurity scattering effect on incommensurate AFM ordering and superconductivity.

In conclusion, I have studied the effect of transition metal substitution on $BaFe_2As_2$ compounds and determined the nature of phase transitions, phase diagrams as well as impurity scattering effect on incommensurate AFM ordering. Although the studies of structural and magnetic properties in transition metal substituted $BaFe_2As_2$ do not explicitly explain "unconventional" superconductivity in the FeAs-based superconductors, these studies reveal (1) the "stripe" antiferromagnetic ordering or fluctuations as a driving force for the structural transition, (2) an indirect evidence of the significance of the "stripe" antiferromagnetic ordering and fluctuations for superconductivity, and (3) the significance of impurity scattering effects on incommensurability and superconductivity. Considering that transition metal substituted $BaFe_2As_2$ compounds exhibits many general features appearing in different families of the FeAs-based superconductors, the experimental observations presented in this dissertation will help to understand physical properties and "unconventional" superconductivity in the entire FeAs-based superconductors.

6.2 Outlook

Over the past few years, a spin excitations (fluctuations) mediated pairing mechanism has been proposed based on inelastic neutron scattering studies together with theories of superconductivity in the FeAs-based superconductors.[30] Large numbers of inelastic neutron scattering experiments have been performed and revealed intriguing spin excitations and the superconducting resonance (the redistribution of magnetic intensity from low energies to high energies below T_c) which are reminiscent of heavy fermion and cuprate superconductors. I have shown the incommensurate AFM order in Co and Ni substituted $BaFe_2As_2$ which is also reminiscent of IC-AFM in the cuprate superconductors. A naturally arising question is: Will the superconducting resonance in spin excitations in the FeAs-based superconductors be similar to the cuprate superconductors? In a spirit of two itinerant and localized pictures, someone can expect

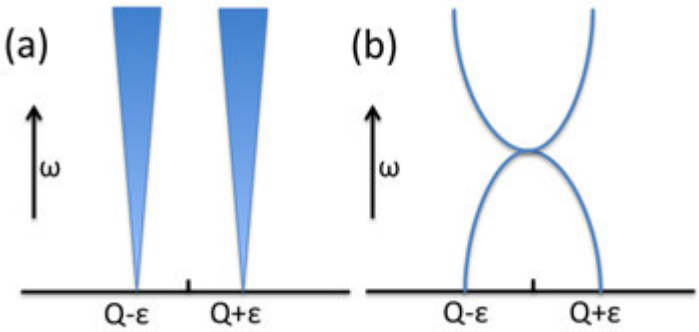

Figure 6.1 Schematic dispersion diagram for a model system (a) Cr metals and (b) cuprate superconductors. For $Ba(Fe_{1-x}TM_x)_2As_2$ (TM = Co, Ni), $\vec{Q} = (1, 0, 1)_O$ and $\vec{\varepsilon} \approx (0, 0.03, 0)_O$.

in these two limits that the dispersion of spin resonance resembles as either a model system (1) Cr metals [Fig. 6.1 (a)] or (2) cuprate superconductors [Fig. 6.1 (b)]. Therefore, it is of great interest to investigate how the dispersion of spin resonance along the orthorhombic $\vec{b}$ direction changes with energy transfer and how the resonance appears in a momentum transfer $\vec{Q}$ scan performed along the orthorhombic $\vec{b}$ direction. Figure 6.2 displays preliminary results on the spin excitations in 3.7% Ni doped $BaFe_2As_2$. The observed spin resonance is dispersive in the FeAs-based superconductors. Further studies of the dispersive spin resonance are necessary and in progress. Another interesting aspect of the dispersive spin resonance observed in 3.7% Ni doped $BaFe_2As_2$ is whether the dispersion is originated from the incommensurate AFM Bragg point, which is the case in the cuprate superconductors. Studies of the low energy (below 2 meV energy transfer) spin excitations in both normal and superconducting state should provide an answer. However, the required high Q resolution to observe the small incommensurability in the spin excitations would make the observation difficult. Alternatively, investigation on the occurrence of a dispersive spin resonance in a compound which exhibit a commensurate AFM order would answer whether the dispersion is originated from the IC-AFM Bragg point.

Moreover, in the cuprate superconductors, IC-AFM order is accompanied by charge ordering [charge density wave (CDW)]. When the IC-AFM order is described by $\vec{Q}_{\rm AFM} = \vec{Q} \pm n\vec{\varepsilon}$ with n = odd integers and incommensurability $\vec{\varepsilon}$, CDW appears at $m\vec{\varepsilon}$ with m = even integers.

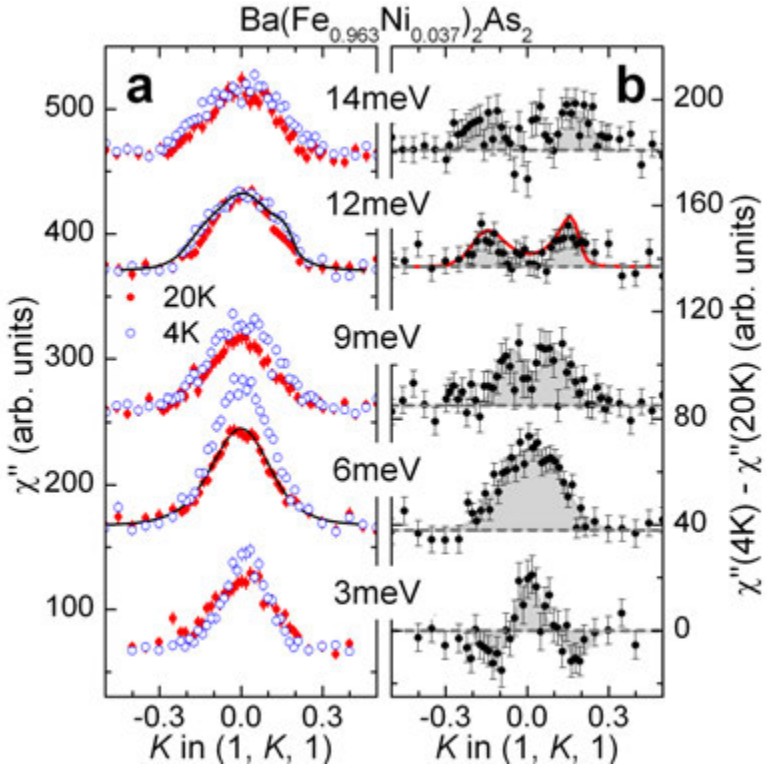

Figure 6.2 (a) Imaginary part of the dynamic susceptibility measured by inelastic neutron scattering experiments at 20 K (solid red circles) and 4 K (open blue circles). The black line at 12 meV data is the sum of the normal state spin excitation (20 K) and the spin resonance appearing as red line in (b). The black line for the normal state data at 6 meV is from calculations using a diffusive model. (b) Resonance intensities obtained by subtracting the normal state (20 K) intensity from intensities in the superconducting state (4 K). Red line at 20 K is from calculations using a spin wave model. The data were collected at HB3 triple-axis spectrometer at the High Flux Isotope Reactor at the Oak Ridge National Laboratory with 14.7 meV final energy and 48'-60'-80'-120' collimation.

Motivated by IC-AFM order in Co and Ni substituted $BaFe_2As_2$ compounds, I have investigated the occurrence of CDW in 5.4% and 5.7% Co substituted $BaFe_2As_2$ compound. The 5.4% Co substitution shows C-AFM at $\vec{Q}_{\rm AFM} = (\frac{1}{2}, \frac{1}{2}, 1)_{\rm T}$ [$\equiv (1, 0, 1)_{\rm O}$] while 5.7% Co substitution shows IC-AFM order at $\vec{Q}_{\rm AFM} = (\frac{1}{2}, \frac{1}{2}, 1)_{\rm T} \pm (\epsilon, -\epsilon, 0)_{\rm T}$ [$\equiv (1, 0, 1)_{\rm O} \pm (0, \varepsilon, 0)_{\rm O}$ with $\varepsilon = 2\epsilon$ (I will keep this relation from now on)]. If there is CDW, I expect to see additional scattering intensity at $\vec{Q}_{\rm T} \pm (2\epsilon, -2\epsilon, 0)_{\rm T}$ [$\equiv \vec{Q}_{\rm O} \pm (0, 2\varepsilon, 0)_{\rm O}$] where $\vec{Q}_{\rm T}$ ($\equiv \vec{Q}_{\rm O}$) is charge Bragg peak positions [e.g. $(2, -2, 0)_{\rm T} \equiv (0, 4, 0)_{\rm O}$]. However, I observed additional scattering intensities at $\vec{Q}_{\rm T} \pm (\epsilon, \epsilon, 0)_{\rm T}$) [$\equiv \vec{Q}_{\rm O} \pm (\varepsilon, 0, 0)_{\rm O}$] as shown in Fig. 6.3 (a). Since the positions of additional scattering intensities do not match with conventional knowledge of CDW, I studied a 5.4% Co substituted compound, which shows a commensurate AFM ordering, to test whether the observed intensities in 5.7% Co substitution are related to IC-AFM ordering and found that additional scattering intensities in 5.4% Co substitution appear at similar positions [Fig. 6.3 (b)]. I also measured temperature dependence of intensities of the additional peaks. The intensities remain finite above $T_{\rm N}$, closely follow the temperature dependence of the orthorhombic distortion, and disappear at $T_{\rm S}$ [Fig. 6.3 (b)]. Taken together, the observed additional scattering intensities are likely not related to the IC-AFM ordering but possibly to the structural transition. Further investigation will help to understand the observation and may lead to deeper understanding of the structural properties.

As shown in the previous chapter, the enhanced impurity scattering in Cu substitution, than Co and Ni substitutions, broadens the Fermi surface topology and leads to C-AFM order. If the Fermi surface topology alters, I would expect to observe changes in spin fluctuations. Earlier inelastic neutron scattering measurements on low Cu (2.9%) and Co (4.7%) doped $BaFe_2As_2$ compounds, which have C-AFM ordering and similar $T_{\rm S}, T_{\rm N}$ and ordered moment sizes, show that the normal state spin fluctuations are both qualitatively and quantitatively similar. It is of great interest to study spin fluctuations in high Cu ($\sim 4.4\%$) and Co ($\sim 5.7\%$) or Ni ($\sim 3.7\%$) substituted $BaFe_2As_2$, which may shed a light on understanding impurity scattering effects.

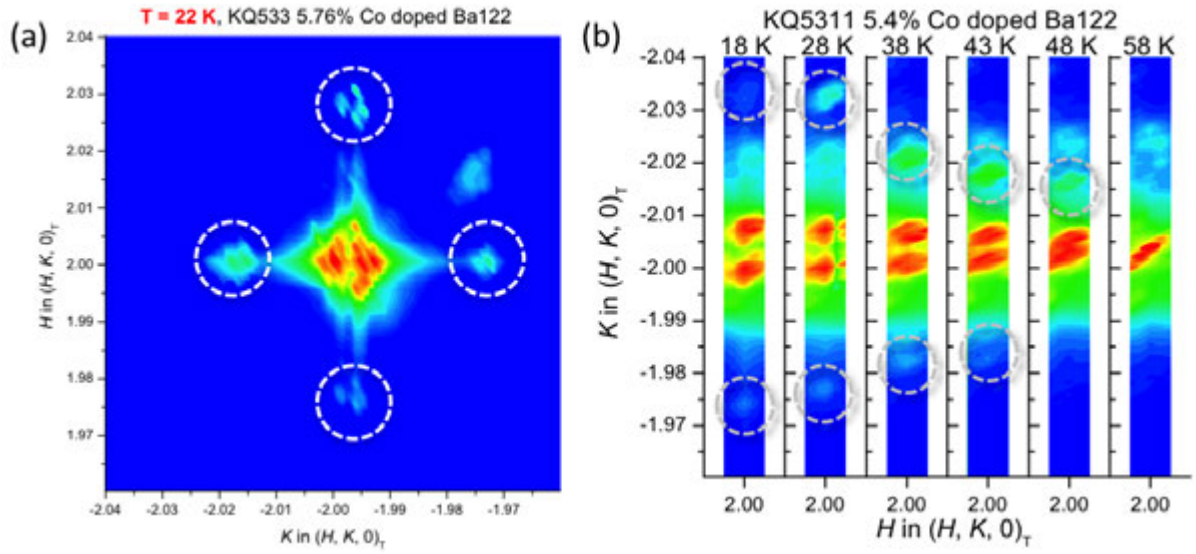

Figure 6.3 (a) Contour map around a charge peak (2, -2, 0)$_{\mathrm{T}}$ measured by x-ray on 5.76% Co doped $BaFe_2As_2$ ($T_{\mathrm{S}} \approx 43$ K, $T_{\mathrm{N}} \approx 30$ K, and $T_{\mathrm{c}} \approx 21$ K). Central intensities at (2, -2, 0)$_{\mathrm{T}}$ are from orthorhombic twin domains. Additional scattering intensities are denoted with dotted circles which are nearly symmetric. The intensity at approx. (2.015, -1.985, 0) is spurious and remains at all temperatures. (b) Contour map at selected temperatures for 5.4% Co doped $BaFe_2As_2$ ($T_{\mathrm{S}} \approx 50$ K, $T_{\mathrm{N}} \approx 36$ K, and $T_{\mathrm{c}} \approx 19$ K). Additional scattering intensities are denoted by dotted circles and they become closer to the charge Bragg peak position (2, -2, 0)$_{\mathrm{T}}$ as temperature increases and vanishes above T_{S}. The data were collected at 6ID-B at the Advanced Photon Source at the Argonne National Laboratory with 16.2 keV incident x-ray energy, 2 mm $\times$ 0.5 mm (horizontal $\times$ vertical) beam size and without analyzer.

BIBLIOGRAPHY

[1] Yoichi Kamihara, Takumi Watanabe, Masahiro Hirano, and Hideo Hosono. Iron-Based layered superconductor La[$O_{1-x}F_x$]FeAs (x = 0.05−0.12) with T_c = 26 K. *Journal of the American Chemical Society*, 130:3296–3297, 2008.

[2] Marianne Rotter, Marcus Tegel, and Dirk Johrendt. Superconductivity at 38 K in the iron arsenide ($Ba_{1-x}K_x$)Fe_2As_2. *Physical Review Letter*, 101:107006, 2008.

[3] David C. Johnston. The puzzle of high temperature superconductivity in layered iron pnictides and chalcogenides. *Advances in Physics*, 59:803–1061, 2010.

[4] G. R. Stewart. Superconductivity in iron compounds. *Reviews of Modern Physics*, 83:1589–1652, 2011.

[5] H. K. Onnes. The resistance of pure mercury at helium temperatures. *Communications from the Physical Laboratory at the University of Leiden*, 12:120, 1911.

[6] B. T. Matthias, T. H. Geballe, and V. B. Compton. Superconductivity. *Reviews of Modern Physics*, 35:1–22, 1963.

[7] J. E. Kunzler. Superconductivity in high magnetic fields at high current densities. *Reviews of Modern Physics*, 33:501–509, 1961.

[8] R. Flükiger, S. Y. Hariharan, R. Küntzler, H. L. Luo, F. Weiss, T. Wolf, and J. Q. Xu. Nb based alloys and compounds. *SpringerMaterials - The Landolt-Börnstein Database*, 21b2, 1994.

[9] S. H. Autler. Superconducting electromagnets. *Review of Scientific Instruments*, 31:369–373, 1960.

[10] Z. Z. Sheng and A. M. Hermann. Bulk superconductivity at 120 K in the Tl-Ca/Ba-Cu-O system. *Nature*, 332:138–139, 1988.

[11] Elbio Dagotto. Correlated electrons in high-temperature superconductors. *Reviews of Modern Physics*, 66:763–840, 1994.

[12] M. A. Kastner, R. J. Birgeneau, G. Shirane, and Y. Endoh. Magnetic, transport, and optical properties of monolayer copper oxides. *Reviews of Modern Physics*, 70:897–928, 1998.

[13] D. N. Basov and T. Timusk. Electrodynamics of high-T_c superconductors. *Reviews of Modern Physics*, 77:721–779, 2005.

[14] N. P. Armitage, P. Fournier, and R. L. Greene. Progress and perspectives on electron-doped cuprates. *Reviews of Modern Physics*, 82:2421–2487, 2010.

[15] G. R. Stewart. Heavy-fermion systems. *Reviews of Modern Physics*, 56:755–787, 1984.

[16] Christian Pfleiderer. Superconducting phases of f-electron compounds. *Reviews of Modern Physics*, 81:1551–1624, 2009.

[17] T. Ishiguro and K Yamaji. Organic superconductors. *Springer-Verlag*, 1990.

[18] J. Bardeen, L. N. Cooper, and J. R. Schrieffer. Microscopic theory of superconductivity. *Physical Review*, 106:162–164, 1957.

[19] J. Bardeen, L. N. Cooper, and J. R. Schrieffer. Theory of superconductivity. *Physical Review*, 108:1175–1204, 1957.

[20] Leon N. Cooper. Bound electron pairs in a degenerate Fermi gas. *Physical Review*, 104:1189–1190, 1956.

[21] Michael Tinkham. Introduction to superconductivity. *Dover*, New York, USA, 1996.

[22] Keith Burnett, Mark Edwards, and Editors Charles Clark. Special Issue: Bose-Einstein Condensation. *Journal of Research of National Institute of Standards and Technology*, 101:419–593, 1996.

[23] Emanuel Maxwell. Isotope effect in the superconductivity of mercury. *Physical Review*, 78:477–477, 1950.

[24] C. A. Reynolds, B. Serin, W. H. Wright, and L. B. Nesbitt. Superconductivity of isotopes of mercury. *Physical Review*, 78:487–487, 1950.

[25] V. Z. Kresin and S. A. Wolf. *Colloquium* : Electron-lattice interaction and its impact on high T_c superconductivity. *Reviews of Modern Physics*, 81:481–501, 2009.

[26] Johnpierre Paglione and Richard L. Greene. High-temperature superconductivity in iron-based materials. *Nature Physics*, 6:645–658, 2010.

[27] I. I. Mazin and M. D. Johannes. A key role for unusual spin dynamics in ferropnictides. *Nature Physics*, 5:141 – 145, 2009.

[28] Daniel L. Cox and M. Brian Maple. Electronic pairing in exotic superconductors. *Physics Today*, 48:32, 1995.

[29] C. W. Chu. Alive and kicking. *Nature Physics*, 5:787, 2009.

[30] M. D. Lumsden and A. D. Christianson. Magnetism in Fe-based superconductors. *Journal of Physics: Condensed Matter*, 22:203203, 2010.

[31] G. F. Chen, Z. Li, G. Li, J. Zhou, D. Wu, J. Dong, W. Z. Hu, P. Zheng, Z. J. Chen, H. Q. Yuan, J. Singleton, J. L. Luo, and N. L. Wang. Superconducting properties of the Fe-Based layered superconductor $LaFeAsO_{0.9}F_{0.1-\delta}$. *Physical Review Letter*, 101:057007, 2008.

[32] Hai-Hu Wen, Gang Mu, Lei Fang, Huan Yang, and Xiyu Zhu. Superconductivity at 25 K in hole-doped $(La_{1-x}Sr_x)OFeAs$. *Europhysics Letters*, 82:17009, 2008.

[33] X. H. Chen, T. Wu, G. Wu, R. H. Liu, H. Chen, and D. F. Fang. Superconductivity at 43 K in $SmFeAsO_{1-x}F_x$. *Nature*, 453:761–762, 2008.

[34] Z. A. Ren, J. Yang, W. Lu, W. Yi, G. C. Che, X. L. Dong, L. L. Sun, and Z. X. Zhao. Superconductivity at 52 K in iron based F doped layered quaternary compound $Pr[O_{1-x}F_x]FeAs$. *Materials Research Innovations*, 12:105–106, 2008.

[35] Z. A. Ren, J. Yang, W. Lu, W. Yi, X. L. Shen, Z. C. Li, G. C. Che, X. L. Dong, L. L. Sun, F. Zhou, and Z. X. Zhao. Superconductivity in the iron based F-doped layered quaternary compound $Nd[O_{1-x}F_x]FeAs$. *Europhysics Letters*, 82:57002, 2008.

[36] F. Hunte, J. Jaroszynski, A. Gurevich, D. C. Larbalestier, R. Jin, A. S. Sefat, M. A. McGuire, B. C. Sales, D. K. Christen, and D. Mandrus. Two-band superconductivity in $LaFeAsO_{0.89}F_{0.11}$ at very high magnetic field. *Nature*, 453:903–905, 2008.

[37] Ren Zhi-An, Lu Wei, Yang Jie, Yi Wei, Shen Xiao-Li, Zheng-Cai, Che Guang-Can, Dong Xiao-Li, Sun Li-Ling, Zhou Fang, and Zhao Zhong-Xian. Superconductivity at 55 K in Iron-Based F-Doped layered quaternary compound $Sm[O_{1-x}F_x]FeAs$. *Chinese Physics Letters*, 25:2215, 2008.

[38] G. F. Chen, Z. Li, D. Wu, G. Li, W. Z. Hu, J. Dong, P. Zheng, J. L. Luo, and N. L. Wang. Superconductivity at 41 K and its competition with Spin-Density-Wave instability in layered $CeO_{1-x}F_xFeAs$. *Physical Review Letter*, 100:247002, 2008.

[39] Peng Cheng, Lei Fang, Huan Yang, XiYu Zhu, Gang Mu, HuiQian Luo, ZhaoSheng Wang, and HaiHu Wen. Superconductivity at 36 K in gadilinium-arsenide oxides $GdO_{1-x}F_xFeAs$. *Science in China Series G*, 51:719–722, 2008.

[40] Zhi-An Ren, Guang-Can Che, Xiao-Li Dong, Jie Yang, Wei Lu, Wei Yi, Xiao-Li Shen, Zheng-Cai Li, Li-Ling Sun, Fang Zhou, and Zhong-Xian Zhao. Superconductivity and phase diagram in iron-based arsenic-oxides $ReFeAsO_{1-\delta}$ (Re = rare-earth metal) without fluorine doping. *Europhysics Letters*, 83:17002, 2008.

[41] Jie Yang, Zheng-Cai Li, Wei Lu, Wei Yi, Xiao-Li Shen, Zhi-An Ren, Guang-Can Che, Xiao-Li Dong, Li-Ling Sun, Fang Zhou, and Zhong-Xian Zhao. Superconductivity at 53.5 K in $GdFeAsO_{1-\delta}$. *Superconductor Science and Technology*, 21:082001, 2008.

[42] Hijiri Kito, Hiroshi Eisaki, and Akira Iyo. Superconductivity at 54 K in F-Free $NdFeAsO_{1-y}$. *Journal of the Physical Society of Japan*, 77:063707, 2008.

[43] Zheng Li, Gengfu Chen, Jing Dong, Gang Li, Wanzheng Hu, Dan Wu, Shaokui Su, Ping Zheng, Tao Xiang, Nanlin Wang, and Jianlin Luo. Strong-coupling superconductivity in the nickel-based oxypnictide $LaNiAsO_{1-x}F_x$. *Physical Review B*, 78:060504, 2008.

[44] Cao Wang, Linjun Li, Shun Chi, Zengwei Zhu, Zhi Ren, Yuke Li, Yuetao Wang, Xiao Lin, Yongkang Luo, Shuai Jiang, Xiangfan Xu, Guanghan Cao, and Zhu'an Xu. Thorium-doping-induced superconductivity up to 56 K in $Gd_{1-x}Th_xFeAsO$. *Europhysics Letters*, 83:67006, 2008.

[45] Athena S. Sefat, Ashfia Huq, Michael A. McGuire, Rongying Jin, Brian C. Sales, David Mandrus, Lachlan M. D. Cranswick, Peter W. Stephens, and Kevin H. Stone. Superconductivity in $LaFe_{1-x}Co_xAsO$. *Physical Review B*, 78:104505, 2008.

[46] Yanpeng Qi, Zhaoshun Gao, Lei Wang, Dongliang Wang, Xianping Zhang, and Yanwei Ma. Superconductivity in Co-doped SmFeAsO. *Superconductor Science and Technology*, 21:115016, 2008.

[47] Satoru Matsuishi, Yasunori Inoue, Takatoshi Nomura, Masahiro Hirano, and Hideo Hosono. Cobalt-Substitution-Induced superconductivity in a new compound with ZrCuSiAs-type structure, SrFeAsF. *Journal of the Physical Society of Japan*, 77:113709, 2008.

[48] Satoru Matsuishi, Yasunori Inoue, Takatoshi Nomura, Hiroshi Yanagi, Masahiro Hirano, and Hideo Hosono. Superconductivity induce by Co-doping in quaternary fluoroarsenide CaFeAsF. *Journal of the American Chemical Society*, 130:14428–14429, 2008.

[49] Karolina Kasperkiewicz, Jan-Willem G. Bos, Andrew N. Fitch, Kosmas Prassides, and Serena Margadonna. Structural and electronic response upon hole doping of rare-earth iron oxyarsenides $Nd_{1-x}Sr_xFeAsO$ ($0 < x \leq 0.2$). *Chemical Communications*, pages 707–709, 2009.

[50] Kiichi Miyazawa, Kunihiro Kihou, Parasharam M. Shirage, Chul-Ho Lee, Hijiri Kito, Hiroshi Eisaki, and Akira Iyo. Superconductivity above 50 K in LnFeAsO$_{1-y}$ (Ln = Nd, Sm, Gd, Tb, and Dy) synthesized by high-pressure technique. *Journal of the Physical Society of Japan*, 78:034712, 2009.

[51] Gang Mu, Bin Zeng, Xiyu Zhu, Fei Han, Peng Cheng, Bing Shen, and Hai-Hu Wen. Synthesis, structural, and transport properties of the hole-doped superconductor $Pr_{1-x}Sr_xFeAsO$. *Physical Review B*, 79:104501, 2009.

[52] Satoru Matsuishi, Yasunori Inoue, Takatoshi Nomura, Youichi Kamihara, Masahiro Hirano, and Hideo Hosono. Effect of 3d transition metal doping on the superconductivity in quaternary fluoroarsenide CaFeAsF. *New Journal of Physics*, 11:025012, 2009.

[53] Guanghan Cao, Shuai Jiang, Xiao Lin, Cao Wang, Yuke Li, Zhi Ren, Qian Tao, Chunmu Feng, Jianhui Dai, Zhu'an Xu, and Fu-Chun Zhang. Narrow superconducting window in $LaFe_{1-x}Ni_xAsO$. *Physical Review B*, 79:174505, 2009.

[54] Yong Liang Chen, Cui Hua Cheng, Ya Jing Cui, Han Zhang, Yong Zhang, Ye Yang, and Yong Zhao. Ir doping-induced superconductivity in the SmFeAsO system. *Journal of the American Chemical Society*, 131:10338–10339, 2009.

[55] Yuke Li, Xiao Lin, Qian Tao, Cao Wang, Tong Zhou, Linjun Li, Qingbo Wang, Mi He, Guanghan Cao, and Zhu'an Xu. Effect of Zn doping on magnetic order and superconductivity in LaFeAsO. *New Journal of Physics*, 11:053008, 2009.

[56] Cao Wang, Shuai Jiang, Qian Tao, Zhi Ren, Yuke Li, Linjun Li, Chunmu Feng, Jianhui Dai, Guanghan Cao, and Zhu an Xu. Superconductivity in $LaFeAs_{1-x}P_xO$: Effect of chemical pressures and bond covalency. *Europhysics Letters*, 86:47002, 2009.

[57] Yanpeng Qi, Lei Wang, Zhaoshun Gao, Dongliang Wang, Xianping Zhang, Zhiyu Zhang, and Yanwei Ma. Superconductivity in Ir-doped $LaFe_{1-x}Ir_xAsO$. *Physical Review B*, 80:054502, 2009.

[58] Y. K. Li, X. Lin, T. Zhou, J. Q. Shen, Q. Tao, G. H. Cao, and Z. A. Xu. Superconductivity induced by Ni doping in $SmFe_{1-x}Ni_xAsO$. *Journal of Physics: Condensed Matter*, 21:355702, 2009.

[59] David Berardan, Lidong Zhao, Loreynne Pinsard-Gaudart, and Nita Dragoe. Superconductivity at 15 K in $NdFe_{0.9}Rh_{0.1}AsO$ without F-doping. *Physica C: Superconductivity*, 470:165–167, 2009.

[60] Y. J. Cui, Y. L. Chen, C. H. Cheng, Y. Yang, J. Jiang, Y. Z. Wang, Y. Zhang, and Y. Zhao. Superconductivity and magnetism in Ir-doped GdFeAsO. *Physica C: Superconductivity*, 470:1077–1080, 2010.

[61] Marianne Rotter, Marcus Tegel, Dirk Johrendt, Inga Schellenberg, Wilfried Hermes, and Rainer Pöttgen. Spin-density-wave anomaly at 140 K in the ternary iron arsenide $BaFe_2As_2$. *Physical Review B*, 78:020503, 2008.

[62] C. Krellner, N. Caroca-Canales, A. Jesche, H. Rosner, A. Ormeci, and C. Geibel. Magnetic and structural transitions in layered iron arsenide systems: AFe$_2$As$_2$ versus RFeAsO. *Physical Review B*, 78:100504, 2008.

[63] N. Ni, S. L. Bud'ko, A. Kreyssig, S. Nandi, G. E. Rustan, A. I. Goldman, S. Gupta, J. D. Corbett, A. Kracher, and P. C. Canfield. Anisotropic thermodynamic and transport properties of single-crystalline $Ba_{1-x}K_xFe_2As_2$ (x= 0 and 0.45). *Physical Review B*, 78:014507, 2008.

[64] Kalyan Sasmal, Bing Lv, Bernd Lorenz, Arnold M. Guloy, Feng Chen, Yu-Yi Xue, and Ching-Wu Chu. Superconducting Fe-based compounds $(A_{1-x}Sr_x)Fe_2As_2$ with A=K and Cs with transition temperatures up to 37 K. *Physical Review Letter*, 101:107007, 2008.

[65] Chen Gen-Fu, Li Zheng, Li Gang, Hu Wan-Zheng, Dong Jing, Zhou Jun, Zhang Xiao-Dong, Zheng Ping, Wang Nan-Lin, and Luo Jian-Lin. Superconductivity in hole-doped $(Sr_{1-x}K_x)Fe_2As_2$. *Chinese Physics Letters*, 25:3403, 2008.

[66] J.-Q. Yan, A. Kreyssig, S. Nandi, N. Ni, S. L. Bud'ko, A. Kracher, R. J. McQueeney, R. W. McCallum, T. A. Lograsso, A. I. Goldman, and P. C. Canfield. Structural transition and anisotropic properties of single-crystalline $SrFe_2As_2$. *Physical Review B*, 78:024516, 2008.

[67] X. F. Wang, T. Wu, G. Wu, H. Chen, Y. L. Xie, J. J. Ying, Y. J. Yan, R. H. Liu, and X. H. Chen. Anisotropy in the electrical resistivity and susceptibility of superconducting $BaFe_2As_2$ single crystals. *Physical Review Letter*, 102:117005, 2009.

[68] Marcus Tegel, Marianne Rotter, Veronika Weiß, Falko M Schappacher, Rainer Pöttgen, and Dirk Johrendt. Structural and magnetic phase transitions in the ternary iron arsenides $SrFe_2As_2$ and $EuFe_2As_2$. *Journal of Physics: Condensed Matter*, 20:452201, 2008.

[69] Zhi Ren, Zengwei Zhu, Shuai Jiang, Xiangfan Xu, Qian Tao, Cao Wang, Chunmu Feng, Guanghan Cao, and Zhu'an Xu. Antiferromagnetic transition in $EuFe_2As_2$: A possible parent compound for superconductors. *Physical Review B*, 78:052501, 2008.

[70] N. Ni, S. Nandi, A. Kreyssig, A. I. Goldman, E. D. Mun, S. L. Bud'ko, and P. C. Canfield. First-order structural phase transition in $CaFe_2As_2$. *Physical Review B*, 78:014523, 2008.

[71] F. Ronning, T. Klimczuk, E. D. Bauer, H. Volz, and J. D. Thompson. Synthesis and properties of $CaFe_2As_2$ single crystals. *Journal of Physics: Condensed Matter*, 20:322201, 2008.

[72] Parasharam Maruti Shirage, Kiichi Miyazawa, Hijiri Kito, Hiroshi Eisaki, and Akira Iyo. Superconductivity at 26 K in $(Ca_{1-x}Na_x)Fe_2As_2$. *Applied Physics Express*, 1:081702, 2008.

[73] A. Leithe-Jasper, W. Schnelle, C. Geibel, and H. Rosner. Superconducting state in $SrFe_{2-x}Co_xAs_2$ by internal doping of the iron arsenide layers. *Physical Review Letter*, 101:207004, 2008.

[74] F. Ronning, N. Kurita, E. D. Bauer, B. L. Scott, T. Park, T. Klimczuk, R. Movshovich, and J. D. Thompson. The first order phase transition and superconductivity in $BaNi_2As_2$ single crystals. *Journal of Physics: Condensed Matter*, 20:342203, 2008.

[75] Athena S. Sefat, Rongying Jin, Michael A. McGuire, Brian C. Sales, David J. Singh, and David Mandrus. Superconductivity at 22 K in Co-Doped $BaFe_2As_2$ crystals. *Physical Review Letter*, 101:117004, 2008.

[76] E. D. Bauer, F. Ronning, B. L. Scott, and J. D. Thompson. Superconductivity in $SrNi_2As_2$ single crystals. *Physical Review B*, 78:172504, 2008.

[77] Huiqian Luo, Zhaosheng Wang, Huan Yang, Peng Cheng, Xiyu Zhu, and Hai-Hu Wen. Growth and characterization of $A_{1-x}K_xFe_2As_2$ (A = Ba, Sr) single crystals with x = 0-0.4. *Superconductor Science and Technology*, 21:125014, 2008.

[78] H. S. Jeevan, Z. Hossain, Deepa Kasinathan, H. Rosner, C. Geibel, and P. Gegenwart. High-temperature superconductivity in $Eu_{0.5}K_{0.5}Fe_2As_2$. *Physical Review B*, 78:092406, 2008.

[79] Neeraj Kumar, R. Nagalakshmi, R. Kulkarni, P. L. Paulose, A. K. Nigam, S. K. Dhar, and A. Thamizhavel. Anisotropic magnetic and superconducting properties of $CaFe_{2-x}Co_xAs_2$ (x=0, 0.06) single crystals. *Physical Review B*, 79:012504, 2009.

[80] L. J. Li, Y. K. Luo, Q. B. Wang, H. Chen, Z. Ren, Q. Tao, Y. K. Li, X. Lin, M. He, Z. W. Zhu, G. H. Cao, and Z. A. Xu. Superconductivity induced by Ni doping in $BaFe_2A_2$ single crystals. *New Journal of Physics*, 11:025008, 2009.

[81] N. Kurita, F. Ronning, Y. Tokiwa, E. D. Bauer, A. Subedi, D. J. Singh, J. D. Thompson, and R. Movshovich. Low-temperature magnetothermal transport investigation of a Ni-based superconductor $BaNi_2As_2$: Evidence for fully gapped superconductivity. *Physical Review Letter*, 102:147004, 2009.

[82] Athena S. Sefat, Michael A. McGuire, Rongying Jin, Brian C. Sales, David Mandrus, Filip

Ronning, E. D. Bauer, and Yurij Mozharivskyj. Structure and anisotropic properties of $BaFe_{2-x}Ni_xAs_2$ (x=0, 1, and 2) single crystals. *Physical Review B*, 79:094508, 2009.

[83] Deepa Kasinathan, Alim Ormeci, Katrin Koch, Ulrich Burkhardt, Walter Schnelle, Andreas Leithe-Jasper, and Helge Rosner. AFe_2As_2 (A = Ca, Sr, Ba, Eu) and $SrFe_{2-x}TM_xAs_2$ (TM = Mn, Co, Ni): crystal structure, charge doping, magnetism and superconductivity. *New Journal of Physics*, 11:025023, 2009.

[84] Zhi Ren, Qian Tao, Shuai Jiang, Chunmu Feng, Cao Wang, Jianhui Dai, Guanghan Cao, and Zhu'an Xu. Superconductivity induced by phosphorus doping and its coexistence with ferromagnetism in $EuFe_2(As_{0.7}P_{0.3})_2$. *Physical Review Letter*, 102:137002, 2009.

[85] Fei Han, Xiyu Zhu, Peng Cheng, Gang Mu, Ying Jia, Lei Fang, Yonglei Wang, Huiqian Luo, Bin Zeng, Bing Shen, Lei Shan, Cong Ren, and Hai-Hu Wen. Superconductivity and phase diagrams of the 4*d*- and 5*d*-metal-doped iron arsenides $SrFe_{2-x}M_xAs_2$ (M=Rh, Ir, Pd). *Physical Review B*, 80:024506, 2009.

[86] Shilpam Sharma, A. Bharathi, Sharat Chandra, V. Raghavendra Reddy, S. Paulraj, A. T. Satya, V. S. Sastry, Ajay Gupta, and C. S. Sundar. Superconductivity in Ru-substituted polycrystalline $BaFe_{2-x}Ru_xAs_2$. *Physical Review B*, 81:174512, 2010.

[87] Yanpeng Qi, Lei Wang, Zhaoshun Gao, Dongliang Wang, Xianping Zhang, and Yanwei Ma. Superconductivity induced by doping Ru in $SrFe_{2-x}Ru_xAs_2$. *Physica C: Superconductivity*, 469:1921–1924, 2009.

[88] Athena S. Sefat, David J. Singh, Lindsay H. VanBebber, Yurij Mozharivskyj, Michael A. McGuire, Rongying Jin, Brian C. Sales, Veerle Keppens, and David Mandrus. Absence of superconductivity in hole-doped $BaFe_{2-x}Cr_xAs_2$ single crystals. *Physical Review B*, 79:224524, 2009.

[89] P. C. Canfield, S. L. Bud'ko, Ni Ni, J. Q. Yan, and A. Kracher. Decoupling of the superconducting and magnetic/structural phase transitions in electron-doped $BaFe_2As_2$. *Physical Review B*, 80:060501, 2009.

[90] S. R. Saha, N. P. Butch, K. Kirshenbaum, and Johnpierre Paglione. Evolution of bulk superconductivity in $SrFe_2As_2$ with Ni substitution. *Physical Review B*, 79:224519, 2009.

[91] N. Ni, A. Thaler, A. Kracher, J. Q. Yan, S. L. Bud'ko, and P. C. Canfield. Phase diagrams of $Ba(Fe_{1-x}M_x)_2As_2$ single crystals (M= Rh and Pd). *Physical Review B*, 80:024511, 2009.

[92] Eun Deok Mun, Sergey L. Bud'ko, Ni Ni, Alex N. Thaler, and Paul C. Canfield. Thermoelectric power and hall coefficient measurements on $Ba(Fe_{1-x}T_x)_2As_2$ (T= Co and Cu). *Physical Review B*, 80:054517, 2009.

[93] Shuai Jiang, Hui Xing, Guofang Xuan, Cao Wang, Zhi Ren, Chunmu Feng, Jianhui Dai, Zhu'an Xu, and Guanghan Cao. Superconductivity up to 30 K in the vicinity of the quantum critical point in $BaFe_2(As_{1-x}P_x)_2$. *Journal of Physics: Condensed Matter*, 21:382203, 2009.

[94] Neeraj Kumar, Songxue Chi, Ying Chen, Kumari Gaurav Rana, A. K. Nigam, A. Thamizhavel, William Ratcliff, S. K. Dhar, and Jeffrey W. Lynn. Evolution of the bulk properties, structure, magnetic order, and superconductivity with Ni doping in $CaFe_{2-x}Ni_xAs_2$. *Physical Review B*, 80:144524, 2009.

[95] X. L. Wang, H. Y. Shi, X. W. Yan, Y. C. Yuan, Z. Y. Lu, X. Q. Wang, and T. S. Zhao. Microstructure and superconductivity of Ir-doped $BaFe_2As_2$ superconductor. *Applied Physics Letter*, 96:012507, 2010.

[96] S. Kasahara, K. Hashimoto, R. Okazaki, H. Shishido, M. Yamashita, K. Ikada, S. Tonegawa, N. Nakata, Y. Sensyu, H. Takeya, K. Hirata, T. Shibauchi, T. Terashima, and Y. Matsuda. Superconductivity induced by isovalent doping in single crystals of $BaFe_2(As_{1-x}P_x)$. *Physica C: Superconductivity*, 470:S462–S463, 2010.

[97] Y. Liu, D. L. Sun, J. T. Park, and C. T. Lin. Aliovalent ion-doped $BaFe_2As_2$: Single crystal growth and superconductivity. *Physica C: Superconductivity*, 470:S513–S515, 2010.

[98] S. R. Saha, T. Drye, K. Kirshenbaum, N. P. Butch, P. Y. Zavalij, and Johnpierre Paglione. Superconductivity at 23 K in Pt doped BaF_2As_2 single crystals. *Journal of Physics: Condensed Matter*, 22:072204, 2010.

[99] Xiyu Zhu, Fei Han, Gang Mu, Peng Cheng, Jun Tang, Jing Ju, Katsumi Tanigaki, and Hai-Hu Wen. Superconductivity induced by doping platinum in $BaFe_2As_2$. *Physical Review B*, 81:104525, 2010.

[100] J. S. Kim, Seunghyun Khim, H. J. Kim, M. J. Eom, J. M. Law, R. K. Kremer, Ji Hoon Shim, and Kee Hoon Kim. Electron-hole asymmetry in Co- and Mn-doped $SrFe_2As_2$. *Physical Review B*, 82:024510, 2010.

[101] Yoshihiro Nishikubo, Satomi Kakiya, Masataka Danura, Kazutaka Kudo, and Minoru Nohara. Superconductivity in $SrFe_2As_2$ with Pt doping. *Journal of the Physical Society of Japan*, 79:095002, 2010.

[102] A. Thaler, N. Ni, A. Kracher, J. Q. Yan, S. L. Bud'ko, and P. C. Canfield. Physical and magnetic properties of $Ba(Fe_{1-x}Ru_x)_2As_2$ single crystals. *Physical Review B*, 82:014534, 2010.

[103] Kevin Kirshenbaum, Shanta R. Saha, Tyler Drye, and Johnpierre Paglione. Superconductivity and magnetism in platinum-substituted $SrFe_2As_2$ single crystals. *Physical Review B*, 82:144518, 2010.

[104] Yanpeng Qi, Lei Wang, Zhaoshun Gao, Dongliang Wang, Xianping Zhang, Chunlei Wang, Chao Yao, and Yanwei Ma. Superconductivity induced by doping Rh in $CaFe_{2-x}Rh_xAs_2$. *New Journal of Physics*, 13:033020, 2011.

[105] Yanpeng Qi, Zhaoshun Gao, Lei Wang, Xianping Zhang, Dongliang Wang, Chao Yao, Chunlei Wang, Chengduo Wang, and Yanwei Ma. Superconductivity at 22 K in Ir-doped $CaFe_{2-x}Ir_xAs_2$ single crystals. *Europhysics Letters*, 96:47005, 2011.

[106] Joshua H. Tapp, Zhongjia Tang, Bing Lv, Kalyan Sasmal, Bernd Lorenz, Paul C. W.

Chu, and Arnold M. Guloy. LiFeAs: An intrinsic FeAs-based superconductor with T_c = 18 K. *Physical Review B*, 78:060505, 2008.

[107] Michael J. Pitcher, Dinah R. Parker, Paul Adamson, Sebastian J. C. Herkelrath, Andrew T. Boothroyd, and Richard M. Ibberson. Structure and superconductivity of LiFeAs. *Chemical Communications*, pages 5918–5920, 2008.

[108] X. C. Wang, Q. Q. Liu, Y. X. Lv, W. B. Gao, L. X. Yang, R. C. Yu, F. Y. Li, and C. Q. Jin. The superconductivity at 18 K in LiFeAs system. *Solid State Communications*, 148:538–540, 2008.

[109] Dinah R. Parker, Michael J. Pitcher, Peter J. Baker, Isabel Franke, Tom Lancaster, Stephen J. Blundell, and Simon J. Clarke. Structure, antiferromagnetism and superconductivity of the layered iron arsenide NaFeAs. *Chemical Communications*, pages 2189–2191, 2009.

[110] F. L. Pratt, P. J. Baker, S. J. Blundell, T. Lancaster, H. J. Lewtas, P. Adamson, M. J. Pitcher, D. R. Parker, and S. J. Clarke. Enhanced superfluid stiffness, lowered superconducting transition temperature, and field-induced magnetic state of the pnictide superconductor LiFeAs. *Physical Review B*, 79:052508, 2009.

[111] G. F. Chen, W. Z. Hu, J. L. Luo, and N. L. Wang. Multiple phase transitions in single-crystalline $Na_{1-\delta}FeAs$. *Physical Review Letter*, 102:227004, 2009.

[112] K. Sasmal, B. Lv, Z. J. Tang, F. Chen, Y. Y. Xue, B. Lorenz, A. M. Guloy, and C. W. Chu. Unusual doping dependence of superconductivity in Na_yFeAs. *Physical Review B*, 79:184516, 2009.

[113] C. W. Chu, F. Chen, M. Gooch, A. M. Guloy, B. Lorenz, B. Lv, K. Sasmal, Z. J. Tang, J. H. Tapp, and Y. Y. Xue. The synthesis and characterization of LiFeAs and NaFeAs. *Physica C: Superconductivity*, 469:326–331, 2009.

[114] Dinah R. Parker, Matthew J. P. Smith, Tom Lancaster, Andrew J. Steele, Isabel Franke, Peter J. Baker, Francis L. Pratt, Michael J. Pitcher, Stephen J. Blundell, and Simon J.

Clarke. Control of the competition between a magnetic phase and a superconducting phase in cobalt-doped and nickel-doped NaFeAs using electron count. *Physical Review Letter*, 104:057007, 2010.

[115] Yoo Jang Song, Jin Soo Ghim, Byeong Hun Min, Yong Seung Kwon, Myung Hwa Jung, and Jong-Soo Rhyee. Synthesis, anisotropy, and superconducting properties of LiFeAs single crystal. *Applied Physics Letter*, 96:212508, 2010.

[116] Michael J. Pitcher, Tom Lancaster, Jack D. Wright, Isabel Franke, Andrew J. Steele, Peter J. Baker, Francis L. Pratt, William Trevelyan Thomas, Dinah R. Parker, Stephen J. Blundell, and Simon J. Clarke. Compositional control of the superconducting properties of LiFeAs. *Journal of the American Chemical Society*, 132:10467–10476, 2010.

[117] XianCheng Wang, QingQing Liu, YuXi Lv, Zheng Deng, Kan Zhao, RiChen Yu, JinLong Zhu, and ChangQing Jin. Superconducting properties of "111" type LiFeAs iron arsenide single crystals. *Science China Physics, Mechanics and Astronomy*, 53:1199–1201, 2010.

[118] Fong-Chi Hsu, Jiu-Yong Luo, Kuo-Wei Yeh, Ta-Kun Chen, Tzu-Wen Huang, Phillip M. Wu, Yong-Chi Lee, Yi-Lin Huang, Yan-Yi Chu, Der-Chung Yan, and Maw-Kuen Wu. Superconductivity in the PbO-type structure α-FeSe. *Proceedings of the National Academy of Sciences*, 105:14262–14264, 2008.

[119] Kuo-Wei Yeh, Tzu-Wen Huang, Yi lin Huang, Ta-Kun Chen, Fong-Chi Hsu, Phillip M. Wu, Yong-Chi Lee, Yan-Yi Chu, Chi-Lian Chen, Jiu-Yong Luo, Der-Chung Yan, and Maw-Kuen Wu. Tellurium substitution effect on superconductivity of the α-phase iron selenide. *Europhysics Letters*, 84:37002, 2008.

[120] Wei Bao, Y. Qiu, Q. Huang, M. A. Green, P. Zajdel, M. R. Fitzsimmons, M. Zhernenkov, S. Chang, Minghu Fang, B. Qian, E. K. Vehstedt, Jinhu Yang, H. M. Pham, L. Spinu, and Z. Q. Mao. Tunable ($\delta\pi$, $\delta\pi$)-Type antiferromagnetic order in α-Fe(Te,Se) superconductors. *Physical Review Letter*, 102:247001, 2009.

[121] M. H. Fang, H. M. Pham, B. Qian, T. J. Liu, E. K. Vehstedt, Y. Liu, L. Spinu, and Z. Q. Mao. Superconductivity close to magnetic instability in $Fe(Se_{1-x}Te_x)_{0.82}$. *Physical Review B*, 78:224503, 2008.

[122] Yoshikazu Mizuguchi, Fumiaki Tomioka, Shunsuke Tsuda, Takahide Yamaguchi, and Yoshihiko Takano. Substitution effects on FeSe superconductor. *Journal of the Physical Society of Japan*, 78:074712, 2009.

[123] T. M. McQueen, Q. Huang, V. Ksenofontov, C. Felser, Q. Xu, H. Zandbergen, Y. S. Hor, J. Allred, A. J. Williams, D. Qu, J. Checkelsky, N. P. Ong, and R. J. Cava. Extreme sensitivity of superconductivity to stoichiometry in $Fe_{1+\delta}Se$. *Physical Review B*, 79:014522, 2009.

[124] B. C. Sales, A. S. Sefat, M. A. McGuire, R. Y. Jin, D. Mandrus, and Y. Mozharivskyj. Bulk superconductivity at 14 K in single crystals of $Fe_{1+y}Te_xSe_{1-x}$. *Physical Review B*, 79:094521, 2009.

[125] G. F. Chen, Z. G. Chen, J. Dong, W. Z. Hu, G. Li, X. D. Zhang, P. Zheng, J. L. Luo, and N. L. Wang. Electronic properties of single-crystalline $Fe_{1.05}Te$ and $Fe_{1.03}Se_{0.30}Te_{0.70}$. *Physical Review B*, 79:140509, 2009.

[126] A. J. Williams, T. M. McQueen, V. Ksenofontov, C. Felser, and R. J. Cava. The metal-insulator transition in $Fe_{1.01-x}Cu_xSe$. *Journal of Physics: Condensed Matter*, 21:305701, 2009.

[127] T. Taen, Y. Tsuchiya, Y. Nakajima, and T. Tamegai. Superconductivity at $T_c \sim 14$ K in single-crystalline $FeTe_{0.61}Se_{0.39}$. *Physical Review B*, 80:092502, 2009.

[128] Rongwei Hu, Emil S. Bozin, J. B. Warren, and C. Petrovic. Superconductivity, magnetism, and stoichiometry of single crystals of $Fe_{1+y}(Te_{1-x}S_x)_z$. *Physical Review B*, 80:214514, 2009.

[129] Junyi Ge, Shixun Cao, Shaoxi Shen, Shujuan Yuan, Baojuan Kang, and Jincang Zhang.

The transport properties in antimony doped iron selenide $Fe(Se_{1-x}Sb_x)_{0.92}$ system. *Cryogenics*, 51:253–256, 1956.

[130] Swati Pandya, Siya Sherif, L. S. Sharath Chandra, and V. Ganesan. Magneto-transport studies of $FeSe_{0.9-x}M_x$ (M = Si, Sb). *Superconductor Science and Technology*, 24:045011, 2011.

[131] Yoichi Kamihara, Hidenori Hiramatsu, Masahiro Hirano, Ryuto Kawamura, Hiroshi Yanagi, Toshio Kamiya, and Hideo Hosono. Iron-based layered superconductor: LaOFeP. *Journal of the American Chemical Society*, 128:10012–10013, 2006.

[132] Takumi Watanabe, Hiroshi Yanagi, Toshio Kamiya, Yoichi Kamihara, Hidenori Hiramatsu, Masahiro Hirano, and Hideo Hosono. Nickel-based oxyphosphide superconductor with a layered crystal structure, LaNiOP. *Inorganic Chemistry*, 46:7719–7721, 2007.

[133] Michael A. McGuire, David J. Singh, Athena S. Sefat, Brian C. Sales, and David Mandrus. Suppression of spin density wave by isoelectronic substitution in $PrFe_{1-x}Ru_xAsO$. *Journal of Solid State Chemistry*, 182:2326, 2009.

[134] Anand Pal, Arpita Vajpayee, V. P. S. Awana, M. Husain, and H. Kishan. Suppression of spin density wave character of (Sm/Gd)FeAsO by substitution of Ru at Fe site. *Physica C*, 470:S491–S492, 2010.

[135] I. Pallecchi, F. Bernardini, M. Tropeano, A. Palenzona, A. Martinelli, C. Ferdeghini, M. Vignolo, S. Massidda, and M. Putti. Magnetotransport in La(Fe,Ru)AsO as a probe of band structure and mobility. *Physical Review B*, 84:134524, 2011.

[136] R. D. Shannon. Revised effective ionic radii and systematic studies of interatomic distances in Halides and Chalcogenides. *Acta Crystallographica*, A 32:751, 1976.

[137] Anke Köhler and Günter Behr. WDX-Analysis of the new superconductors $RO_{1-x}F_xFeAs$ and its consequences on the electronic phase diagram. *Journal of Superconductivity and Novel Magnetism*, 22:565–567, 2009.

[138] Athena S. Sefat, Karol Marty, Andrew D. Christianson, Bayrammurad Saparov, Michael A. McGuire, Mark D. Lumsden, Wei Tian, and Brian C. Sales. Effect of molybdenum 4*d* hole substitution in $BaFe_2As_2$. *Physical Review B*, 85:024503, 2012.

[139] Charles Kittel. Introduction to Solid State Physics. *John Wiley and Sons, Inc.*, Hoboken, USA, 2005.

[140] Clarina de la Cruz, Q. Huang, J. W. Lynn, Jiying Li, W. Ratcliff II, J. L. Zarestky, H. A. Mook, G. F. Chen, J. L. Luo, N. L. Wang, and Pengcheng Dai. Magnetic order close to superconductivity in the iron-based layered $LaO_{1-x}F_xFeAs$ systems. *Nature*, 453:899–902, 2008.

[141] T. Nomura, S. W. Kim, Y. Kamihara, M. Hirano, P. V. Sushko, K. Kato, M. Takata, A. L. Shluger, and H. Hosono. Crystallographic phase transition and high-T_c superconductivity in LaFeAsO:F. *Superconductor Science and Technology*, 21:125028, 2008.

[142] H.-H. Klauss, H. Luetkens, R. Klingeler, C. Hess, F. J. Litterst, M. Kraken, M. M. Korshunov, I. Eremin, S.-L. Drechsler, R. Khasanov, A. Amato, J. Hamann-Borrero, N. Leps, A. Kondrat, G. Behr, J. Werner, and B. Büchner. Commensurate spin density wave in LaFeAsO: A local probe study. *Physical Review Letter*, 101:077005, 2008.

[143] Michael A. McGuire, Andrew D. Christianson, Athena S. Sefat, Brian C. Sales, Mark D. Lumsden, Rongying Jin, E. Andrew Payzant, David Mandrus, Yanbing Luan, Veerle Keppens, Vijayalaksmi Varadarajan, Joseph W. Brill, Raphaël P. Hermann, Moulay T. Sougrati, Fernande Grandjean, and Gary J. Long. Phase transitions in LaFeAsO: Structural, magnetic, elastic, and transport properties, heat capacity and Mössbauer spectra. *Physical Review B*, 78:094517, 2008.

[144] Ying Chen, J. W. Lynn, J. Li, G. Li, G. F. Chen, J. L. Luo, N. L. Wang, Pengcheng Dai, C. dela Cruz, and H. A. Mook. Magnetic order of the iron spins in NdFeAsO. *Physical Review B*, 78:064515, 2008.

[145] Jun Zhao, Q. Huang, Clarina de la Cruz, Shiliang Li, J. W. Lynn, Y. Chen, M. A. Green, G. F. Chen, G. Li, Z. Li, J. L. Luo, N. L. Wang, and Pengcheng Dai. Structural

and magnetic phase diagram of $CeFeAsO_{1-x}F_x$ and its relation to high-temperature superconductivity. *Nature Materials*, 7:953–959, 2008.

[146] Y. Qiu, Wei Bao, Q. Huang, T. Yildirim, J. M. Simmons, M. A. Green, J. W. Lynn, Y. C. Gasparovic, J. Li, T. Wu, G. Wu, and X. H. Chen. Crystal structure and antiferromagnetic order in $NdFeAsO_{1-x}F_x$ (x=0.0 and 0.2) superconducting compounds from neutron diffraction measurements. *Physical Review Letter*, 101:257002, 2008.

[147] Q. Huang, Jun Zhao, J. W. Lynn, G. F. Chen, J. L. Luo, N. L. Wang, and Pengcheng Dai. Doping evolution of antiferromagnetic order and structural distortion in $LaFeAsO_{1-x}F_x$. *Physical Review B*, 78:054529, 2008.

[148] S. A. J. Kimber, D. N. Argyriou, F. Yokaichiya, K. Habicht, S. Gerischer, T. Hansen, T. Chatterji, R. Klingeler, C. Hess, G. Behr, A. Kondrat, and B. Büchner. Magnetic ordering and negative thermal expansion in PrFeAsO. *Physical Review B*, 78:140503, 2008.

[149] Jun Zhao, Q. Huang, Clarina de la Cruz, J. W. Lynn, M. D. Lumsden, Z. A. Ren, Jie Yang, Xiaolin Shen, Xiaoli Dong, Zhongxian Zhao, and Pengcheng Dai. Lattice and magnetic structures of PrFeAsO, $PrFeAsO_{0.85}F_{0.15}$, and $PrFeAsO_{0.85}$. *Physical Review B*, 78:132504, 2008.

[150] Serena Margadonna, Yasuhiro Takabayashi, Martin T. McDonald, Michela Brunelli, G. Wu, R. H. Liu, X. H. Chen, and Kosmas Prassides. Crystal structure and phase transitions across the metal-superconductor boundary in the $SmFeAsO_{1-x}F_x$ ($0 \leq x \leq 0.20$) family. *Physical Review B*, 79:014503, 2009.

[151] C. R. Rotundu, D. T. Keane, B. Freelon, S. D. Wilson, A. Kim, P. N. Valdivia, E. Bourret-Courchesne, and R. J. Birgeneau. Phase diagram of the $PrFeAsO_{1-x}F_x$ superconductor. *Physical Review B*, 80:144517, 2009.

[152] Yongkang Luo, Qian Tao, Yuke Li, Xiao Lin, Linjun Li, Guanghan Cao, Zhu-an Xu, Yun Xue, Hiroshi Kaneko, Andrey V. Savinkov, Haruhiko Suzuki, Chen Fang, and Jiangping

Hu. Evidence of magnetically driven structural phase transition in RFeAsO (R= La, Sm, Gd, and Tb): A low-temperature x-ray diffraction study. *Physical Review B*, 80:224511, 2009.

[153] D. H. Ryan, J. M. Cadogan, C. Ritter, F. Canepa, A. Palenzona, and M. Putti. Coexistence of long-ranged magnetic order and superconductivity in the pnictide superconductor $SmFeAsO_{1-x}F_x$ (x=0, 0.15). *Physical Review B*, 80:220503, 2009.

[154] Yoichi Kamihara, Takatoshi Nomura, Masahiro Hirano, Jung Eun Kim, Kenichi Kato, Masaki Takata, Yasuhiro Kobayashi, Shinji Kitao, Satoshi Higashitaniguchi, Yoshitaka Yoda, Makoto Seto, and Hideo Hosono. Electronic and magnetic phase diagram of superconductors, $SmFeAsO_{1-x}F_x$. *New Journal of Physics*, 12:033005, 2010.

[155] Lorenzo Malavasi, Gianluca A. Artioli, Clemens Ritter, M. Cristina Mozzati, Beatrice Maroni, Bholanath Pahari, and Andrea Caneschi. Phase diagram of $NdFeAsO_{1-x}F_x$: essential role of chemical composition. *Journal of the American Chemical Society*, 132:2417–2420, 2010.

[156] N. Qureshi, Y. Drees, J. Werner, S. Wurmehl, C. Hess, R. Klingeler, B. Büchner, M. T. Fernández-Díaz, and M. Braden. Crystal and magnetic structure of the oxypnictide superconductor $LaFeAsO_{1-x}F_x$: A neutron-diffraction study. *Physical Review B*, 82:184521, 2010.

[157] W. Tian, W. Ratcliff, M. G. Kim, J.-Q. Yan, P. A. Kienzle, Q. Huang, B. Jensen, K. W. Dennis, R. W. McCallum, T. A. Lograsso, R. J. McQueeney, A. I. Goldman, J. W. Lynn, and A. Kreyssig. Interplay of Fe and Nd magnetism in NdFeAsO single crystals. *Physical Review B*, 82:060514, 2010.

[158] H.-F. Li, W. Tian, J.-Q. Yan, J. L. Zarestky, R. W. McCallum, T. A. Lograsso, and D. Vaknin. Phase transitions and iron-ordered moment form factor in LaFeAsO. *Physical Review B*, 82:064409, 2010.

[159] S. Nandi, Y. Su, Y. Xiao, S. Price, X. F. Wang, X. H. Chen, J. Herrero-Martín, C. Mazzoli, H. C. Walker, L. Paolasini, S. Francoual, D. K. Shukla, J. Strempfer, T. Chatterji,

C. M. N. Kumar, R. Mittal, H. M. Rønnow, Ch. Rüegg, D. F. McMorrow, and Th. Brückel. Strong coupling of Sm and Fe magnetism in SmFeAsO as revealed by magnetic x-ray scattering. *Physical Review B*, 84:054419, 2011.

[160] Stephen Blundell. Magnetism in condensed matter. *Oxford University Press*, Oxford, Great Britain, 2001.

[161] A. Jesche, N. Caroca-Canales, H. Rosner, H. Borrmann, A. Ormeci, D. Kasinathan, H. H. Klauss, H. Luetkens, R. Khasanov, A. Amato, A. Hoser, K. Kaneko, C. Krellner, and C. Geibel. Strong coupling between magnetic and structural order parameters in $SrFe_2As_2$. *Physical Review B*, 78:180504, 2008.

[162] Jun Zhao, W. Ratcliff, J. W. Lynn, G. F. Chen, J. L. Luo, N. L. Wang, Jiangping Hu, and Pengcheng Dai. Spin and lattice structures of single-crystalline $SrFe_2As_2$. *Physical Review B*, 78:140504, 2008.

[163] K. Kaneko, A. Hoser, N. Caroca-Canales, A. Jesche, C. Krellner, O. Stockert, and C. Geibel. Columnar magnetic structure coupled with orthorhombic distortion in the antiferromagnetic iron arsenide $SrFe_2As_2$. *Physical Review B*, 78:212502, 2008.

[164] Haifeng Li, Wei Tian, Jerel L. Zarestky, Andreas Kreyssig, Ni Ni, Sergey L. Bud'ko, Paul C. Canfield, Alan I. Goldman, Robert J. McQueeney, and David Vaknin. Magnetic and lattice coupling in single-crystal $SrFe_2As_2$: A neutron scattering study. *Physical Review B*, 80:054407, 2009.

[165] Y. Lee, David Vaknin, Haifeng Li, Wei Tian, Jerel L. Zarestky, N. Ni, S. L. Bud'ko, P. C. Canfield, R. J. McQueeney, and B. N. Harmon. Magnetic form factor of iron in $SrFe_2As_2$. *Physical Review B*, 81:060406, 2010.

[166] W. Ratcliff, P. A. Kienzle, Jeffrey W. Lynn, Shiliang Li, Pengcheng Dai, G. F. Chen, and N. L. Wang. Magnetic form factor of $SrFe_2As_2$: Neutron diffraction measurements. *Physical Review B*, 81:140502, 2010.

[167] A. I. Goldman, D. N. Argyriou, B. Ouladdiaf, T. Chatterji, A. Kreyssig, S. Nandi, N. Ni, S. L. Bud'ko, P. C. Canfield, and R. J. McQueeney. Lattice and magnetic instabilities in $CaFe_2As_2$: A single-crystal neutron diffraction study. *Physical Review B*, 78:100506, 2008.

[168] A. Kreyssig, M. A. Green, Y. Lee, G. D. Samolyuk, P. Zajdel, J. W. Lynn, S. L. Bud'ko, M. S. Torikachvili, N. Ni, S. Nandi, J. B. Leão, S. J. Poulton, D. N. Argyriou, B. N. Harmon, R. J. McQueeney, P. C. Canfield, and A. I. Goldman. Pressure-induced volume-collapsed tetragonal phase of $CaFe_2As_2$ as seen via neutron scattering. *Physical Review B*, 78:184517, 2008.

[169] A. I. Goldman, A. Kreyssig, K. Prokeš, D. K. Pratt, D. N. Argyriou, J. W. Lynn, S. Nandi, S. A. J. Kimber, Y. Chen, Y. B. Lee, G. Samolyuk, J. B. Leão, S. J. Poulton, S. L. Bud'ko, N. Ni, P. C. Canfield, B. N. Harmon, and R. J. McQueeney. Lattice collapse and quenching of magnetism in $CaFe_2As_2$ under pressure: A single-crystal neutron and x-ray diffraction investigation. *Physical Review B*, 79:024513, 2009.

[170] K. Prokeš, A. Kreyssig, B. Ouladdiaf, D. K. Pratt, N. Ni, S. L. Bud'ko, P. C. Canfield, R. J. McQueeney, D. N. Argyriou, and A. I. Goldman. Evidence from neutron diffraction for superconductivity in the stabilized tetragonal phase of $CaFe_2As_2$ under uniaxial pressure. *Physical Review B*, 81:180506, 2010.

[171] S. Ran, S. L. Bud'ko, D. K. Pratt, A. Kreyssig, M. G. Kim, M. J. Kramer, D. H. Ryan, W. N. Rowan-Weetaluktuk, Y. Furukawa, B. Roy, A. I. Goldman, and P. C. Canfield. Stabilization of an ambient-pressure collapsed tetragonal phase in $CaFe_2As_2$ and tuning of the orthorhombic-antiferromagnetic transition temperature by over 70 K via control of nanoscale precipitates. *Physical Review B*, 83:144517, 2011.

[172] Javier Herrero-Martín, Valerio Scagnoli, Claudio Mazzoli, Yixi Su, Ranjan Mittal, Yinguo Xiao, Thomas Brueckel, Neeraj Kumar, S. K. Dhar, A. Thamizhavel, and Luigi Paolasini. Magnetic structure of $EuFe_2As_2$ as determined by resonant x-ray scattering. *Physical Review B*, 80:134411, 2009.

[173] Y. Xiao, Y. Su, M. Meven, R. Mittal, C. M. N. Kumar, T. Chatterji, S. Price, J. Persson, N. Kumar, S. K. Dhar, A. Thamizhavel, and Th. Brueckel. Magnetic structure of $EuFe_2As_2$ determined by single-crystal neutron diffraction. *Physical Review B*, 80:174424, 2009.

[174] Q. Huang, Y. Qiu, Wei Bao, M. A. Green, J. W. Lynn, Y. C. Gasparovic, T. Wu, G. Wu, and X. H. Chen. Neutron-diffraction measurements of magnetic order and a structural transition in the parent $BaFe_2As_2$ compound of FeAs-based high-temperature superconductors. *Physical Review Letter*, 101:257003, 2008.

[175] Y. Su, P. Link, A. Schneidewind, Th. Wolf, P. Adelmann, Y. Xiao, M. Meven, R. Mittal, M. Rotter, D. Johrendt, Th. Brueckel, and M. Loewenhaupt. Antiferromagnetic ordering and structural phase transition in $BaFe_2As_2$ with Sn incorporated from the growth flux. *Physical Review B*, 79:064504, 2009.

[176] Simon A. J. Kimber, Andreas Kreyssig, Yu-Zhong Zhang, Harald O. Jeschke, Roser Valentí, Fabiano Yokaichiya, Estelle Colombier, Jiaqiang Yan, Thomas C. Hansen, Tapan Chatterji, Robert J. McQueeney, Paul C. Canfield, Alan I. Goldman, and Dimitri N. Argyriou. Similarities between structural distortions under pressure and chemical doping in superconducting $BaFe_2As_2$. *Nature Materials*, 8:471–475, 2009.

[177] M. Kofu, Y. Qiu, Wei Bao, S.-H. Lee, S. Chang, T. Wu, G. Wu, and X. H. Chen. Neutron scattering investigation of the magnetic order in single crystalline $BaFe_2As_2$. *New Journal of Physics*, 11:055001, 2009.

[178] K. Matan, R. Morinaga, K. Iida, and T. J. Sato. Anisotropic itinerant magnetism and spin fluctuations in $BaFe_2As_2$: A neutron scattering study. *Physical Review B*, 79:054526, 2009.

[179] Stephen D. Wilson, Z. Yamani, C. R. Rotundu, B. Freelon, E. Bourret-Courchesne, and R. J. Birgeneau. Neutron diffraction study of the magnetic and structural phase transitions in $BaFe_2As_2$. *Physical Review B*, 79:184519, 2009.

[180] Stephen D. Wilson, C. R. Rotundu, Z. Yamani, P. N. Valdivia, B. Freelon, E. Bourret-Courchesne, and R. J. Birgeneau. Universal magnetic and structural behaviors in the iron arsenides. *Physical Review B*, 81:014501, 2010.

[181] C. Lester, Jiun-Haw Chu, J. G. Analytis, S. C. Capelli, A. S. Erickson, C. L. Condron, M. F. Toney, I. R. Fisher, and S. M. Hayden. Neutron scattering study of the interplay between structure and magnetism in $Ba(Fe_{1-x}Co_x)_2As_2$. *Physical Review B*, 79:144523, 2009.

[182] D. K. Pratt, W. Tian, A. Kreyssig, J. L. Zarestky, S. Nandi, N. Ni, S. L. Bud'ko, P. C. Canfield, A. I. Goldman, and R. J. McQueeney. Coexistence of competing antiferromagnetic and superconducting phases in the underdoped $Ba(Fe_{0.953}Co_{0.047})_2As_2$ compound using x-ray and neutron scattering techniques. *Physical Review Letter*, 103:087001, 2009.

[183] A. D. Christianson, M. D. Lumsden, S. E. Nagler, G. J. MacDougall, M. A. McGuire, A. S. Sefat, R. Jin, B. C. Sales, and D. Mandrus. Static and dynamic magnetism in underdoped superconductor $BaFe_{1.92}Co_{0.08}As_2$. *Physical Review Letter*, 103:087002, 2009.

[184] Y. Laplace, J. Bobroff, F. Rullier-Albenque, D. Colson, and A. Forget. Atomic coexistence of superconductivity and incommensurate magnetic order in the pnictide $Ba(Fe_{1-x}Co_x)_2As_2$. *Physical Review B*, 80:140501, 2009.

[185] S. Nandi, M. G. Kim, A. Kreyssig, R. M. Fernandes, D. K. Pratt, A. Thaler, N. Ni, S. L. Bud'ko, P. C. Canfield, J. Schmalian, R. J. McQueeney, and A. I. Goldman. Anomalous suppression of the orthorhombic lattice distortion in superconducting $Ba(Fe_{1-x}Co_x)_2As_2$ single crystals. *Physical Review Letter*, 104:057006, 2010.

[186] Rafael M. Fernandes, Daniel K. Pratt, Wei Tian, Jerel Zarestky, Andreas Kreyssig, Shibabrata Nandi, Min Gyu Kim, Alex Thaler, Ni Ni, Paul C. Canfield, Robert J. McQueeney, Jörg Schmalian, and Alan I. Goldman. Unconventional pairing in the iron arsenide superconductors. *Physical Review B*, 81:140501, 2010.

[187] D. K. Pratt, M. G. Kim, A. Kreyssig, Y. B. Lee, G. S. Tucker, A. Thaler, W. Tian, J. L. Zarestky, S. L. Bud'ko, P. C. Canfield, B. N. Harmon, A. I. Goldman, and R. J.

McQueeney. Incommensurate spin-density wave order in electron-doped $BaFe_2As_2$ superconductors. *Physical Review Letter*, 106:257001, 2011.

[188] Miaoyin Wang, Huiqian Luo, Jun Zhao, Chenglin Zhang, Meng Wang, Karol Marty, Songxue Chi, Jeffrey W. Lynn, Astrid Schneidewind, Shiliang Li, and Pengcheng Dai. Electron-doping evolution of the low-energy spin excitations in the iron arsenide superconductor $BaFe_{2-x}Ni_xAs_2$. *Physical Review B*, 81:174524, 2010.

[189] A. Kreyssig, M. G. Kim, S. Nandi, D. K. Pratt, W. Tian, J. L. Zarestky, N. Ni, A. Thaler, S. L. Bud'ko, P. C. Canfield, R. J. McQueeney, and A. I. Goldman. Suppression of antiferromagnetic order and orthorhombic distortion in superconducting $Ba(Fe_{0.961}Rh_{0.039})_2As_2$. *Physical Review B*, 81:134512, 2010.

[190] Miaoyin Wang, Huiqian Luo, Meng Wang, Songxue Chi, Jose A. Rodriguez-Rivera, Deepak Singh, Sung Chang, Jeffrey W. Lynn, and Pengcheng Dai. Magnetic field effect on static antiferromagnetic order and spin excitations in the underdoped iron arsenide superconductor $BaFe_{1.92}Ni_{0.08}As_2$. *Physical Review B*, 83:094516, 2011.

[191] M. P. M. Dean, M. G. Kim, A. Kreyssig, J. W. Kim, X. Liu, P. J. Ryan, A. Thaler, S. L. Bud'ko, W. Strassheim, P. C. Canfield, J. P. Hill, and A. I. Goldman. Magnetically polarized ir dopant atoms in superconducting $Ba(Fe_{1-x}Ir_x)_2As_2$. *Physical Review B*, 85:140514, 2012.

[192] Chang Liu, A. D. Palczewski, R. S. Dhaka, Takeshi Kondo, R. M. Fernandes, E. D. Mun, H. Hodovanets, A. N. Thaler, J. Schmalian, S. L. Bud'ko, P. C. Canfield, and A. Kaminski. Importance of the fermi-surface topology to the superconducting state of the electron-doped pnictide $Ba(Fe_{1-x}Co_x)_2As_2$. *Physical Review B*, 84:020509, 2011.

[193] K. Prokeš, S. Mat'aš, L. Harnagea, S. Singh, S. Wurmehl, D. N. Argyriou, and B. Büchner. Effect of Co substitution on the magnetic order in $Ca(Fe_{1-x}Co_x)_2As_2$ single crystals studied by neutron diffraction. *Physical Review B*, 83:104414, 2011.

[194] S. L. Bud'ko, S. Nandi, N. Ni, A. Thaler, A. Kreyssig, A. Kracher, J.-Q. Yan, A. I. Goldman, and P. C. Canfield. Structural phase transition in $Ba(Fe_{0.973}Cr_{0.027})_2As_2$ single crystals. *Physical Review B*, 80:014522, 2009.

[195] Yogesh Singh, M. A. Green, Q. Huang, A. Kreyssig, R. J. McQueeney, D. C. Johnston, and A. I. Goldman. Magnetic order in $BaMn_2As_2$ from neutron diffraction measurements. *Physical Review B*, 80:100403, 2009.

[196] K. Marty, A. D. Christianson, C. H. Wang, M. Matsuda, H. Cao, L. H. VanBebber, J. L. Zarestky, D. J. Singh, A. S. Sefat, and M. D. Lumsden. Competing magnetic ground states in nonsuperconducting $Ba(Fe_{1-x}Cr_x)_2As_2$ as seen via neutron diffraction. *Physical Review B*, 83:060509, 2011.

[197] J. P. Clancy, B. D. Gaulin, and A. S. Sefat. High-resolution x-ray scattering studies of structural phase transitions in $Ba(Fe_{1-x}Cr_x)_2As_2$. *Physical Review B*, 85:054115, 2012.

[198] Y. Nakai, T. Iye, S. Kitagawa, K. Ishida, H. Ikeda, S. Kasahara, H. Shishido, T. Shibauchi, Y. Matsuda, and T. Terashima. Unconventional superconductivity and antiferromagnetic quantum critical behavior in the isovalent-doped $BaFe_2(As_{1-x}P_x)_2$. *Physical Review Letter*, 105:107003, 2010.

[199] J. T. Park, D. S. Inosov, Ch. Niedermayer, G. L. Sun, D. Haug, N. B. Christensen, R. Dinnebier, A. V. Boris, A. J. Drew, L. Schulz, T. Shapoval, U. Wolff, V. Neu, Xiaoping Yang, C. T. Lin, B. Keimer, and V. Hinkov. Electronic phase separation in the slightly underdoped iron pnictide superconductor $Ba_{1-x}K_xFe_2As_2$. *Physical Review Letter*, 102:117006, 2009.

[200] Marianne Rotter, Marcus Tegel, Inga Schellenberg, Falko M Schappacher, Rainer Pöttgen, Joachim Deisenhofer, Axel Günther, Florian Schrettle, Alois Loidl, and Dirk Johrendt. Competition of magnetism and superconductivity in underdoped $(Ba_{1-x}K_x)Fe_2As_2$. *New Journal of Physics*, 11:025014, 2009.

[201] S. Avci, O. Chmaissem, E. A. Goremychkin, S. Rosenkranz, J.-P. Castellan, D. Y. Chung, I. S. Todorov, J. A. Schlueter, H. Claus, M. G. Kanatzidis, A. Daoud-Aladine,

D. Khalyavin, and R. Osborn. Magnetoelastic coupling in the phase diagram of $Ba_{1-x}K_xFe_2As_2$ as seen via neutron diffraction. *Physical Review B*, 83:172503, 2011.

[202] D. S. Inosov, A. Leineweber, Xiaoping Yang, J. T. Park, N. B. Christensen, R. Dinnebier, G. L. Sun, Ch. Niedermayer, D. Haug, P. W. Stephens, J. Stahn, O. Khvostikova, C. T. Lin, O. K. Andersen, B. Keimer, and V. Hinkov. Suppression of the structural phase transition and lattice softening in slightly underdoped $Ba_{1-x}K_xFe_2As_2$ with electronic phase separation. *Physical Review B*, 79:224503, 2009.

[203] M.-H. Julien, H. Mayaffre, M. Horvati, C. Berthier, X. D. Zhang, W. Wu, G. F. Chen, N. L. Wang, and J. L. Luo. Homogeneous vs. inhomogeneous coexistence of magnetic order and superconductivity probed by NMR in Co- and K-doped iron pnictides. *Europhysics Letters*, 87:37001, 2009.

[204] Erwin Wiesenmayer, Hubertus Luetkens, Gwendolyne Pascua, Rustem Khasanov, Alex Amato, Heidi Potts, Benjamin Banusch, Hans-Henning Klauss, and Dirk Johrendt. Microscopic coexistence of superconductivity and magnetism in $Ba_{1-x}K_xFe_2As_2$. *Physical Review Letter*, 107:237001, 2011.

[205] S. R. Saha, N. P. Butch, T. Drye, J. Magill, S. Ziemak, K. Kirshenbaum, P. Y. Zavalij, J. W. Lynn, and J. Paglione. Structural collapse and superconductivity in rare-earth-doped $CaFe_2As_2$. *Physical Review B*, 85:024525, 2012.

[206] Shiliang Li, Clarina de la Cruz, Q. Huang, G. F. Chen, T.-L. Xia, J. L. Luo, N. L. Wang, and Pengcheng Dai. Structural and magnetic phase transitions in $Na_{1-\delta}FeAs$. *Physical Review B*, 80:020504, 2009.

[207] J. D. Wright, T. Lancaster, I. Franke, A. J. Steele, J. S. Möller, M. J. Pitcher, A. J. Corkett, D. R. Parker, D. G. Free, F. L. Pratt, P. J. Baker, S. J. Clarke, and S. J. Blundell. Gradual destruction of magnetism in the superconducting family $NaFe_{1-x}Co_xAs$. *Physical Review B*, 85:054503, 2012.

[208] Shiliang Li, Clarina de la Cruz, Q. Huang, Y. Chen, J. W. Lynn, Jiangping Hu, Yi-Lin Huang, Fong-Chi Hsu, Kuo-Wei Yeh, Maw-Kuen Wu, and Pengcheng Dai. First-

order magnetic and structural phase transitions in $Fe_{1+y}Se_xTe_{1-x}$. *Physical Review B*, 79:054503, 2009.

[209] Serena Margadonna, Yasuhiro Takabayashi, Martin T. McDonald, Karolina Kasperkiewicz, Yoshikazu Mizuguchi, Yoshihiko Takano, Andrew N. Fitch, Emmanuelle Suard, and Kosmas Prassides. Crystal structure of the new $FeSe_{1-x}$ superconductor. *Chemical Communications*, pages 5607–5609, 2008.

[210] Satoshi Iikubo, Masaki Fujita, Seiji Niitaka, and Hidenori Takagi. Antiferromagnetic fluctuations in $Fe(Se_{1-x}Te_x)_{0.92}$ ($x = 0.75$, 1) observed by inelastic neutron scattering. *Journal of the Physical Society of Japan*, 78:103704, 2009.

[211] A. Martinelli, A. Palenzona, M. Tropeano, C. Ferdeghini, M. Putti, M. R. Cimberle, T. D. Nguyen, M. Affronte, and C. Ritter. From antiferromagnetism to superconductivity in $Fe_{1+y}Te_{1-x}Se_x$ ($0 \leq x \leq 0.20$): Neutron powder diffraction analysis. *Physical Review B*, 81:094115, 2010.

[212] D. Fruchart, P. Convert, P. Wolfers, R. Madar, J.P. Senateur, and R. Fruchart. Structure antiferroma gnetique de $Fe_{1.125}Te$ accompagnee d'une deformation monoclinique. *Materials Research Bulletin*, 10:169 – 174, 1975.

[213] R. Khasanov, M. Bendele, A. Amato, P. Babkevich, A. T. Boothroyd, A. Cervellino, K. Conder, S. N. Gvasaliya, H. Keller, H.-H. Klauss, H. Luetkens, V. Pomjakushin, E. Pomjakushina, and B. Roessli. Coexistence of incommensurate magnetism and superconductivity in $Fe_{1+y}Se_xTe_{1-x}$. *Physical Review B*, 80:140511, 2009.

[214] Kazumasa Horigane, Haruhiro Hiraka, and Kenji Ohoyama. Relationship between structure and superconductivity in $FeSe_{1-x}Te_x$. *Journal of the Physical Society of Japan*, 78:074718, 2009.

[215] Jinsheng Wen, Guangyong Xu, Zhijun Xu, Zhi Wei Lin, Qiang Li, W. Ratcliff, Genda Gu, and J. M. Tranquada. Short-range incommensurate magnetic order near the superconducting phase boundary in $Fe_{1+\delta}Te_{1-x}Se_x$. *Physical Review B*, 80:104506, 2009.

[216] Naoyuki Katayama, Sungdae Ji, Despina Louca, Seunghun Lee, Masaki Fujita, Taku J. Sato, Jinsheng Wen, Zhijun Xu, Genda Gu, Guangyong Xu, Ziwei Lin, Masanori Enoki, Sung Chang, Kazuyoshi Yamada, and John M. Tranquada. Investigation of the spin-glass regime between the antiferromagnetic and superconducting phases in $Fe_{1+y}Se_xTe_{1-x}$. *Journal of the Physical Society of Japan*, 79:113702, 2010.

[217] Nathalie C. Gresty, Yasuhiro Takabayashi, Alexey Y. Ganin, Martin T. McDonald, John B. Claridge, Duong Giap, Yoshikazu Mizuguchi, Yoshihiko Takano, Tomoko Kagayama andYasuo Ohishi, Masaki Takata, Matthew J. Rosseinsky, Serena Margadonna, and Kosmas Prassides. Structural phase transitions and superconductivity in $Fe_{1+\delta}Se_{0.57}Te_{0.43}$ at ambient and elevated pressures. *Journal of the American Chemical Society*, 131:16944–16952, 2009.

[218] M. Tegel, C. Löhnert, and D. Johrendt. The crystal structure of $FeSe_{0.44}Te_{0.56}$. *Solid State Communications*, 150:383–385, 2010.

[219] P. Babkevich, M. Bendele, A. T. Boothroyd, K. Conder, S. N. Gvasaliya, R. Khasanov, E. Pomjakushina, and B. Roessli. Magnetic excitations of $Fe_{1+y}Se_xTe_{1-x}$ in magnetic and superconductive phases. *Journal of Physics: Condensed Matter*, 22:142202, 2010.

[220] George Grüner. Density waves in solids. *Perseus Publishing*, Cambridge, USA, 1994.

[221] Bruce N. Harmon. private communication. 2012.

[222] A. B. Vorontsov, M. G. Vavilov, and A. V. Chubukov. Superconductivity and spin-density waves in multiband metals. *Physical Review B*, 81:174538, 2010.

[223] Edited by Ø. Fischer and M. B. Maple. Topics in Current Physics. *Springer-Verlag, New York*, 1983.

[224] Paul C. Canfield, Peter L. Gammel, and David J. Bishop. New magnetic superconductors: A toy box for solid-state physicists. *Physics Today*, 51:40, 1998.

[225] J. W. Lynn, B. Keimer, C. Ulrich, C. Bernhard, and J. L. Tallon. Antiferromagnetic ordering of Ru and Gd in superconducting $RuSr_2GdCu_2O_8$. *Physical Review B*, 61:R14964–R14967, 2000.

[226] G. Aeppli, E. Bucher, C. Broholm, J. K. Kjems, J. Baumann, and J. Hufnagl. Magnetic order and fluctuations in superconducting UPt_3. *Physical Review Letter*, 60:615–618, 1988.

[227] E. D. Isaacs, P. Zschack, C. L. Broholm, C. Burns, G. Aeppli, A. P. Ramirez, T. T. M. Palstra, R. W. Erwin, N. Stücheli, and E. Bucher. Antiferromagnetism and its relation to the superconducting phases of UPt_3. *Physical Review Letter*, 75:1178–1181, 1995.

[228] J. G. Lussier, M. Mao, A. Schröder, J. D. Garrett, B. D. Gaulin, S. M. Shapiro, and W. J. L. Buyers. Neutron-scattering study of incommensurate magnetic order in the heavy-fermion superconductor UNi_2Al_3. *Physical Review B*, 56:11749–11760, 1997.

[229] Daniel K. Pratt. Studies of long range order and excitations in the iron arsenide superconductors. *Ph. D. thesis at Iowa State University*, Ames, USA, 2011.

[230] R. M. Fernandes, L. H. VanBebber, S. Bhattacharya, P. Chandra, V. Keppens, D. Mandrus, M. A. McGuire, B. C. Sales, A. S. Sefat, and J. Schmalian. Effects of nematic fluctuations on the elastic properties of iron arsenide superconductors. *Physical Review Letter*, 105:157003, 2010.

[231] A. Cano, M. Civelli, I. Eremin, and I. Paul. Interplay of magnetic and structural transitions in iron-based pnictide superconductors. *Physical Review B*, 82:020408, 2010.

[232] B. D. Cullity. Elements of x-ray diffraction. *Addison-Wesley Publishing Company*, Reading, USA, 1956.

[233] F. de Bergevin and M. Brunel. Observation of magnetic superlattice peaks by x-ray diffration on an antiferromagnetic NiO crystal. *Physical Review Lett*, 34:141, 1972.

[234] Dennis M. Mills. Third-generation hard x-ray synchrotron radiation sources: source propeties, optics, and experimental techniques. *Wiley-VCH*, New York, USA, 2002.

[235] Philip John Duke. Synchrotron radiation: Production and properties. *Oxford University Press*, Oxford, Great Britain, 2009.

[236] D. Gibbs, D. E. Moncton, K. L. D'Amico, J. Bohr, and B. H. Grier. Magnetic x-ray scattering studies of holmium using synchrotron radiation. *Physical Review Letter*, 55:234, 1985.

[237] S. W. Lovesey and S. P. Collins. X-ray scattering and absorption by magnetic materials. *Oxford Science Publications*, Oxford, Great Britain, 1996.

[238] J. P. Hannon, G. T. Trammell, M. Blume, and Doon Gibbs. X-ray resonance exchange scattering. *Physical Review Letter*, 61:1245, 1988.

[239] E. D. Isaacs, D. B. McWhan, C. Peters, G. E. Ice, D. P. Siddons, J. B. Hastings, C. Vettier, and O. Vogt. X-ray resonance exchange scattering in UAs. *Physical Review Letter*, 62:1671–1674, 1989.

[240] Hélio C. N. Tolentino, Júlio C. Cezar, Narcizo M. Souza-Neto, and Aline Y. Ramos. Linear and circularly polarized light to study anisotropy and resonant scattering in magnetic thin films. *Journal of Synchrotron Radiation*, 12:168–176, 2004.

[241] J. P. Hill and D. F. McMorrow. Resonant exchange scattering: Polarization dependence and correlation function. *Acta Crystallographica, Section A: Foundations of Crystallography*, 52:236, 1996.

[242] B. Bohnenbuck, I. Zegkinoglou, J. Strempfer, C. Schüßler-Langeheine, C. S. Nelson, Ph. Leininger, H.-H. Wu, E. Schierle, J. C. Lang, G. Srajer, S. I. Ikeda, Y. Yoshida, K. Iwata, S. Katano, N. Kikugawa, and B. Keimer. Magnetic structure and orbital state of $Ca_3Ru_2O_7$ investigated by resonant x-ray diffraction. *Physical Review B*, 77:224412, 2008.

[243] Carsten Detlefs. X-ray resonant exchange scattering of rare-earth nickel borocarbides. *Ph. D. thesis at Iowa State University*, Ames, USA, 1997.

[244] Jong-Woo Kim. Investigations of the RNi$_2$Ge$_2$ intermetallic compounds by x-ray resonant magnetic scattering. *Ph. D. thesis at Iowa State University*, Ames, USA, 2005.

[245] Shibabrata Nandi. X-ray resonant magnetic scattering investigations of hexagonal multiferroics RMnO$_3$ (R = Dy, Ho, Er). *Ph. D. thesis at Iowa State University*, Ames, USA, 2009.

[246] J. P. Hill, G. Helgesen, and Doon Gibbs. X-ray-scattering study of charge- and spin-density waves in chromium. *Physical Review B*, 51:10336–10344, 1995.

[247] A. I. Goldman, K. Mohanty, G. Shirane, P. M. Horn, R. L. Greene, C. J. Peters, T. R. Thurston, and R. J. Birgeneau. Magnetic x-ray scattering measurements on MnF$_2$. *Physical Review B*, 36:5609–5612, 1987.

[248] M. Brunel and F. de Baergevin. Diffraction of x-ray by magnetic materials. II. measurements on antiferromagnetic Fe$_2$O$_3$. *Acta Crystallographica*, A37:324–331, 1981.

[249] Kazumichi Namikawa, Masami Ando, and Tetsuo Nakajima. X-ray resonant magnetic scattering. *Journal of the Physical Society of Japan*, 54:4099–4102, 1985.

[250] C. Kao, J. B. Hastings, E. D. Johnson, D. P. Siddons, G. C. Smith, and G. A. Prinz. Magnetic-resonance exchange scattering at the iron $L_{\rm II}$ and $L_{\rm III}$ edges. *Physical Review Letter*, 65:373–376, 1990.

[251] J. M. Tonnerre, M. Jergel, D. Raoux, M. Idir, G. Soullier, R. Barchewitz, and B. Rodmacq. Resonant magnetic soft x-ray diffraction at Ni L$_{II}$ edge: ferro- and antiferromagnetism in Ag-Ni multilayers. *Journal of Magnetism and Magnetic Materials*, 121:230–233, 1993.

[252] J. P. Hill, C.-C. Kao, and D. F. McMorrow. K-edge resonant x-ray magnetic scattering from a transition-metal oxide: NiO. *Physical Review B*, 55:R8662–R8665, 1997.

[253] W. Neubeck, C. Vettier, K.-B. Lee, and F. de Bergevin. K-edge resonant x-ray magnetic scattering from CoO. *Physical Review B*, 60:R9912–R9915, 1999.

[254] A. Stunault, F. de Bergevin, D. Wermeille, C. Vettier, Th. Brückel, N. Bernhoeft, G. J. McIntyre, and J. Y. Henry. K-edge resonant x-ray magnetic scattering from $RbMnF_3$. *Physical Review B*, 60:10170–10179, 1999.

[255] J. P. Hill, D. F. McMorrow, A. T. Boothroyd, A. Stunault, C. Vettier, L. E. Berman, M. v. Zimmermann, and Th. Wolf. X-ray-scattering study of copper magnetism in non-superconducting $PrBa_2Cu_3O_{6.92}$. *Physical Review B*, 61:1251–1255, 2000.

[256] Manabu Takahashi, Manabu Usuda, and Jun-ichi Igarashi. Magnetic resonant x-ray scattering in $KCuF_3$. *Physical Review B*, 67:064425, 2003.

[257] S. B. Wilkins, P. D. Hatton, M. D. Roper, D. Prabhakaran, and A. T. Boothroyd. Soft x-ray resonant magnetic diffraction. *Physical Review Letter*, 90:187201, 2003.

[258] S. B. Wilkins, N. Stojić, T. A. W. Beale, N. Binggeli, C. W. M. Castleton, P. Bencok, D. Prabhakaran, A. T. Boothroyd, P. D. Hatton, and M. Altarelli. Resonant soft x-ray scattering investigation of orbital and magnetic ordering in $La_{0.5}Sr_{1.5}MnO_4$. *Physical Review B*, 71:245102, 2005.

[259] Th. Brückel. Lecture notes on "Scattering techniques II: Magnetic X-ray Scattering". http://www.fz-juelich.de/SharedDocs/Downloads/PGI/PGI-4/EN/Skript_FS05_pdf.html, 2005.

[260] I. Zegkinoglou, J. Strempfer, C. S. Nelson, J. P. Hill, J. Chakhalian, C. Bernhard, J. C. Lang, G. Srajer, H. Fukazawa, S. Nakatsuji, Y. Maeno, and B. Keimer. Orbital ordering transition in Ca_2RuO_4 observed with resonant x-ray diffraction. *Physical Review Letter*, 95:136401, 2005.

[261] B. Bohnenbuck, I. Zegkinoglou, J. Strempfer, C. S. Nelson, H.-H. Wu, C. Schüßler-Langeheine, M. Reehuis, E. Schierle, Ph. Leininger, T. Herrmannsdörfer, J. C. Lang, G. Srajer, C. T. Lin, and B. Keimer. Magnetic structure of $RuSr_2GdCu_2O_8$ determined by resonant x-ray diffraction. *Physical Review Letter*, 102:037205, 2009.

[262] F. de Bergevin, M. Brunel, R. M. Galèra, C. Vettier, E. Elkaïm, M. Bessière, and S. Lefèbvre. X-ray resonant scattering in the ferromagnet CoPt. *Physical Review B*, 46:10772–10776, 1992.

[263] D. Mannix, S. Coad, G. H. Lander, J. Rebizant, P. J. Brown, J. A. Paixão, S. Langridge, S. Kawamata, and Y. Yamaguchi. Neutron and synchrotron diffraction study of UPtGe. *Physical Review B*, 62:3801–3810, 2000.

[264] D. F. McMorrow, S. E. Nagler, K. A. McEwen, and S. D. Brown. Large enhancement of x-ray magnetic scattering at the L edge of the 5d transition metal antiferromagnet K_2ReCl_6. *Journal of Physics: Condensed Matter*, 15:L59–L66, 2003.

[265] B. J. Kim, H. Ohsumi, T. Komesu, S. Sakai, T. Morita, H. Takagi, and T. Arima. Phase-sensitive observation of a spin-orbit mott state in Sr_2IrO_4. *Science*, 323:1329, 2009.

[266] X. Liu, T. Berlijn, W.-G. Yin, W. Ku, A. Tsvelik, Young-June Kim, H. Gretarsson, Yogesh Singh, P. Gegenwart, and J. P. Hill. Long-range magnetic ordering in Na_2IrO_3. *Physical Review B*, 83:220403, 2011.

[267] Kenya Ohgushi, Jun ichi Yamaura, Hiroyuki Ohsumi, Kunihisa Sugimoto, Soshi Takeshita, Akihisa Tokuda, Hidenori Takagi, Masaki Takata, and Taka hisa Arima. Resonant x-ray diffration study of strongly spin-orbit-coupled mott insulator $CaIrO_3$. *arXiv:1108.4523v1*, 2011.

[268] Stephen W. Lovesey. Theory of neutron scattering from condensed matter. *Oxford Science Publications*, Volume 2, Oxford, Great Britain, 1984.

[269] Kurt Sköld and David L. Price. Methods of experimental physics Part A. *Academic Press*, Volume 23, Orlando, USA, 1986.

[270] Yimei Zhu. Modern techniques for charaterizing magnetic materials. *Springer*, Chapter 1, New York, USA, 2005.

[271] Tapan Chatterji. Neutron scattering from magnetic materials. *Elsevier*, Amsterdam, Netherlands, 2006.

[272] Kurt Sköld and David L. Price. Methods of experimental physics Part C. *Academic Press*, Volume 23, Orlando, USA, 1986.

[273] Gen Shirane, Stephen M. Shapiro, and John M. Tranquada. Neutron scattering with a triple-axis spectrometer. *Cambridge University Press*, Cambridge, Great Britain, 2002.

[274] N. Ni, M. E. Tillman, J.-Q. Yan, A. Kracher, S. T. Hannahs, S. L. Bud'ko, and P. C. Canfield. Effects of co substitution on thermodynamic and transport properties and anisotropic H_{c2} in $Ba(Fe_{1-x}Co_x)_2As_2$ single crystals. *Physical Review B*, 78:214515, 2008.

[275] M. A. Tanatar, A. Kreyssig, S. Nandi, N. Ni, S. L. Bud'ko, P. C. Canfield, A. I. Goldman, and R. Prozorov. Direct imaging of the structural domains in the iron pnictides AFe_2As_2 (A= Ca, Sr, Ba). *Physical Review B*, 79:180508, 2009.

[276] W. Neubeck, C. Vettier, F. de Bergevin, F. Yakhou, D. Mannix, O. Bengone, M. Alouani, and A. Barbier. Probing the $4p$ electron-spin polarization in NiO. *Physical Review B*, 63:134430, 2001.

[277] P. Blaha, K. Schwarz, GKH Madsen, D. Kvasnicka, and J. Luitz. Wien2K: An Augmented Plane Wave + Local Orbitals Program for Calculating Crystal Properties. *Karlheinz Schwarz, Techn. Universität Wien, Austria*, 2001.

[278] John P. Perdew and Yue Wang. Accurate and simple analytic representation of the electron-gas correlation energy. *Physical Review B*, 45:13244–13249, 1992.

[279] M. O. Krause and J. H. Oliver. Natural width of atomic K and L levels, K_α X-ray lines and several KLL auger lines. *Journal of Physical and Chemical Reference Data*, 8:329, 2001.

[280] C. R. Rotundu, B. Freelon, T. R. Forrest, S. D. Wilson, P. N. Valdivia, G. Pinuellas, A. Kim, J.-W. Kim, Z. Islam, E. Bourret-Courchesne, N. E. Phillips, and R. J. Birgeneau. Heat capacity study of $BaFe_2As_2$: Effects of annealing. *Physical Review B*, 82:144525, 2010.

[281] P. M. Chaikin and T. C. Lubensky. Principles of condensed matter physics. *Cambridge University Press*, Cambridge, Great Britain, 1995.

[282] Chen Fang, Hong Yao, Wei-Feng Tsai, JiangPing Hu, and Steven A. Kivelson. Theory of electron nematic order in LaFeAsO. *Physical Review B*, 77:224509, 2008.

[283] Cenke Xu, Markus Müller, and Subir Sachdev. Ising and spin orders in the iron-based superconductors. *Physical Review B*, 78:020501, 2008.

[284] P. Chandra, P. Coleman, and A. I. Larkin. Ising transition in frustrated heisenberg models. *Physical Review Letter*, 64:88–91, 1990.

[285] I. Eremin and A. V. Chubukov. Magnetic degeneracy and hidden metallicity of the spin-density-wave state in ferropnictides. *Physical Review B*, 81:024511, 2010.

[286] Victor Barzykin and Lev P. Gor'kov. Role of striction at magnetic and structural transitions in iron pnictides. *Physical Review B*, 79:134510, 2009.

[287] Yang Qi and Cenke Xu. Global phase diagram for magnetism and lattice distortion of iron-pnictide materials. *Physical Review B*, 80:094402, 2009.

[288] Giuseppe Fadda, Lev Truskinovsky, and Giovanni Zanzotto. Unified landau description of the tetragonal, orthorhombic, and monoclinic phases of zirconia. *Physical Review B*, 66:174107, 2002.

[289] M. Yoshizawa, D. Kimura, T. Chiba, S. Simayi, Y. Nakanish, K. Kihou, C.-H. Lee, A. Iyo, H. Eisaki, M. Nakajima, and S. Uchida. Structural quantum criticality and superconductivity in iron-based superconductor $Ba(Fe_{1-x}Co_x)_2As_2$. *Journal of the Physical Society of Japan*, 81:024604, 2012.

[290] C. Liu, T. Kondo, R. M. Fernandes, A. D. Palczewski, E. D. Mun, N. Ni, A. N. Thaler, A. Bostwick, E. Rotenberg, J. Schmalian, S. L. Bud'ko, P. C. Canfield, and A. Kaminski. *Nature Physics*, 6:419, 2010.

[291] Paul C. Canfield and Sergey L. Bud'ko. FeAs-based superconductivity: A case study of the effects of transition metal doping on $BaFe_2As_2$. *Annual Review of Condensed Matter Physics*, 1:27–50, 2010.

[292] L. E. Klintberg, S. K. Goh, S. Kasahar, Y. Nakai, K. Ishida, M. Sutherland, T. Shibauchi, Y. Matsuda, and T. Terashima. Chemical pressure and physical pressure in $BaFe_2(As_{1-x}P_x)_2$. *Journal of the Physical Society of Japan*, 79:123706, 2010.

[293] H. Shishido, A. F. Bangura, A. I. Coldea, S. Tonegawa, K. Hashimoto, S. Kasahara, P. M. C. Rourke, H. Ikeda, T. Terashima, R. Settai, Y. Omacrnuki, D. Vignolles, C. Proust, B. Vignolle, A. McCollam, Y. Matsuda, T. Shibauchi, and A. Carrington. Evolution of the fermi surface of $BaFe_2(As_{1-x}P_x)_2$ on entering the superconducting dome. *Physical Review Letter*, 104:057008, 2010.

[294] F. Rullier-Albenque, D. Colson, A. Forget, P. Thuéry, and S. Poissonnet. Hole and electron contributions to the transport properties of $Ba(Fe_{1-x}Ru_x)_2As_2$ single crystals. *Physical Review B*, 81:224503, 2010.

[295] V. Brouet, F. Rullier-Albenque, M. Marsi, B. Mansart, M. Aichhorn, S. Biermann, J. Faure, L. Perfetti, A. Taleb-Ibrahimi, P. Le Fèvre, A. Forget, and D. Colson. Significant reduction of electronic correlations upon isovalent Ru substitution of $BaFe_2As_2$. *Physical Review Letter*, 105:087001, 2010.

[296] R. S. Dhaka, Chang Liu, R. M. Fernandes, Rui Jiang, C. P. Strehlow, Takeshi Kondo, A. Thaler, Jörg Schmalian, S. L. Bud'ko, P. C. Canfield, and Adam Kaminski. What controls the phase diagram and superconductivity in ru-substituted $BaFe_2As_2$. *Physical Review Letter*, 107:267002, 2011.

[297] D. J. Singh, A. S. Sefat, M. A. McGuire, B. C. Sales, D. Mandrus, L. H. VanBebber, and V. Keppens. Itinerant antiferromagnetism in $BaCr_2As_2$: Experimental characterization and electronic structure calculations. *Physical Review B*, 79:094429, 2009.

[298] Weicheng Lv, Jiansheng Wu, and Philip Phillips. Orbital ordering induces structural phase transition and the resistivity anomaly in iron pnictides. *Physical Review B*, 80:224506, 2009.

[299] C.-C. Chen, J. Maciejko, A. P. Sorini, B. Moritz, R. R. P. Singh, and T. P. Devereaux. Orbital order and spontaneous orthorhombicity in iron pnictides. *Physical Review B*, 82:100504, 2010.

[300] A. B. Vorontsov, M. G. Vavilov, and A. V. Chubukov. Interplay between magnetism and superconductivity in the iron pnictides. *Physical Review B*, 79:060508, 2009.

[301] Vladimir Cvetkovic and Zlatko Tesanovic. Valley density-wave and multiband superconductivity in iron-based pnictide superconductors. *Physical Review B*, 80:024512, 2009.

[302] J. Fink, S. Thirupathaiah, R. Ovsyannikov, H. A. Dürr, R. Follath, Y. Huang, S. de Jong, M. S. Golden, Yu-Zhong Zhang, H. O. Jeschke, R. Valentí, C. Felser, S. Dastjani Farahani, M. Rotter, and D. Johrendt. Electronic structure studies of $BaFe_2As_2$ by angle-resolved photoemission spectroscopy. *Physical Review B*, 79:155118, 2009.

[303] P. Vilmercati, A. Fedorov, I. Vobornik, U. Manju, G. Panaccione, A. Goldoni, A. S. Sefat, M. A. McGuire, B. C. Sales, R. Jin, D. Mandrus, D. J. Singh, and N. Mannella. Evidence for three-dimensional Fermi-surface topology of the layered electron-doped iron superconductor $Ba(Fe_{1-x}Co_x)_2As_2$. *Physical Review B*, 79:220503, 2009.

[304] D. J. Singh. Electronic structure and doping in $BaFe_2As_2$ and lifeas: Density functional calculations. *Physical Review B*, 78:094511, 2008.

[305] J. T. Park, D. S. Inosov, A. Yaresko, S. Graser, D. L. Sun, Ph. Bourges, Y. Sidis, Yuan Li, J.-H. Kim, D. Haug, A. Ivanov, K. Hradil, A. Schneidewind, P. Link, E. Faulhaber, I. Glavatskyy, C. T. Lin, B. Keimer, and V. Hinkov. Symmetry of spin excitation spectra in the tetragonal paramagnetic and superconducting phases of 122-ferropnictides. *Physical Review B*, 82:134503, 2010.

[306] S. Graser, A. F. Kemper, T. A. Maier, H.-P. Cheng, P. J. Hirschfeld, and D. J. Scalapino. Spin fluctuations and superconductivity in a three-dimensional tight-binding model for $BaFe_2As_2$. *Physical Review B*, 81:214503, 2010.

[307] P. Bonville, F. Rullier-Albenque, D. Colson, and A. Forget. Incommensurate spin density wave in Co-doped $BaFe_2As_2$. *Europhysics Letters*, 89:67008, 2010.

[308] A. Olariu, P. Bonville, F. Rullier-Albenque, D. Colson, and A. Forget. Incommensurate spin density wave versus local magnetic inhomogeneities in $Ba(Fe_{1-x}Ni_x)_2As_2$: a ^{57}Fe Mössbauer spectroscopy study. *New Journal of Physics*, 14:053044, 2012.

[309] P. Marsik, K. W. Kim, A. Dubroka, M. Rössle, V. K. Malik, L. Schulz, C. N. Wang, Ch. Niedermayer, A. J. Drew, M. Willis, T. Wolf, and C. Bernhard. Coexistence and competition of magnetism and superconductivity on the nanometer scale in underdoped $BaFe_{1.89}Co_{0.11}As_2$. *Physical Review Letter*, 105:057001, 2010.

[310] F. L. Ning, K. Ahilan, T. Imai, A. S. Sefat, R. Jin, M. A. McGuire, B. C. Sales, and D. Mandrus. ^{59}Co and ^{75}As NMR investigation of lightly doped $Ba(Fe_{1-x}Co_x)_2As_2$ (x=0.02,0.04). *Physical Review B*, 79:140506, 2009.

[311] A. F. Kemper, C. Cao, P. J. Hirschfeld, and H.-P. Cheng. Effects of cobalt doping and three-dimensionality in $BaFe_2As_2$. *Physical Review B*, 80:104511, 2009.

[312] A. P. Dioguardi, N. apRobertsWarren, A. C. Shockley, S. L. Bud'ko, N. Ni, P. C. Canfield, and N. J. Curro. Local magnetic inhomogeneities in $Ba(Fe_{1-x}Ni_x)_2As_2$ as seen via ^{75}As NMR. *Physical Review B*, 82:140411, 2010.

[313] E. Fawcett et al. Spin-density-wave antiferromagnetism in chromium alloys. *Reviews of Modern Physics*, 66:25, 1994.

[314] B. J. Sternlieb et al. Magnetism in the spin-density-wave alloy $Cr_{1-x}Mn_x$ (x=0.007). *Physical Review B*, 50:16438–16443, 1994.

[315] R. S. Eccleston et al. Calorimetric and neutron diffraction studies of the commensurate - incommensurate spin-density-wave phase transition of Cr+0.3 at.% Ru alloy. *Journal of Physics: Condensed Matter*, 8:7837, 1996.

[316] R. S. Fishman and S. H. Liu. Free energy and phase diagram of chromium alloys. *Physical Review B*, 48:3820–3829, 1993.

[317] N. Ni, A. Thaler, J. Q. Yan, A. Kracher, E. Colombier, S. L. Bud'ko, P. C. Canfield, and S. T. Hannahs. Temperature versus doping phase diagrams for $Ba(Fe_{1-x}TM_x)_2As_2$ (TM = Ni, Cu, Co, Cu/Co) single crystals. *Physical Review B*, 82:024519, 2010.

[318] R. M. Fernandes, M. G. Vavilov, and A. V. Chubukov. Enhancement of T_c by disorder in underdoped iron pnictide superconductors. *Physical Review B*, 85:140512, 2012.

[319] H. Wadati, I. Elfimov, and G. A. Sawatzky. Where are the extra d electrons in transition-metal-substituted iron pnictides? *Physical Review Letter*, 105:157004, 2010.

[320] E. M. Bittar, C. Adriano, T. M. Garitezi, P. F. S. Rosa, L. Mendonça-Ferreira, F. Garcia, G. de M. Azevedo, P. G. Pagliuso, and E. Granado. Co-substitution effects on the Fe valence in the $BaFe_2As_2$ superconducting compound: A study of hard x-ray absorption spectroscopy. *Physical Review Letter*, 107:267402, 2011.

[321] G. Levy, R. Sutarto, D. Chevrier, T. Regier, R. Blyth, J. Geck, S. Wurmehl, L. Harnagea, H. Wadati, T. Mizokawa, I.S. Elfimov, A. Damascelli, and G.A. Sawatzky. Probing the role of Co substitution in the elctronic structure of iron-pnictide. *arXiv:1203.5814v1*, 2012. unpublished.

[322] D. K. Pratt, M. G. Kim, A. Kreyssig, Y. B. Lee, G. S. Tucker, A. Thaler, W. Tian, J. L. Zarestky, S. L. Bud'ko, P. C. Canfield, B. N. Harmon, A. I. Goldman, and R. J. McQueeney. Incommensurate spin-density wave order in electron-doped $BaFe_2As_2$ superconductors. *Physical Review Letter*, 106:257001, 2011.

[323] Huiqian Luo, Rui Zhang, Mark Laver, Zahra Yamani, Meng Wang, Xingye Lu, Miaoyin Wang, Yanchao Chen, Shiliang Li, Sung Chang, Jeffrey W. Lynn, and Pengcheng Dai.

Coexistence and competition of the short-range incommensurate antiferromagnetic order with the superconducting state of $BaFe_{2-x}Ni_xAs_2$. *Physical Review Letter*, 108:247002, 2012.

[324] J. T. Park et al. Symmetry of spin excitation spectra in the tetragonal paramagnetic and superconducting phases of 122-ferropnictides. *Physical Review B*, 82:134503, 2010.

[325] D. D. Johnson, D. M. Nicholson, F. J. Pinski, B. L. Gyorffy, and G. M. Stocks. Density-Functional Theory for Random Alloys: Total Energy within the Coherent-Potential Approximation. *Physical Review Letter*, 56:2088–2091, 1986.

[326] Aftab Alam and D. D. Johnson. Optimal site-centered electronic structure basis set from a displaced-center expansion: Improved results via *a priori* estimates of saddle points in the density. *Physical Review B*, 80:125123, 2009.

[327] Aftab Alam, Brent Kraczek, and D. D. Johnson. Structural, magnetic, and defect properties of Co-Pt-type magnetic-storage alloys: Density-functional theory study of thermal processing effects. *Physical Review B*, 82:024435, 2010.

[328] Tom Berlijn, Chia-Hui Lin, William Garber, and Wei Ku. Do transition-metal substitutions dope carriers in iron-based superconductors? *Physical Review Letter*, 108:207003, 2012.

[329] M. G. Vavilov and A. V. Chubukov. Phase diagram of iron pnictides if doping acts as a source of disorder. *Physical Review B*, 84:214521, 2011.

[330] G. S. Tucker, D. K. Pratt, M. G. Kim, S. Ran, A. Thaler, G. E. Granroth, K. Marty, W. Tian, J. L. Zarestky, M. D. Lumsden, S. L. Bud'ko, P. C. Canfield, A. Kreyssig, A. I. Goldman, and R. J. McQueeney. Competition between stripe and checkerboard magnetic instabilities in Mn-doped $BaFe_2As_2$. *Physical Review B*, 86:020503, 2012.

ACKNOWLEDGMENTS

Foremost, I am deeply grateful to my advisors Alan I. Goldman and Andreas Kreyssig; working with them has been an invaluable experience. They continuously stimulate my curiosity; motivate new ideas; enable me to test my ideas; encourage me to participate in intense discussion; guide and enlighten me when lost in physical, intellectual, and reciprocal spaces. I have been very privileged to get to know them and to be trained by them. My time as a Ph.D. student was sometimes very tough and painful but ultimately successful and worthwhile; I could not imagine a better experience.

Second of all, I would like to thank Robert J. McQueeney, the Ames Laboratory FWP leader. He guided me through inelastic neutron scattering. Whenever I struggled with interpreting inelastic neutron data, he took his time and explained everything to me in great detail. These discussions provided me with a deeper understanding of neutron scattering experiments.

I can not thank enough the people who helped me with my experiments. I would like to thank Paul C. Canfield and his pirates in Zaffarano Hall − Sergey Bud'ko, Ni Ni, Alex Thaler, and Sheng Ran − for their excellent single crystals. I especially thank Alex Thaler and Sheng Ran for their immediate help with characterization of samples and sample preparation. I also would like to thank Jerel Zarestky and Wei Tian for their help with neutron diffraction experiments. Without a wide variety of help from Jerel Zarestky and Wei Tian, I would have failed all the experiments that I performed at the High Flux Isotope Reactor. In addition, I would like to thank Mark Lumsden, Andrew Christianson, and Karol Marty for their assistance with inelastic neutron scattering experiments at the Oak Ridge National Laboratory. Their contribution to my work was indispensable. I would like to thank Jong-Woo Kim, Douglas Robinson, Phillip Ryan, and Jonathan Lang for their enthusiastic help with x-ray resonant magnetic scattering experiments at the Advanced Photon Source. I appreciate all discussion that I had with Jong-Woo Kim and his advice on life as a Ph.D. student. I also thank Thomas

Heitmann at the University of Missouri Research Reactor for excellent experimental support at TRIAX.

Theoretical contributions and calculations have been performed by several people at the Ames Laboratory: Raphael Fernandes, Jörg Schmalian, Yongbin Lee, Bruce N. Harmon, Suffian Khan, and Duane Johnson. I have benefited from their expertise and gained a more profound understanding of the underlying physics.

I am thankful to Bruce N. Harmon, James Cochran, and Ralph E. Napolitano for serving on my program of study committee, providing useful discussion, and allowing me to see outside of a box called "condensed matter physics".

I thank to my fellow group members: Shibabrata Nandi, Daniel K. Pratt, Gregory S. Tucker, and Gustav E. Rustan. I very much enjoyed working with them and I learned many different things from them; not only about research and physics but also about friendship and life in the US. I also thank the new members of our group: Jing han Soh, Wageesha Jayasekara, and Aashish Sapkota. Although the time we have shared is short, watching them endeavoring to learn lab work has made me recall my first-time in the lab and has reminded me why I chose this path.

I thank my friends Sarah Willis, Bert Pablo, Gustav E. Rustan, Gregory S. Tucker, Eundeok Mun, Sung-Ju Kang, Stella Kim, Hyunsoo Kim+Halyna Hodovanets, Kyuil Cho, Joong-Mok Park, Youngsoo Seol, Hyuntae Na, Nakheon Sung, Bongkyu Song, Donghan Shin, and Woosung Jung. I would like to add special thanks to Lei Ding.

Last but not least, I would like to thank to my father, mother, sister and brother-in-law for their infinite support, encouragement, and belief in me. I could not have done this without my family.

This work was supported by the Division of Materials Sciences and Engineering, Office of Basic Energy Sciences, U.S. Department of Energy. Ames Laboratory is operated for the U.S. Department of Energy by Iowa State University under Contract No. DE-AC02-07CH11358. Work at the High Flux Isotope Reactor, Oak Ridge National Laboratory, was sponsored by the Scientific User Facilities Division, DOE/OBES. Use of the Advanced Photon Source was supported by the US DOE under Contract No. DE-AC02-06CH11357.